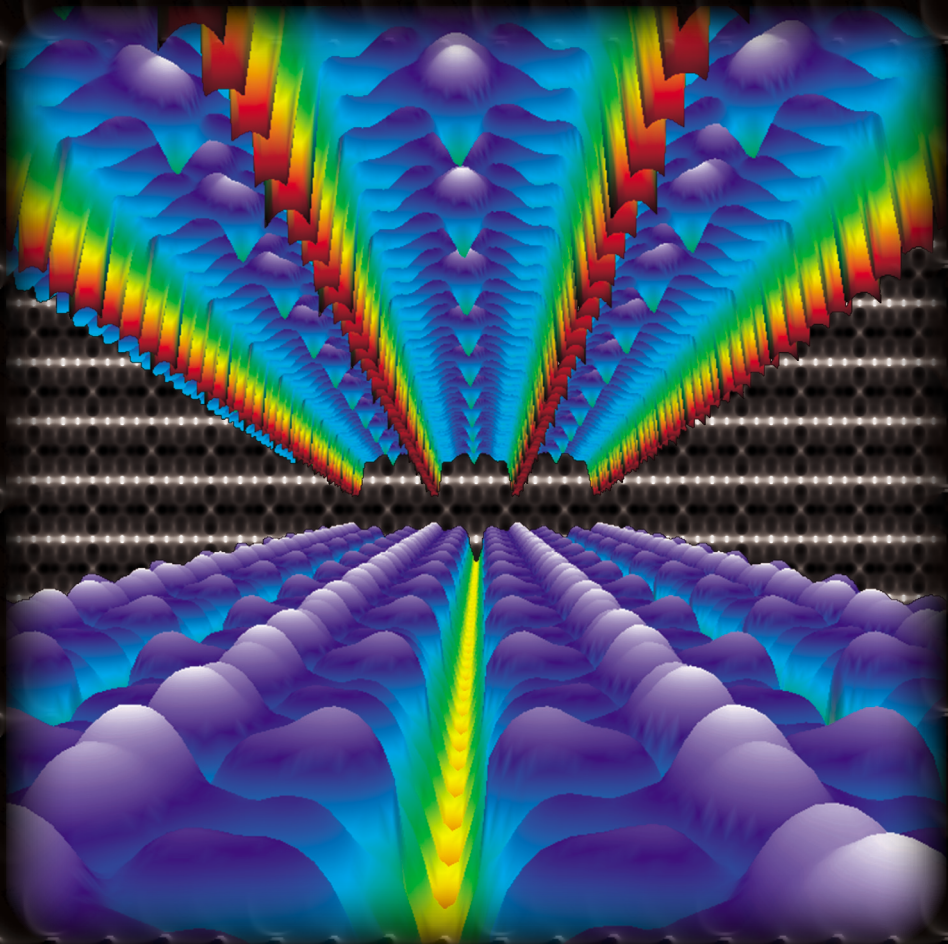


*Ab Initio Study of
Pt Induced Nanowires on Ge(001)*



Danny E. P. Vanpoucke

PROPOSITIONS

belonging to the PhD thesis

“*Ab initio* Study of Pt induced nanowires on Ge(001)”

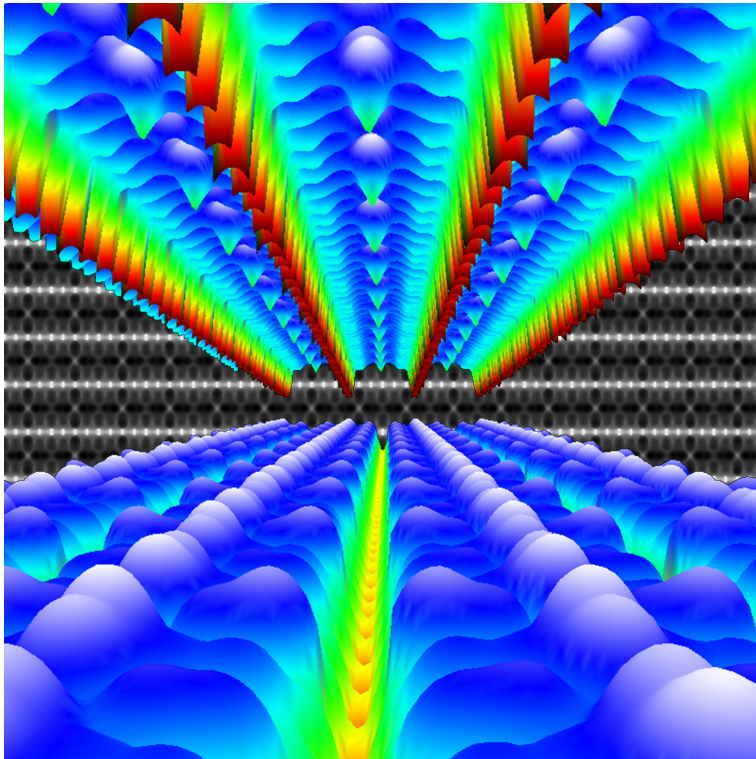
by

Danny E. P. Vanpoucke

1. The amazing thing about Pt nanowires is that they are build of Ge atoms.
2. Total energy calculations have only a limited use when identifying metastable surface configurations. For such systems, calculated STM images provide a powerful tool for simple identification.
3. Computational materials science is as a computer game, only the puzzles are harder to solve.
4. An important drawback of experimental STM is its chemical insensitivity. Since a theoretician knows exactly where which atoms are located, comparison to theoretical STM images is a simple and efficient way to alleviate this problem.
5. Theory without experiment is as poetry, it shows the world as we want it to be in our heart. Experiment without theory is as a fairy tale, it shows us what we imagine that makes the shadows in the night. Only together they can observe the reality that lies in between.
6. Scientific revolutions cannot be planned, despite what any funding agency might hope. Further development of current theories however can, and if we are lucky something unexpected happens which can contain the seed of new scientific progress.
7. Good calculations are computationally expensive. A calculation at half the price can quickly become totally useless.
8. The fundamental idea behind theoretical models is that they represent reality. Whenever a theoretical model and reality diverge, one should never look at reality to blame. It simply means the model wrong or insufficient, and a further or totally new model should be developed, learning from the errors of the old one.
9. The number of peaks in a calculated STM image of an object can never be lower than the number observed in experiment.

Enschede, September 2009

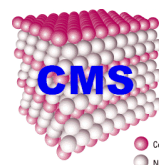
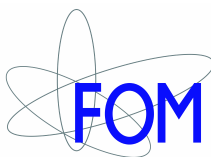
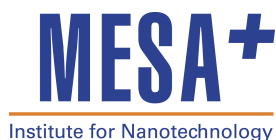
**AB INITIO STUDY OF
Pt INDUCED NANOWIRES ON Ge(001)**



Danny Eric Paul Vanpoucke

Composition of the Graduation Committee

Prof. dr. M. J. Peters	University of Twente, Chairwoman
Prof. dr. P. J. Kelly	University of Twente, Promoter
Dr. G. H. L. A. Brocks	University of Twente, Assistant Promoter
Prof. dr. R. Claessen	University of Würzburg
Prof. dr. C. Filippi	University of Twente, University of Leiden
Prof. dr. J. Pollmann	University of Münster
Prof. dr. S. E. Speller	Radboud University Nijmegen
Prof. dr. ir. H. J. W. Zandvliet	University of Twente



This work is part of the research programme of the ‘Stichting voor Fundamenteel Onderzoek der Materie (FOM)’, which is financially supported by the ‘Nederlandse Organisatie voor Wetenschappelijk Onderzoek (NWO)’.

The work described in this thesis was carried out at the “Computational Material Science” (CMS) group which belongs to the Faculty of Science and Technology (TNW) and the MESA⁺ Institute for Nanotechnology of the University of Twente.

Ab Initio Study of Pt Induced Nanowires on Ge(001)

D. E. P. Vanpoucke,

ISBN: 978-90-365-2873-3

Thesis Universiteit Twente, Enschede.

Publisher: Universiteit Twente, Enschede, The Netherlands

Printed by: Gildeprint Drukkerijen BV, Enschede, the Netherlands

© D. E. P. Vanpoucke, 2009

Cover: *Road To Nanotechnology*, presented at the Science as Art competition of the MRS 2009 Spring meeting. Composition of 3D and inverted grayscale calculated STM images of Pt nanowires on Ge(001).

**AB INITIO STUDY OF
Pt INDUCED NANOWIRES ON Ge(001)**

DISSERTATION

to obtain
the degree of doctor at the University of Twente,
on the authority of the rector magnificus,
prof.dr. H. Brinksma,
on account of the decision of the graduation committee,
to be publicly defended
on Friday 11th of September 2009 at 13:15

by

Danny Eric Paul Vanpoucke

born on April 10, 1980
in Gent, Belgium

This doctoral dissertation is approved by:

Prof. dr. P. J. Kelly Promoter

Dr. G. H. L. A. Brocks Assistant Promoter

facilius enim per partes
in cognitionem totius adducimur



Contents

1	Prelude	1
1.1	Introduction	1
1.2	Experimental background	2
1.3	Thesis outline	5
2	Theoretical background	7
2.1	Ab initio total energy calculations	7
2.1.1	Density Functional Theory	7
2.1.2	Pseudo-potentials and plane waves	13
2.2	Scanning Tunneling Microscopy	18
2.2.1	Experiment	18
2.2.2	Tersoff-Hamann method	20
2.3	Germanium in DFT	22
2.3.1	Bulk Germanium	22
2.3.2	Ge(001) surface reconstructions	27
3	The β-terrace	35
3.1	Introduction	35
3.2	Theoretical method	37
3.2.1	Setup	37
3.2.2	Ge(001)-surface and nomenclature	37
3.3	Theoretical results	40
3.3.1	Geometry and formation energy	40
3.3.1.1	Stability of the β -geometries	40
3.3.1.2	Stability of the γ -geometries	42
3.3.2	Electronic structure	43
3.3.2.1	General properties of the β -geometries	43
3.3.2.2	General properties of the γ -geometries	47
3.3.2.3	β_{6u} -structure as geometry for the β -terrace	47
3.3.2.4	Experimental existence of other β -geometries	52
3.3.3	The β_{6u} -geometry	52
3.3.4	Other geometries	57
3.3.4.1	Pt in the second layer	57

3.3.4.2	Pt in the third layer	59
3.3.4.3	Missing dimers or hidden dimers?	61
3.4	Conclusions	63
Interludium: β_{6u} convergence tests		65
4	Pt nanowires made of Ge atoms.	67
4.1	Introduction	67
4.2	Theoretical method	69
4.3	Results	69
4.3.1	Experimental background	69
4.3.2	First simple model	71
4.3.3	Intermediate geometries	77
4.3.4	Second model	80
4.3.5	Third model	85
4.3.6	Nec plus ultra	90
4.4	Discussion	97
4.4.1	Nanowires and formation paths	97
4.4.1.1	The NW1 geometry for solitary NWs.	99
4.4.1.2	The NW2 geometry for NW-patches	104
4.4.1.3	The WT geometry as precursor to NWs	107
4.4.2	Comparison to literature	108
4.5	Conclusions	110
5	CO on Ge nanowires	113
5.1	Introduction	113
5.2	Theoretical method	115
5.3	Results	115
5.3.1	CO on solitary NWs	116
5.3.2	CO on NW-arrays	120
5.4	Discussion	122
5.4.1	CO adsorption on Pt induced nanowires	123
5.4.2	Molecular electronics on Pt modified Ge(001)?	132
5.5	Conclusions	135
6	Conclusions and outlook	137
6.1	Conclusions: Questions and answers	137
6.2	Designing atomic nanowires.	139
Appendices		
A	Scanning Tunneling Microscopy	143
A.1	STM program	143
B	Geometric data for β and γ surface reconstructions	147

C Comparison of LDA to GGA	149
C.1 GGA setup	149
C.2 The β -terrace	150
C.3 Nanowires	151
C.4 CO on Pt induced NWs	153
C.5 Correlating LDA and GGA values	155
D List of abbreviations and symbols	157
Bibliography	159
Summary	169
Samenvatting	173
Acknowledgements	179
List of Publications	181
Curriculum Vitae	183

Chapter 1

relude

The complexity for minimum component costs has increased at a rate of roughly a factor of two per year . . . Certainly over the short term this rate can be expected to continue, if not to increase. Over the longer term, the rate of increase is a bit more uncertain, although there is no reason to believe it will not remain nearly constant for at least 10 years.

– Gordon E. Moore
(Moore’s Law 1965)

1.1 Introduction

Everybody knows Moore’s Law, [1] or at least has a vague idea of its consequences: “Next years computer will be faster.” In 1965, Gordon Moore observed that the number of components per integrated circuit, that could be produced at the lowest cost, doubled roughly every year.¹ This primarily economical law has meanwhile become a self-fulfilling prophecy, driving the micro-electronics industry. The exponential growth in processing power has mainly been due to ever further miniaturization. However this miniaturization cannot be maintained indefinitely and modern lithographical techniques are expected to meet their limits in the coming decade. [2] Moreover, miniaturization is steadily approaching its ultimate and final limit: atomic size devices connected by atomic wires. [3] To build these ultimate devices, chip makers are looking toward self-assembly of surface nanostructures and nanowires (NWs). [4]

Also from the fundamental theoretical point of view are NWs interesting. Their inherent one dimensional (1D) nature makes them ideal for studying dimensionality effects on, for example, magnetism and electronic structure. [5–12] It also provides

¹In the original article, a doubling every year is calculated based on the five data-points available. Later, Moore refined the period to a doubling every two years, based on further developments in the industry.

an excellent environment to study exotic physical phenomena associated with 1D systems, such as Peierls instability, charge density waves (CDWs) and Luttinger liquid behavior. [7, 13–15] The methods of fabrication are numerous, going from break junction created monatomic wires a few atoms long to self-assembled NWs hundreds of angstroms long, from NWs etched or imprinted on surfaces to monatomic chains build one atom at a time using a scanning tunneling microscope (STM) tip to atomic chains grown at step edges. [4, 16–21] The resulting structures, as can be suspected, show an equal range in variety. This in turn leads to a large spectrum of names: chains, (nano)wires, stripes, rods, *etc.* used for these structures. Definitions differ from author to author and overlap between terms exists. For simplicity, we will only use the term nanowire to refer to all such structures.²

In recent decades, NW structures have been observed for several metal/Ge systems. Pelletier *et al.* [22] note the formation of NWs when depositing Er on Ge(111) at 300°C. Other rare-earth nanorods are reported by Eames *et al.* [21] after deposition of Ho. The In/Ge(001) system, has a somewhat longer history. Submonolayer deposition of In on Ge(001) shows a complex reconstruction behavior, with models of In chains on Ge(001) already present in the work of Rich *et al.* [23] in 1990. Later work by Falkenberg *et al.* [24] proposes rather complex reconstructions for the observed In induced NWs. More recently Pt and Au NWs on Ge(001) attracted attention. After deposition of submonolayer amounts of Pt or Au on Ge(001) large arrays of monatomic NWs hundreds of angstroms long were observed by the groups of Zandvliet and Claessen. [18, 25]

In this thesis, the focus will go mainly to: Pt nanowires on Ge(001), as they are referred to in experimental literature. More specifically, I will try to elucidate its geometrical and electronic structure and relate this to observed experimental features. Since most of this work uses direct comparison with experiment, a description of the experiments and their results should not be omitted. In fact, it is the starting point of this story.

1.2 Experimental background

In 2003, Gürlü *et al.* were the first to observe NW formation on Ge(001) after deposition of roughly 0.25 monolayer (ML) of Pt followed by ten minutes of annealing at 1050 K. [18] They observed one-atom thick wires which could be hundreds of nanometers long, both solitary and in arrays. Their length was only limited by that of the underlying terrace, dubbed β -terrace, where they filled the troughs between dimer rows. This β -terrace has, at first glance, a simple dimer row structure. Upon closer inspection, a $c(4 \times 2)$ symmetry is observed, with the dimer rows consisting of two distinctly different dimer-types, therefore these rows are named ‘*quasi dimer rows*’ (QDRs).

The observed wires were defect- and kink-free, and the separation width between

²By using the phrase ‘wire’ we neither wish to imply the wires to be conducting nor even to consist of metal atoms.

wires in an array was always exactly 1.6 nm,³ *i.e.* every second trough of the underlying β -terrace. Upon closer examination of the NWs, all NWs appeared dimerised, leading to a basic 2×1 periodicity along the NWs. However, for NWs inside NW-arrays a periodicity doubling was observed, leading to a 4×1 translational symmetry along the NWs. This 4×1 periodicity was observed to persist up to at least 77 K, [26] while never appearing for solitary NWs and NWs at the edge of the NW-array. Also interesting is the fact that the buckling of adjacent NWs inside an array is always in phase. This could be a hint that there is an interaction between the wires, either direct, via a two dimensional (2D) electronic interaction, or indirect, via the substrate. The picture of atomic wires becomes even more interesting since Gürlü *et al.* discovered the NW arrays to be metallic.

In a nutshell, metallic wires have been observed with a thickness of 0.4 nm and lengths in the order of a micron: the dream of nearly any chip designer. These wires self-assemble, contrary to some earlier examples of monatomic wires that have to be built manually with an STM tip one atom at a time. They are also very robust: the observations by Gürlü *et al.* were done at room temperature (RT). Furthermore, when the NWs are exposed to the atmosphere, re-annealing them afterward in ultra high vacuum (UHV) showed the wires still to be intact.

The experimental story, however, does not end here. In 2005, Öncel *et al.* presented the observation of quantum confinement between the Pt NWs. [27] These 1D states for which the NWs act as barriers show an almost textbook behavior of a particle in a box. This was a somewhat surprising result. Considering the assumption that the wires consist of metal atoms, one would rather expect the wires to act as conductors rather than barriers for these surface states. This group also observed a very small band gap (BG) near the Fermi level, both at 77 K and 300 K, for an array of 1.6 nm spaced NWs, contrary to the observation of Gürlü.⁴ In 2006, Schäfer *et al.* [28] created Pt NWs on Ge(001) using a slightly lower anneal temperature of 600°C. However, they found the presence conduction states on the wires. Recent work by de Vries *et al.* [29] seems to indicate that the NWs wires with a 2×1 periodicity along the wire are metallic while the observation of a small BG combined with the periodicity doubling leads van Houselt *et al.* [26] to interpret this 4×1 periodicity in terms of a Peierls instability. They observe a phase transition from a 4×1 periodicity to 2×1 periodicity for the array NWs, when the system temperature goes up from 4.7 K to RT, while observing that the 4×1 periodicity can persist up to temperatures of 77 K. The issue of the metallicity of the wires seems to be a difficult one, and the experimental observations point toward a quite complex electronic structure around the Fermi level.

This is not the only complex behavior shown by the NWs. The most playful one up till now is called the atomic pinball machine (APM). [30] Saedi *et al.* discovered that pairs of NW-dimers could be controlled using the current of the STM tip, flip-

³Distances of 2.4 nm (and more) are also observed, but these wires belong to different “patches” of NW-array on the same terrace.

⁴The dI/dV curve of the NW arrays given by Gürlü *et al.* show an asymmetric dip toward zero near de Fermi level. The minimum value reached is of the order of 0.01 nA/V, which could make both results consistent within the error.

ping them back and forth like the flippers of a pinball machine.

Access to these nicely organized ultra-fine wires also opens the way to 1D molecular electronics, if one succeeds in decorating chains with selected molecules. In 2006, Öncel *et al.* [31] studied the diffusion and binding of CO on the NWs. They found that CO coverage of the NWs was independent of the pressure. Furthermore, only one adsorption site was observed, showing a protrusion in filled state STM images and a large depression in the empty state images.⁵ From this, Öncel *et al.* concluded the adsorption site was located on top of one of the NW dimer atoms. The CO molecules also appeared to be highly mobile in this RT experiment, performing a 1D random walk. Later experiments by Kockmann *et al.* [32] studied CO adsorption at 77 K, and they discovered two more adsorption sites, located at the long and short NW dimer bridge positions.⁶ Contrary to the RT experiment by Öncel *et al.*, CO molecules here are reported to be immobile at 77 K. Using statistical analysis of nearest neighbor spacings, a long range (3–4 nm) repulsive interaction between the CO molecules was revealed.

The choice of CO, by Öncel and Kockmann, was based on the argument that CO has a high sticking probability and affinity for Pt while it is low for Ge. It also served a different purpose: as an attempt at the characterization of the NWs.

Despite all the beautiful experiments, a good structural model to correlate and explain all the observations was missing. STM images are invaluable in all the experiments presented here, but there is one important detail missing: “What species of atom is being observed?” STM is chemically insensitive, so intuition and educated guesses usually take over this in part of the analysis.

Some important questions have remained unanswered:

- Although a quarter ML of Pt is deposited, only a fraction of the surface is covered with β -terraces, and only a fraction of the β -terraces contains NWs. So what is the local Pt density in the NW arrays?
- Connected to this issue, and the chemical insensitivity of an STM: Where are the Pt atoms located? To put it bluntly: what is the geometry of the NWs? And more specifically, why do NWs grow only every *second* trough of the β -terrace?
- What causes the long range repulsive interaction between adsorbed CO molecules?
- Why are there conducting states between the wires, while the wires themselves are not clearly metallic, although they are supposed to consist of metal (platinum) atoms?

Most of these questions trace back to the need for a good theoretical model of this system. From this model, the problems with regard to the electronic structure near the Fermi level can be addressed. Also the adsorption behavior of CO and other molecules can only be studied once a decent model for the wires is presented.

⁵The depression had a width of roughly 2.0 nm, while the length of a NW dimer is only 0.8 nm, making it 2.5 dimers long!

⁶Short means on a dimer, and long refers to the bridge site between two NW dimers.

1.3 Thesis outline

Ab initio is Latin for “*from the beginning*”. It is often used in condensed matter physics to refer to calculations which (optimally) do not use any empirical or other parameters, except the physical constants, and start purely from the known laws of physics.⁷ Next to using *ab initio* calculations we try, wherever possible, to work using an *ab initio*-principle: This means that to study a complex problem/system, we start from a more simple problem/system and then add increasing layers of complexity until we arrive at the actual problem/system we want to study. Throughout this dissertation this way of working is applied, both for the entire thesis as for smaller parts such as chapters and sections. It serves as a guide, not to lose track of the intended goal.

The main goal of this work is the development of a sound structural model of Pt NWs on Ge(001) and the interpretation and explanation of the unexpected and strange behavior of the NWs in experiments. In short, we try to formulate a consistent and hopefully simple answer to the questions stated in the previous paragraph.

The outline of this thesis is as follows: In **Chapter 2** we give an overview of the theoretical methods used. We have a look at bulk Ge and the Ge(001) surface, and how they behave in the DFT framework: what are the known problems, are there solutions, and do we need these solutions? Since the NWs are inherently connected to the underlying surface reconstruction, modeling this reconstruction is our first task. This is done in **Chapter 3**. During this study, we also identify some previously not understood surface reconstructions of the α -terrace. With the knowledge of the β -terrace, we move on, and in **Chapter 4** we develop a model for the experimentally observed Pt NWs. This turns out not to be a trivial task, and multiple subsequent generations of models with increasing Pt density pass by, converging to a final model giving a perfect match with the experiments introduced in **Sec. 1.2**. As will become clear, our final model differs considerably from the intuitive tentative model proposed by Gürlü *et al.* and even seems to contradict the observation of CO adsorption on the NWs. In **Chapter 5**, we therefore study the adsorption of CO on our model NWs, and show how CO adsorption fits into the story.

In the final chapter, **Chapter 6**, we draw conclusions and extend these into an outlook, placing this work in the setting of (nano-) materials engineering. We also look at the use of calculated STM images as a means to overcome the chemical insensitivity of a real-life STM. At the end, a summary is given.

⁷This is why some also refer to them as ‘first principles’ calculations.

Chapter 2

heoretical background

All exact science is dominated by the idea of approximation.
– Bertrand Russell

2.1 Ab initio total energy calculations

In this thesis, we perform DFT calculations using the Vienna Ab-initio Simulation Package (VASP). This program solves the Hohenberg-Kohn-Sham equations numerically to find the total energy of a given system. For this reason, this type of calculations is also sometimes called: *total energy calculations*. To solve these equations efficiently the projector augmented wave method is used. [33, 34] In the following sections, we will give a short introduction to these topics and the basic ideas behind them. Those interested in a more in-depth derivation and historical background are referred to the large amount of literature which exists on these topics. The references provided in this section should provide a good starting point.

2.1.1 Density Functional Theory: Hohenberg-Kohn-Sham equations

Most of the properties of solids can be traced back to the behavior of their constituent parts, more specifically the electrons gluing the nuclei together. In quantum mechanics (QM), a system of a single particle of mass m is described by the single particle Schrödinger equation: [35]

$$\hat{\mathcal{H}}\Psi = E\Psi, \quad (2.1)$$

with E the total energy of the particle, Ψ its wavefunction and with the Hamiltonian $\hat{\mathcal{H}}$ given by

$$\hat{\mathcal{H}} = \hat{T} + \hat{V} = \frac{-\hbar^2}{2m}\nabla^2 + V_{ext}(\mathbf{r}), \quad (2.2)$$

consisting of the kinetic energy term \hat{T} and a potential energy term \hat{V} due to an external potential V_{ext} at position \mathbf{r} .¹ A solid however consists of many particles, all interacting with one another. For the simpler noninteracting many-particle system the Schrödinger equation looks formally exactly like the one given in Eq. (2.1), but now the kinetic and potential terms in the Hamiltonian are the sum of all the single particle kinetic and potential energy terms. To include the particle interactions in the system, a potential energy term \hat{V}_{ij} is added for each pair of particles. The sum of these potential energy terms is divided by two to avoid double counting, resulting in an interacting Hamiltonian:

$$\hat{\mathcal{H}} = \sum_i (\hat{T}_i + \hat{V}_i) + \frac{1}{2} \sum_{\substack{i,j \\ i \neq j}} \hat{V}_{ij}. \quad (2.3)$$

In what follows, we will assume a solid to consist of only two types of particles: electrons and nuclei.² This allows us to rewrite Eq. (2.3) as:

$$\hat{\mathcal{H}} = \sum_i \left(\hat{T}_{N_i} + \hat{V}_{N_i} + \frac{1}{2} \sum_{j \neq i} \hat{V}_{N_i N_j} \right) + \sum_i \left(\hat{T}_{e_i} + \hat{V}_{e_i} + \frac{1}{2} \sum_{j \neq i} \hat{V}_{e_i e_j} \right) + \sum_{i,j} \hat{V}_{N_i e_j}, \quad (2.4)$$

where the indices N refer to nuclei, and e to electrons.

Because the mass of a nucleus is 10^3 – 10^5 times larger than that of an electron, its velocity will be much smaller, resulting in two different timescales for particle motion in the system: a small timescale which is defined by the electron motion and a large timescale defined by the motion of the nuclei. For the fast moving electrons, the nuclei appear static, so their motion can be approximated as being on a constant potential energy surface due to the nuclei (Born-Oppenheimer or adiabatic approximation [36]). This allows for a separation of the wavefunction Ψ in a nuclear wavefunction $\chi(\mathbf{R})$, which is a function of the nuclear positions $\mathbf{R} = \mathbf{R}_1, \dots, \mathbf{R}_m$, and an electronic wavefunction $\phi(\mathbf{r}, \mathbf{R})$, which is a function of both the nuclear (\mathbf{R}) and electronic ($\mathbf{r} = \mathbf{r}_1, \dots, \mathbf{r}_n$) positions:

$$\Psi = \phi(\mathbf{r}, \mathbf{R}) \chi(\mathbf{R}). \quad (2.5)$$

This allows our single Schrödinger equation (2.4) to be rewritten as a set of coupled Schrödinger equations :

$$\begin{cases} \sum_i \left(\hat{T}_{e_i} + \frac{1}{2} \sum_{j \neq i} \hat{V}_{e_i e_j} + \sum_{k \neq i} \hat{V}_{e_i N_k} \right) \phi_n(\mathbf{r}, \mathbf{R}) = \varepsilon_n(\mathbf{R}) \phi_n(\mathbf{r}, \mathbf{R}) \\ \sum_i \left(\hat{T}_{N_i} + \frac{1}{2} \sum_{j \neq i} \hat{V}_{N_i N_j} + \varepsilon(\mathbf{R}) \right) \chi(\mathbf{R}) = E \chi_n(\mathbf{R}). \end{cases} \quad (2.6)$$

For the nuclear motion on the other hand, due to its much larger timescale, the nuclei can be assumed to move on the potential energy surface of the electronic ground

¹We will use bold symbols to indicate vectors, or sets of vectors.

²We ignore the existence of particles like protons, neutrons, quarks, ... and thus consider a nucleus to have no internal structure, so it can be regarded as a closed system, interacting as a single point particle.

state. A further assumption that can be made with regard to the nuclei, is that the quantum effects on their motion are negligible. This allows their movement to be described by the much easier classical Newtonian equations of motion instead of their time-dependent Schrödinger equation. The initially fully QM system is now replaced by a system of classical nuclei and QM electrons.

We now turn our attention toward the many-electron wavefunction $\phi(\mathbf{r}, \mathbf{R})$. From the Pauli exclusion principle, [37] we know that each electron has its own private state,³ which can be coupled to a single particle wavefunction, within the independent particle model.⁴ We also know that there are $N!$ ways to distribute N particles over N states. So the electronic many particle wavefunction can be written as a linear combination (LC) of $N!$ products of N single particle wavefunctions. Since electrons are fermions, the many-electron wavefunction has to be antisymmetric, *i.e.* the exchange of two single particle wavefunctions in such a product results in an extra minus sign, leading to $\frac{N!}{2}$ negative terms in the LC. The simplest way to represent such a LC is a determinant of an $N \times N$ matrix, called Slater determinant: [39]

$$\phi(\mathbf{r}, \mathbf{R}) = \frac{1}{\sqrt{N!}} \begin{vmatrix} \varphi_1(\mathbf{r}_1) & \dots & \varphi_1(\mathbf{r}_N) \\ \vdots & & \vdots \\ \varphi_N(\mathbf{r}_1) & \dots & \varphi_N(\mathbf{r}_N) \end{vmatrix}, \quad (2.7)$$

where we require the wavefunctions to be orthonormal, *i.e.* $\int \varphi_\lambda^*(\mathbf{r}_i) \varphi_\mu(\mathbf{r}_i) d\mathbf{r}_i = \delta_{\lambda\mu} \quad \forall i, \mu, \lambda \in \{1..N\}$. Starting from an electronic Hamiltonian

$$\hat{\mathcal{H}} = \sum_i \frac{-\hbar^2}{2m} \nabla_i^2 + \hat{V}_{\text{ext}} + \frac{1}{2} \sum_{j \neq i} \frac{e^2}{(4\pi\epsilon_0) \|\mathbf{r}_i - \mathbf{r}_j\|}, \quad (2.8)$$

where the second term is due to the potential generated by the nuclei combined with any other external potentials working on the system and the third term is just the Coulomb interaction between the electrons, with a factor one half to prevent double

³If states are not spin-dependent, two electrons fit into a single state: one with spin up, and one with spin down.

⁴In this model, the interaction between the N particles is replaced by an effective potential which represents the average effect on a particle by the remaining $N - 1$ particles. This effectively replaces a system of N interacting particles by a system of N non-interacting particles in an effective potential. [38]

counting, the total energy ε of this system can be found via:

$$\begin{aligned}
\varepsilon &= \langle \phi(\mathbf{r}, \mathbf{R}) | \hat{\mathcal{H}} | \phi(\mathbf{r}, \mathbf{R}) \rangle = \int \phi^*(\mathbf{r}, \mathbf{R}) \hat{\mathcal{H}} \phi(\mathbf{r}, \mathbf{R}) d\mathbf{r} \\
&= N! \sum_{\mu} \frac{1}{N!} \int \varphi_{\mu}^*(\mathbf{r}_i) \left(\frac{-\hbar^2}{2m} \nabla_{\mathbf{r}_i}^2 + \hat{V}_{\text{ext}}(\mathbf{r}_i) \right) \varphi_{\mu}(\mathbf{r}_i) d\mathbf{r}_i \\
&\quad + \frac{N!}{2} \sum_{\substack{\lambda, \mu \\ \lambda \neq \mu}} \left[\frac{1}{N!} \int \varphi_{\lambda}^*(\mathbf{r}_i) \varphi_{\mu}^*(\mathbf{r}_j) \frac{e^2}{(4\pi\varepsilon_0) \|\mathbf{r}_i - \mathbf{r}_j\|} \varphi_{\mu}(\mathbf{r}_j) \varphi_{\lambda}(\mathbf{r}_i) d\mathbf{r}_i d\mathbf{r}_j \right. \\
&\quad \left. - \frac{1}{N!} \int \varphi_{\lambda}^*(\mathbf{r}_i) \varphi_{\mu}^*(\mathbf{r}_j) \frac{e^2}{(4\pi\varepsilon_0) \|\mathbf{r}_i - \mathbf{r}_j\|} \varphi_{\lambda}(\mathbf{r}_j) \varphi_{\mu}(\mathbf{r}_i) d\mathbf{r}_i d\mathbf{r}_j \right].
\end{aligned} \tag{2.9}$$

The last two terms represent the Coulomb electron-electron interaction, with the first term the direct Coulomb interaction and the second term the exchange interaction.⁵ A full derivation can be found in standard physics textbooks, like reference [38]. The groundstate of the system is found based on a variational principle. Starting from the variational condition

$$\delta\varepsilon = \delta \int \phi^*(\mathbf{r}, \mathbf{R}) \hat{\mathcal{H}} \phi(\mathbf{r}, \mathbf{R}) d\mathbf{r} = 0, \tag{2.10}$$

with $\int \phi^*(\mathbf{r}, \mathbf{R}) \phi(\mathbf{r}, \mathbf{R}) d\mathbf{r} = 1$ (which follows directly from Eq. (2.7)) and constraints $\int \varphi_{\lambda}^*(\mathbf{r}_i) \varphi_{\mu}(\mathbf{r}_i) d\mathbf{r}_i = \delta_{\lambda\mu}$. We introduce N^2 **constant** Lagrangian multipliers $k_{\lambda\mu}$ from which follows: [40]

$$\delta \int k_{\lambda\mu} \varphi_{\lambda}^*(\mathbf{r}_i) \varphi_{\mu}(\mathbf{r}_i) d\mathbf{r}_i = 0. \tag{2.11}$$

Combining Eqs. (2.10) and (2.11), we obtain:

$$\delta \underbrace{\int \phi^*(\mathbf{r}, \mathbf{R}) \hat{\mathcal{H}} \phi(\mathbf{r}, \mathbf{R}) - \sum_{\lambda\mu} k_{\lambda\mu} \varphi_{\lambda}^*(\mathbf{r}) \varphi_{\mu}(\mathbf{r}) d\mathbf{r}}_{=g} = 0. \tag{2.12}$$

The new function g defined in Eq. (2.12) has to satisfy the Euler-Lagrange equations: [41]

$$\frac{\partial g}{\partial y_i} - \sum_j \frac{\partial}{\partial x_j} \frac{\partial g}{\partial (\partial y_i / \partial x_j)} = 0, \tag{2.13}$$

where x_j is a spatial coordinate (there are $3N$ of them) and y_j is one of the single particle wavefunctions φ_{λ} or its complex conjugate. Solving Eq. (2.13) for the many

⁵Although the derivation starts with sums over i and j (from Hamiltonian Eq. (2.8)), at the end of the derivation the i and j indices are coupled to the μ and λ indices of the single particle wavefunctions. The sums over λ and μ however give a better feel of the range of the summation, so they are used here instead of i and j .

particle system described here can be considered a trivial yet very tedious task, due to all the parameters and summations involved. To make things a little easier one can start from Eq. (2.9) and make use of

$$\int \psi^* \frac{\partial^2 \psi}{\partial x^2} dx = \psi^* \frac{\partial \psi}{\partial x} \Big| - \int \frac{\partial \psi^*}{\partial x} \frac{\partial \psi}{\partial x} dx, \quad (2.14)$$

where we assume ψ to vanish quick enough, such that the first term becomes zero. For $y_j = \varphi_\alpha$, the second term of Eq. (2.13) simply reduces to $\nabla^2 \varphi_\alpha$. The first term is a bit more complicated,⁶ but keeping in mind the constraints given earlier, the Euler-Lagrange equations can be written as:

$$\begin{aligned} \left(\frac{-\hbar^2}{2m} \nabla^2 + \hat{V}_{\text{ext}} \right) \varphi_\alpha(\mathbf{r}) + \sum_{\mu \neq \alpha} \left[\frac{e^2}{4\pi\epsilon_0} \int \frac{\varphi_\mu^*(\mathbf{r}') \varphi_\mu(\mathbf{r}')}{\|\mathbf{r} - \mathbf{r}'\|} d\mathbf{r}' \varphi_\alpha(\mathbf{r}) \right. \\ \left. - \frac{e^2}{4\pi\epsilon_0} \int \frac{\varphi_\mu^*(\mathbf{r}') \varphi_\alpha(\mathbf{r}')}{\|\mathbf{r} - \mathbf{r}'\|} d\mathbf{r}' \varphi_\mu(\mathbf{r}) \right] - k_{\alpha\alpha} \varphi_\alpha(\mathbf{r}) = 0 \\ \Rightarrow \hat{\mathcal{H}} \varphi_\alpha(\mathbf{r}) = k_{\alpha\alpha} \varphi_\alpha(\mathbf{r}) \quad , \end{aligned} \quad (2.15)$$

which looks like a set of eigenvalue equations with the Lagrangian multipliers as eigenvalues.⁷ This set of equations is known as the Hartree-Fock (HF) equations. [42, 43] Note that the factors $\frac{1}{2}$ of Eq. (2.9) have vanished due to taking the derivative $\frac{\partial g}{\partial y_j}$ in Eq. (2.9) of the double sums.

The HF approximation, described above, starts from the independent particle model. [38] Since the number of particles in a solid is given in terms of Avogadro's number N_A ,⁸ [45] it is not practical to calculate all these N^2 interaction terms directly. To reduce this number, one can use a mean field approximation, where every particle interacts with the potential surface generated by all other particles. Using a self-consistent iterative scheme, only order N interactions need to be calculated, giving this approach a linear scaling with the system size.

The mean field idea of abstracting ‘the interaction with the other electrons’ into an external field, leads us to another way of abstracting the system of electrons. Because electrons are indistinguishable from one another and we are only interested in the total behavior, we can replace the electrons by their density, and define the energy function(al) as function of the electron density, instead of electron position. This approach is known as density functional theory (DFT). [46, 47] The electrons lose their identity as a particle with classical properties, and we move to a probabilistic view.

⁶The N^2 Lagrangian multipliers can be considered the elements of an $N \times N$ Hermitian matrix. Such a matrix can be diagonalized by a unitary transformation, making all $k_{\mu,\lambda} = 0$ for $\mu \neq \lambda$. This unitary transformation only changes the phase-factor of the Slater determinant and does not influence the energy functional, so for simplicity we keep the old notations.

⁷To be exact, they are not genuine eigenvalue equations, since the electron-electron interaction potentials depend on the wavefunctions. To solve this set of ‘almost’ eigenvalue equations, an iterative method can be used.

⁸ $N_A = 6.02214179(30) \times 10^{23} \text{ mol}^{-1}$ [44]

One might compare this to the classical transition from a microscopic description to a macroscopic description of a system, where it is not necessary to know the exact motion of every particle to find global properties of the system. From the numerical point of view, the advantage is obvious, the computational effort does not scale with the number of particles anymore, but with the spatial grid used to represent the electron density.

In DFT, the groundstate of a system is found by the minimization of the functional of the particle (in this case electrons) density $n(\mathbf{r})$:

$$E_0 = \min \left\{ E[n_0(\mathbf{r})] \right\} \quad \text{and} \quad \left. \frac{\delta E[n(\mathbf{r})]}{\delta n(\mathbf{r})} \right|_{n(\mathbf{r})=n_0(\mathbf{r})} = 0, \quad (2.16)$$

with the indices 0 indicating groundstate values. The total energy functional is constructed as:

$$E[n(\mathbf{r})] = T[n(\mathbf{r})] + V_{\text{ext}}[\mathbf{r}] + E^H[n(\mathbf{r})] + E^{xc}[n(\mathbf{r})], \quad (2.17)$$

where the first term represents the kinetic energy, the second term the potential energy due to interaction with the nuclei and possible external potentials, the third term is the Hartree energy or the direct Coulomb interaction (*cf.* third term in Eq. (2.15)) and the fourth term presents the exchange and correlation energy. This last term consists of the exchange energy (also found in the HF equations) and an extra contribution due to correlation effects, which are omitted in the HF approximation. Although this functional looks uncomplicated enough, the problems start when one wants to calculate it. The exact form of both the kinetic and the exchange-correlation term are unknown, and have to be approximated as a consequence. A good initial approximation is to use the values found for a homogeneous electron gas with the same density (local density approximation). The resulting set of equations are called the Hohenberg-Kohn-Sham (HKS) equations:

$$\left\{ \frac{-\hbar^2}{2m} \nabla^2 + V_{\text{ext}} + \frac{e^2}{4\pi\epsilon_0} \int \frac{n(\mathbf{r}')}{\|\mathbf{r} - \mathbf{r}'\|} d\mathbf{r}' + E^{xc}[n(\mathbf{r})] \right\} \varphi_i(\mathbf{r}) = \epsilon_i \varphi_i(\mathbf{r}), \quad (2.18)$$

with $E^{xc}[n(\mathbf{r})] = \frac{\delta \{n(\mathbf{r})\epsilon[n(\mathbf{r})]\}}{\delta n(\mathbf{r})}$. The total energy of this system is found through summing over all ϵ_i . However, if we just sum everything, some terms will be counted double. The origin of this double counting can be traced back to our derivation of the ground state energy in the HF approximation. The $\frac{\partial g}{\partial \varphi_\alpha}$ -term of the Euler-Lagrange equations combined with the double sums of Eq. (2.9) results in an energy contribution for an electron (state) α as a consequence of its interaction with the other electrons. Because this energy contribution represents the total interaction between two electrons, summing over all electrons will count these contributions for both electrons involved. To correct for this double counting a correction for the Hartree term is introduced: $-\frac{1}{2} \int \frac{e^2}{4\pi\epsilon_0} \frac{n(\mathbf{r})n(\mathbf{r}')}{\|\mathbf{r} - \mathbf{r}'\|} d\mathbf{r}d\mathbf{r}'$. The contribution of the exchange-correlation term to the total energy should be $\epsilon_{xc}[n(\mathbf{r})]$, but the variational

approach leads to $\frac{\delta\{n(\mathbf{r}\varepsilon[n(\mathbf{r})])\}}{\delta n(\mathbf{r})} = \varepsilon_{xc}[n(\mathbf{r})] + n(\mathbf{r})\frac{\delta\varepsilon_{xc}[n(\mathbf{r})]}{\delta n(\mathbf{r})}$, so the term $n(\mathbf{r})\frac{\delta\varepsilon_{xc}[n(\mathbf{r})]}{\delta n(\mathbf{r})}$ has to be subtracted again. The corrected total energy for this system within the local density approximation of the HKS equations is then given by:

$$E_{\text{tot}} = \sum_i \varepsilon_i - \frac{e^2}{2(4\pi\varepsilon_0)} \int \frac{n(\mathbf{r})n(\mathbf{r}')}{\|\mathbf{r} - \mathbf{r}'\|} d\mathbf{r}d\mathbf{r}' - n(\mathbf{r})\frac{\delta\varepsilon_{xc}[n(\mathbf{r})]}{\delta n(\mathbf{r})}. \quad (2.19)$$

As we already noted before, the HKS-approach makes two approximations: for the ground-state kinetic energy term and the exchange-correlation term. For the ground-state kinetic energy an exact formula exists:

$$\tilde{T} = \sum_i n_i \langle \tilde{\psi}_i | \frac{-\hbar^2}{2m} \nabla^2 | \tilde{\psi}_i \rangle, \quad (2.20)$$

with $\tilde{\psi}_i$ and n_i the orbitals and their occupation number. In a system with interacting electrons however, the number of terms in the sum becomes infinite, which is impractical for numerical purposes. Kohn and Sham [47] replace this by the kinetic energy for a system of noninteracting electrons:

$$T = \sum_i^N \langle \psi_i | \frac{-\hbar^2}{2m} \nabla^2 | \psi_i \rangle, \quad (2.21)$$

where ψ_i are the N lowest eigenstates of the one-electron Hamiltonian. Although the latter is a good functional of the density, it differs slightly from the kinetic energy given in Eq. (2.20). This small difference between the exact \tilde{T} and replacing T is then added to the exchange-correlation term via its definition. [48] This allows us to consider T as exact, and the exchange-correlation term the only approximation left in the HKS-approach. This also means that any improvement on calculations made within the HKS-approach will have to come from an improved exchange-correlation functional. Within solid state calculations the most common approximations for E^{xc} are the local density approximation (LDA) and generalized gradient approximation (GGA). In LDA, E^{xc} is derived from the exchange-correlation energy of a uniform electron gas with the same density, one could see this as a zeroth order approximation, which tends to give good results for slowly varying densities. One step up, is when also the gradient of the density is included, which is done in GGA.

2.1.2 Solving the HKS equations: Pseudo-potentials and plane waves

To solve the HKS Eqs. (2.18), one needs to choose a basis set (ψ_i). In a perfect crystalline solid, the crystal structure is repeated periodically, allowing for the use of periodic boundary conditions in calculations. The electrostatic potential in such a system shows the same periodicity, and electrons moving in this periodic potential are described by a *Bloch wave*. Such a Bloch wave consists of two parts, a plane wave and a periodic function $u(\mathbf{r})$ with the same periodicity as the crystal lattice:

$$\psi_{n\mathbf{k}}(\mathbf{r}) = u_{n\mathbf{k}}(\mathbf{r})e^{i\mathbf{k}\cdot\mathbf{r}}, \quad (2.22)$$

with \mathbf{k} a wave vector and n a band index.⁹ The Bloch theorem [49, 50] states that in such a periodic system the eigenfunctions $\psi_{n\mathbf{k}}(\mathbf{r})$ have the property $\psi_{n\mathbf{k}}(\mathbf{r} + \mathbf{R}) = \psi_{n\mathbf{k}}(\mathbf{r})e^{i\mathbf{k}\cdot\mathbf{R}}$, where \mathbf{R} is a lattice vector. This is a direct consequence of the property of the periodic function $u_{n\mathbf{k}}(\mathbf{r} + \mathbf{R}) = u_{n\mathbf{k}}(\mathbf{r})$. Another general property of a periodic function $u_{n\mathbf{k}}(\mathbf{r})$ is that it can be decomposed in a Fourier series of plane waves, which in turn allows us to write the Bloch eigenfunctions $\psi_{n\mathbf{k}}(\mathbf{r})$ as a Fourier series of plane waves. Hence, the choice to use plane waves as a basis set to solve the HKS equations becomes quite obvious.

From the numerical point of view, there are more advantages. Plane waves are ideally suited to use fast Fourier transform (FFT) to pass between real and reciprocal space.¹⁰ Hellmann-Feynman forces [51, 52] on the ions do not need corrections, where the use of localized orbitals would require Pulay corrections. [53] Furthermore, plane waves allow for a good control of the basis set convergence.

However, plane waves have one serious drawback: slow convergence. This slow convergence is caused by the necessity to reproduce the nodal character of the valence orbitals, which in turn is a consequence of the valence orbitals being orthogonal to the fast oscillating tightly bound core orbitals. So the heart of the problem is traced back to the cores.

This problem is solved through the introduction of pseudo-potentials (PP). The basic idea behind PP, which dates back to the work of Fermi, [54] is to replace the strongly interacting ionic potential due to the nucleus and tightly bound core electrons, with a weakly interacting effective potential. Since the core states are chemically inert and chemical binding happens far away from the ionic cores, a PP should have exactly the same scattering properties as the original potential in this region, while in the core-region it is smooth enough such that no nodes are present in the pseudo-wavefunctions. As a consequence of this approach, the core electrons have to be kept frozen.¹¹ Since PP for a given system are not unique, they can be created for specific needs and with specific properties. For example, a general PP for a given system will generate pseudo-wavefunctions which are not orthonormal. Because orthonormality is a highly appreciated property for wavefunctions, *i.e.* we would like to get the correct charge distribution between the core region and the interstitial region, PP that are norm-conserving were developed. The pseudo-wavefunctions of these so-called norm-conserving PP (NCPP) are normalized and are solutions of a PP chosen to reproduce the properties of the valence electrons of an all-electron calculation, making them more accurate.

Within the realm of PP, NCPP are the most simple version. A slightly more complex type of PP are the Ultra-Soft PP (USPP), where the requirement of or-

⁹For a given wavefunction ψ , the single-particle Schrödinger equation in a system with boundary conditions (*e.g.* particle in a box) has a restricted set of solutions. For electrons in solids these solutions are called one-electron bands, and can be given a discrete index n .

¹⁰Some properties are easy to calculate in real-space but hard in reciprocal space (*e.g.* potential energy term) and *vice versa* (*e.g.* kinetic energy term).

¹¹The core electrons are precalculated in their atomic environment and kept frozen during later calculations. This can be done under the assumption that only valence electrons are influenced by and interact with the chemical environment.

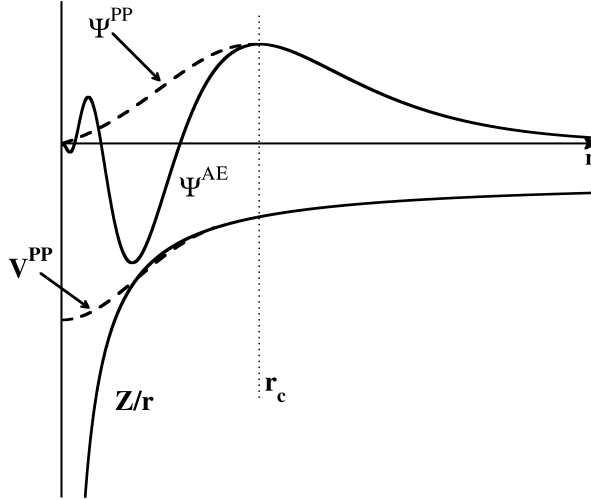


Figure 2.1: Pseudo-potentials are generated in such a way that the pseudo-wavefunction contains no nodes inside the core region $r < r_c$ and becomes the exact all-electron wavefunction for $r > r_c$.

thogonality is not maintained. Even more general are the plane augmented waves (PAW), which are used for the calculations in this thesis. Although the PAW-method is formally an all-electron formalism, the PAWs are formulated in the style of USPP in the VASP program. Because of this, and because the basic idea behind NCPP and USPP is the same, we have a more in-depth look at these NCPP in the following paragraphs. Afterward we will give a rough sketch of the differences with PAWs as used in the VASP program.

Desired properties for NCPP.

To build a “good” PP, one starts with a list defining the desired properties. Such a list of properties for an *ab-initio* PP was given by Hamann, Schlüter and Chiang: [55]

1. All-electron (AE) and pseudo valence eigenvalues agree for a chosen atomic reference configuration:

$$\varepsilon_l^{\text{PP}} = \varepsilon_l^{\text{AE}}. \quad (2.23)$$

2. The normalized all-electron and pseudo (radial) wavefunctions agree beyond the chosen core radius r_c :

$$R_l^{\text{PP}}(r) = R_l^{\text{AE}}(r) \quad \text{for } r \geq r_c. \quad (2.24)$$

3. The integrated charge for the pseudo (valence) wavefunctions inside the core radius r_c agrees with that of the all electron valence wavefunctions. (norm-conservation)

4. The logarithmic derivatives and their first energy derivatives of the all-electron and pseudo-wavefunctions agree for $r \geq r_c$.

Properties 1 and 2 reflect the fact that we want to recover the correct scattering properties in the interstitial region of our system, so the PP should be exactly the same as the real atomic potential far, *i.e.* $r \geq r_c$, from the core. Property 3 introduces the norm-conservation, although the radial pseudo-wavefunction $R_i^{\text{PP}}(r)$ and the real radial wavefunction $R_i^{\text{AE}}(r)$ differ inside the core region ($r < r_c$) it requires that the integrated charge,

$$Q = \int_0^{r_c} |R_i^{\text{PP}}(r)|^2 r^2 dr = \int_0^{r_c} |R_i^{\text{AE}}(r)|^2 r^2 dr, \quad (2.25)$$

is the same for each valence state. As a consequence, the *normalized* pseudo-wavefunction will be equal to the all-electron wavefunction outside the core region. The final property, more specifically the equality of first energy derivatives, ensures the transferability of the PP from the simple environment where it was generated (*e.g.* spherical atom) to the complex environment where it will be used (*e.g.* solid, molecule). Hamann *et al.* [55] showed that the equality of the first energy derivatives is implied by the norm-conservation property.

One of the main aims when building a PP is to make it as smooth as possible, such that decomposition can be done in an as small as possible number of plane waves. This leads to a fifth desired property:

5. The pseudo-wavefunctions generated from the PP should contain no nodes.

Now that we know what we want in a PP, we can have a look at how one is constructed.

Construction of NCPP.

Over the years many schemes have been devised to generate PP. [55–57] We will follow the recipe by Troullier and Martins for the construction of a NCPP. [58]

PP are generally generated from all-electron atomic calculations. This is done by solving the radial Schrödinger equation:

$$\left[\frac{-1}{2} \frac{d^2}{dr^2} + \frac{l(l+1)}{2r} + V(\rho, r) \right] r R_{nl}(r) = \varepsilon_{nl} r R_{nl}(r), \quad (2.26)$$

with $V(\rho, r)$ the self-consistent one electron potential,

$$V(\rho, r) = \frac{-Z}{r} + V^{\text{H}}(\rho, r) + V^{xc}(\rho), \quad (2.27)$$

where $V^{\text{H}}(\rho, r)$ is the Hartree potential and $V^{xc}(\rho)$ the exchange-correlation potential within the LDA approximation. To generate their NCPP, Troullier and Martins start by defining the radial pseudo-wavefunction, following Kerker,¹² as:

$$R_i^{\text{PP}}(r) = \begin{cases} R_i^{\text{AE}}(r) & r \geq r_c \\ r^l \exp(p(r)) & r \leq r_c. \end{cases} \quad (2.28)$$

¹²The original radial wavefunction for $r \leq r_c$ Kerker used, contained a polynomial of order $n = 4$. [56]

with $p(r)$ a polynomial of order six in r^2 .¹³

$$p(r) = c_0 + c_2r^2 + c_4r^4 + c_6r^6 + c_8r^8 + c_{10}r^{10} + c_{12}r^{12}. \quad (2.29)$$

All seven coefficients c_i are then determined by seven conditions: the norm-conservation, continuity of the pseudo-wavefunction and its first four derivatives at r_c and the zero curvature of the PP at the origin. Now that the pseudo-wavefunction is obtained, inversion of the radial Schrödinger Eq. (2.26) allows us to recover the screened PP,

$$V_{l,\text{src}}^{\text{PP}} = \begin{cases} V_l^{\text{AE}}(r) & r \geq r_c \\ \varepsilon_l + \frac{l+1}{r} \frac{p'(r)}{2} + \frac{p''(r) + (p'(r))^2}{2} & r \leq r_c. \end{cases} \quad (2.30)$$

Eq. (2.30) shows that if we want the PP to be continuous the radial pseudo-wavefunction and if first and second derivative need to be continuous, which is satisfied here through the construction of the pseudo-wavefunction. When generating a PP, we want it to be transferable to a different chemical environment. In the construction given above, there is still a component present which depends highly on the chemical environment: screening from the valence electrons. So, to create a highly transferable PP, one would like a PP which does not contain this screening. This unscreened PP can be obtained by subtracting the Hartree and exchange-correlation potentials calculated from the valence pseudo-wavefunctions obtained with the screened PP,

$$V_{l,\text{unscr}}^{\text{PP}}(r) = V_{l,\text{scr}}^{\text{PP}}(r) - V_{\text{val}}^{\text{H}}(r) - V_{\text{val}}^{\text{xc}}(r). \quad (2.31)$$

Since both the Hartree and exchange-correlation potentials are not dependent on the angular momentum, a different unscreened PP, $V_{l,\text{unscr}}^{\text{PP}}(r)$, will present itself to the different angular momentum components of a wavefunction, resulting in a more complex PP-operator with an angular momentum dependency.¹⁴ Despite this increased complexity, we can now generate a PP which satisfies all our desires (given above) and can easily be transferred from the atomic calculation to a bulk or molecular system.

Because the cost of calculations scales with the size of the used basis set, efforts are made to reduce this basis set as much as possible. For PP, this is connected to the “softness” of the PP, leading to PP which are optimized to maximize their smoothness, the so-called Ultra-Soft PP, as proposed by Blöchl [59] and Vanderbilt [60]. With the advent of the PAW method [33, 34] accuracy increased and computational cost decreased at the cost of even more complex implementation. For an in-depth description and discussion of this method we refer to the existing literature. Here we will only give a rough sketch.

The basic idea is similar to that of the PP described above. Again the system is split up into regions inside and outside a chosen core radius r_c . A pseudization

¹³The polynomial expansion in terms of r^2 also avoids the need to make the coefficient c_1 zero, to avoid a singularity in the PP at $r = 0$.

¹⁴“The law of conservation of misery” kicks in here, the increased usefulness of the PP is accompanied by the increased difficulty of implementing it.

scheme as for USPP is used, resulting in a very smooth PP.¹⁵ The trick of PAW lies in the construction of the pseudo-wavefunctions. In this case, the ultra-soft part inside the core region is replaced by the exact all-electron part, resulting in an obvious increase in accuracy. So for both inside and outside the core-region we have the all-electron case, making this formally an all-electron method. However, like the PP described above, this core part is kept frozen. Since there is no interaction between the different spheres and the plane waves, and the decomposition holds for the wavefunctions, the Hamiltonian, and the charge densities, this tends to be a very efficient method. Therefore, in the calculations for this thesis, the PAW-method is used.

2.2 Scanning Tunneling Microscopy

When it comes to atoms, language can be used only as in poetry. The poet, too, is not nearly so concerned with describing facts as with creating images.

– Niels Bohr

2.2.1 Experiment

In surface science, one of the most important points of interest is the determination of the surface structure of a system. Everything else traces back to this fundamental knowledge. The ultimate dream here, from the experimental point of view, is to observe the surface at atomic resolution, showing the real-space positions of the atoms involved. The development of the scanning tunneling microscope by Gerd Binnig and Heinrich Rohrer in 1981 at the IBM lab in Zürich made this dream come true. [61–63] So, it should not come as a surprise that this invention earned them the Nobel Prize in Physics in 1986. [64] An STM consists of a needle with an atomically sharp metallic tip, in general tungsten or platinum-iridium is used, but also gold and recently carbon nanotubes have been used. This tip is brought very close to the surface, at a typical distance of 4–7 Å, and then scans over the surface while measuring the tunnel current/resistance. Because the tip does not physically touch the surface, a vacuum barrier between the tip and the surface exists. Classically, a particle with energy lower than the barrier would not be able to move from the tip to the surface: in QM however, this becomes possible through a mechanism called *tunneling*. The probability of an electron with energy E tunneling through a square barrier of height $V > E$ with a width d is given by:¹⁶

$$P_{\text{tr}} \cong e^{-\alpha d}, \quad (2.32)$$

with $\alpha = \frac{-2}{\hbar} \sqrt{2m_e(V - E)}$. This exponential relation causes even a small difference in d to give a large change in the tunneling probability, resulting in a high spatial resolution in the z -direction for an STM experiment.

There are two modes of operation to scan a surface with STM:

¹⁵This PP, however, is not norm-conserving, one of the drawbacks of USPP.

¹⁶In the WentzelKramersBrillouin or WKB approximation.

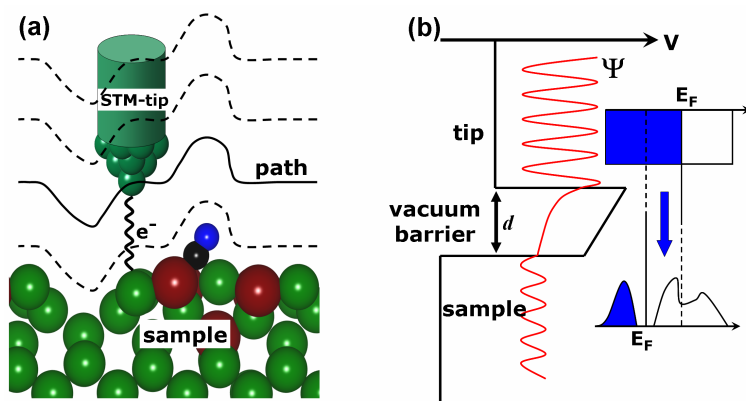


Figure 2.2: a) Schematic representation of an STM experiment in constant current mode. An atomically sharp STM tip is brought close to the surface, such that electrons can tunnel between sample and tip. Keeping the current constant, the tip will follow a path parallel to the surface. b) Quantum tunneling. An electron with incoming wavefunction Ψ and energy close to the Fermi level of the tip, tunnels through the vacuum barrier with thickness d into an empty state in the sample.

Constant-Height mode In this mode, the STM tip is kept at a constant height while scanning over the surface. The change in tunnel current is measured, and resulting images give contour maps of this tunnel current. This allows for very fast scans but requires very flat surfaces as to prevent the tip from crashing into the surface.

Constant-Current mode In this mode, the current is kept constant using a feedback-loop while scanning over the surface. In this case, not the tunnel current but the z -position is tracked. The resulting images in this case are topographical maps of a constant current surface.

Though STM images tell a lot, they miss one key piece of information: what atom type we are actually looking at. Because STM only maps the electron clouds, it is chemically insensitive: it can show where an atom is located, but not what type of atom it is. This blind spot can be alleviated, by comparison to calculated STM images. If calculated and experimentally observed STM images are identical, one can very reasonably assume that the underlying geometry is the same. This argument is of the same class as: “If it walks like a duck and talks like a duck, than it is most probably a duck” ... though in some rare circumstances it turns out to be a platypus.¹⁷ This shows that the symbiosis between theory and experiment could make of STM an even stronger tool than it already is, by the introduction of chemical sensitivity. But also from the theoretical side it provides an additional powerful tool

¹⁷In Chapter 4 we discover such a platypus.

to study and compare theoretical models. One important success, realized already more than a decade ago, was the correct identification of the CO adsorption sites on Pt(111) from DFT calculations.¹⁸ [65, 66]

2.2.2 Theory: Tersoff-Hamann method

The first theoretical description and simulation of STM by Tersoff and Hamann is as old as the experimental work. [67, 68] They showed that the tunneling current in an STM experiment is proportional to the local density of states (LDOS). Starting from a tunneling current, given by first order perturbation theory in Bardeen's formalism [69]

$$I = \left(\frac{2\pi e}{\hbar} \right) \sum_{\mu, \nu} f(E_\mu) \left[1 - f(E_\nu + eV) \right] |M_{\mu\nu}|^2 \delta(E_\mu - E_\nu), \quad (2.33)$$

with $f(E)$ the Fermi function, V the applied bias, $M_{\mu\nu}$ the tunneling matrix between the tip states ψ_ν with energy E_ν and the surface states ψ_μ with energy E_μ . In the limit of small voltage and temperature, Eq. (2.33) reduces to

$$I = \left(\frac{2\pi e^2 V}{\hbar} \right) \sum_{\mu, \nu} |M_{\mu\nu}|^2 \delta(E_\mu - E_F) \delta(E_\nu - E_F), \quad (2.34)$$

with the tunneling matrix element shown by Bardeen to be: [69]

$$M_{\mu\nu} = \left(\frac{-\hbar^2}{2m} \right) \int (\psi_\mu^* \nabla \psi_\nu - \psi_\nu \nabla \psi_\mu^*) \cdot d\mathbf{S}, \quad (2.35)$$

with the integral over a surface in the barrier between the tip and the sample. In case the tip is simplified to a point-source,¹⁹ Eq. (2.34) reduces even further to:

$$I \propto \sum_{\nu} |\psi_\nu(\mathbf{r}_0)|^2 \delta(E_\nu - E_F). \quad (2.36)$$

This is nothing more than the surface LDOS at E_F . Translated to the calculations performed in this thesis, this becomes: "The experimentally measured surface of constant current is equivalent to a calculated surface of constant charge-density, from states close to E_F ." In this thesis, we use this most simple approximation to simulate the STM images for the structures studied. The main reason for this being the lack of structural information for the STM tip, and since we are trying to identify an unknown surface reconstruction, this would only complicate things further.

As a consequence of this point-source tip approximation, the detail in the theoretical STM images is much higher than could ever be achieved in experiment. This leads to what could be called the **no-fewer-peaks-rule**:

¹⁸Further details on the history of this problem can be found in the introduction of **Chapter 5**.

¹⁹This approximation has some advantages from the theoretical point of view. Since the tip is practically ignored, there is no need for any information with regard to the tip geometry and calculated images will have a perfect resolution, making them ideal to distinguish surface features in experimental STM images from tip induced features.

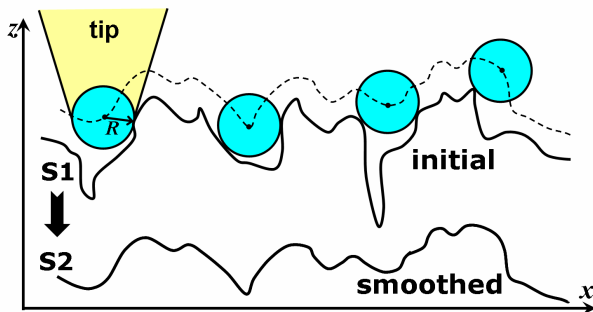


Figure 2.3: Schematic 1D representation of the graphical smoothing technique. A heightmap $S1$ generated using a point-source STM tip is smoothed by tracking the z coordinate (dashed curve) of the center of a ball with radius R (assuming an STM tip with curvature $1/R$) when moving it over surface $S1$. The resulting smoothed image is heightmap $S2$.

“The number of peaks in a calculated STM image of an object can never be lower than the number observed in experiment.”²⁰

In a real STM-experiment, the width of the tip (one atom in the best-case scenario) causes a smoothing of the image, with regard to the point-source calculated STM images. In the following, two possible approaches to include the tip in the calculations are given.

1) Exact Physics This is the straightforward idea of implementing a tip geometry in the calculation, and doing actual transport calculations. This however, requires a correct model of the tip geometry, and is rather complicated to implement. Obtaining STM images using this approach requires relatively expensive calculations.

2) Graphical Smoothing A second approach starts from the graphical point of view. Starting from the calculated STM image $S1$ (cf. Fig. 2.3), generated for a point-source tip in constant-current mode, a graphical smoothing transformation can be applied.

The physical idea behind this approach is that the current will follow the path of least resistance, *i.e.* the shortest path between the center of the tip and the sample assuming the resistance is constant in each of the three regions (tip, vacuum barrier, surface). This creates a sphere of radius R centered around the point-source.²¹ Rolling this sphere over heightmap $S1$ and mapping the z coordinate of its center (dashed curve in Fig. 2.3) as a function of x and y results in a new heightmap $S2$ (cf.

²⁰This rule will be used when we are looking for the nanowire geometry in **Chapter 4**.

²¹From the QM point of view this sphere would then represent the s -wave of the tip atom (although the $5d$ orbitals of W, which was used for the STM tip in the experiments, also have a relatively spherical distribution when added).

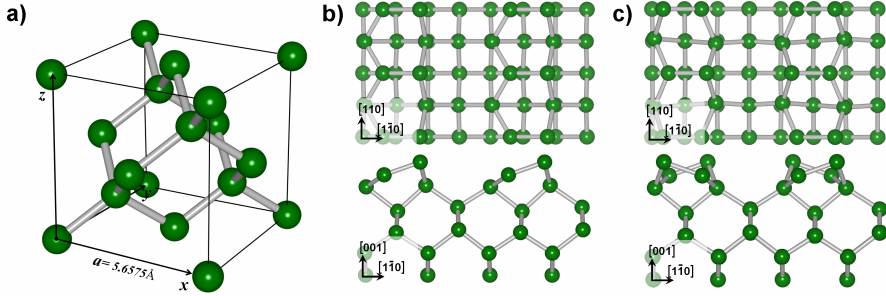


Figure 2.4: a) Ball and stick model of the Ge lattice structure. b) and c) Ball and stick model of the reconstructed Ge(001) surface with an asymmetric b(2×1) and c(4×2) reconstruction respectively.

Fig. 2.3). This heightmap S_2 will then be a smoothed STM image, with all the fine and sharp depressions smoothed out, and sharp protrusions broadened. In contrast to the Exact Physics approach, this method is extremely fast, but only a qualitative comparison to experiment should be expected. This method also requires an extra fitting parameter: the sphere radius R . In the later stages of the thesis, this type of smoothing was also implemented in the STM-program. For more information on the implementation of the STM program, the reader is referred to **Appendix A.1**.

2.3 Germanium in DFT

The system studied in this thesis can be considered a surface-modification of the reconstructed Ge(001) surface. So it is important to have a correct, sufficiently converged model of the Ge(001) surface, such that both electronic and structural modifications can be identified and characterized accurately. In this section, we therefore give an overview of the convergence tests and comparisons done for the germanium system. Based on these results, computational parameters were chosen for application in the rest of the thesis.

2.3.1 Bulk Germanium

Bulk Ge has a cubic diamond lattice structure (*cf.* Fig. 2.4a) with a lattice constant of 5.6575 Å. [70] VASP provides four different PAW potential files for Ge. Two potential files with the 4s and 4p electrons in the valence shell and two potentials including also the 3d electrons in the valence shell, each in an LDA (Ceperley and Alder parameterized by Perdew and Zunger) and GGA (Perdew-Wang 91) flavor. [71–73] We will use the index d to indicate the 3d electrons are included in the potential. Volume scans were performed for different k -point sets and kinetic energy cutoffs. Table 2.1 shows the lattice constants obtained with the four potentials, using a $20 \times 20 \times 20$ k -point grid. The lattice constants show the expected behavior

Ge bulk

	LDA	LDA _d	GGA	GGA _d	exp.
a (Å)	5.6466	5.6265	5.7785	5.7578	5.6575 ^a
direct BG (eV)	0	0	0	0	0.89 ^b
indirect BG (eV)	0.093	0.116	-0.011	0.020	0.744 ^b
E _{bulk} (eV)	-5.175	-5.139	-4.521	-4.489	-
E _{coh} (eV)	-4.616	-4.636	-3.821	-3.837	-3.85 ^c

Table 2.1: Calculated lattice constant a and BGs extracted from the band structure for the different potentials for bulk Ge. The index d indicates that the $3d$ electrons were included as valence electrons in the potential. The lattice constants were obtained via a volume scan, using a $20 \times 20 \times 20$ k -point grid and kinetic energy cutoff of 430 eV for the LDA and GGA potentials with d electrons in the valence shell, and 261 eV for those without. The uncertainty on these values is 0.0005 Å. The width of the BG was determined by the difference in energy at special k -points Γ and L of the bands involved, $\Gamma_{3,4}$ and Γ_5 for the direct BG and $\Gamma_{3,4}$ and L_5 for the indirect BG (cf. Fig. 2.6). The bulk energy per atom, E_{bulk} , was calculated using a kinetic energy cutoff of 345 eV and $21 \times 21 \times 21$ k -point grid. These values are with regard to the nonspinpolarized atom groundstate. The cohesive energy, with regard to the spinpolarized atom groundstate is given by E_{coh} .

^a Reference [70].

^b as quoted in Reference [74].

^c Reference [75].

of LDA potentials slightly underestimating the lattice constant by $\sim 0.35\%$, due to over-binding, while the GGA potentials show an overestimation of $\sim 2\%$ due to under-binding. Figure 2.5 shows all four potentials to have the same convergence behavior as function of the used k -point set. A k -point grid of $8 \times 8 \times 8$ k -points shows already a convergence of less than 1 meV per atom. Convergence with regard to the kinetic energy cutoff shows for both LDA and GGA the need to use at least 1.25 times the advised cutoff to reach a 1 meV per atom convergence,²² if the $3d$ electrons are not included in the valence shell. Including them for GGA does not improve the behavior, while for LDA, 1 meV accuracy per atom is already reached at the advised energy cutoff. Figure 2.6a shows the DOS obtained using a $41 \times 41 \times 41$ k -point grid²³ and kinetic energy cutoff of 345 eV.²⁴ The low lying d -bands are shown to have no influence on the DOS of the s and p valence electrons. Different exchange-correlation functionals on the other hand have large influence on the DOS.

²²The advised kinetic energy cutoff for the potentials without $3d$ electrons is 174 eV and for the potentials with the $3d$ electrons included is 287 eV. All behavioral comparisons of the potentials are made using these as reference energies for the respective potentials.

²³This is the densest k -point grid allowed by VASP.

²⁴This choice for the kinetic energy cutoff comes from similar energy convergence tests performed for Pt.

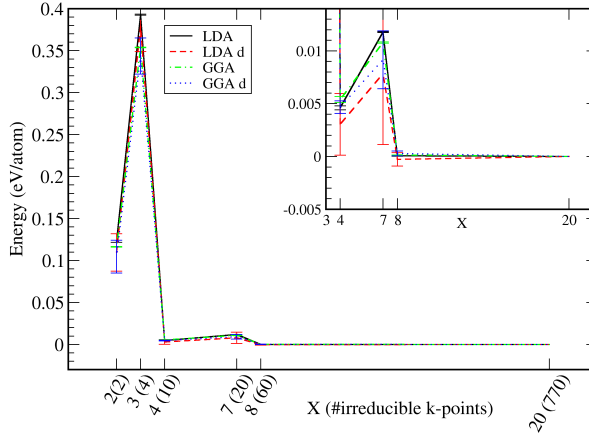


Figure 2.5: *K-point convergence of bulk Ge for $X \times X \times X$ Monkhorst pack grids. The curves show the average energy difference per Ge atom with regard to the $20 \times 20 \times 20$ k-point grid. The error bars show the standard deviation. For each potential, kinetic energy cutoffs of 0.75, 1.00, 1.25, and 1.50 times the advised kinetic energy cutoff were used. A magnification is shown in the inset.*

Though it remains qualitatively the same, the DOS compresses toward the Fermi-level going from the LDA to the GGA potentials, aggravating the BG-problem. The semi-logarithmic inset shows the absence of a BG for bulk Ge. DFT is well known for underestimating the BG in semiconductors,²⁵ with Ge being one of the worst cases, since the BG vanishes entirely. Much effort is directed to solving this BG problem, mostly using more complex exchange-correlation functionals. Next to for example hybrid functionals,²⁶ the GW approximation (GWA) is known to be successful in estimating the correct Ge BG. [74] However these methods and functionals all tend to be computationally very expensive, making them not really useful during geometry optimization searches, as performed in this thesis.

The electronic band structure is also not influenced by the incorporation of $3d$ electrons in the valence shell. The difference between LDA and GGA however is again a shift toward the Fermi level of the GGA bands, as shown in Fig. 2.6b. The Γ -point crossing shows a further difference between GGA and LDA. Where in LDA four bands cross (the middle band is degenerate), in GGA the lower band is pulled downward. Comparison to the LDA (dashed) and GWA (solid) results of Pollmann *et al.* [74] in Fig. 2.6c, shows very good agreement between the LDA results. It also

²⁵DFT is a ground state theory and does not handle excited states very well. This results in underestimating the energy positions of bands above the BG, which are in essence excited states.

²⁶A more unconventional alternative would be to use the LDA+U method with a negative U: this also does the trick for Ge. You will however need to fix the lattice because the introduction of U will shrink/expand the lattice considerably. This way of introducing a BG could be compared to using a scissor-operator.

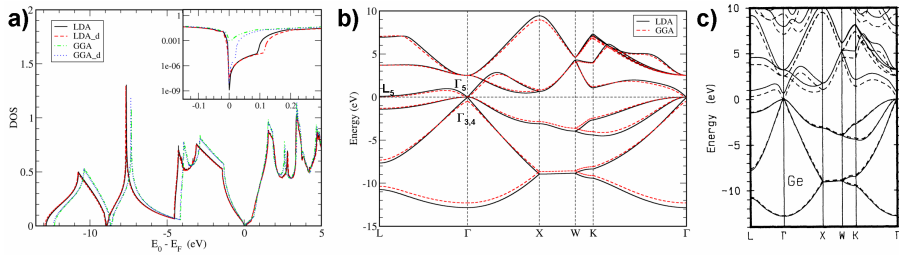


Figure 2.6: a) The Ge bulk DOS, calculated with the provided LDA and GGA potentials. The inset shows a semi-log magnification of the states around the Fermi-level. b) Comparison of the LDA and GGA Ge band structure along lines of high symmetry. The Fermi energy is chosen as the energy zero. c) Ge band structure taken from reference [74] for comparison. Dashed lines are LDA calculations, solid lines GWA calculations.

shows the modifications for the GGA potentials move the band structure in the wrong direction compared to the ‘correct’ GWA results. In these calculations we use the lattice constant obtained for the specific potential. However if we perform the same band structure calculation for the GGA potential using the LDA lattice constant, effectively compressing the lattice with regard to the GGA value, the picture becomes a bit different. On the large scale, the same band structure as for LDA is obtained, showing the main part of the GGA modification of the band structure to be related to the GGA lattice constant. Zooming in on the band structure, small difference, of the order of 10 meV, become visible. Below the Fermi level the bands generally are shifted slightly downward, while above they are shifted slightly upward. Around the Fermi level at the Γ -point, the most interesting modification happens. Where for both LDA and GGA the valence band (VB) and conduction band (CB) are degenerate, they split up in this configuration resulting in a small direct BG of about 80 meV. To check whether this BG is a consequence of the GGA potential or the compression of the lattice we also perform an LDA band structure calculation where the LDA lattice is compressed 2.7%. Near the Fermi level at the Γ -point we observe the same behavior of the bands, however in this case the Direct BG is much larger, ~ 0.7 eV, showing this behavior is related to the lattice constant rather than the exchange-correlation functional.

Table 2.1 shows all potentials to generate a direct BG which is zero, while in experiments the direct BG is observed to be 0.89 eV at low temperature. The indirect BG is not zero, however still largely underestimated by LDA. In GGA the indirect BG is even smaller or negative, which is in line with the above observations. Close examination of the inset in Fig. 2.6a shows a clear step in the DOS at the edges of the indirect BG.

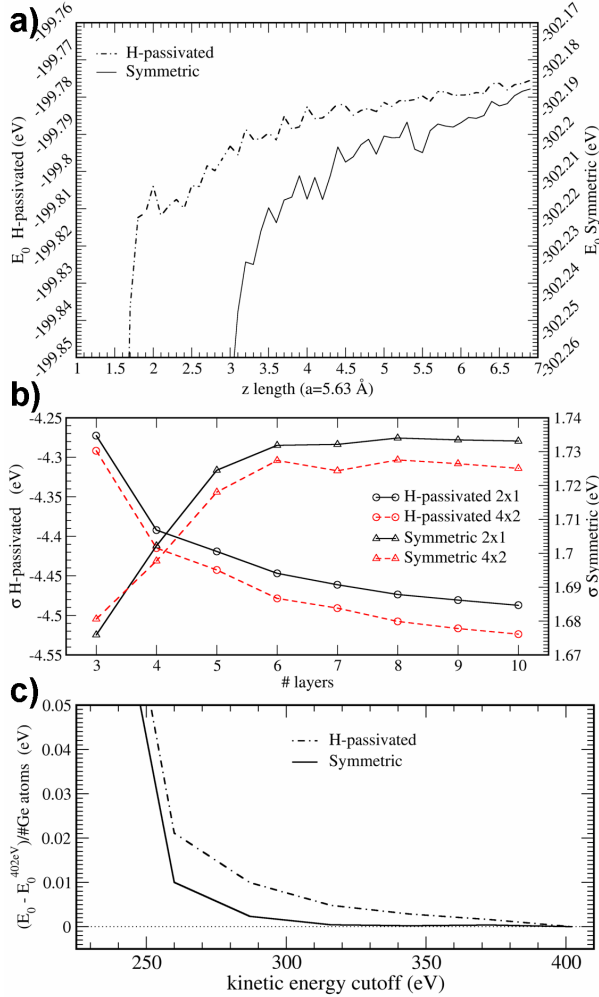


Figure 2.7: a) Vacuum thickness convergence for a 4-layer system with 2×4 surface cell. The slab-thickness of the symmetric system is $2a$, while the H-passivated slab has a thickness of $1.25a$. b) Surface energy convergence calculated using Eq. (2.37). c) Kinetic energy cutoff convergence for a 4-layer symmetric and H-passivated system with 2×4 surface cell. Due to the different number of Ge atoms in both systems, and the presence of H in one, the convergence was calculated as the difference between the system at a given kinetic energy cutoff and the system at a kinetic energy cutoff of 402 eV. This to negate the H-contribution in the H-passivated system. The resulting values are then divided by the number of Ge atoms present in the system, to allow for direct comparison.

2.3.2 Ge(001) surface reconstructions

Convergence behavior

Based on the above results and the fact that we are mainly interested in the geometry, we used the LDA_d potential to investigate the convergence behavior of the Ge(001) surface.

We compare two ways of modeling the Ge surface slab. The first model consists of a Ge slab of a given thickness of which the surface layer on one side is fixed and the dangling bonds are passivated with H atoms. This side of the slab should then represent the bulk phase. The other surface is allowed to relax and will be referred to as ‘the surface’. When counting the number of layers in this type of system, the layer of H atoms is never included, only the Ge layers are counted. The second model is a symmetric model. Here both faces of the slab are allowed to relax and/or reconstruct, while the two layers at the center are kept fixed to represent the bulk phase. For the symmetric system we will refer to the thickness as the number of layers counting from a surface layer to the bulk phase layers. This means that a 4 layer symmetric system contains 8 layers of Ge, 4 layers going from one surface to the bulk, and 4 layers going from the bulk to the other surface. During the convergence tests performed below, no surface dimer-reconstructions are allowed, only relaxation of the layers along the z -direction, *i.e.* orthogonal to the surface.

The k -point convergence shows that for a system with a 2×4 surface cell a k -point grid of $6 \times 3 \times 1$ is sufficient to reach a total energy convergence < 1 meV/atom. For a 1×2 surface cell this requires a $14 \times 7 \times 1$ k -point grid.

Because of the periodic boundary conditions, the 2×4 or 1×2 surface cell is duplicated infinitely in the x and y directions. In the z direction however, the periodic boundary conditions introduce periodic copies of the slab. To prevent these copies from interacting, a sufficiently large vacuum region is necessary. Figure 2.7a shows the convergence behavior with regard to the vacuum thickness for a 4-layer system. Both for the H-passivated and the symmetric system it clearly shows the ground state energy keeps rising at a roughly constant rate for vacuum thicknesses larger than ~ 2.5 a (≈ 14 Å). Because we are using a plane-wave approach, the vacuum we are introducing is not empty, but is filled with plane waves, contributing to the total energy of the system. The jaggedness of the curves is due to basis set incompleteness (when the volume changes, additional plane waves are added resulting in a discontinuous change of the energy) and the discontinuous change of the FFT grid when the volume changes. The vacuum thickness was therefore chosen at the beginning of the linear region, giving a thickness of 2.75 a (≈ 15.5 Å).

In slab calculations, as performed in this thesis, only a finite number of layers can be included. Similar as with the vacuum thickness, we also do not want both faces of the slab interacting through the slab and we want the slab to be thick enough to be able to fully relax the surface, *i.e.* the slab should be thick enough such that one or more layers can be considered bulk phase. The convergence of the surface energy σ , calculated using the equation

$$\sigma = \frac{1}{2A} \left(E_{\text{slab}} - N_{\text{Ge}} E_{\text{BulkGe}} \right), \quad (2.37)$$

with A the surface area, E_{slab} the total energy of the slab, N_{Ge} the number of Ge atoms in the system and E_{BulkGe} the energy of a Ge atom in the bulk geometry, shows how close each new layer added to the system is to the bulk regime. The factor 2 is present because there are two faces on a slab. Figure 2.7b shows that for a symmetric slab the bulk regime is already reached for a 6 layer slab,²⁷ while for a H-passivated surface at least 10 layers of Ge are needed to get similar convergence.²⁸

The qualitative difference between the curves for the symmetric and H-passivated system is due to the H atoms present in the later. Their contribution to the total energy results in a constant shift of the surface energy. Although we would like the H-passivated surface not to contribute to the surface energy, it does, resulting in the surface energy to be the sum of the surface energy of the Ge surface and the H-passivated surface. A quick test calculation, using a symmetric slab with H-passivation on both sides, shows the surface energy of a H-passivated surface to be negative, and larger than that of a Ge surface. As a result, the total surface energy of a slab with one H-passivated surface and one Ge surface becomes lower than the surface energy of a symmetric slab with two Ge surfaces. The negative trend for increasing slab-thickness is due to the decreasing interaction between the two faces of the H-passivated slab. A second way of looking at surface relaxation are Layer oscillations. Surface atoms try to lower their energy by moving inward (this is generally the case for metals), or outward (in case of semiconductors), of the surface. These changes of the bond length vary with the depth from the surface. We will refer to these oscillations in the planar spacing between layers near the surface as layer oscillations. The layer oscillations presented in Fig. 2.8 show clearly that the H atoms introduce a long-range distortion from the ‘bulk’ side into the slab. To suppress this effect, multiple Ge layers should be kept fixed at the bulk side of the slab, increasing the system size significantly. For the symmetric system, the layer oscillations vanish for systems with 6 or more layers. Combining the results from the layer oscillations and the surface energy convergence shows that a 6-layer symmetric system is sufficiently converged for our needs. The H-passivated system on the other hand shows two serious problems. First of all, the surface energy of the Ge surface cannot be determined easily in a straightforward way due to the H atoms present. Secondly, due to the strong effect that the H atoms have on their side of the slab, a very thick slab (≥ 10 Ge layers) with multiple fixed Ge layers is needed, negating the initial size advantage over the symmetric system.

Figure 2.7c shows the convergence with regard to the kinetic energy cutoff. For the symmetric system, the total energy per Ge atom has already converged to 2 meV at the advised kinetic energy cutoff, while for the H-passivated system a kinetic energy cutoff at least 25% higher is needed.

Because of the size of the system under study, it is important to have a good understanding of its computational cost when considering the input parameters. Is the increase in accuracy sufficient to justify the increased cost? Figure 2.9 shows some relations of the required amount of memory (a, c, e) and CPU time (b, d,

²⁷This means the symmetric system contains $2 \times 6 = 12$ layers of Ge.

²⁸Note that Eq. (2.37) is aimed at symmetric slabs with both surfaces equivalent. Because this is not the case for the H-passivated system, we have to remove the factor 2.

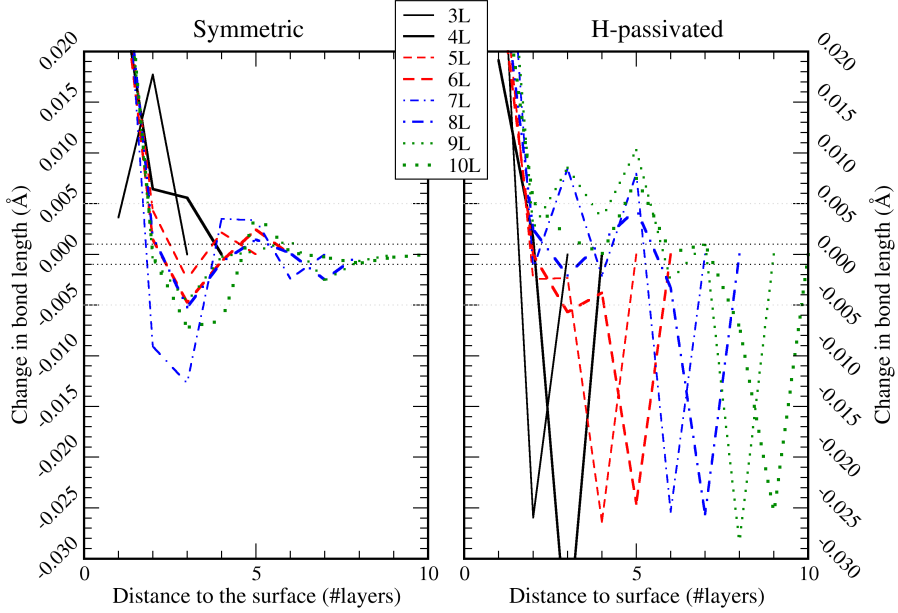


Figure 2.8: Layer oscillations calculated for symmetric and H-passivated slabs with a 2×4 surface cell. Layer 1 is the surface-layer of the slabs. For the symmetric system, the layer oscillations of only one side are shown. The two central layers of a symmetric slab were kept fixed. For the H-passivated systems, only the H atoms and the bottom layer Ge connected to them were kept fixed. The Ge-Ge bulk inter layer distance is 1.4075 \AA .

f) with regard to system size, k -point set and kinetic energy cutoff. The memory requirements scale linearly in each case, as could be expected, making it possible to easily extrapolate to the hardware limit of a calculation. The scaling behavior with regard to time is more interesting when considering the feasibility of a calculation. Figure 2.9b shows a linear, albeit steep, relation between the required CPU time and kinetic energy cutoff. For every 10% increase in kinetic energy cutoff, the required CPU time increases roughly 20%. With regard to the number of irreducible k -points, the CPU time scales linearly with a one-to-one relation, as should be expected, since the calculations perform a sum over the irreducible k -points. The size dependence however, is more troublesome. Figure 2.9f shows a power law behavior for the CPU time, T:

$$T = N^\alpha, \quad (2.38)$$

with N the system size, and $\alpha \approx 1.89 - 2.17$ the exponent. This makes system size the most crucial parameter with regard to the cost.

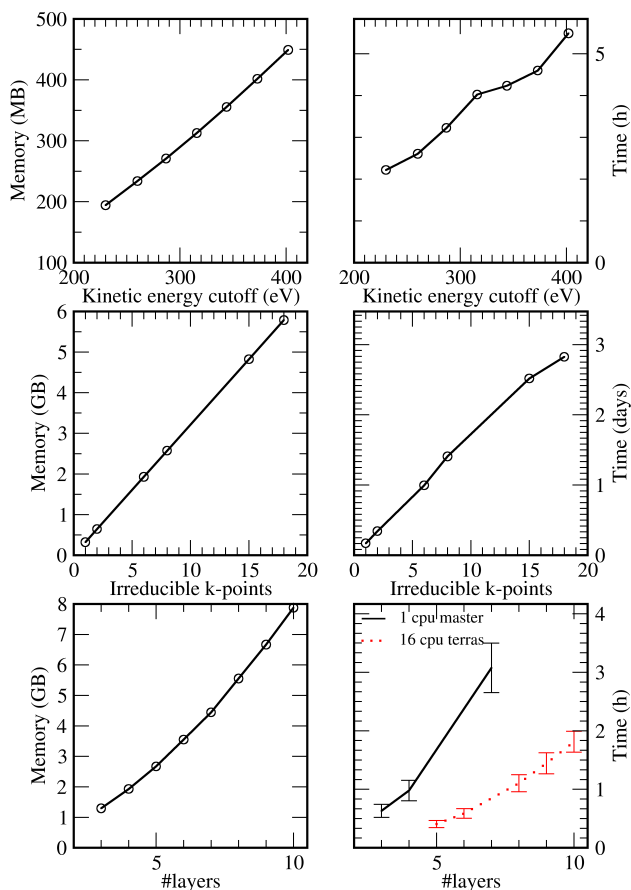


Figure 2.9: Computational cost and scaling behavior of VASP calculations. A symmetric slab with 2×4 surface cell was used. a) and b) Behavior of memory-requirements and CPU time with regard to the kinetic energy cutoff. Single CPU self-consistent calculations, taking 22 electronic steps to converge. A $2 \times 1 \times 1$ k-point grid was used for a 4-layer symmetric slab. c) and d) Scaling of memory and CPU time as function of the number of irreducible k-points. Single CPU self-consistent calculations, for a 4-layer slab, with kinetic energy cutoff of 287 eV. e) and f) Scaling of CPU time and memory requirements with system size. A $6 \times 3 \times 1$ k-point grid and 287 eV kinetic energy cutoff were used. The CPU time values were obtained by averaging the CPU times of the electronic steps during relaxation calculations. The error bars show the standard deviation. Master refers to the former group cluster and Terras refers to the former high performance cluster at SARA (Amsterdam).

Summary

- For a 2×4 surface cell, a $6 \times 3 \times 1$ k -point grid is sufficient in both cases, although slightly better results are found for the H-passivated systems.
- The vacuum convergence behavior is also similar for both cases, resulting in the same vacuum thickness of 2.75 lattice constants, or ~ 15.5 Å.
- With regard to the kinetic energy cutoff, the symmetric system does much better, needing only 287 eV, whereas the H-passivated system requires at least ~ 350 eV to show similar convergence.
- Although at first sight slab thickness favors the H-passivated systems, sufficiently converged surface energy and the presence of layer oscillations induced by the fixed H atoms show the necessary number of Ge layers to be at least the same, if not more, than what is needed for the symmetric system.

Furthermore, the presence of two different surfaces in the H-passivated system make it very hard to give a simple and consistent definition of the surface energy. Also, the presence of the H atoms will introduce extra bands and states in the electronic structure, complicating the analysis of the density of states (DOS) and electronic band structure of the system. Based on all these arguments we decide to use the symmetric slab model for further calculations in this thesis.

Four Ge(001) surface reconstructions

Starting with a 6 layer symmetric system²⁹ and kinetic energy cutoff of 287 eV, we investigate the four Ge(001) surface reconstructions:

1. The relaxed surface, with Ge surface atoms only displaced in the z direction. No dimers are formed here.
2. The symmetric surface dimer system.
3. The $b(2 \times 1)$ asymmetric dimer system, containing tilted surface dimers (*cf.* Fig. 2.4b).
4. The $c(4 \times 2)$ asymmetric dimer system, also containing tilted surface dimers (*cf.* Fig. 2.4c).

Table 2.2 shows the relative formation energy E_{fr} and some geometrical parameters for the surface dimers on these (reconstructed) surfaces. Based on geometrical and symmetry arguments, it can easily be understood that in calculations the Ge(001) surface should not reconstruct into dimers spontaneously. Consider the two surface atoms in a 2×1 surface cell. Although they form a dimer, this does not happen due to the periodic boundary conditions and the symmetry of the system. The first atom will experience equal and opposite forces coming from the two neighboring copies of

²⁹This means there are 12 layers in total for the entire slab. This fourfold number of layers has the additional advantage of creating a system with inversion symmetry.

Ge(001) surface reconstructions

	E_{fr} (eV/dimer)	dz (Å)	dr (Å)	α (°)
relaxed	0.960	0	3.981	0
sym (2×1)	0	0.017	2.512	0.39
asym $b(2 \times 1)$	-0.302	0.815	2.450	19.42
asym $c(4 \times 2)$	-0.374	0.849	2.511	19.76
		(0.842)		(-19.60)

Table 2.2: Relative formation energy per surface dimer and some structural parameters for the dimers on the reconstructed Ge(001) surface. The relaxed surface is included for comparison. The values between brackets for the asymmetric $c(4 \times 2)$ structure show the values for the second oppositely buckled dimer, if they differ from those of the first.

the second atom, and *vice versa*. Only when this symmetry is broken, the forces will become different and reconstruction becomes possible. The same goes for supercells, because the equivalent atoms are indistinguishable from the periodic copies in the 2×1 surface cell.

We will have to break the symmetry ‘manually’ if we want to observe the formation of surface dimers. The symmetric dimer system on the other hand proves quite unstable, with the tendency to buckle quite rapidly, as can be seen from the results in Table 2.2. Buckling of the dimer has already started. The relative formation energy was found by calculating the formation energy E_{f} and then setting the formation energy of the symmetric dimer to zero. The formation energy was obtained using the equation

$$E_{\text{f}} = (E_{\text{surf}} - N_{\text{Ge}}E_{\text{Ge}})/N_{\text{dim}}, \quad (2.39)$$

with E_{surf} the total ground state energy of the slab, E_{Ge} the bulk energy of a Ge atom (as given in Table 2.1), N_{Ge} the number of Ge atoms in the system and N_{dim} the total number of surface dimers in the system, *i.e.* the sum of both surfaces on the slab.³⁰

The formation of surface dimers seems extremely favorable in case of the Ge(001) surface, with an energy gain of ~ 1 eV per dimer. Buckling of the dimers increases this by another ~ 0.3 eV per dimer. Table 2.2 also shows that the buckled dimers are not influenced (much) by the global symmetry of the system. All dimers have a buckling angle of 19° and the dimer length dr for the dimers in the $c(4 \times 2)$ geometry is only stretched 2.5% compared to the dimers in the symmetric and asymmetric (2×1) symmetry. The difference in z position of the dimer atoms is, for all buckled dimers, ~ 0.81 Å. All these values show very good agreement with the values found in literature. Needels *et al.* present a difference in E_{f} between the $b(2 \times 1)$ and $c(4 \times 2)$ reconstruction of -66 meV, [76] compared to -72 meV found here. The difference between the symmetric and asymmetric surface dimer reconstructions they provide

³⁰With regard to the relaxed system, we counted the number of pairs of surface atoms.

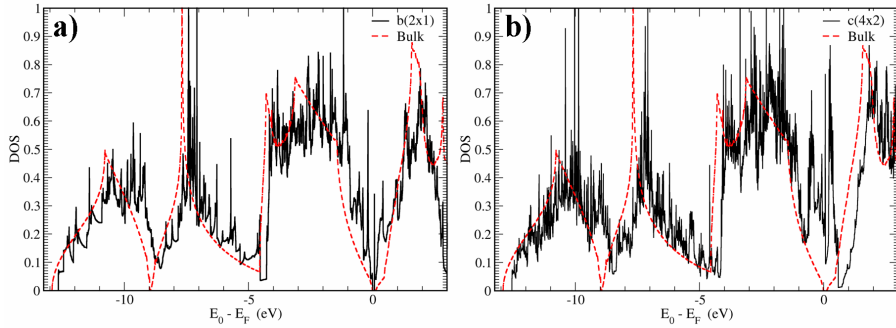


Figure 2.10: Total DOS of the Ge(001) reconstructions: a) the asymmetric $b(2 \times 1)$ reconstruction, b) the $c(4 \times 2)$ reconstruction. The DOS is normalized to the number of Ge atoms, and the bulk Ge DOS is added for comparison.

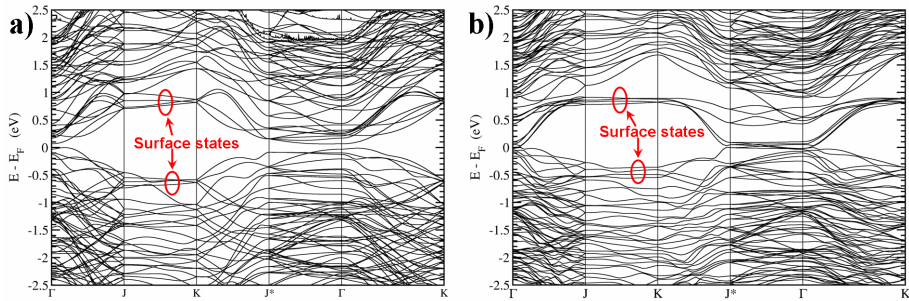


Figure 2.11: Electronic band structure along lines of high symmetry for the Ge(001) $b(2 \times 1)$ (a) and $c(4 \times 2)$ (b) reconstructions. For both systems the band structure along the high symmetry lines of the 4×2 surface cell is used.

is only -0.24 eV, [77] contrary to the -0.30 eV shown in Table 2.2. Furthermore, the same group reports in reference [77] a dimer buckling of only 14° . Jenkins and Srivastava on the other hand quote experimental values for the dimer buckling of $20 - 21^\circ$ and further theoretical values of $\sim 19^\circ$ for the $b(2 \times 1)$ reconstruction,³¹ in good agreement with what we find. They also quote an experimental bond length of 2.44 Å, and theoretical values ranging from 2.38 to 2.46 Å, while reporting a difference in z -position of 0.76 Å, [78] all showing good agreement with the values presented in Table 2.2. In the geometrical data presented by Gay *et al.*, [79] we find differences in z positions, of buckled dimers in a (2×1) and (2×2) reconstruction, of 0.77 and 0.84 Å. Furthermore, Gay *et al.* calculate the accompanying dimer lengths and buckling angles to be 2.38 and 2.45 Å, and 19.0° and 20.1° , respectively.

With the knowledge that the surface reconstructions we generated are of good quality, we can now have a look at the associated electronic structure. Figure 2.10

³¹Table 1 in Reference [78].

shows the total DOS for the $b(2 \times 1)$ and $c(4 \times 2)$ reconstructions of the Ge(001) surface. In both cases, the DOS follows roughly the bulk DOS. The main difference appears in the BG-region. Here, surface states are located just above the valence band and below the conduction band, filling up the already vanishing BG. This shows that despite the DFT problem of the missing BG, we still can draw the correct qualitative conclusions. The electronic band structure close to the Fermi level for these two system is shown in Fig. 2.11. Again, despite the vanishing BG, surface bands located in the BG can clearly be identified, as indicated in Fig. 2.11 with the red circles.

Comparison of the Ge(001) $b(2 \times 1)$ band structure to the asymmetric dimer model band structure presented by Krüger *et al.* [80] shows a good qualitative behavior of the surface state bands. When comparing Fig. 2.11 to figure 1 in Reference [80], some differences between the systems need to be mentioned. i) The surface unit cell used in this work is a (4×2) unit cell, which results in downfolding of the bands both in the Γ -J and Γ -J* directions, doubling the number of surface bands. ii) The dimers at the opposing faces of the slab are shifted by $\frac{1}{4}$ unitlength due to the symmetry of the slab, resulting in slightly different bands, again doubling the number of surface bands. iii) The notation used in this work and Reference [80] have the k -points J and J* switched. As a result of points (i) and (ii), instead of one D_{up} and one D_{down} band, there are 4 double degenerate D_{up} and 4 double degenerate D_{down} bands present for both Ge(001) surface reconstructions. For both reconstructions we find a strong dispersion along the Γ -J and K-J* directions due to the interaction between neighboring dangling bonds. On the other hand, along the Γ -J* and J-K directions the surface bands show almost no dispersion at all. Although the Ge(001) surface is known from experiment to be semiconducting, no BG is visible in the band structures of Fig. 2.11, this is due to the DFT band gap problem.

With the DOS and band structure at hand for the reconstructed Ge(001) surface, we now have a baseline for comparison of the DOS and band structure of the β -terrace and nanowire systems. Furthermore, even though DFT gives a vanishing BG for Ge, it should be possible to recognize and identify new surface states due to further modifications of the Ge(001) surface.

Chapter 3

FT study of Pt-induced nanowires on Ge(001) I: β -terrace substrate.

Some things should be simple,
– Editors
(An End Has A Start, 2007)

Pt deposited on a Ge(001) surface spontaneously forms nanowire arrays. These nanowires are thermodynamically stable and can be hundreds of atoms long. The nanowires only occur on a reconstructed Pt-Ge-surface where they fill the troughs between the dimer rows on the surface. This unique connection between the nanowires and the underlying substrate make a thorough understanding of the latter necessary for understanding the growth of the nanowires. In this chapter we study possible surface structures containing 0.25 and 0.5 of a ML of Pt. Comparison of calculated STM images to experimental STM images of the surface reconstruction reveal that the Pt atoms are located in the top layer, creating a structure with rows of alternating Pt-Ge and Ge-Ge dimers in a $c(4 \times 2)$ arrangement. Our results also show that Pt atoms in the second or third layer can not be responsible for the experimentally observed STM images of the β -terrace.

3.1 Introduction

Metal/semiconductor interface interactions continue to attract interest in both fundamental and applied research, and are of vital importance for the semiconductor and microelectronics industry. With miniaturization pushing into the nanoscale regime, new ways of constructing nanoscale devices are investigated. Bottom-up approaches such as atomic size reconstructions, self assembly and metal NWs are

investigated as alternatives for the usual top-down techniques, such as etching and lithography. [4] Generally, the focus lies on metal/Si interfaces because of the importance of Si in the semiconductor industry. Of these, the Au/Si(001) interface, due to the high conductivity of Au, is one of the most well studied interfaces.

For this system, it has been shown that different types of reconstructions appear depending on the Au coverage and the annealing temperature. [81–83] The metal/Ge interface is less well studied, notwithstanding its importance in the development of radiation detector systems and high speed electronic devices. Recent experimental studies of the Pt/Ge(001) interface, done at the submonolayer Pt coverage regime, have shown the formation of self-organized Pt NW arrays after high temperature annealing. [18, 27, 28] It has been suggested that this reconstruction was due to a strengthened interaction of the $5d$ metals with the Ge surface: relativistic mass effects which contract the s shell, reducing its energy and thus increase the s occupancy at the expense of the d electrons. This partially depletes the antibonding d states, strengthening the d bonds. [84] The same mechanism was thought to be responsible for the one dimensional chain structures of Au on Ge. [19, 20] There certainly are similarities between the growth of Au and Pt chains on Ge(001), such as the appearance of dimer vacancies before the chains appear. Yet, there are also important differences between the two systems. The Pt NWs only form after annealing at over 1000 K, while the Au chains appear after deposition at 675 K and disappear into the bulk Ge when annealed at 1000 K. [18, 20] Moreover, while the Pt NWs have a thickness of a single Pt atom, the Au chains are dimer rows containing Au-Au or Au-Ge dimers. [19] The Pt NWs are thermodynamically stable and their length is only limited by the size of the underlying terrace. This terrace is a previously unknown Pt-Ge-surface reconstruction of which, to date, only a tentative model proposed by Gürlü *et al.* exists. [18] The unique connection between this terrace and the NWs makes a thorough understanding of the reconstruction desirable before one can study and understand the NW arrays and the physical phenomena associated with them. [27]

In this chapter, we present a geometry for the so called β -terraces based on the comparison of the simulated STM images (henceforth referred to as pseudo-STM images) to experimental STM images. The current experimental information on the β -terraces is very limited. At the moment of writing only STM images are available.

The structure of this chapter is as follows: In **Sec. 5.2** we describe the applied theoretical method and introduce the index-notation used for the different geometries. In **Sec. 3.3** we present our theoretical results starting with a comparison of the formation energies of the different geometries followed by a general review of the pseudo-STM images. We identify one particular geometry as the structure of the β -terrace, which is discussed in more detail. As a last point of **Sec. 3.3**, we take a look at some geometries containing Pt atoms in the second and third layer and show that these can not be responsible for the β -terrace STM pictures, but they could be responsible for the indented dimer and two dimer vacancy images seen in the STM pictures of the α -terrace. [18] Finally, in **Sec. 3.4** the conclusions are given.

3.2 Theoretical method

3.2.1 Setup

DFT calculations are carried out using the PAW method [33, 34] and the LDA functional with the exchange and correlation function calculated by Ceperley and Alder (CA),¹ as implemented in the VASP program. [71, 85, 86] A plane wave basis set with kinetic energy cutoff of 287 eV is applied and the semicore d shell of Ge is included in the valence shell for better accuracy. The surface is modeled by periodically repeated slabs of 12 layers of Ge atoms. Extensive convergence tests, presented in **Sec. 2.3.2**, showed no advantage in time/accuracy for the H-passivated Ge slab over the symmetric Ge slab. Based on the advantages of the higher symmetry of the symmetric slab, we choose to use the later. The slabs are mirrored in the z -direction with reconstructions on both surfaces, in which specific Ge atoms are replaced by Pt atoms. A vacuum region of ~ 15.5 Å is used to separate the slabs along the z axis. The Brillouin zone (BZ) of the (2×4) surface unit cell is sampled using a 6×3 Monkhorst-Pack special k -point mesh. [87] To optimize the geometry of the slabs the conjugate gradient method is used in zero-temperature calculations. The positions of the Ge atoms in the two center layers are fixed as to represent the bulk phase of the system.

3.2.2 Ge(001)-surface and nomenclature

To model the β -terrace we first model the clean Ge(001)-surface. Both the buckled $b(2 \times 1)$ and $c(4 \times 2)$ reconstructions using a (2×4) supercell and the symmetric (2×1) reconstruction were generated using a (1×2) supercell. After relaxation, the $b(2 \times 1)$ and the $c(4 \times 2)$ reconstruction were found to be 0.302 and 0.374 eV per dimer lower in energy than the symmetric (2×1) dimer. Furthermore, a buckling angle of $\sim 19.5^\circ$ was found for both asymmetric reconstructions, and a dimer length of 2.45 Å for the $b(2 \times 1)$ reconstruction and 2.51 Å for the $c(4 \times 2)$ reconstruction was calculated, all in accordance with previous theoretical and experimental results. [76–79]

Based on experimental evidence, [18, 27] we assume that the β -terrace contains 0.25 ML of Pt. Furthermore, we assume that these Pt-atoms are located in the top layer of the Ge slab (we will show in **Sec. 3.3.4** that Pt in the second or third layer can not be responsible for the experimentally obtained STM images). To model the β -terrace, all possible non-isomorphic geometries are examined. We generate these geometries by substitution of two surface Ge atoms, of the $b(2 \times 1)$ surface reconstruction in the (2×4) supercell, by Pt atoms. Ignoring the buckling of the Ge dimers for a moment, this leads to seven non-isomorphic geometries. The first Pt atom replaces the Ge surface atom in position 0, while the second Pt atom replaces one of the other seven surface Ge atoms (*cf.* Fig. 3.1). We will refer to these geometries as β_1 to β_7 . If the buckling of the Ge dimers in the $b(2 \times 1)$ reconstruction is taken into

¹A qualitative comparison of LDA and GGA results is presented in **Appendix C.2**.

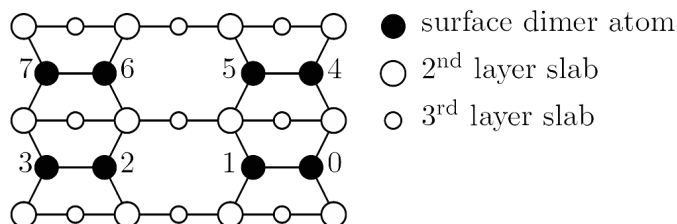


Figure 3.1: Top view of the $Ge(001)$ surface with symmetric (2×1) reconstruction. 0–7 are indexes for the surface dimer atoms and are used in the nomenclature of the geometries (see text).

account, some of the symmetry is lost. Let us assume for a moment that the atoms of the dimers in Fig. 3.1 with an even index are the down dimer atoms and those with an odd index are the up dimer atoms. In what follows we will keep referring to those positions in this manner. We now notice that in some geometries both Pt atoms are located at an up (down)-dimer atom position and in other cases one Pt atom is located in an up dimer atom position while the other Pt atom is located in a down dimer atom position.² While for the latter all combinations that are isomorphic stay isomorphic when tilting is taken into account this is not the case in the former situation. Take for example the β_2 geometry with its Pt atoms in positions 0 and 2, an isomorphic geometry in the symmetric reconstruction is one with Pt atoms in positions 1 and 3. In the $b(2 \times 1)$ geometry, as described above, the first β_2 geometry has both Pt atoms at down dimer atom sites, while the second has them at up dimer atom sites. To distinguish these two different geometries, indices u and d are used to indicate the up or down location of the Pt atoms. So the first β_2 geometry is called β_{2d} and the second one β_{2u} .³ For geometries with one atom at an up and one at a down dimer atom site both the u and d -index are used to indicate just this (e.g. $\beta_3 \rightarrow \beta_{3ud}$). This results into ten non-isomorphic geometries to start from.

To complete the picture of this system we also included possible geometries containing 0.5 ML of Pt in the top layer. Such a surface then consists entirely of Pt-Ge dimers. Geometries containing pure Pt and pure Ge dimers were not considered based on our results for the β -geometries.

The three possible geometries considered are a 1×2 reconstruction (γ_1) with all Pt atoms at the even (or odd) positions, a 2×2 reconstruction (γ_2) with the Pt atoms at positions 0, 2, 5, and 7, and a 2×4 reconstruction (γ_3) with the Pt atoms

²For the sake of simplicity and ease of writing we refer to any bound atom-pair on the surface and in its top-layer as a dimer, even if it consists of two different atoms. If the atom-types are important we will refer to the dimer as an X-Y dimer, with X and Y its constituent atoms. Also a shorter notation will be used where Ge dimers is used to refer to Ge-Ge dimers and Pt dimers is used to refer to dimers containing at least 1 Pt atom. For the latter it will follow from the context if this refers to Pt-Ge dimers, Pt-Pt dimers or both.

³Note that the u and d index only indicate the position in the $Ge(001)$ reconstruction geometry, and tells nothing about the relative z -position of the Pt atoms with regard to the Ge atom in the specific Pt-Ge dimer.

Formation energies and buckling angles.

	E_f (meV)	Pt-Ge buckling (degrees)	Ge-Ge buckling (degrees)
$b(2 \times 1)$	0	-	19.42
$c(4 \times 2)$	-73	-	19.67
β_{1ud}	589	20.57	19.07 (18.25)
β_{2u}	-16	-4.42	21.03
β_{2d}	94	-0.15	18.23
β_{3ud}	34	-4.43(u) -1.82(d)	21.85(u) 18.13(d)
β_{4u}	-61	1.92	18.85
β_{4d}	-25	0.50	18.85
β_{5ud}	83	-5.04(u) 7.38(d)	19.06(u) 18.43(d)
β_{6u}	-25	-4.25	20.82
β_{6d}	82	-0.88	18.13
β_{7ud}	29	-4.83(u) -1.30(d)	21.43(u) 18.06(d)
$\gamma_1 (1 \times 2)$	-47	1.95	-
$\gamma_2 (2 \times 2)$	80	6.13 , -6.46	-
$\gamma_3 (2 \times 4)$	89	5.75 , -6.11	-

Table 3.1: The formation energy and dimer buckling angles of the β and γ -surfaces compared to Ge(001) surface reconstructions and the buckling angles of the dimers. For the β_{1ud} geometry the Pt-Ge dimer buckling refers to the buckling of the Pt-Pt dimer and the value between brackets for the Ge-Ge buckling refers to the buckling of the Ge-Ge dimers located in the same dimer row as the Pt-Pt dimers. The notations (u) and (d) in the column of the Pt-Ge buckling refer to the position of the Pt atom in the dimer, while in the Ge-Ge buckling column they indicate if the Ge dimer is in a dimer row with the Pt atom in the up or down position (except for β_{5ud} where it refers to the location of the Pt atom in a Pt-Ge dimer in the adjacent dimer row). For γ_2 and γ_3 the buckling angles of both dimers of a single dimer row are given.

at positions 0, 3, 5, and 6.⁴ All these geometries were optimized using the conjugate gradient method while keeping the positions of the Ge atoms in the two center layers fixed.

⁴Or any of the possible equivalent geometries.

3.3 Theoretical results

3.3.1 Geometry and formation energy

3.3.1.1 Stability of the β -geometries

The stability of the different geometries was investigated by comparison of their formation energies to the formation energy of the Ge $b(2 \times 1)$ surface reconstruction. The formation energy of a certain geometry, β_x , can be calculated using the expression:⁵

$$E_f = [(E_{\beta_x} + N_{Pt}E_{Ge}) - (E_{b(2 \times 1)} + N_{Pt}E_{Pt})]/N_{Pt-dimers}, \quad (3.1)$$

with E_{β_x} the total energy of the β_x -geometry, N_{Pt} the number of Pt atoms in the system, E_{Ge} and E_{Pt} the bulk energy of a Ge and a Pt atom, $E_{b(2 \times 1)}$ the total energy of the Ge $b(2 \times 1)$ surface reconstruction and $N_{Pt-dimers}$ the number of surface dimers containing Pt atoms. Negative values for E_f indicate an increase in stability caused by replacing a Ge atom by a Pt atom.

Table 3.1 clearly shows that formation energy of the β_{1ud} -surface is much higher than that of the other structures. This is the only structure containing a Pt-Pt dimer; all the other surface models contain mixed Pt-Ge dimers. It shows that replacing a Ge atom in a Pt-Ge dimer with a Pt atom will require about 0.5 to 0.6 eV. This allows us to rule out the formation of Pt-Pt dimers in the β terrace. Table 3.1 also shows a preference for geometries which contain Pt-Ge dimer rows with the Pt atom in the *up* position. The entire set of formation energies, with exception of β_{1ud} , is

⁵An alternative way of calculating the formation energy (which gives exactly the same results) is by calculating the surface formation energy E_{sb} of the β -surface using the expression,

$$E_{sb} = E_T[\beta_x] - N_{Pt}E_{Pt} - N_{Ge}E_{Ge},$$

where $E_T[\beta_x]$ is the total energy of the β_x -surface, N_X the number of atoms of type X in the slab with E_X the corresponding bulk energy per atom. This formation energy we can now consider to be the sum of the formation energies of the separate surface dimers. Because the surface consists of two types of dimers, it is reasonable to assume that they will contribute differently to the total formation energy. The formation energy of a Ge-Ge dimer is found by calculating the formation energy per surface dimer for a Ge(001) $b(2 \times 1)$ surface reconstruction. Subtraction of the formation energy caused by the Ge-Ge dimers gives:

$$E_{sb2} = E_{sb} - N_{Ge-dimers}E_{s Ge-dimer},$$

with $N_{Ge-dimers}$ the number of Ge-Ge dimers in the β -surface and $E_{s Ge-dimer}$ the formation energy of a Ge dimer in the $b(2 \times 1)$ surface reconstruction. The resulting energy E_{sb2} can then be considered the contribution by the Pt-Ge dimers to E_{sb} .

If we again subtract the formation energy $E_{s Ge-dimer}$ from the calculated energy contribution per Pt-Ge dimer, $E_{sb2}/N_{Pt-dimers}$, the formation energy per Pt-Ge dimer as given in Eq. (3.1) is obtained.

In this derivation the physical meaning of the formation energy becomes clear: “the energy gained/needed to replace a Ge-Ge dimer by a Pt containing dimer”. This is true under the assumption that there is no contribution to the surface energy due to dimer-dimer interactions or (as we will do) if all changes herein are attributed to the Pt containing dimers and they are assumed to be equal in a single geometry. This allows us to estimate the energy contributions to the surface formation energy due to inter- and intra dimer row interactions, by comparison of similar geometries.

spread over a relatively small energy interval of ~ 150 meV, which is of the same order of magnitude as the thermal energy corresponding to the annealing temperature. In experiment, the germanium samples on which the Pt is deposited need to be annealed at a temperature of > 1000 K (≈ 86 meV) before the β -teras (and nanowires) appear. [18] This makes it impossible to exclude any structures, in addition to the β_{1ud} -structure, based solely on energetics.

All formation energies are given per Pt containing dimer. This means that it is the average energy to form a Pt-Ge dimer in the β_2 – β_7 structures.⁵ In the structures indicated with the ud -subscript the Pt-Ge dimers are not equivalent. To make a distinction between these two types of dimers we will refer to a Pt-Ge dimer with the Pt atom in the up position as a Pt-up dimer, and similar for a Pt-down dimer. The β_{3ud} -structure contains a Pt-up and a Pt-down dimer, while the β_{2u} - and β_{2d} -structures contain either only Pt-up or Pt-down dimers.

If we take the average of the formation energy of a Pt-up and a Pt-down dimer from the β_{2u} - and β_{2d} -structures we get 39 meV, comparable to the formation energy of an average Pt-Ge dimer in the β_{3ud} -structure. Comparison of the β_{7ud} -structure with the β_{6u} - and β_{6d} -structures gives a similar result, 28.5 meV for the average of the β_{6u} - and β_{6d} -structure compared to 29 meV for the average β_{7ud} Pt-Ge dimer. The pattern of Pt-Ge and Ge-Ge dimers in these two sets of three geometries is the same, indicating that the energy due to interactions between neighboring dimer rows is small compared to the formation energy. It also shows the formation energy of the Pt-Ge dimer to depend strongly on the surrounding dimers in the dimer row.

The third triplet of similarly patterned structures (β_{5ud} , β_{4u} and β_{4d}) shows this last point even more clearly. In this case the average of the formation energy of a Pt-Ge dimer of the β_{4u} - and β_{4d} -structure is -43 meV, much less than the average formation energy for a Pt-Ge dimer in the β_{5ud} -structure. Unlike the previous examples, the Pt-Ge dimers of the β_{5ud} -structure have a different surrounding along the dimer row than those in the β_4 -structures: antiparallel instead of parallel Pt-Ge dimers. This shows that the interaction between neighboring dimers in a single dimer row is strong, and provides a large contribution to the formation energy of a Pt-Ge dimer. It also shows that rotation of a Pt-Ge dimer in the β_{5ud} -surface cell would give an energy gain of roughly 0.2–0.3 eV per surface unit cell.

Based on such comparisons we can make an estimate of the inter and intra dimer row energy contributions to the formation energy of a Pt-Ge dimer, E_f . To estimate the interaction energy between neighboring dimer rows, we compare structures with different inter dimer row neighbors for the Pt-Ge dimers. Comparison of the β_2 - to the β_6 -structures, the β_{3ud} - to the β_{7ud} -structure, the β_4 - to the γ_1 -structure, the γ_2 - to the γ_3 -structure, and β_{5ud} - to the γ_2 - and γ_3 -structures, shows that this interaction energy is of the order of about 5–10 meV per Pt-Ge dimer.

A similar estimate can be made for the interaction energy along a dimer row by comparing structures with different neighbors in a single dimer row for a Pt-Ge dimer. Comparing the β_4 - to the β_6 - and the β_{5ud} -structures, and comparing the γ_1 - to the γ_2 - and γ_3 -structures, gives an interaction energy in the range of 50–150 meV per Pt-Ge dimer, about one order of magnitude larger than the inter-dimer-row interaction energy. It also shows that the proximity of the second Pt atom has a

large influence, both for better (β_{4u}) and for worse (β_{5ud}), on the formation energy.

Furthermore, we found that the length of the dimers was not influenced by the different surface structures, with the sole exception of β_{1ud} , which is the only surface structure containing a Pt-Pt dimer. The lengths of the Ge-Ge dimers were found to be $2.45 \pm 0.01 \text{ \AA}$ ($2.34 \pm 0.03 \text{ \AA}$ for β_{1ud}) and for the Pt-Ge dimers 2.35 \AA (2.58 \AA for the Pt-Pt dimer in β_{1ud}) (*cf.* **Appendix B**). The buckling angles on the other hand do show a dependence on the location of nearby Pt atoms. Noteworthy is the fact that the Pt-Ge dimers show little to no buckling and the little buckling effect they show depends on the location of the Pt atom: if the Pt atom is located in the up position then the buckling angle is about $4\text{--}5^\circ$, while it is less than 2° when the Pt atom is located in the down position. The sign used for the buckling angles indicates whether dimers are buckled in the same (same sign) or opposite (opposite sign) direction. In all cases, except β_{1ud} and β_4 , the Pt-Ge dimers are buckled in the opposite direction of the Ge-Ge dimers thus creating a (2×2) or (4×2) surface reconstruction. These reconstructions also modify the Ge positions in the second and third layer in a similar way as found for the Ge $c(4 \times 2)$ surface reconstruction, which will be discussed in more detail in **Sec. 3.3.3**. [77, 79] Table 3.1 also shows that the Ge-Ge dimers are slightly influenced by the Pt-Ge dimers in the same dimer row, increasing the buckling angle to about $21\text{--}22^\circ$ for Pt-Ge dimers with the Pt atom in the up position and decreasing it to about 18° if the Pt atom in the Pt-Ge dimer is in the down position.

Another difference between Pt-Ge dimers with the Pt atom in the up or down position becomes clear when they are considered in a dimer row containing both Pt-Ge and Ge-Ge dimers. The Pt-Ge dimer shifts orthogonal to the dimer row. If the Pt atom is located in the up position this shift is very small ($\sim 0.03 \text{ \AA}$) and almost entirely due to the Pt atom moving in the direction of the up position. On the other hand, if the Pt atom is located in the down position, the shift is in the down direction and both the Ge and the Pt atom of the Pt-Ge dimer are shifted over a distance of $\sim 0.4 \text{ \AA}$.

Comparison of the average z -position of the dimers shows the Pt-Ge dimers to be 0.01 to 0.14 \AA lower than the Ge-Ge dimers for each of the considered structures. All the geometrical information of the Pt-Ge dimers combined with the formation energies given in Table 3.1 shows a preference for Pt atoms to be surrounded by Ge atoms which stick further out of the surface than these Pt atoms. This can be traced back to the preference for Ge-terminated surfaces in Pt/Ge alloys. [88]

3.3.1.2 Stability of the γ -geometries

The stability of the γ -geometries is investigated the same way as for the β -geometries. Equation (3.1) is used to calculate the formation energy per Pt containing surface dimer, making close comparison with the β -geometries possible (*cf.* footnote 5). In the previous paragraph we found the inter dimer row interaction to be very small, compared to the intra dimer row interaction. This allows us to compare the γ_1 -geometry to the β_{4x} -geometries, and the γ_2 and γ_3 -geometries to the β_{5ud} -geometry. The main difference between these geometries is the presence of a

Ge-Ge dimer row in the β -geometries. Table 3.1 shows the formation energies for the γ -geometries to be in the range expected from the comparable β -geometries. As was shown in the previous paragraph, the interaction between neighboring dimer rows is relatively small for β_{5ud^-} , γ_2^- and γ_3^- -geometries, and a larger part of the formation energy can be attributed to strain between sequential Pt-Ge dimers. For the β_{4x^-} and γ_1^- -geometries the influence of the neighboring dimer rows is more important. Although the geometry of the Pt-Ge dimer in the γ_1^- - and β_{4u^-} -geometry is nearly indistinguishable (*cf.* Appendix B), and thus quite different from that of the one in the β_{4d^-} -geometry, the formation energy is about the average of that of the β_{4u^-} - and the β_{4d^-} -geometry. The geometries of the Pt-Ge dimers in the β_{5ud^-} , γ_2^- and γ_3^- -geometries are almost identical (*cf.* Appendix B) and the angle between the antiphase Pt-Ge dimers in a dimer row is in each case about 12° with the Pt atoms on the geometrically lower side of the dimer. Furthermore, looking at the positions of sequential dimers in a dimer row, a shift orthogonal to the dimer row is observed. This shift increases the distance between the Pt atoms with 0.56–0.61 Å in the direction orthogonal to the dimer row. It is larger than any of such shifts produced with normal Ge-Ge dimers in the dimer row, indicating the crucial role of the Pt atoms in this matter.

3.3.2 Electronic structure

3.3.2.1 General properties of the β -geometries

Since there is no clear evidence based on energetics alone to put forward a single reconstruction as *the* β -terrace, a more direct comparison with the STM observations is needed. This was done by calculating the LDOS $\rho(\mathbf{r}, \varepsilon)$. [68] The theoretical (integrated) LDOS was calculated as $\bar{\rho}(\mathbf{r}, \varepsilon) \propto \int_{\varepsilon}^{\varepsilon_F} \rho(\mathbf{r}, \varepsilon') d\varepsilon'$, with ε_F the Fermi energy. A surface of constant density is then constructed according to $\bar{\rho}(x, y, z, \varepsilon) = C$, with C a real constant. This construction gives the height z , as a function of the lateral position (x, y) , which is mapped linearly onto a gray scale. This mimics the presentation of STM images in the usual constant-current mode of operation.

Figure 3.2 shows some pseudo-STM images of the β_{2u^-} , β_{2d^-} , and β_{7ud^-} -surface for both filled and empty states. The filled state image of the β_{2u^-} -surface shows a bright peak above the up-atom of the Ge dimer and a slightly less bright peak above the Ge atom of the Pt-Ge dimer. This creates a zigzag pattern of bright spots (of two different intensities). Comparison of the filled-state pictures of the β_{2u^-} and β_{2d^-} -surface, shows images for the Pt-Ge dimers that are clearly different. Where there is a clear peak when the Pt atom was located between up-Ge atoms (β_{2u^-}) there is a relatively evenly spread rectangular feature when the Pt atom is located between down-Ge atoms (β_{2d^-}). This feature is spread out over both atoms of the Pt-Ge dimer and is slightly higher at the position of the Ge atom. The difference in height of the feature at the (x, y) positions of the dimer atoms is five times smaller than the difference in height between similar points of the feature produced by the Ge dimer. The Pt-Ge feature, in the β_{2d^-} filled-state picture, has a height equal to the average height of the Ge dimer and does not protrude as far in the trough between the dimer rows as the

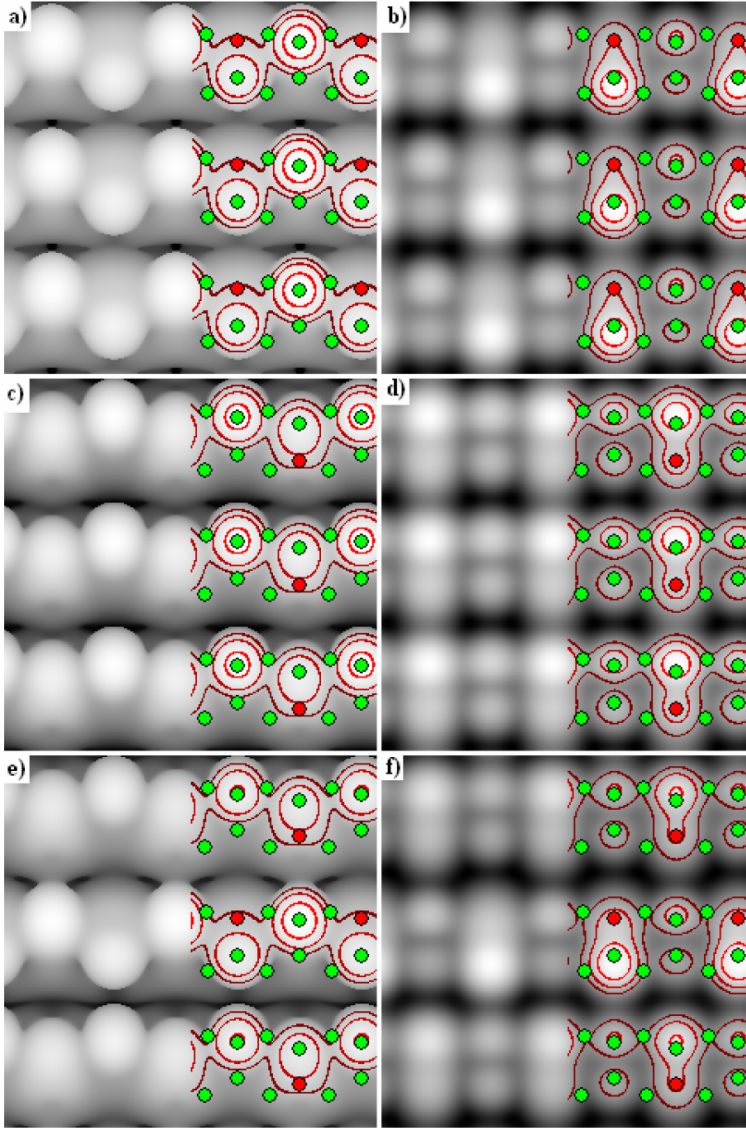


Figure 3.2: Pseudo-STM images showing filled (a, c, e) and empty (b, d, f) states of the β_{2u^-} (a, b), β_{2d^-} (c, d), and β_{7ud^-} (e, f) geometries. For the filled-state images $\varepsilon = \varepsilon_F - 0.70$ eV and for the empty-state images $\varepsilon = \varepsilon_F + 1.50$ eV is used. The constant density used, is chosen such that the maximum z is at 3.0 Å above the highest atom. The small black (red) filled circles represent the Pt atoms in the top layer, the small grey (green) circles represent the positions of the Ge atoms in the two top layers. Contours are added to indicate the main features discussed in the text.

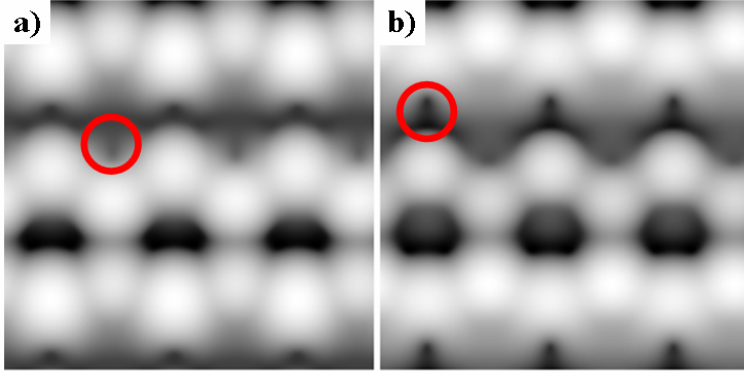


Figure 3.3: Pseudo-STM images showing filled (a) and empty (b) states of the β_{7ud} -geometry close to the Fermi level, with $\varepsilon = \varepsilon_F \pm 0.30$ eV. The maximum z is at 4 Å above the highest atom. There is a clear difference between the dimer rows with the Pt atoms located between up-Ge atoms (middle zigzag row) and the dimer rows with the Pt atoms located between down-Ge atoms (top and bottom row). A notch (circle) in the constant density surface above the location of the Pt atoms is visible for both the filled- and empty-state image.

Ge dimer. This gives the overall impression of ‘battlements’ (cf. all dimer rows in Fig. 3.2c and the upper and lower dimer row in Fig. 3.2e).

The β_{7ud} -surface contains both a Pt atom between up-Ge atoms and one between down-Ge atoms. As could be expected from the filled-state images of the β_{2u} - and β_{2d} -surfaces the filled-state image of the β_{7ud} -surface shows a zigzag row and a battlement row alternatingly. A further study of the pseudo-STM images of the other β -geometries shows these same structures reappearing in different combinations.

A Pt atom located between up-Ge atoms causes a feature which is about three times as steep as the feature caused by a Pt atom between down-Ge atoms. The Pt atom is also always located at the lower end of these features, even though sometimes the geometry shows the Pt atom to be the higher atom of the dimer. For the β_{4x} -geometries, the dimer row of the Pt-Ge dimers shows a $b(2 \times 1)$ structure while a (2×2) structure is found in case of the β_{5ud} -geometry. This Pt-Ge dimer row is always a much dimmer than the Ge dimer row, but it still shows nicely distinct dimer patterns. Another careful look at the pseudo-STM structure of a Pt-Ge dimer with the Pt atom between up-Ge atoms shows that unlike the Ge-dimer this structure has a dim tail directed toward the Pt atom. Although this is best visible in the empty-state pictures of Fig. 3.2, it is present for both filled- and empty-state images.

The above analysis of the pseudo-STM images shows that the filled-state images of single dimers can be used as building blocks to reconstruct the geometry of the β -terrace (this will be shown in Sec. 3.3.2.4).

The empty-state pseudo-STM images for a bias far above the Fermi level show a

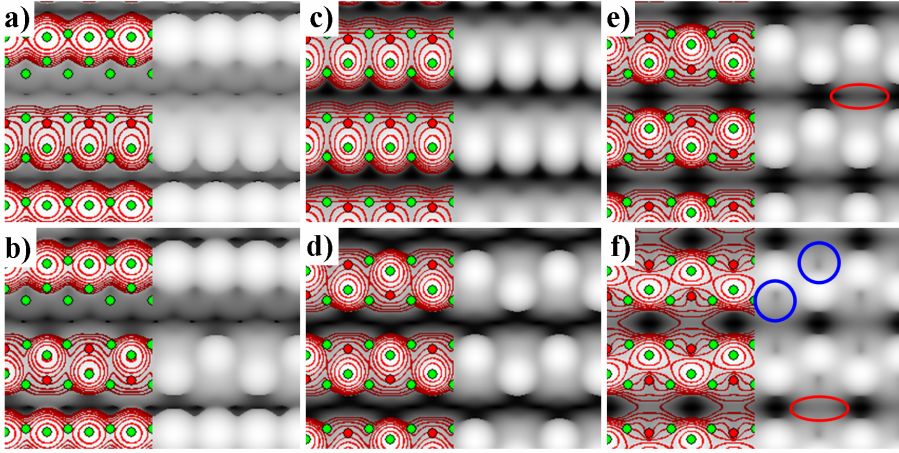


Figure 3.4: Comparison of β and γ structures. Filled state pseudo-STM images of the β_{4u} - (a), β_{5ud} - (b), γ_1 - (c), γ_2 - (d), and γ_3 -structure (e) with $\varepsilon = \varepsilon_F - 0.70$ eV and an empty state pseudo-STM image of the γ_3 -structure (f) close to the Fermi level with $\varepsilon = \varepsilon_F + 0.30$ eV. The maximum z is at 3 \AA above the highest atom. The green (red) discs indicate the positions of the Ge (Pt) atoms in the two top layers of the system. Contours separated 0.2 \AA are added to guide the eye. The circles indicate the ‘notch’, while the ellipse shows the position of the ‘bridge’. The Ge dimer row in (a) and (b) show slightly broader and higher dimer images than the Pt-Ge dimer row.

very simple picture, with little or no dependence of the position and size of the Pt atom features on the neighboring Ge atoms. The Ge dimer shows up as a set of two separate peaks, while the Pt-Ge dimer is smeared out, showing a bright ball on the side of the Ge atom and a dim wide tail on the side of the Pt atom. Though the Pt-Ge dimer images look very similar in the empty-state pseudo-STM pictures, they are not exactly the same. The empty-state picture of β_{7ud} in Fig. 3.2 shows clearly that the Pt-Ge dimer with Pt in the up position is slightly brighter and has a somewhat more egg-like shape. Close to the Fermi level, the pseudo-STM images of filled and empty states are nearly indistinguishable and some interesting features appear in the pseudo-STM images. The most eye-catching feature is the notch in the isosurface, indicated by a circle in Fig. 3.3a and b. It is caused by the Pt atom at that location. Though clearest for the Pt atom between up-Ge atoms in a filled-state images and clearest for the Pt atom between down-Ge atoms in the empty-state images, both are present at either side of the Fermi level and were found in all geometries. Checking contour plots of cross-sections in the z direction at the position of these notches, showed they are caused by the gap between two lobes of the d -orbitals of the Pt atom underneath.

3.3.2.2 General properties of the γ -geometries

The pseudo-STM pictures of the γ -geometries show in general the same image for the Pt-Ge dimer rows as was seen for the corresponding Pt-Ge dimer rows in the β_{4x} and β_{5ud} pictures (cf. Fig. 3.4). For the γ_1 -geometry, the pseudo-STM pictures show dimer rows with a bright spot at the Ge dimer atom position. This spot becomes sharper when the bias becomes smaller, both above and below the Fermi energy. The γ_2 - and γ_3 -geometries show nearly identical pictures (cf. Fig. 3.4d and e), the main difference being the phaseshift between neighboring dimer rows, which causes the appearance of a very dim (at least 1.5 Å lower than the dimer peaks in the pseudo-STM pictures) bridge between the Pt atoms of neighboring dimer rows, indicated with an ellipse in Fig. 3.4e and f. This bridge is most clear in the empty state pictures. Again it is the Ge side of the Pt-Ge dimers which lights up very bright, causing a zigzag pattern of bright spots along each dimer row. For small biases this zigzag pattern becomes more pronounced and also the notch above the Pt atoms appears, as indicated with the circles in Fig. 3.4f. At a large negative bias the bright spot has a dim tail directed toward the Pt atom. All Pt-Ge dimer images for γ_2 and γ_3 are identical, unlike for the β -geometries.

3.3.2.3 β_{6u} -structure as geometry for the β -terrace

In this paragraph we will show that, although most β -structures studied are energetically available, only the β_{6u} -geometry can be related to the experimentally observed β -terrace. Figures 3.5 and 3.6 show (experimental) STM images of the β -terrace at biases of -0.30 V and $+0.30$ V. The filled-state image clearly shows two types of dimers alternating in each dimer row. One of the dimer types shows up as a big bright spot on one side of the dimer row while the other dimer type shows up as a smaller somewhat dimmer spot on the other side of the dimer row, with a dim tail extending to the opposite side of the dimer row. These are the only two types of dimers appearing in the image. Comparing this to the results of the pseudo-STM images seen in the previous paragraph, the first type of dimer is the Ge-Ge dimer while the second type of dimer presents all the typical features of the Pt-Ge dimer with the Pt atom located between up-Ge atoms. This allows us to exclude all β -geometries containing Pt at a down location, leaving only the β_{2u^-} , β_{4u^-} , and β_{6u} -geometry. Taking the relative ordering of the features of neighboring dimer rows into account, the geometry which represents the β -terrace can only be the β_{6u} -geometry. Filled- and empty-state pseudo-STM images of the β_{6u} -geometry are displayed on top of the experimental pictures in Fig. 3.5 and 3.6. The empty-state pseudo-STM image (Fig. 3.6) shows some very specific features of this geometry. There are *triangular holes* where the Pt atom is located and the Ge atoms of the top layer also create a triangular feature dominated by the zigzag structure of the up-Ge atoms and the Ge atoms in the Pt-Ge dimers. Comparison of the empty-state images in Fig. 3.6 reveals the existence of these features in both images, further strengthening our belief that the β_{6u} -geometry is the geometry of the β -terrace. Another look at Table 3.1 also confirms this geometry to be more stable than the Ge $b(2 \times 1)$ surface reconstruction. Furthermore, for the β_{6x} -geometries, the Pt atoms are also distributed in the most

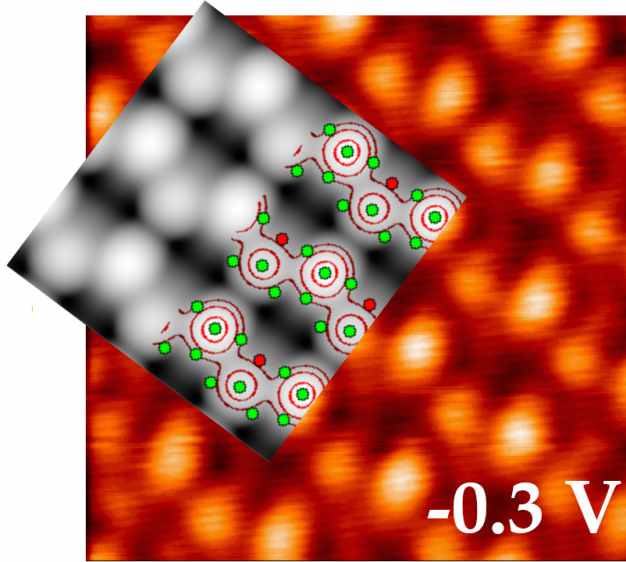


Figure 3.5: Comparison of the filled-state pseudo STM image of the β_{6u} -geometry (gray scale overlay) with the corresponding experimental STM image of the β -terrace. The STM image is obtained using a sample bias of -0.3 V, while the pseudo STM image is generated using $\varepsilon = \varepsilon_F - 0.70$ eV and a maximum z of 4 Å above the highest atom. The small red discs represent the positions of the Pt atoms in the top layer, while the green discs represent the positions of the Ge atoms in the top two layers. The QDRs are clearly visible, in both STM images, as is the presence of two different types of dimer.

homogeneous way. The pseudo-STM images show only for the β_{6u} -geometry this level of agreement with the experimental STM images, allowing the β_{6u} -structure to be presented as *the* geometry of the experimentally observed β -terrace.

Figure 3.8b shows the band structure of the β_{6u} -geometry along the high symmetry lines Γ -J-K- J' - Γ -K of the surface BZ (*cf.* Fig. 3.7). Figure 3.8a shows the band structure of the Ge(001) $c(4 \times 2)$ reconstruction along the same lines for comparison. In general, the two band structures show similar behavior. Perpendicular to the dimer row direction, along the J-K and J' - Γ line, the bands show little dispersion. Along the J' - Γ line, a few of these bands cross the Fermi level. The main difference between the two band structures is located along the Γ -J and K- J' lines. For the β_{6u} -structure we find bands with a strong dispersion opposite to what is seen for the Ge(001) surface. These bands are indicated with the ellipses in Fig. 3.8b. Furthermore, these bands also cross the Fermi level in the second half of the Γ -J line and in the first half of the K- J' line, resulting in the metallic behavior observed for the β -terrace. [89] Taking a closer look at these specific bands near the crossing of the Fermi level, we find that their character contains three main components. The

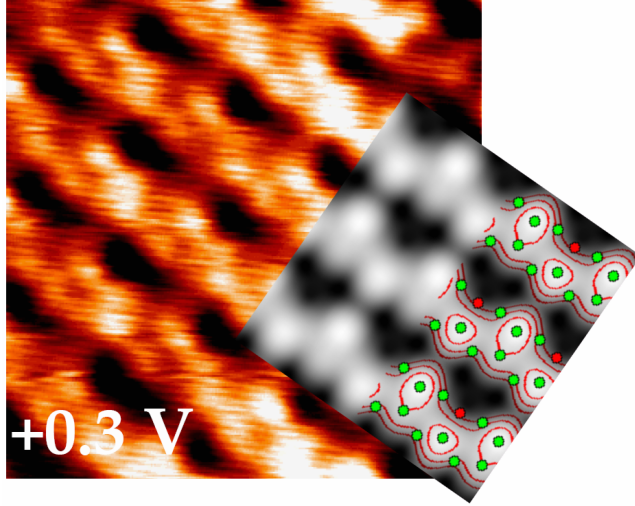


Figure 3.6: Same as Fig. 3.5 but now for the empty-state images. The sample bias used for the STM image is +0.3 V and $\varepsilon = \varepsilon_F + 0.70$ eV is used for the pseudo STM image. Note the triangular holes above the Pt atoms (red discs) which are present in both the theoretical and the experimental STM image. This is a unique feature for the β_{6u} -structure.

largest component has a Pt-like character. The other two (smaller) components have a Ge-like character: more specifically, the second layer Ge atoms bound to the Pt atoms in the top layer and the Ge up-atom, of the Ge surface dimer, which is located in between the Pt atoms. The orbital character of the Pt contribution is mainly p_x , p_y and d_{xz} , d_{yz} , making it highly planar. The Ge contribution depends on the Ge atoms involved. The orbital character of the contribution of second layer Ge atoms is mainly sp^3 , while the top layer Ge atoms bound to the Pt atom contribute mainly a p_z orbital character, indicating the presence of a π -bond with energy close to the Fermi level for the Pt-Ge dimer. Interestingly, the Ge up-atoms of the Ge dimers in between Pt atoms along the dimer row have a significant contribution to most of the bands we are interested in. The orbital character in this case is mostly p_x and p_y . The presence of bands close to (and crossing) the Fermi level connected to an orbital character directed along the dimer row direction, indicates the possible presence of surface conduction channels along this direction. These bands could be the source of the confined states observed in Ref. [27] and [90].

Figure 3.9 shows the DOS of the β_{6u} -geometry and the LDOS of the surface atoms.⁶ The total DOS roughly shows the DOS observed for bulk Ge, as could be expected. The main difference is found in the BG region. Here, three distinct peaks

⁶The zero, or nearly zero, band gap for germanium is a known failure of LDA. Although a band gap can be opened using for example the GW method, it is not necessary for the qualitative comparison we are making here.

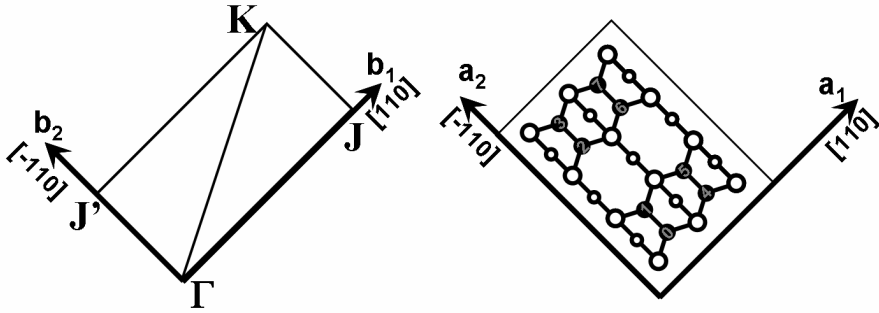


Figure 3.7: High symmetry lines and points of the surface Brillouin zone (left) for the β -structures. A surface unitcell is shown on the right, indicating the orientation of the dimer rows.

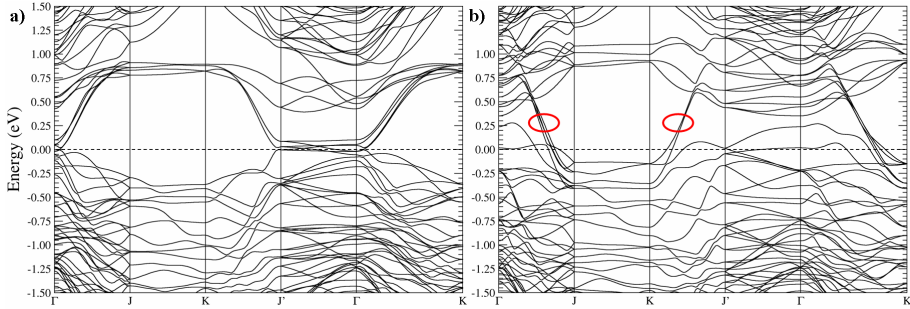


Figure 3.8: Comparison of the band structure, along high symmetry lines (cf. Fig. 3.7), of the Ge(001) $c(4 \times 2)$ reconstruction (a) and the β_{6u} -geometry (b). The energy zero is set at the Fermi level.

can be observed, indicated by the labels 1, 2, and 3 in Fig. 3.9. The two outer peaks (1 and 3) are also observed for a reconstructed Ge(001) surface, where they are linked to the dangling bonds of the Ge surface dimer atoms. Since half the surface dimers of the β_{6u} -geometry are Ge dimers, it is not surprising to observe these states. Figure 3.9b shows the LDOS of the up and down atoms of the Ge surface dimers. Comparison to the Ge(001) $c(4 \times 2)$ and $b(2 \times 1)$ reconstruction, shows the peak due to the Ge-down atom (3) to be quite broad, giving it a width comparable to what is found for the $b(2 \times 1)$ reconstruction. This broadening probably originates from the small tilt-angle of the Pt-Ge dimers. This makes the angle between subsequent dimers in a QDR smaller, moving toward the zero angle of the $b(2 \times 1)$ reconstruction. The Ge-up atom, on the other hand, shows two peaks in the BG (1 and 2 in Fig. 3.9b). The strong peak, labeled 1 is also found for the Ge-up atom of the Ge(001) $c(4 \times 2)$ and $b(2 \times 1)$ reconstructions. The weaker second peak has a non-zero value for the DOS at the Fermi level and is one of the contributions to peak 2 in the total DOS.

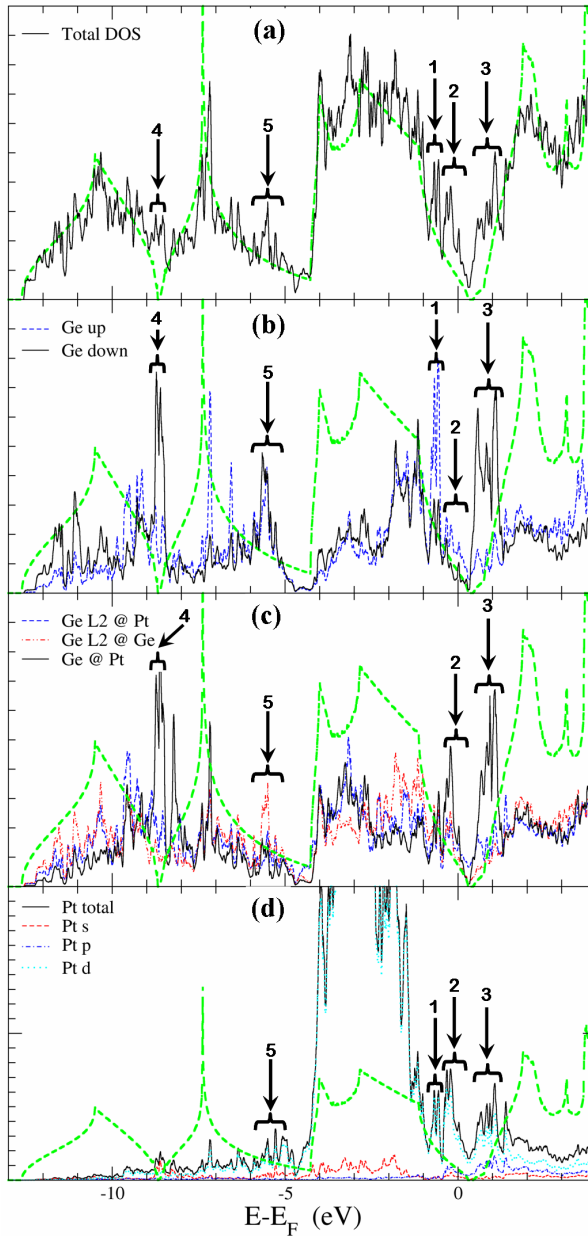


Figure 3.9: Total DOS of the β_{6u} -geometry and the LDOS of the surface atoms. The bold dashed green curve shows the DOS of Bulk Ge, it is shifted to align the edges of the BG regions.

The LDOS image of the Ge atoms bound directly to the Pt atom shows something interesting (*cf.* Fig. 3.9c). The Ge atom of the Pt-Ge dimer also has two peaks in the BG region, contributing to peaks 2 and 3 in the total DOS. A sharp peak around the same value as seen for the Ge down atom at the conduction band (CB) side (3), and a second peak near the valence band (VB) side of the BG region (2). This second peak is located just at the Fermi level. Between these two peaks the LDOS goes to zero, just above the Fermi level.

The second layer Ge atoms (indicated with L2 in Fig. 3.9) show roughly the same structure, both have a small contribution to the conducting peak 2 of the total DOS. However, in the BG region it are only the second layer Ge atoms bound to the Pt atoms of the top layer that have non-zero values over the entire BG region (*cf.* blue dashed curve in Fig. 3.9c). Second layer Ge atoms bound to the Ge atoms of the top layer have a LDOS which goes to zero. The LDOS for the Pt atoms, presented in Fig. 3.9d, shows the presence of Pt d states at and around the Fermi level, with 3 peaks at the same locations as found for the Ge atoms bound to these Pt atoms. For the Ge atoms, it are mainly p states contributing to these peaks near the Fermi level, showing clearly the presence of a hybridization of Ge p with Pt d states. Together with the Ge up-atoms and Pt atoms, the Ge atoms bound to the Pt atoms form a corridor of ‘metallic’ atoms along the edge of the QDR, giving rise to the metallic peak 2 of the total DOS, in agreement with what was shown from the band structure and the experimental observations. [89]

The additional peaks, 4 and 5, in the total DOS are related to the surface Ge atoms, and are also observed for the Ge(001) $c(4 \times 2)$ and $b(2 \times 1)$ reconstructions.

3.3.2.4 Experimental existence of other β -geometries

Although the comparison between experimental and pseudo-STM images in Fig. 3.5 and 3.6 shows clearly that the clean β -terrace has a β_{6u} -geometry, the formation energies given in Table 3.1 indicate that also other geometries should be observed experimentally. Investigation of experimental STM images has shown the existence of (small) regions where dimer rows contain a mix of different (non β_{6u}) geometries. These geometries were mostly found near distortions of the normal β -terrace, such as dimer vacancies and the endpoints of a nanowire. Because these geometries seem related to defects, we will not go into the details of their geometry and focus solely on the β_{6u} -geometry.

3.3.3 The β_{6u} -geometry

To study the geometry of the β_{6u} structure, it is compared to the geometry of the Ge $b(2 \times 1)$ and $c(4 \times 2)$ reconstructions. This shows a slight shift of the second and third layer Ge atoms of the β_{6u} structure in the surface plane with regard to the Ge $b(2 \times 1)$ equilibrium positions. In what follows we will show that this deformation of the geometry can be understood as a combination of three geometric modifications,

Bond lengths and dimer tilt angle.

	ω	A	B ₁	B ₂	C ₁	C ₂	C ₃	C ₄
Ge b(2 × 1)	19.42	2.450	2.512	2.426	2.475	2.449	2.543	2.475
Ge c(4 × 2)	19.60	2.511	2.506	2.430	2.463	2.481	2.481	2.462
β_{6u} Ge-dimer	20.82	2.462	2.552	2.433	2.479	2.435	2.492	2.469
β_{6u} Pt-dimer	-4.25	2.354	2.378	2.521	2.479	2.435	2.492	2.469

	d ₁	d ₂	d ₃	t ₁	t ₂	t ₃	t ₄
Ge b(2 × 1)	0.815	0.775	0.099	3.818	0	0	0
Ge c(4 × 2)	0.842	0.749	0.007	3.817	0.283	0.335	0.332
β_{6u} Ge-dimer	0.875	0.731	0.027	3.764	0.153	0.049	0.003
β_{6u} Pt-dimer	0.174	1.358	0.027	3.764	0.153	0.049	0.003

Table 3.2: Bond lengths and distances in Å and the dimer tilt angle ω in degrees. All as defined in Fig. 3.10.

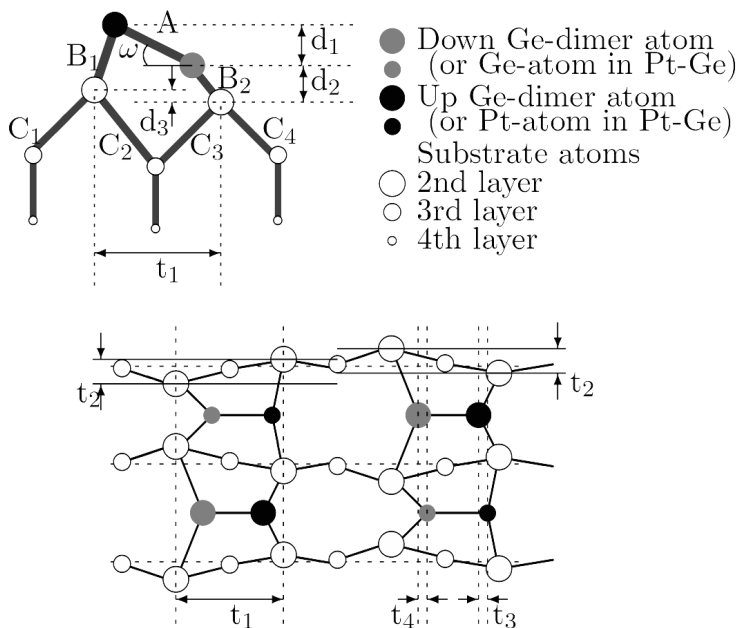


Figure 3.10: Top: Diagram showing a side view of a relaxed Ge-Ge dimer, including the labeling used for both Ge-Ge and Ge-Pt surface dimers. Bottom: Top view schematic representation of the β_{6u} -reconstruction.

each linked to a symmetry breaking of the top layer structure.

In the second layer of the β_{6u} geometry, two inequivalent sites are present: i) a Ge atom between a top layer Ge up atom and a Pt atom, and ii) a Ge atom between a top layer Ge down atom and a Ge atom of a Pt-Ge dimer. The Ge atom at the latter site is displaced toward the neighboring Ge atom of the Pt-Ge dimer, while the Ge atom at the former site is displaced toward the neighboring Ge up atom (*cf.* Fig. 3.10). In comparison to the Ge $b(2 \times 1)$ reconstruction, these atoms appear, in the surface plane, as twisted around the in-plane position of the third layer Ge atom in between them. For this reason, such a modification of the geometry, *i.e.* the twisting of the tetrahedral structure, is known in the literature as *twisting*. [79]

The Ge (2×2) surface reconstruction, for which a diagrammatic representation can be found in figure 2 of Ref. [79], is a simple Ge surface reconstruction which only shows the *twisting* modification with regard to the $b(2 \times 1)$ reconstruction. *Twisting* is believed to be a strain release mechanism, where strain (orthogonal to the surface) due to different surface dimer buckling is (partially) compensated by an in-plane modification of the second layer geometry, indicated with t_2 in Fig. 3.10. This means that the *twisting* parameter t_2 is related to the relative buckling angle of sequential surface dimers in a dimer row. Assuming a linear relation as first order approximation one finds $t_2 \sim |\omega_{\text{dimer1}} - \omega_{\text{dimer2}}| = \Delta\omega$, where ω_{dimerX} is the buckling angle ω shown in Table 3.2 for each of the dimers involved. Because the relative angle between sequential dimers can be used as a measure for the *twisting*, it becomes possible to estimate the *twisting* for similar surfaces via the ratio of their *twisting*

$$R = \frac{t_2^{\text{rec1}}}{t_2^{\text{rec2}}} = \frac{\Delta\omega^{\text{rec1}}}{\Delta\omega^{\text{rec2}}}, \quad (3.2)$$

where rec1 and rec2 refer to each of the two reconstructions being compared.

Unlike the *twisting* observed for Ge surface reconstructions with differently buckled surface dimers, the *twisting* found in the β_{6u} geometry is asymmetric. From Fig. 3.10 follows that t_2 can be considered to consist of two parts; the component along the dimer row direction of the bond C_2 and the component along the dimer row direction of the bond C_3 . The ratio of the contributions of C_2 and C_3 to t_2 is 1 : 1 for the Ge (2×2) and Ge $c(4 \times 2)$ reconstructions, while it is 6.3 : 9 for the β_{6u} reconstruction. This means that, in comparison to the Ge $c(4 \times 2)$ reconstruction, the second layer Ge atom between the Pt atom and the Ge up atom is pulled slightly back toward the Pt atom in the surface plane.

Using Eq. (3.2) to calculate the ratio R of the *twisting* of the β_{6u} reconstruction to the Ge $c(4 \times 2)$ reconstruction making use of the values for t_2 presented in Table 3.2 we find a value of 0.5406 for R . However, making use of the relative buckling angle we find a value of 0.6395 for R . Unlike the Ge $c(4 \times 2)$ reconstruction, there are different kinds of surface dimers on the β_{6u} surface. To include this inhomogeneity of the surface dimers in Eq. (3.2), we add weight factors to the angle contributions. We found the mass percentages of the dimers to be good weight factors. This leads

to a *twisting* ratio for the β_{6u} to the Ge $c(4 \times 2)$ structure:

$$\begin{aligned}
 R &= \frac{\left| \left(\frac{M_{\text{Ge}} + M_{\text{Pt}}}{3M_{\text{Ge}} + M_{\text{Pt}}} \right) \omega_{\beta_{6u}\text{Pt dimer}} - \left(\frac{2M_{\text{Ge}}}{3M_{\text{Ge}} + M_{\text{Pt}}} \right) \omega_{\beta_{6u}\text{Ge dimer}} \right|}{\omega_{c(4 \times 2)}} \\
 &= \frac{t_2^{\beta_{6u}}}{t_2^{\text{Ge}c(4 \times 2)}},
 \end{aligned} \tag{3.3}$$

with M_x the atomic mass of a single (average) atom of type x , and ω_y the angle ω shown in Table 3.2 for the specific dimer y . Using Eq. (3.3) a value of 0.5142 is found for the ratio R , in agreement with the value obtained for the ratio of the t_2 parameters. Also for other β structures, equations equivalent to Eq. (3.3) give an improvement of the estimated ratios of t_2 over the ratios obtained through Eq. (3.2). *E.g.* for the β_{1ud} structure compared to the Ge $c(4 \times 2)$ structure, the ratio of the *twisting* parameters t_2 is 0.5477. Using the relative buckling angles in Eq. (3.2) one finds a value of 0.0354, which is much too small. However, using the weighted buckling angles, as in Eq. (3.3), one finds a value of 0.5121, in good agreement with the ratio of the parameters t_2 .

This shows t_2 to be a useful parameter for comparison of the asymmetry induced strain in these systems. As a result, the difference of the *twisting* parameter, t_2 , between the Ge $c(4 \times 2)$ and β_{6u} -reconstruction can be attributed to the introduced Pt atoms. On the one hand by leveling out the Pt-Ge dimer, *i.e.* the ω term, and on the other hand through the contribution in the mass for the weight factor.

So the first of three surface modifications of the β_{6u} structure, is *twisting*; a result of the relative buckling angle of sequential dimers in a dimer row which is influenced strongly by the Pt atoms present in the β_{6u} structure.

Figure 3.11 gives, somewhat exaggerated, diagrams of the top view of a row of second and third layer Ge atoms in geometries with increasing complexity. The horizontal dashed lines give an arbitrary zero-line with regard to which all amplitudes are given. The Ge (2×2) -reconstruction shows the simple image of *twisting* of the tetrahedral arrangement, discussed above. The image of the Ge $c(4 \times 2)$ reconstruction presents, in addition to *twisting*, a *bending* of the entire second and third layer structure, indicated with the gray curve in Fig. 3.11. It shows a slight displacement of the third layer Ge atoms in the plane along the dimer row direction. This is due to the asymmetry between the C_1 , C_4 and the C_2 , C_3 bonds as a result of the opposite buckling of dimers in adjacent dimer rows.

In the β_{6u} structure, just like the Ge $c(4 \times 2)$ reconstruction, the surface dimers in adjacent dimer rows show an opposite buckling which results in a *bending*, as shown with the gray curve in the bottom picture of Fig. 3.11. Furthermore, the presence of Pt atoms in the top layer dimers seems to increase the amplitude of the bending by a factor of two and the extrema of the bending curve move from the third layer atoms between the dimer rows to the third layer atoms underneath the dimer rows.

The presence of two different dimer types in the β_{6u} structure complicates this image even further, as can be seen in the bottom picture of Fig. 3.11. On top of the previous two distortions a *shift* of the *twisting* t_2 between adjacent dimer rows

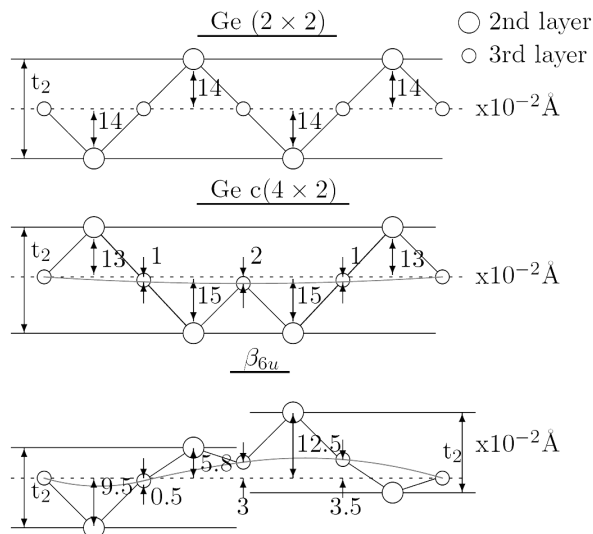


Figure 3.11: The diagrams show a top view of the upper row, as represented in the diagram of the β_{6u} -reconstruction in Fig. 3.10, of second and third layer Ge atoms in a Ge(2×2)-, Ge $c(4 \times 2)$ - and β_{6u} -reconstruction. The adjacent top layer atoms, as represented in the bottom diagram of Fig. 3.10, are then from left to right:

Ge (2×2): Ge up-dimer atom, down-dimer atom, up-dimer atom and down-dimer atom.

Ge $c(4 \times 2)$: Ge down-dimer atom, up-dimer atom, up-dimer atom and down-dimer atom.

β_{6u} : Ge atom, Pt atom, Ge down-dimer atom and Ge up-dimer atom.

(Data for the Ge (2×2)-reconstruction is taken from Gay et al. [79])

is present. *Shift* is the displacement of the horizontal lines defining the *twisting* parameter t_2 between neighboring dimer rows (cf. bottom pictures of Fig. 3.10 and Fig. 3.11), in other words; it is the *shift* along the dimer row direction of the *twisting* parameter t_2 its bounding box between adjacent dimer rows. This *shift* is a consequence of the induced asymmetry in the components along the dimer row direction of the C_2 and C_3 bonds contributing to t_2 , which in turn is due to the asymmetry of having different dimer types in a dimer row, as well as in adjacent dimer rows.

In case of the β_{6u} structure, the *shift* is directed toward the Pt-Ge dimer, away from the Ge-Ge dimer (cf. Fig. 3.10, bottom picture). This makes *shift*, which is due to different dimer types in one system, the third surface modification present in the β_{6u} geometry. It shrinks the surface cell containing the Pt-Ge dimer in favor of the Ge-Ge dimer surface cell. Table 3.2 also shows a decrease of the parameter t_1 , reducing the size of the Pt-Ge dimer surface cell even further and partially compensating

the expansion of the Ge-Ge dimer surface cell.

The bond length of the Ge-dimer in the β_{6u} reconstruction is only slightly longer than it was in the $b(2 \times 1)$ -reconstruction but still significantly shorter than it is in the $c(4 \times 2)$ -reconstruction. The accompanying change in buckling angle accounts for this slight elongation. Also, the back bonds of the Ge atoms of all dimers are longer than their counterparts in the asymmetric Ge surface reconstructions. This while the height of these back bonds for the Ge-Ge dimers is similar to the one found for the $c(4 \times 2)$ -reconstruction. t_3 and t_4 show us the in-plane displacement along the surface dimer bond direction between sequential dimers in a single dimer row (*cf.* Fig. 3.10). Although they are not zero, they are at least one order of magnitude smaller than the values obtained for the $c(4 \times 2)$ -reconstruction, and unlike the $c(4 \times 2)$ -reconstruction there is an asymmetry between the two displacements.

The C_n -bonds between the second and third layer Ge atoms have lost all symmetry, this is due to the two types of surface dimers present in the β_{6u} structure. This is unlike the reconstructions studied by Gay *et al.* [79] where only one type of surface dimer is present in each system, and as a consequence the C_n bonds show much symmetry.

3.3.4 Other geometries

Though the previous section shows clearly that the β -terrace has a β_{6u} -geometry, it is still interesting to have a look at some geometries containing Pt atoms in the second or third layer of the system. Previous calculations and experimental observations have shown that Pt atoms can also be found in subsurface positions. [91] Before the transformation to the β -terrace, there is what Gürlü *et al.* call an α -terrace. This type of terrace is characterized by its large number of dimer vacancy defects.

Also, in this initial stage of Pt growth on Ge(001) there are still a number of features which are not entirely understood, *e.g.* ‘*indented dimers*’.

Figure 3.12 shows the positions where Ge atoms were substituted with Pt atoms in the second and third layer of the system. The final geometries were obtained the same way as the β -geometries, *i.e.* substitution of Ge atoms by Pt atoms in a Ge(001) $b(2 \times 1)$ -reconstructed slab and relaxation of the geometry using the conjugate gradient method keeping the positions of the two center layers fixed.

3.3.4.1 Pt in the second layer

When Ge atoms in the second layer are substituted with Pt atoms, there are two possible inequivalent sites to consider. One under the down Ge atoms and one under the up Ge atoms of the surface dimers. Table 3.3 shows the formation energy per Pt atom for these two locations differs only 64 meV and Pt favors the position under the up Ge dimer atoms. Table 3.3 also shows that the introduction of a second Pt atom in the second layer improves the stability of the system considerably, increasing the formation energy by 28 and 123 meV per Pt atom. This difference from what would be expected from the single Pt substitution results, shows there is a strong positive correlation between the Pt atoms in the second layer. Furthermore, comparison of

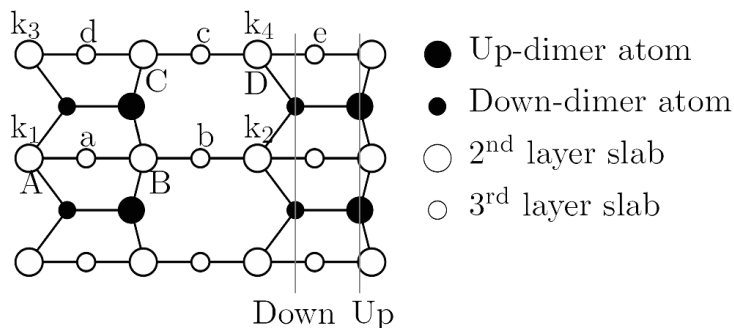


Figure 3.12: Locations of Ge atoms substituted by Pt atoms in the second (capital) and third (small) layer. The second layer Ge atoms pushed to the surface by third layer Pt atoms are marked by the k_x .

Table 3.1 and Table 3.3 shows the formation energies per surface unit are roughly in the same range as the formation energies per surface unit of the studied β - and γ -geometries, making these structures energetically also viable candidates as source of the β -geometry. Pseudo-STM images on the other hand clearly show this is not the case. The top part of Fig. 3.13 shows the influence of the substitution of a single Ge atom by a single Pt atom in the second layer of the system. In both cases the images of the two Ge dimers on top of the Pt atom merge into one image, with the location of the overlap on the side where the Pt atom is located.

For a Pt atom located at the down side this fusing is only seen for small bias voltages, for large bias the images are almost indistinguishable from the normal Ge dimer images. Also, the brightness of the dimers is roughly the same as for the Ge dimers on a normal Ge(001) surface.

In case the Pt atom is located at the up side of the dimer row, the position where the two images of the Ge dimers merge moves from being on top of the Pt atom, for large negative biases, to being on top of the Ge atom in between two Pt atoms, for small negative biases and all positive biases. Also, in this case there is a clear difference in brightness between the normal Ge dimers and the dimers on top of a Pt atom. For negative biases, the normal Ge dimers are most bright while for positive biases, the modified dimers are brighter. The brightest part of the modified dimers extends over the entire dimer for small biases, while for large positive (and negative) bias the brightest part of the image is at the side of the up Ge atoms. This gives the impression of a dimer located at one side of the dimer row, and directed along this dimer row. This is only an impression because these structures are formed by the bending, toward and away from the Pt atom, of the Ge p orbitals. When all Ge atoms at the up side in the second layer under a dimer row are substituted by Pt atoms, the images of the above Ge dimers do not merge anymore. Their image only lengthens and becomes a long oval shape which is dimmer than the normal Ge dimer at negative bias and brighter than the normal Ge dimer at positive bias. This

Formation energy.

Layer	Pt position(s)	E_f (meV)
2	A (down)	24
2	B (up)	-40
2	A & D (down)	-4
2	B & C (up)	-163
3	a (row)	-1115
3*(k_1)	a (row)	-155
3	b (trough)	68
3	a & b	-630
3*(k_1 & k_2)	a & b	467
3	a & c	-467
3*(k_1)	a & c	-66
3	a & d	-616
3*(k_1 & k_3)	a & d	-32
3	a & e	-1141
3*(k_1 & k_4)	a & e	-346

Table 3.3: Formation energy per Pt atom of reconstructions containing Pt atoms in the second and third layer. The Pt positions are shown in Fig. 3.12. The * indicates that the Ge atoms at the k_x positions (between brackets) are removed from the system, and the values were obtained after relaxation of the modified system.

elongated shape persists at positive bias such that there is a clear difference between this image and the image of a normal Ge dimer, for which the single dimer image is replaced by two spots, one for each Ge atom.

3.3.4.2 Pt in the third layer

Substitution in the third layer can also be done at two inequivalent sites. The first is under the dimer row and the second is in the trough, between dimer rows. Table 3.3 shows a clear preference for Pt to be positioned under a dimer row, while a Pt atom in the trough position is less favorable than the original $b(2 \times 1)$ -reconstruction. This again shows the preference of Pt to be surrounded by Ge atoms. This is understandable since the Pt-Ge bond is energetically favorable over a Pt-Pt or a Ge-Ge bond. Table 3.3 also shows that the introduction of a second Pt atom in the third layer about halves the formation energy per Pt atom, if the second Pt is located at a nearest neighbor position. Though this might be expected for a combination of one row and one trough positioned Pt atom, it is also the case for two Pt atoms in row positions. Unlike Pt in the second layer, Pt in the third layer prefers to be positioned far from other Pt atoms. Positions *a* and *e* seem to be separated enough to remove this negative correlation. Comparing Table 3.1 and Table 3.3 shows clearly

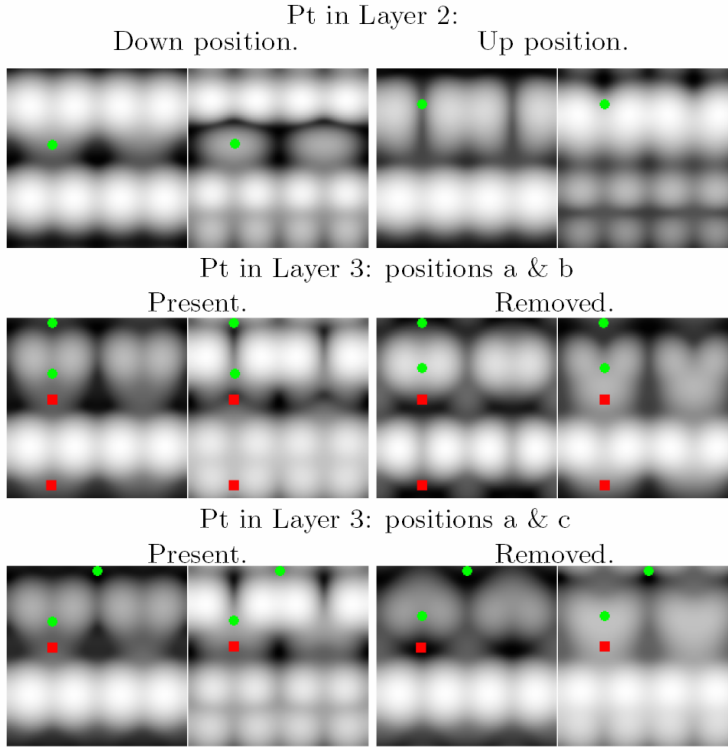


Figure 3.13: Pseudo-STM images showing filled- (left of each pair) and empty- (right of each pair) state images for the geometries containing Pt in the second and third layer. $\varepsilon = \varepsilon_F \pm 0.70$ eV is used in these simulations and the maximum z is chosen at 4 \AA above the highest atom. The positions of the Pt atoms are indicated by the (green) discs and the (red) squares indicate the positions of second layer Ge atoms which are pushed up to the first layer level. ‘Present’ and ‘removed’ refers to these Ge atoms being present or having been removed (*-configurations of Table 3.3). The bottom dimer row in each picture shows Ge dimers which are not (or barely) influenced by the Pt atoms present. The dimers at the top of each picture show a clear modification caused by the Pt atoms present underneath.

that Pt under a dimer row is energetically the most favorable configuration, with a formation energy about one order of magnitude larger than the other configurations, in agreement with previous calculations. [18]

Geometrically the most impressive change is caused by a Pt atom under a dimer row at site a (or equivalent). The atom pushes the second layer Ge atom (in case of site a, indicated with k_1 in Fig. 3.12) at the down side of the row up to the first layer deforming the surface geometry. Also in the case where the geometry contains

Pt atoms at positions a and b , the lifting of Ge atom k_2 might be considered caused by the Pt atom at position a . The Pt atom (site a) pushes Ge atom k_1 up to a first layer position, but it also pushes the Ge atom (site B) in between the two Pt atoms a little bit away. This Ge atom in turn pushes against the second Pt atom (site b) which then lifts Ge atom k_2 creating a chain effect in which a horizontal displacement is transformed into a vertical one. Table 3.3 shows the removal of these Ge atoms (after relaxation to a new equilibrium geometry) costs about 0.6 to 1.1 eV per Ge atom removed. So if the Ge atoms are to be considered as ejected atoms which move away to a position at a step edge, then the energy gained from placing a Pt atom in a row position is almost entirely lost and we again end up in the energy range of the β - and γ -geometries. The exception being the geometry placing Pt atoms in positions a and e , which resembles the β_6 -geometry, and thus could be considered a possible starting position for the β_{6u} -geometry.

The influence on the pseudo-STM pictures is similar as seen for the Pt atoms in the second layer. The charge lobes of the up Ge dimer atoms are pulled toward one another over the Pt atom at negative bias while for positive bias they are pushed away. For the down Ge dimer atoms, the charge lobes are always pulled toward one another over the Pt atom. The merging of the dimer images in the pseudo-STM pictures of Fig. 3.13 show this nicely. A more important effect caused by this deformation of the charges is the dimming at negative and the brightening at positive biases of the nearby Ge dimers, which can be substantial, as shown in Fig. 3.13. This indicates a charge transfer from Ge to Pt atoms. Removal of the k_x Ge atoms forces the down Ge atoms to make a new bond, which generally is with a third layer atom, either the Pt atom under the dimer row or the Ge atom in the trough. This removal causes a lowering of the dimer structure into the surface consequently causing a lowering of the electronic structure and hence dimming the dimer image in the pseudo-STM pictures even further. The change in the z -position of the dimer atoms is not the only geometrical effect caused by this removal. The dimers also bend toward one another over the location of the removed Ge atom. Consequently the two dimer images in the pseudo-STM picture merge into one single heart-shaped feature, of which the orientation depends on the bias, as can be seen in Fig. 3.13.

3.3.4.3 Missing dimers or hidden dimers?

In the previous two paragraphs it was shown that the introduction of Pt in the second or third layer causes significant changes in the electronic structure of the surface. The difference in height/brightness of the dimer images in the pseudo-STM pictures depends largely on the simulated bias. Combining the information from the visual STM-image with the height differences, at different biases (both positive and negative), of the maxima should make it possible to clearly distinguish the different geometries containing Pt in the second and third layer in experiment.

For the following investigation, we generated pseudo-STM images for all the structures containing Pt in the second or third layer, using simulated biases of -1.50 , -0.70 , $+0.70$, and $+1.50$ V to study the influence of varying bias. For each bias, a

set of STM images was generated using different values for z (2.5 Å, 3.0 Å, and 4.0 Å) to construct surfaces of different constant current, allowing us to study the effect of varying current. However, on top of the approximations involved in generating the pseudo-STM images, there are other variables (such as tip geometry) present in real STM experiments which influence the final STM picture. As a consequence, one should not interpret the values given below as absolutes, but instead as relative values indicating the trends which should be observed in experiment for these structures.

For a Pt atom in the second layer at the down location, the maxima calculated for dimers on top of the Pt atom and dimers without Pt nearby, are roughly the same (less than 0.1 Å). Here the image at positive bias would give the telltale signature with the dimmed oval structure over a pair of down Ge dimer atoms, which is ~ 0.45 Å lower at +0.70 V and ~ 0.3 Å lower than the maxima at +1.50 V bias.

For second layer Pt atoms at the up location there is the merging of two dimer images into one single rectangular feature, which at low negative bias will shift one full dimer position with regard to the positive bias position. Furthermore, at increasing positive bias the maximum will seem to move to one side of the dimer row. At negative bias, the maximum of the structure will be ~ 0.25 Å lower than that of a normal Ge dimer, with this height difference becoming larger at smaller bias. At positive bias on the other hand the maximum will be about 0.3 Å higher than of a normal Ge dimer.

Pt in the third layer also modifies the electronic structure in a recognizable way. Pt under the dimer row lowers the peaks of the above dimer row by 0.5 to 0.7 Å at negative bias, while a Pt atom in the trough modifies the Ge dimer, with its up Ge atom nearby, by lowering the maxima of these dimers only ~ 0.25 Å. For the latter, these dimers are also slightly more asymmetric than the normal ones and at small positive bias the dimer image is still one feature while for a normal dimer the image splits up into two separate atom images. This splitting still occurs for the modified dimer but at a larger positive bias. At positive bias the modified dimers are highest for both Pt positions. For low positive biases they are ~ 0.25 Å higher, than the normal dimers, while for large positive bias this difference shrinks to only ~ 0.1 Å. Removal of the Ge atoms, which were pushed to the top layer, changes the electronic structure dramatically from the normal Ge dimer image. In each case two dimer images are merged into one single large heart-shaped feature which is about 0.6 to 0.7 Å lower than the maxima of the normal dimers at negative bias, and about 0.8 Å lower at small positive bias. At large positive bias this difference reduces to ~ 0.25 Å at which point the maximum of the structure is located at one side of the dimer row, giving the feature a somewhat butterfly-like appearance.

Combinations as seen in Fig. 3.13 give similar results. For example, the height difference of the dimer images, for Pt in the third layer at positions a and c in the filled-state image is ~ 0.8 Å and in the empty-state image this is ~ 0.2 Å. When the k_1 Ge atom is removed, the filled-state image now gives a height difference of ~ 1.0 Å while the empty-state image shows one of ~ 0.6 Å. For both filled- and empty- state images the normal dimers are highest.

Although we used a very simple model to calculate the pseudo-STM pictures, the values obtained suggest that some of these geometries could cause experimentally

observed features in the α -terrace, such as indented dimers or two dimer vacancies. Indented dimers are a structure two dimers long and based on the above results we conclude that this feature is caused by a Pt atom in a second layer up position or a third layer trough position. Two dimer vacancies on the other hand might not be actual missing dimers but merely due to the charge transfer from Ge-Ge dimers to a Pt atom in a third layer row position underneath. At this moment the above remains uncertain. A high resolution STM study over varying bias of these defects however, should make a conclusive statement on this subject possible.

3.4 Conclusions

In this chapter, we studied the possible geometries containing 0.25 and 0.5 ML of Pt substituted in the top layer of a Ge(001) reconstructed surface. Zero temperature *ab initio* calculations showed that the formation of Pt-Ge dimer rows are the most favorable reconstructions. They also showed the spontaneous formation of alternate buckling in most geometries due to the introduction of Pt. Comparison of calculated STM images with experimental observations was necessary to show the β -terrace has a β_{6u} geometry, which has some similarities with the Ge(001) $c(4 \times 2)$ reconstruction. It is shown that the Pt-Ge dimers are tilted in anti-phase to the Ge-Ge dimers, and a thorough description the β_{6u} geometry is given in terms of *twisting*, due to the anti-phase buckling of dimers in a dimer row, *bending*, due to the anti-phase buckling of dimers in adjacent dimer rows, and *shift*, due to the asymmetry of having two types of dimers present on the surface, of the original tetrahedral structure of the second and third layer Ge atoms. Additionally, we studied geometries containing Pt atoms substituted in the second and third layer and showed the most stable configuration to be one with Pt atoms located under the Ge dimer row. It was also shown that Pt atoms in this position push a second layer Ge atom to the surface and that the removal of this atom does not increase the formation energy but instead decreases it. In all these ‘other’ geometries, with exception of those where Ge atoms were removed, the presence of Pt atoms both modifies and dims the Ge dimers on top for negative bias and brightens them for positive bias. The height differences found indicate that these other geometries could be responsible for experimentally observed indented dimers and two dimer vacancies. Also, the calculated STM images of these other geometries show clearly that they can not be responsible for the β -terrace, though some are energetically more stable, indicating that the β_{6u} -geometry is a local minimum.

Interludium:

β_{6u} convergence tests

In **Chapter 3** a Ge potential, which includes the $3d$ electrons in the valence shell, is used to model the β -terrace. These d electrons represent approximately seventy percent of all electrons present in our unit cell. If we could include these electrons in the frozen core of the Ge potential, the computational cost for this system would be reduced significantly. Figure 3.14a shows the d -projected states for all atoms in our unit cell of the β_{6u} -geometry. For the Ge atoms, the $3d$ electrons give rise to a very narrow peak roughly 25 eV below the Fermi level, and some minor contributions closer to the Fermi level. For the Pt atoms, the d states give rise to a broad band of states between 1 and 4 eV below the Fermi level, and some secondary peaks at the Fermi level. In Fig. 3.14b the d -projected states of the Pt atom are compared to the spd -projected states of the Ge atom of the Pt-Ge surface dimer. Near the Fermi level the d -projected states of Ge are barely visible compared to the s - and p -projected states. Figure 3.14b also shows clearly the hybridization of Ge p and Pt d states at the Fermi level.

Based on the observation that the Ge d states do not play a significant role in the electronic structure close to the Fermi level, we decide to include them in the frozen

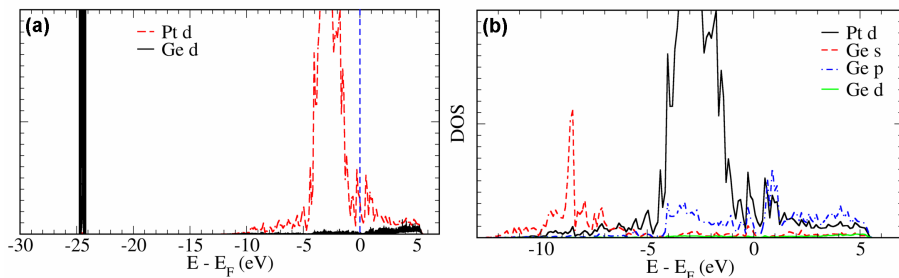


Figure 3.14: a) The d -projected states of all Ge and Pt atoms of the β_{6u} -geometry. b) Comparison of the spd -projected states of the Ge atom to the d -projected states of the Pt atom in the surface Pt-Ge dimers of the β_{6u} -geometry.

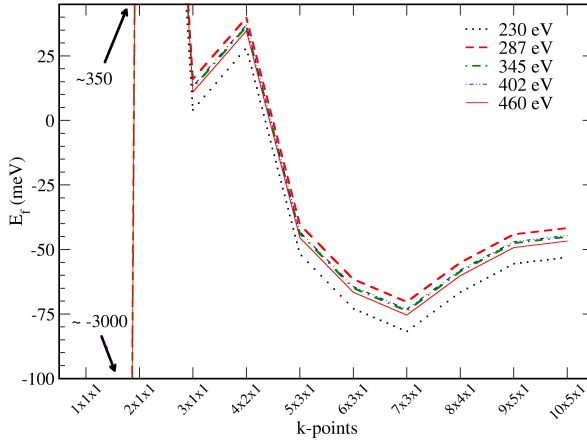


Figure 3.15: Convergence behavior of the formation energy E_f for the β_{6u} -geometry. Different curves represent different kinetic energy cutoffs.

core of the Ge potential.

In **Sec. 2.3** we observed a different convergence behavior between the potentials including the Ge $3d$ electrons in the valence shell and those including the $3d$ electrons in the frozen core. Because of this and the fact that the β_{6u} -geometry will serve as basis for our further study, a convergence test of the β_{6u} -system is the proper way to proceed.

Figure 3.15 shows the formation energy per 4×2 surface cell, E_f , of the β_{6u} -geometry as function of the k -point set and kinetic energy cutoff. As before, the curves show that the convergence behavior with regard to the k -point set is independent of the kinetic energy cutoff used. At a kinetic energy cutoff of 345 eV, the formation energy has converged to less than 2 meV per 4×2 surface cell.

To get a comparable convergence with regard to the k -point set, at least a $9 \times 5 \times 1$ k -point grid would be needed. However, an $8 \times 4 \times 1$ k -point grid still gives a reasonable convergence, but at half the computational cost of the $9 \times 5 \times 1$ k -point grid.⁷

Based on these results we can estimate the error bar on formation energies calculated using a kinetic energy cutoff of 345 eV and an $8 \times 4 \times 1$ k -point grid to be in the range 10–20 meV per 4×2 unit cell.

The difference in formation energy between omitting and including the d -electrons into the valence shell for the β_{6u} structure lies in this range. The formation energy E_f per Pt-Ge dimer is calculated to be -25 meV if the d -electrons are included in the valence shell and -39 meV if they are omitted.

⁷The $9 \times 5 \times 1$ k -point grid has 15 irreducible k -points, while the $8 \times 4 \times 1$ k -point grid only has 8 for the β_{6u} -geometry.

Chapter 4

FT study of Pt-induced nanowires on Ge(001) II: Nanowire formation.

Nature uses only the longest threads to weave her patterns, so that each small piece of her fabric reveals the organization of the entire tapestry.

– Richard P. Feynman

In this chapter we study formation of the nanowires formed after deposition of Pt on a Ge(001) surface. The nanowires form spontaneously after high temperature annealing. They are thermodynamically stable, only one atom wide and up to a few hundred atoms long. The nanowires only grow on the mixed Pt-Ge-surface we studied in **Chapter 3**. *Ab initio* density functional theory calculations are performed to identify possible structures of the Pt-Ge (001) surface with nanowires on top. A large number of structures with nanowires is studied. These nanowires are formed out of Pt or Ge dimers or mixed Pt-Ge dimers. By comparing simulated scanning tunneling microscope images with experimental scanning tunneling microscope images, the formation of the nanowires can be understood, and geometries of different phases in the formation process identified. We find that the formation of nanowires on a Pt-Ge(001) surface is a complex process based on increasing the Pt density in the top layers of the Ge(001) surface. Most remarkably we find the nanowires to consist of *germanium* dimers placed in troughs lined by mixed Pt-Ge dimer rows.

4.1 Introduction

Ever since Gordon Moore in 1965 observed the doubling of processing power every year, electronics industry has been driven forward by Moore's law making it a

self-fulfilling prophecy. The exponential growth in processing power has been made possible by producing ever smaller devices. This progress, with regard to further miniaturization, is steadily coming up to its ultimate and final limit: devices of atomic sizes connected by atomic wires. [3] Next to being of interest from this industrial point of view, nanowires (NWs) are also important at the fundamental theoretical and experimental level because of their inherent 1D nature. One-dimensional electronic systems present exotic physical phenomena such as Peierls instability, charge density waves and Luttinger liquid behavior. [7, 13–15] Also dimensionality effects on, for example, magnetism and electronic properties can be studied in such systems. [5–12] NWs can be produced in many different ways, resulting in a large range of sizes and properties. This goes from break junction created monatomic Au wires to NWs grown on imprinted surfaces, from atomic chains build one atom at a time using an STM tip to atomic Co chains grown on Pt(997) step edges and self-assembled wires and stripes. [4, 16–21] Because of its high conductance and general resistance to corrosion and oxidation, Au is a favored metal to use in the creation of atomic wires, both as free hanging wires and as reconstructed wires, chains or stripes on semiconductor surfaces. [17, 19, 20] Recently metal/Ge structures attracted interest because of the observation of self-assembled NWs in these systems. For instance, the deposition of Ho on Ge(111) results in stripe-like wires, while deposition of sub-monolayer amounts of Pt or Au on Ge(001) induces the formation of monatomic wires, hundreds nanometers long. [18, 21, 25] In 2003, Gürlü *et al.* created arrays of self-assembled NWs by deposition of a quarter monolayer of Pt on a Ge(001)-surface and annealing it at over 1050 K. [18, 28] These NWs are defect and kink free, and only one atom wide. Their length is only limited by the underlying Pt reconstructed Ge(001)-surface. This reconstructed surface contains 0.25 ML of Pt in its top layer forming a checkerboard pattern of Ge-Ge and Pt-Ge dimers, as was shown in **Chapter 3**.

In this chapter we present possible geometries of different phases during the NW formation on a Pt modified Ge surface. Based on comparison of simulated STM images to experimental STM images we will show that the NWs consist of *germanium atoms* in a trough lined with Pt atoms. Furthermore we will propose some geometries for the experimentally observed widened trough (WT), a precursor to the NW formation, based on comparison of STM images and possible structural evolution of the WT to a NW.

This chapter is organized as follows: In **Sec. 5.2** we describe the theoretical methods used for the total energy calculations and the generation of calculated STM images (or pseudo-STM images). In **Sec. 5.3** we present our results for simulations of different surface models with increasing Pt density. In **Sec. 4.4** we propose possible formation paths linking calculated geometries to experimentally observed structures. We have a closer look at the NWs and WT geometries, and finish by making a comparison with the models present in literature. Finally, in **Sec. 5.5** the conclusions are given.

4.2 Theoretical method

DFT calculations are carried out using the PAW method [33, 34] and the CA LDA functional,¹ as implemented in the VASP program. [85, 86] A plane wave basis set with kinetic energy cutoff of 345 eV is applied. Extensive convergence tests, presented in **Sec. 2.3.2**, showed no advantage in time/accuracy for the H-passivated Ge slab over the symmetric Ge slab. Based on the advantages of the higher symmetry of the symmetric slab, such as for example the presence of only a single type of surface, we choose to use the later. The surface is modeled by periodically repeated slabs of 12 layers of Ge atoms. The slabs are mirrored in the z -direction with reconstructions on both surfaces, in which specific Ge atoms are replaced by Pt atoms. A vacuum region of ~ 15.5 Å is used to separate the slabs along the z -axis. The BZ of the (2×4) surface unit cell is sampled using a 8×4 Monkhorst-Pack special k -point mesh. [87] To optimize the geometry of the slabs we use the conjugate gradient method and keep the positions of the Ge atoms in the center two layers fixed as to represent the bulk of the system.

Pseudo-STM images are calculated using the Tersoff-Hamann method, which states that the tunneling current in an STM experiment is proportional to the LDOS integrated from the Fermi level to the bias. [68] It was implemented in its most basic formulation, approximating the STM tip by an infinitely small point source. The integrated LDOS is calculated as $\bar{\rho}(\mathbf{r}, \varepsilon) \propto \int_{\varepsilon}^{\varepsilon_F} \rho(\mathbf{r}, \varepsilon') d\varepsilon'$, with ε_F the Fermi energy. An STM in constant current mode follows a surface of constant current, which translates into a surface of constant integrated LDOS $\bar{\rho}(x, y, z, \varepsilon) = C$, with C a real constant. For each C , this construction returns a height z as a function of the position (x, y) . This heightmap is then mapped linearly onto a gray scale. We choose C such that the isosurface has a height z between 2 and 4 Å above the highest atom of the surface.

4.3 Results

4.3.1 Introduction: The experimental background

In this section we will be presenting and briefly discussing the results of our work done with regard to the NWs. We will mainly be comparing all the different surface structures we examined, an in depth discussion of the NW models we present in this work and their integration in possible formation paths is the subject of **Sec. 4.4**. Because of the large quantity of data we present here, we will start in this subsection with a short review of the relevant experiments to serve as reference and background for the rest of the chapter. We will also give a brief description of what we are going to present in the following subsections, which can serve as road map for the rest of this section.

The formation of Pt induced NWs was first observed by Gürlü *et al.* [18] in 2003 and later on by Schäfer *et al.* [28] After deposition of 0.25 ML of Pt on a clean

¹A comparison of LDA and GGA results is presented in **Appendix C.3**.

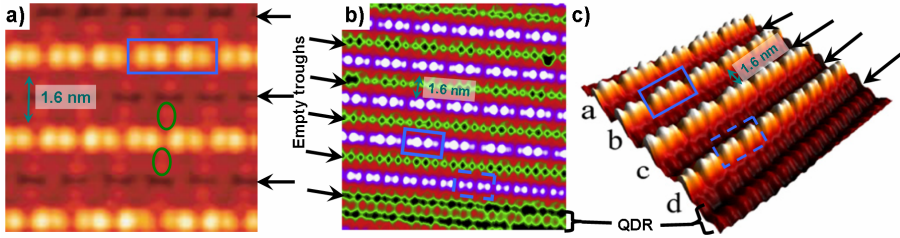


Figure 4.1: Three typical experimental STM images. a) A section of figure 3a in Reference [27], showing an empty state STM image of several NWs at 77 K using a bias of 0.15 V and a tunnel current of 0.437 nA. b) and c) From Reference [26], 2D and 3D filled state STM images recorded at 4.7 K, using a bias voltage of -1.5 V and a tunneling current of 0.5 nA.

The ellipses indicate the symmetric bulges, while the rectangles indicate two NW dimers showing (4×1) periodicity. The dashed rectangles show the (2×1) periodicity for edge NWs. Empty troughs are indicated with the arrows and have a width of 1.6 nm. In (b) and (c) also a QDR of the β -terrace is visible.

Ge(001) surface, and subsequent annealing at 1050 K, Gürlü *et al.* observed the formation of one atom thick NWs which could be hundreds of nanometers long. These wires are defect and kink free, and are observed both as solitary wires and arrays of wires with a constant spacing of 1.6 nm. The NWs are located in the troughs between the QDRs of a Pt modified Ge(001) surface. So the 1.6 nm spacing in the arrays means that only every second trough a NW can be present. The Zandvliet group also discovered that although the NW-arrays are conducting, it are not the wires themselves but rather the space in between the wires which contains confined surface states. [27, 29]

Figure 4.1 shows some experimental STM images of the NWs. We indicated typical features which should be present in the calculated STM image of a geometry for it to be successful. i) The NW image should be dimerised (solid and dashed rectangles). ii) The NW dimer images should be double peaked for the filled state images (and empty state images close to the Fermi level, see Fig. 4.1a) and they should present only one peak at large positive bias (empty state images). iii) Bulges, symmetric to both sides of the NW should be present, and should be located ‘between’ the NW dimer images (ellipses). iv) A NW image should be present only every second trough. And v) the NW dimer images in an array should have a (4×1) periodicity along the NW.

The last feature, the (4×1) periodicity, has been linked to the presence of a Peierls instability by van Houselt *et al.* [26] This allows us to neglect the (4×1) periodicity initially and start from a smaller unitcell, containing only a single NW dimer. In the following sections we will present a set of surface models and adsorption geometries with increasing Pt density in the top layers. This Pt density will in general refer to the amount of Pt present in the substrate, omitting the Pt atoms present to form the actual wire. The calculated STM images will serve as main indicator, to identify the

experimentally observed NWs. The calculated STM images which we will present in the following sections are selected with this purpose in mind, and will serve to present the appearance of specific NW related features.

In **Sec. 4.3.2**, starting from the geometry of the β -terrace (*cf.* **Chapter 3**), two simple scenarios are presented which result a β_6 or a Ge(001) substrate with 2 additional Pt atoms on top. Various adsorption geometries for Pt adatoms and addimers are studied and it will be shown that none of the calculated STM images for these structures resemble the experimental STM images at all. Two important observations will be made: i) the preference of Pt to build into the substrate forming Pt-Ge surface dimers, and ii) the fact that Ge atoms bound to Pt atoms show up brightly in the calculated STM images, in contrast to the Pt atoms which show up very dark.

Via the investigation in **Sec. 4.3.3** of some intermediate structures based on these observations, we propose new symmetric substrate models, with 0.5 ML of Pt in the top layers, in **Sec. 4.3.4**. The adsorption of both Pt and Ge dimers is investigated, and it is shown that Pt NWs are invisible, while Ge dimers present bright NW dimer images. Also the symmetric bulges are identified. Although the model presented in **Sec. 4.3.4** shows reasonable agreement with the experiment, the double peaked NW dimer images in the filled state pictures are missing. The observation that Ge dimers bound on top of Pt dimers produce such double peaked images leads to a third substrate model in **Sec. 4.3.5**. In this model 0.75 ML of Pt are present in the top layers. Again the adsorption of both Pt and Ge dimers is investigated, and it is shown that a Ge NW on this substrate model shows excellent agreement with the experimental STM images, presenting all features with the exception of the (4×1) periodicity due to the size of the unitcell. In **Sec. 4.3.6** we investigate the experimentally observed (4×1) periodicity. We note that it is not present in the proposed model if the unitcell is doubled, and no Peierls distortion is observed. By placing additional atoms in the trough of the NW, we will show that a surface containing 0.8125 ML of Pt is sufficient to generate the experimentally observed (4×1) periodicity, and thus contains all typically observed features of the NWs.

4.3.2 First simple model: Pt-adatoms and wires

Experimental STM images of the Pt modified Ge surface with NWs show the NWs to be build of dimers positioned in the troughs between the QDRs of the β -terrace (*cf.* Fig. 4.1). [18] Figure 4.2 shows an experimental STM image of the domain boundary (DB) between an α and a β -terrace. The QDRs of the β -terrace show perfect alignment with the dimer rows of the α -terrace, so the dimer row structure of the Ge(001) surface is maintained in the β -terrace. Based on this observation, we assume that the formation of the β -terrace and the NWs does not modify the dimer row periodicity of the β -terrace (or Ge(001)) reconstruction dramatically, except for the possible substitution of atomic species. More practically this means that the NWs, in STM images, should be positioned at the center of the trough between the QDRs. Furthermore, experimental observations also show that Pt atoms deposited at room temperature initially move to the subsurface, which is shown theoretically to be an energetically favorable situation. After high temperature annealing the Pt

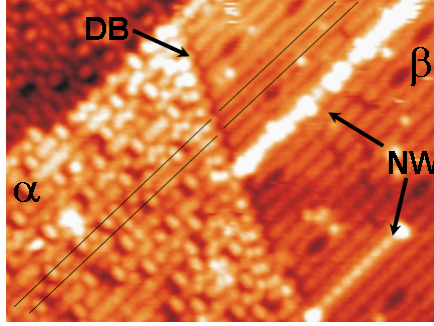


Figure 4.2: The DB between an α - and β -terrace. [92] Although many vacancies are present in the α -terrace, the dimer rows can still be recognized. Lines show two neighboring QDRs on the β -terrace, and two neighboring dimer rows on the α -terrace.

atoms are assumed to pop up again from the bulk as Pt dimers. [93]

Since the NWs are inherently connected to the β -terrace, this geometry is a good starting point for a simple model of the NWs. Based on the experimental observations two scenarios can be envisaged. In a first possible scenario the top layer of the β -terrace remains as it is, and extra subsurface Pt atoms are ejected onto the surface to form the NWs. In the experiment roughly a quarter monolayer of Pt is deposited. After annealing the surface shows different terraces with different reconstructions. So we can easily assume that these patches might contain different platinum densities, such that the local platinum density can be more than one quarter monolayer. Since the β -terrace appears before the NWs during the NW formation process, a second scenario consists of the ejection onto the surface of the Pt atoms from the β -terrace. These ejected Pt atoms then form Pt dimers on the surface, while Ge atoms from the bulk take their positions in the dimer rows. This way a Ge(001) surface is formed with Pt ad-dimers. We use the Ge(001) $b(2 \times 1)$ geometry for the clean Ge(001) surface and the β_{6u} -geometry, we found in **Chapter 3** for the β -terrace, and place Pt atoms on specific adsorption sites on the dimer rows and in the troughs of these surfaces. In the following we will refer to the β_{6u} -geometry simply as β_6 -geometry. Figure 4.3a shows the initial positions of Pt ad-atoms on the β_6 -geometry and Fig. 4.3b of ad-dimers on the β_6 - and Ge(001)-surface. After relaxation we calculated formation energies for these geometries, as listed in Table 4.1. The surface formation energy, E_f , was calculated with regard to the Ge $b(2 \times 1)$, geometry using the expression:

$$E_f = (E_{NW} - E_{Ge(001)} - \Delta N_{Pt}E_{Pt} - \Delta N_{Ge}E_{Ge})/2, \quad (4.1)$$

with E_{NW} the total energy of the relaxed structure, $E_{Ge(001)}$ the total energy of the Ge(001) $b(2 \times 1)$ surface reconstruction, E_{Pt} and E_{Ge} the bulk energy for a Pt and a Ge atom respectively and $\Delta N_{Pt}(\Delta N_{Ge})$ the difference in number of Pt(Ge) atoms between the relaxed structure and the Ge(001) $b(2 \times 1)$ geometry. The division by 2

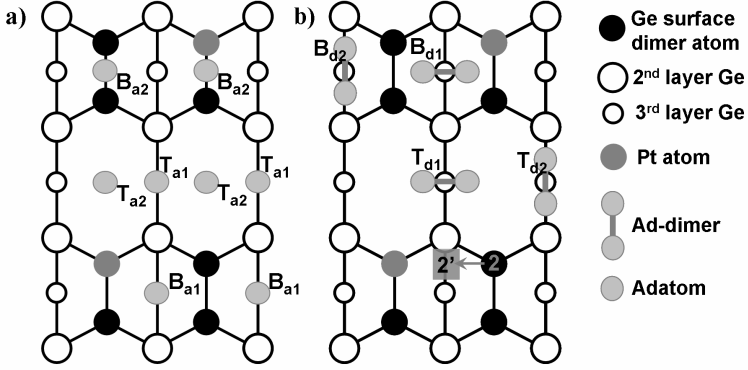


Figure 4.3: Adsorption sites before relaxation.

a) Adsorption sites for Pt adatoms on the β_6 -geometry. (see **Chapter 3**)
 b) Adsorption sites of Pt ad-dimers on the β_6 (shown here) and Ge $b(2 \times 1)$ surface geometry.

Formation and adsorption energy.

	E_f (meV)	E_{ad} (meV)	r_{ad} (Å)
β_6	-74	-	-
β_6 B _{a1}	-473	-200	2.957
β_6 B _{a2}	3128	1601	4.019
β_6 T _{a1}	658	366	2.661
β_6 T _{a2}	161	117	4.146
β_6 B _{d1}	1776	925	2.552
β_6 B _{d2}	120	97	3.421
β_6 T _{d1}	-1405	-665	4.001
β_6 T _{d2}	1303	688	2.623
Ge $b(2 \times 1)$ B _{d1}	2077	1038	2.655
Ge $b(2 \times 1)$ B _{d2}	2262	1131	2.538
Ge $b(2 \times 1)$ T _{d1}	359	180	3.980
Ge $b(2 \times 1)$ T _{d2}	176	88	2.851

Table 4.1: Formation and adsorption energies for adsorption of adatoms and addimers on the β_6 and Ge(001) $b(2 \times 1)$ surface reconstructions shown in Fig. 4.3. r_{ad} is the distance between the adatoms after relaxation, it indicates whether bonds are formed between the adsorbed atoms.

is because of the symmetry of the system, giving two modified surfaces on the slab. Negative values of E_f indicate a stable structure compared to segregation in a Ge(001) surface and Pt bulk. However, since different substrate reconstructions contribute

differently to this total formation energy, we want to separate the contribution to the formation energy of the substrate from that of the NW. This would allow us to compare the stability of the actual NW or other adstructures on different surfaces. For this purpose we introduce an adsorption energy, E_{ad} . It is calculated using the expression,

$$E_{\text{ad}} = (E_{\text{NW}} - E_{\text{subs}} - \Delta N_{\text{Pt}} E_{\text{Pt}} - \Delta N_{\text{Ge}} E_{\text{Ge}}) / N_{\text{adatom}}, \quad (4.2)$$

where E_{subs} is the total energy of the surface without adstructure (and without reconstructions induced by the adstructure), ΔN_{Ge} (ΔN_{Pt}) the difference in number of Ge (Pt) atoms between the system containing the adstructure and the substrate system without the adstructure, and N_{adatom} is the number of adatoms used for the adstructure. Negative values of E_{ad} indicate that the adatoms form a stable structure on the surface. Although the relation between the values of E_f and E_{ad} is quite trivial in case of Table 4.1, this will not be the case in the following sections. The values presented here are to allow easy comparison later on.

In the following we will discuss the adsorption geometries shown in Fig. 4.3. Starting with the first scenario, Table 4.1 shows that Pt atoms on a β_6 -surface in general create an unstable structure. Only the $B_{\text{a}1}$ - and $T_{\text{d}1}$ -geometry relax into a stable structure.

In the $B_{\text{a}1}$ - and $T_{\text{a}1}$ -geometry the Pt adatoms move toward one another forming dimers with a length of 2.957 Å and 2.661 Å respectively. In case of the $B_{\text{a}1}$ -structure the stability of the structure is improved because the Pt dimer breaks up the surface Ge dimer (this bond is weaker than the Pt-Ge dimer bond) which allows the Pt adatoms to sink into the subsurface where they each can create four Pt-Ge bonds, which are energetically favorable over Pt-Pt and Ge-Ge bonds. The Pt dimer in the $T_{\text{a}1}$ configuration, on the other hand, sinks into the trough, increasing the coordination number of the Pt adatoms to three.

The $B_{\text{a}2}$ geometry is the most unstable geometry. After relaxation, the Pt atoms are still located on top of the Pt-Ge dimer and the Ge-Ge dimer putting them ~ 2 Å above the dimer row (*cf.* Fig. 4.3). The bond length of the three Pt-Ge bonds of the Pt adatoms is about 2.3 Å while the bond length between the Pt adatom and the Pt surface dimer atom is 2.5 Å. This gives the impression that the Pt adatom on top of the Pt-Ge dimer is slightly tilted toward the Ge atom while on the Ge-Ge dimer the Pt adatom is centered. The Ge-Ge dimers on which adatoms are located are almost flat, with a tilt angle of $< 1^\circ$, much less than the usual tilt angle of $\sim 20^\circ$ found for Ge-Ge dimers on a Ge(001) $c(4 \times 2)$ and β_6 surface reconstruction.

The adatoms in the $T_{\text{a}2}$ -geometry sink deep into the trough creating five Pt-Ge bonds per adatom. In spite of the large number of Pt-Ge bonds of the adatoms, this structure turns out to be unstable (*cf.* Table 4.1) because of the distortion of the lattice in the surface layers.

When Pt dimers are placed on the β_6 -geometry we see in Table 4.1 that only the $T_{\text{d}1}$ -structure is stable. The most unstable structures are $B_{\text{d}1}$ and $T_{\text{d}2}$. After relaxation the $B_{\text{d}1}$ -structure is very similar to the $B_{\text{a}2}$ -structure, but in this case the Pt adatom on top of the Ge-Ge dimer is tilted toward the second Pt adatom to form 2 extra Pt-Pt bonds, one with the second adatom and one with the surface Pt atom,

explaining the increase in stability when going from the B_{a2} - to the B_{d1} -structure. The Pt ad-dimer in the B_{d1} -structure is stretched only by a small amount to a length of 2.552 Å, while it is tilted over an angle of 16.5°. After relaxation, the T_{d2} -structure shows a Pt dimer in a bridge position. This dimer has a tilt angle of roughly 1° and a length of 2.62 Å. Due to the Pt-Pt bond on one side of the trough the dimer makes an angle of 8.7° with the direction perpendicular to the dimer row. Each adatom also forms an extra Pt-Ge bond with a second-layer Ge atom, while breaking a Ge-Ge bond between the first and second layer.

In the B_{d2} -geometry, the Pt dimer breaks up during relaxation. The adatoms cause drastic deformations of the QDR to form up to five Pt-Ge bonds. Both backbonds of one of the Ge atoms of the Ge-Ge surface-dimer are broken and the atom is pushed up, while a Pt adatom takes its place. Now one side of what previously was a QDR has become a Pt-Ge zigzag-chain, orthogonal to the surface plane, with the Ge atoms at the high points and the Pt atoms at the low points.

The most stable structure is the T_{d1} -structure. Although the initial geometry is very simple (*cf.* Fig. 4.3b), reconstructions during relaxation cause large deformations, and the resulting calculated STM images do not resemble the experimental STM images at all (*cf.* Fig. 4.4b). Again, we notice that the Pt atoms try to move into the subsurface. The ad-dimer breaks up and one of the Pt atoms replaces the Ge atom at position 2 (*cf.* Fig. 4.3b) pushing it to position 2' on top of the surface (dimer row). This ejected Ge atom, indicated by a yellow disc in Fig. 4.4b, gives rise to a large round bulge, centered on its location, in the calculated STM images. This exchange also causes the QDR to transform into a dimer row containing Pt atoms on one side and Ge atoms on the other side, what we previously called a γ_1 -geometry.² This γ_1 -geometry is the most stable surface reconstruction containing 0.5 ML of Pt atoms in the top layer, explaining the observed improved stability for the T_{d1} structure. From this, we draw an important conclusion for further surface models: the exchange of a Ge atom for a Pt atom in a surface Ge-Ge dimer greatly improves the stability of the structure by creating a straight row of Pt atoms. This is also probably the reason why the B_{d2} -geometry, in which also a straight row of Pt atoms is created, is so much more stable than the B_{d1} -geometry.

None of the structures discussed up to this point result in a calculated STM image that resembles the experimentally observed NWs. Because the β -terrace contains 0.25 ML of Pt, and in STM experiments the nanowires show a structure containing 0.25 ML of adatoms, the second scenario assumes the Pt atoms of the β -terrace are ejected onto the surface and form the NWs. The surface itself would then reconstruct to a normal Ge(001) surface using bulk Ge atoms. Calculations for Pt nanowires on a clean Ge $b(2 \times 1)$ surface were carried out, to check this second scenario. The adsorption geometries considered are shown in Fig. 4.3b and the formation energies are listed in Table 4.1.³ The formation energies clearly show the known trend for Pt on Ge. [88] The further the Pt atoms stick out of the surface the more unstable the structure turns out to be, showing a preference of the Pt atoms to move into the

²See Chapter 3.

³Replacing the Pt atoms by Ge atoms in the surface dimers of the β_{6u} -geometry shown in Fig. 4.3 gives the Ge(2×1) surface reconstruction.

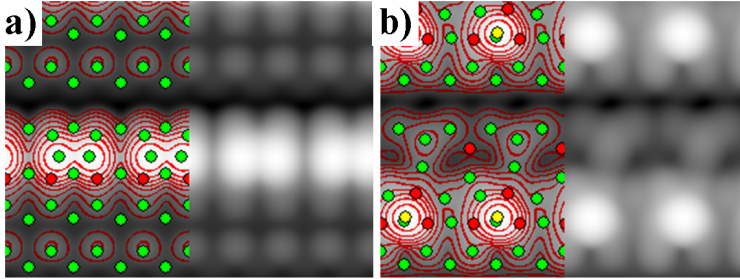


Figure 4.4: Calculated STM images for a Pt dimer at the T_{d1} site of the Ge(001) (a) and β_6 (b) geometries, after relaxation. For these filled state images a simulated bias of -1.5 V, and $z = 3.0$ Å is used. Green (red) discs indicate the locations of the Ge (Pt) atoms in the two top layers. The yellow discs in (b) indicate the position of the ejected Ge atom at position $2'$ (cf. Fig. 4.3). Contours, separated 0.3 Å, are added to guide the eye.

surface.

Pt dimers on a Ge surface are in general unstable, but when placed in the trough they break up and sink in, increasing their coordination and increasing the stability of the system by roughly 2 eV per dimer. In this process Ge atoms from the top most layers are pushed up and stick out of the surface higher than before.

On the other hand, the Pt dimers on top of the dimer rows bind to two Ge dimers, so in this case it are the Pt dimers that stick out far above the surface.

Although none of these structures turn out to be stable, the T_{d1} adsorption structure on the Ge(001) substrate gives a hint of where to look for the ‘platinum’ nanowires. Although this structure is not thermodynamical stable in comparison to the β -terrace, calculated STM images show something remarkable: a bright chain of double peaked dimers images, as can be seen in Fig. 4.4a. There is a large similarity to the experimental STM images of the ‘platinum’ nanowires. There are some problems though. First of all the nanowire is not located in the trough between the QDR, as observed experimentally, but rather on top of one. The Ge dimers forming the NW were originally the bottom side atoms (in Fig. 4.4a) of the Ge dimer row, causing the NW to be located at the extension of a Ge dimer row (or a QDR on the β -terrace) in contradiction to the experimental observation. [18, 93] The Ge atoms of the Pt-Ge dimer row are the top side atoms which originally formed a Ge dimer row with the Ge atoms of the one but last horizontal row in Fig. 4.4a. Also, the symmetric bulges at the sides of the NW are missing and when moving to a positive scanning bias the double peak should disappear, [94] which does not happen for the calculated STM images, as can be seen in Fig. 4.24b. Here the double peak feature remains very pronounced. Although this structure can be discarded as geometrical structure for the observed nanowires on grounds of their formation energy and comparison of the STM images, it are the calculated STM images that show us an important fact: *i.e.* that also Ge dimers should be considered as possible building

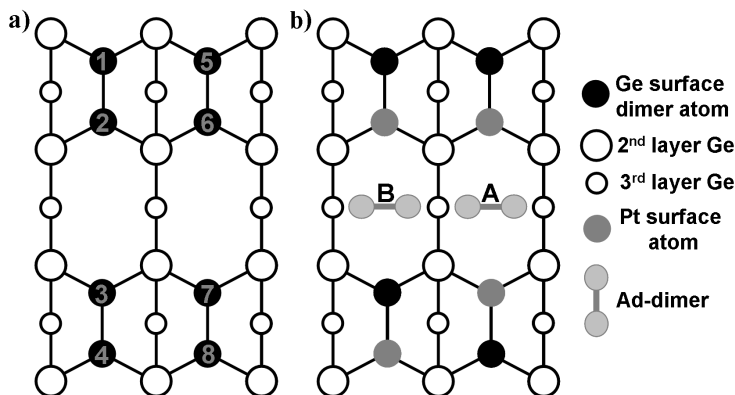


Figure 4.5: a) Possible position indices of Pt atoms in the top layer. b) Adsorption sites of ad-dimers, here shown on a surface containing Pt atoms at positions 2, 4, 6, and 7. Site A is positioned between two Pt atoms, while site B is positioned between a Pt and a Ge atom.

blocks for the experimentally observed nanowires.

It is interesting to note that the T_{d1} structure shows, after relaxation, roughly the same geometry Stekolnikov *et al.* [95] propose as NW geometry. In **Sec 4.4.2** we will address this point in more detail.

4.3.3 Intermediate geometries: PtGe and GeGe wires on a normal and modified β_{6u} reconstruction

In the previous paragraph it was shown that the adsorption of Pt atoms and dimers in general does not lead to stable structures. The Pt atoms try to move into the subsurface, causing large distortions in the original surface structure. This leads to the natural conclusion that different building blocks will be needed to generate the experimentally observed NWs. Two options come to mind. The final structure with Pt adsorbed at the T_{d1} site on Ge(001) showed that Ge-Ge dimers could be a viable candidate to show up as a NW in pseudo-STM images. Another possibility are Pt-Ge dimers, these could then be used to explain the observed asymmetry between the NW-dimer atoms, which results in the observed 4×1 periodicity of the NWs. Because experiments show the NW to be growing in the troughs between the QDRs, and the above calculations also show a preference for adsorption in the troughs, mainly trough configurations will be considered from this point on. Due to the large variety of possible surface structures, these will be defined by indicating the positions of the Pt atoms in the top layer, as shown in Fig. 4.5a. The adsorption sites are shown in Fig. 4.5b.

The stable T_{d1} on β_{6u} structure in **Sec. 4.3.2** showed the exchange of one Pt-dimer atom with a Ge-surface atom. It could now be imagined that the second Pt atom behaves similarly and takes the position of a Ge atom on the opposite side of the

trough. The structure obtained would now contain Pt atoms at positions 2, 4, 6, and 7: Two Pt atoms at positions 4 and 6 from the β_6 geometry, a Pt atom at position 2 from the T_{d1} relaxation, as described in the previous subsection, and, the second Pt atom from the original Pt addimer at position 7. This last position because it is known that Pt-dimers build into the dimer rows are very unstable (see **Chapter 3**), giving preference to position 7 over position 3. During this process two Ge atoms would have been expelled onto the surface. These could bind and form a dimer, with a length of 2.558 Å, bridging the trough, with the dimer parallel to the dimers in the dimer rows. This dimer would have a formation energy $E_f = -568$ meV. Because of the asymmetry between the two sides of the trough it would be buckled over an angle of 17.9° . Conversely, if the two expelled Ge atoms do not dimerise but maximize the number of Pt-Ge bonds the formation energy E_f is calculated to be -768 meV, roughly 0.2 eV more stable than a dimer. Calculated STM images of this last structure show something interesting. Due to the Ge atoms on top of the QDRs the two dimer images of the underlying dimers are replaced by a single image centered between the two dimers. Because of the different geometry of the underlying dimer rows, the new images also show a clear difference, as can be seen in Fig. 4.6c. In experiments a widened trough (WT) is observed before the formation of the NWs. One significant feature of this WT is the fact that the dimer images of the QDRs are replaced by images which are two dimers wide, symmetrically around the trough. The structure described above could be a candidate for this observed structure. The Ge atoms could then during annealing dimerise (dimers bridging the wide trough are also experimentally observed) and rotate from their bridge position into a position parallel to the QDRs, forming the observed NWs.

Using a surface containing Pt atoms at positions 2, 4, 6, and 7, Ge dimers are placed at sites A and B and a Pt dimer at site A. After relaxation we find the Ge dimer that is placed at site B to have broken up and, due to the periodic boundary conditions and the surface unit cell size, moved toward the site A configuration. The formation energy E_f for this B-site structure is calculated to be -609 meV, while that of the A configuration is -713 meV, slightly more stable.

The Ge atoms in the A configuration are spaced 2.577 Å, which is about 6% larger than a normal Ge bulk bond. The Ge atoms are also bound to the Pt atoms at positions 6 and 7 forming a diamond shape structure. Pt-Ge cells with this shape appeared often during relaxations and seemed to represent a relatively stable substructure. Calculated STM images for this structure are shown in Fig. 4.6a and b. They show a good resemblance to the experimentally observed images, but some important discrepancies exist. Although the general structure of the NW and the signatures of the bulges symmetric around the wire are present, the asymmetry of the latter is not in agreement with experiment. However, this can be easily solved by using a more symmetric surface (*cf.* **Sec. 4.3.4**). Also, the images of the wire itself are not entirely consistent with experiment, both at positive and negative bias. Where the filled state image (Fig. 4.6a) should show a double peaked feature and the empty state image (Fig. 4.6b) a single peak, we observe the opposite behavior.

The Pt dimer at site A gives some surprising results. Contrary to what might be expected from the previous subsection this structure seems stable, with a formation

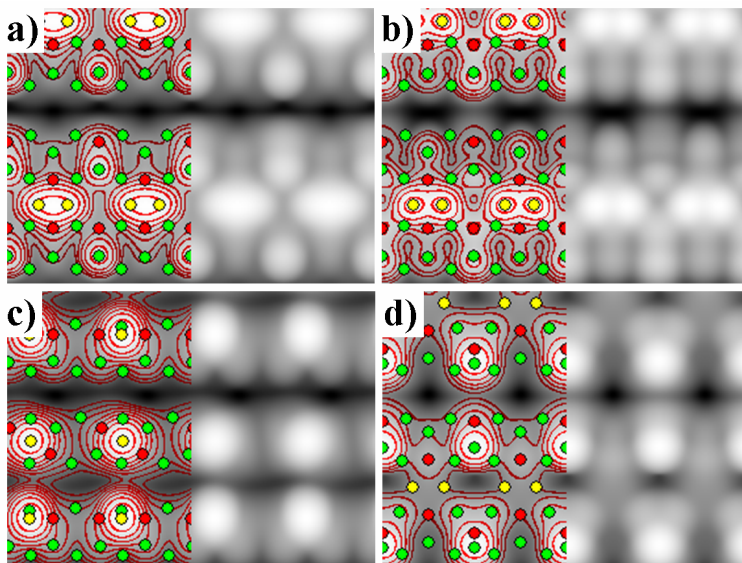


Figure 4.6: Calculated STM images of a Ge NW (a and b), Ge adatoms (c), and a Pt NW (d) on a surface containing Pt atoms at positions 2, 4, 6, and 7 (cf. Fig. 4.5). The green/red discs show the positions of Ge/Pt atoms in the surface, and the yellow discs show the positions of the Ge NW atoms (a and b), Ge adatoms (c), or Pt NW atoms (d). Contours are added to guide the eye. (a, c, and d) Filled state calculated STM images, for $z = 3.0 \text{ \AA}$ and a simulated bias of -1.50 V . (b) Empty state calculated STM image, for $z = 3.0 \text{ \AA}$ and a simulated bias of $+1.50 \text{ V}$.

energy $E_f = -1270 \text{ meV}$, making it about twice as stable as the Ge structures above. Furthermore, the pseudo-STM images also show something comparable to the WT which was experimentally observed (cf. Fig. 4.6d). This time a pair of dimer images is replaced by a single bright image centered ‘on’ a dimer, instead of in between. Most interesting however is the fact that the Pt ad-dimer itself is invisible in the trough, giving further indication that the experimentally observed wires are most likely not formed of Pt atoms.

In general we find that calculations with Ge ad-dimers in the troughs of surfaces with different Pt stoichiometries show a serious improvement in formation energy when Ge atoms can bridge the trough and bind to Pt atoms on both sides of the trough. We also see that the Ge atoms are drawn toward the Pt atoms imbedded in the surface.

Calculations using Pt-Ge dimers indicate similar behavior. Although their pseudo-STM images show very asymmetric dimer images, it also shows them not to be compatible with the assumption that the different atom types could cause the in experiment observed asymmetry of the NW dimers. So Pt-Ge dimers can be ruled

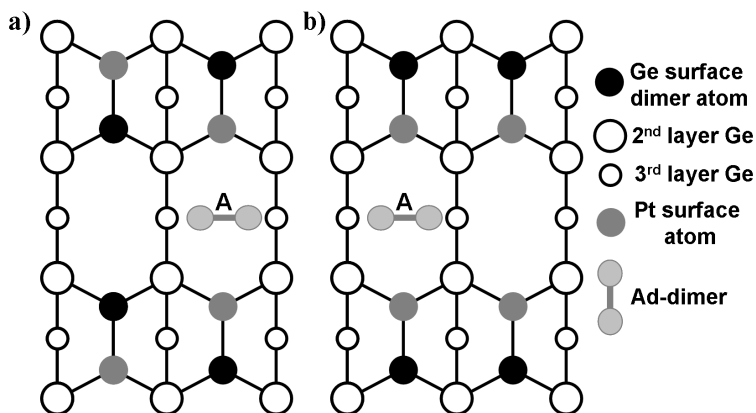


Figure 4.7: Schematic representation of the γ_c (a) and γ_{as} (b) surface geometries, with the NW dimer adsorption site A.

out as origin of the experimentally observed 4×1 periodicity.

4.3.4 Second model: Pt and Ge wires on a Ge(001)-surface with 0.5ML of Pt imbedded

The previous subsection showed some crucial points for further development of the NW model. Firstly, there is the possibility for the NW to be build out of Ge atoms instead of Pt atoms, as was always assumed in experiments. Secondly, the surface supporting the NWs is not a simple β -surface with one quarter monolayer of Pt imbedded, but rather a modified β -terrace containing at least half a monolayer of Pt in the top layer. Thirdly, the experimentally observed symmetry around the wire, which is electronic, should also appear in the surface geometry.

Fig. 4.7 shows the two surface geometries we will use in the following. Both contain 0.5 ML of Pt in the top layer. The first one has Pt at positions 1, 4, 6, and 7 and will be referred to as γ_c (cf. **Chapter 3**), it has a $c(4 \times 2)$ structure and all troughs are equivalent. The second surface geometry contains Pt atoms at positions 2, 3, 6, and 7, and will be referred to as γ_{as} . This is an asymmetric version of the γ_1 geometry presented in **Chapter 3**, it contains alternating Pt lined and Ge lined troughs. The translational periodicity orthogonal to the dimer rows is doubled compared to the γ_1 -geometry. Unlike the γ_c surface the troughs between the dimer rows are not equivalent. Here one trough is lined with Pt atoms while the neighboring trough is lined with Ge atoms. Because of what we learned in the previous paragraph ad-structures will only be placed in the Pt-lined trough. Both Pt and Ge dimers were used as NW at site A in both structures, and after relaxation their formation energies were calculated and are shown in Table 4.2.

Table 4.2 shows that on the γ_c surface both Pt and Ge NW are stable, with

Formation and adsorption energy.

	E_f (meV)	E_{ad} (meV)
γ_c Ge NW	-365	-298
γ_c Pt NW	-199	-215
γ_c Ge NW \times 2	-322	-138
γ_c Pt NW \times 2	289	14
γ_{as} Ge NW	-1003	-379
γ_{as} Pt NW	-371	-63
γ_{as2} bare	387	-
γ_{as2} Pt NW	-1495	-625
γ_{as} Pt NW + Ge NW	-1397	-513
γ_{as} Pt NW + Pt NW	1027	699
γ_{as2} Pt NW + Ge NW	-1029	233
γ_{as2} Pt NW + Pt NW	-443	526

Table 4.2: Formation and adsorption energies of Pt and Ge nanowires adsorbed on the γ_c and γ_{as} surface geometry, shown in Fig. 4.7. The adsorption energies for the Pt NW + X NW geometries, are the adsorption energies only for the ‘X NW’, and were calculated with regard to the surfaces ‘ γ_{as} Pt NW’ and ‘ γ_{as2} Pt NW’.

the highest stability for the Ge NWs. It also shows that both structures are more stable on a γ_{as} surface. This is partly because the formation energy is calculated with regard to the Ge(001) surface, and thus includes the formation energy of the substrate, which shows a higher stability for the γ_{as} than for the γ_c -geometry (*cf.* Table 3.1 in Chapter 3). It is important to note that the experimentally observed NWs do not appear in adjacent troughs. In a single array of NWs there is always one trough spacing between two NWs. Places where two such arrays meet even a spacing of two troughs exists between the different arrays. This means that the growth of NWs in adjacent troughs must somehow be prohibited. In the γ_{as} geometry this can easily be understood. Since only every second trough is lined with Pt atoms, and only the Pt lined troughs allow for stable binding of wires, only every second trough a wire can form. This mean that in the above observation two Ge lined troughs are located in between the two NW arrays. For the γ_c geometry such a substrate related restriction is not the case and the geometry allows for NW to be present in both troughs of the unit cell. Table 4.2 shows that for systems with Ge NWs in each trough (γ_c xx NW \times 2) the formation energy E_f is just a bit smaller, reducing the adsorption energy E_{ad} by more than a factor of 2 weakening the binding of the NW to the surface. For Pt NWs however the formation energy increases with ~ 0.5 eV, making the reconstruction unstable. Even in case this would inhibit the growth of NWs in adjacent troughs it would not prevent the existence of patches where NWs randomly switch between adjacent troughs, littering all troughs with

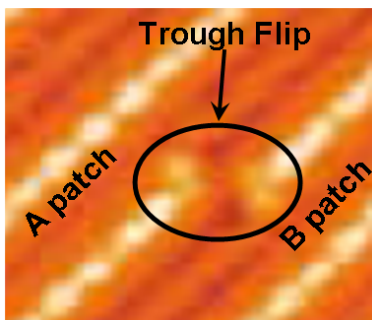


Figure 4.8: Magnification of a section of figure 4 in Reference [93]. An example of a trough flip observed at the boundary of two different NW patches. Note that two nanowires are spaced at least one empty trough in the lateral direction. There is no interdigitation as observed for Au NW on Ge(001). [25]

NW segments. Such a terrace would look like patch of dots and dashes instead of the clean NW-arrays that are observed in experiment. The reason such disordered patches of NWs are not observed can be understood from a comparison between the γ_c and γ_{as} geometry. In **Chapter 3** it was shown that the γ_c -reconstruction is much less stable than the γ_{as} -reconstruction. This is due to the strain between antiparallel Pt-Ge dimers in the QDRs. Flipping from antiparallel to parallel geometries the system gains ~ 0.3 eV per Pt-Ge dimer pair. Since the γ_c -geometry only consists of these anti-parallel pairs, combined with the fact that the stabilizing effect of the adsorbed wires (*i.e.* their adsorption energy) is smaller than on the γ_{as} -geometry, we can assume that the γ_c -structure will not be dominantly present in the structure of the NWs.

However, in some experimental images at the boundary between different NW patches, the boundary NW can be seen to flip from one trough to an adjacent trough (*cf.* Fig. 4.8).⁴ The actual NW is always in between two empty troughs on one side and one empty trough at the other. This shows that inside NW patches the presence of NWs is uniquely connected to the underlying surface geometry, which prevents the presence of NWs in neighboring troughs. A trough flip as seen in Fig. 4.8 would entail a QDR where at one side (bottom half Fig. 4.8) the Pt atoms are on the left side of the QDR, while at the other side (top half of Fig. 4.8) the Pt atoms are on the right side. At the position of the flip an antiparallel pair of Pt-Ge dimers exists, inducing a local strain on the system.

Table 4.2 shows the adsorption energy for the Ge NW on the γ_{as} surface to be ~ 0.3 eV larger than that of the Pt NW. However the latter structure is only a local minimum in phase space. The Pt NW has sunk into the trough, about 0.7 Å

⁴It is important to note that what is described here is a static situation and not a dynamic process of a NW jumping from one trough to another and back. Since this NW flip is only a small part of the boundary between different NW arrays, we will not refer to it as boundary to prevent confusion.

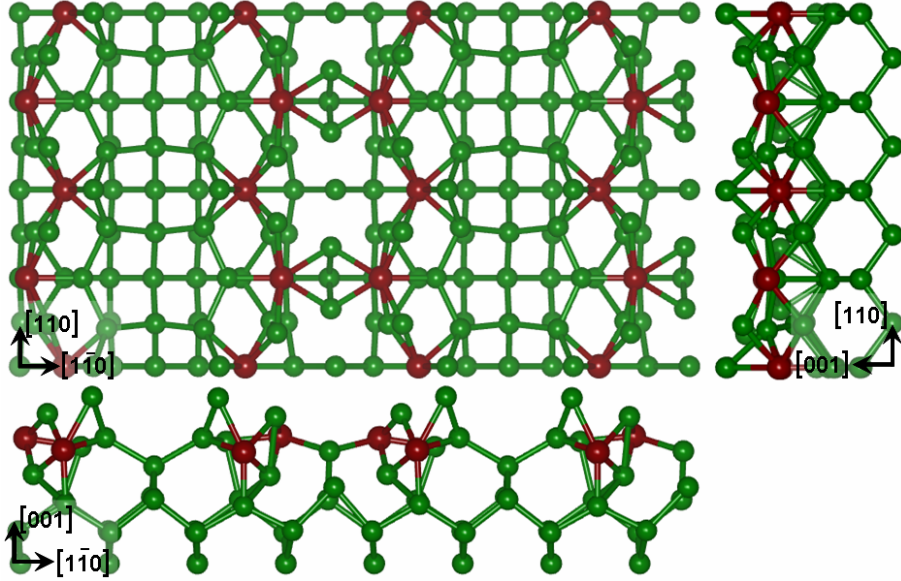


Figure 4.9: Ball-and-stick model of the γ_{as2} -surface reconstruction after relaxation. The top left image shows a top view of the structure, while the top right and bottom images show side views along the $[1\bar{1}0]$ and $[110]$ directions respectively. Green and red balls show the positions of Ge and Pt atoms respectively. The top left figure shows 2×2 -surface unit cells, with three troughs in the x -direction. The middle trough is lined with Pt atoms and is the location of NW adsorption in the calculations. The bottom image clearly shows the large tilting angles of some of the Pt-Ge surface dimers. It also shows the second layer Ge atoms to be pushed up to positions higher than the Pt atoms in the substrate. Also an interesting point to note is the configuration of the Pt atoms of the almost flat Pt-Ge dimers and the third layer Ge atoms that form the bottom of the middle trough. Their configuration looks remarkably like that of the NW shown in Fig. 4.12a. When the third layer Ge atoms are replaced with Pt atoms the γ_{as2}^* surface is generated.

below the average top layer position, and bound to second layer Ge atoms. These Ge atoms can be pushed up to the surface allowing for the Pt atoms at positions 2 and 3 (cf. Fig. 4.5a) to dive into the subsurface increasing the tilt angle of these Pt-Ge dimers from 4.8° to -61.2° . The two remaining Pt-Ge dimers (with Pt at positions 6 and 7) stay almost flat with a tilt angle of 6.3° , while being lowered beneath the pushed up Ge atoms of the second layer. We will refer to this new surface reconstruction (without the Pt NW atoms) as γ_{as2} in what follows. As can be seen in Table 4.2, this reconstruction increases the formation energy of the Pt NW by over 1 eV, making $E_f = -1495$ meV. Figure 4.9 shows a ball and stick representation of the bare γ_{as2} -surface. It was obtained after removal of the Pt NW atoms and

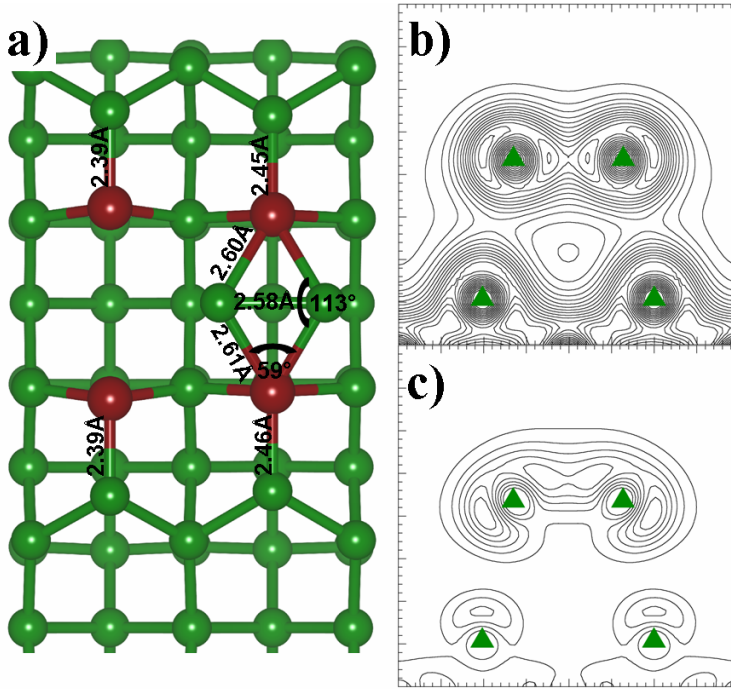


Figure 4.10: a) Geometric structure of the Ge NW on the γ_{as} -surface after relaxation. Pt atoms are shown in red, Ge atoms in green. b) Contour plot of the total charge density of the adsorbed Ge NW, in the vertical plane along the NW. c) Same as b) but now for the partial charge density, for all energy levels from 0.7 eV below the Fermi level up to the Fermi level. Green triangles indicate the position of Ge atoms in the plane. The contours are separated 0.03(0.01) $e/\text{\AA}^3$ for the total (partial) charge density plot. Major tics are separated 1 \AA .

additional relaxation of the system. This γ_{as2} -surface reconstruction is found to be unstable with a formation energy $E_f = 387$ meV. This means that this reconstruction is induced by the presence of the Pt NW in the trough. The pseudo-STM images show for the Pt NW on γ_{as} no signature of a nanowire image. The images of the Pt-Ge dimers in between (with Pt at positions 2 and 3) on the other hand show up more brightly and remind of the symmetric bulges seen in the experiment. Moving to the γ_{as2} -surface the Pt NW remains invisible but the already bright Pt-Ge dimer images from before become larger, and there is no more signature left of the other set of Pt-Ge dimers. For every two Pt-Ge dimers only one bright image remains, centered on a Pt-Ge dimer. This picture again greatly resembles the experimentally observed WT.

Contrary to the Pt NW, the Ge NW on γ_{as} shows after relaxation a nicely

symmetric structure with the Ge NW at the center of the trough, in a slightly elevated position 0.7 Å above the average top layer. The calculated STM images show some of the main features of the experimentally observed NWs. The symmetric bulges are present, as is a clear NW signature, for both filled and empty state images. However the NW dimer images are not double peaked as is observed in the experiments. Examination of the total charge distribution shows that the Ge NW atoms dimerise forming a σ -bond, as can be seen in Fig. 4.10b. From this one might expect to see a double peak feature in the STM images. However, an STM only sees energy levels close to the Fermi-level, and the partial charge density near the Fermi level (Fig. 4.10c) shows the existence of a π -bond above the Ge-dimer, albeit with a much lower charge density than the σ -bond, causing the NW dimer image to show up as a single peak. The state showing the NW is a surface state close to the Fermi-level.

The Ge NW binds to the Pt atoms in the top layer through σ -bonds, forming the diamond shaped structure already noted in Sec. 4.3.2, as can be seen in Fig. 4.10. These bonds with the Pt surface atoms pull the Ge NW slightly into the trough, stretching the Pt-Ge bonds of the dimers in the QDR about 2.5%. The dimer length of the NW dimers is 2.575 Å, only 6% longer than a normal Ge bulk bond.

In Sec. 4.3.2 we saw that a Pt NW on a Ge(001) surface can lead to a chain of double peaked dimer images when Ge dimers are placed on top of Pt atoms. Combined with the fact, noted above in this subsection, that the Ge NW stay above the trough while the Pt NW sinks in, one could imagine the existence of a double layered NW combining these properties. We therefore investigated some systems where a second NW dimer of Ge or Pt atoms was placed on top of the first NW dimer on both the γ_{as} and γ_{as2} surfaces. These calculations show that for both surfaces the extra Ge NW is most stable (*cf.* Table 4.2). In case of the extra NW on the γ_{as} surface however we find an adsorption energy $E_{ad} = -513$ meV for the Ge NW and $E_{ad} = 699$ meV for the Pt NW which means the second Pt wire would not stick to the surface while the Ge wire would. On the other hand we showed that the Pt NW on γ_{as} will induce a reconstruction to γ_{as2} creating a much more stable subsurface. On the γ_{as2} surface however both the extra NW will not stick, since they have an adsorption energy $E_{ad} = 233$ meV and 526 meV for the extra Ge and Pt NW respectively. Furthermore, inspection of the geometries show that the double layered NW fall over sideways in the trough, giving rise to a NW image in the calculated STM pictures which is asymmetric in the trough. Despite all this, the same pseudo-STM images also show the expected double peaked NW dimer images, which means the stacking of Ge on top of Pt atoms needs to be somehow maintained if we want to observe double peaked NW dimer images in the calculated STM images.

4.3.5 Third model: Pt and Ge wires on the γ_{as}^* -surface

It was shown in the previous subsection that the Pt NW atoms on the γ_{as} -surface sink into the trough. Going even further, one could imagine the Pt atoms to exchange positions with the third layer Ge atoms at the bottom of the trough, thus increasing their coordination and increasing the Pt density to 0.75 ML of Pt in the top layers of the surface. We will use the \star -superscript to indicate the presence of Pt atoms

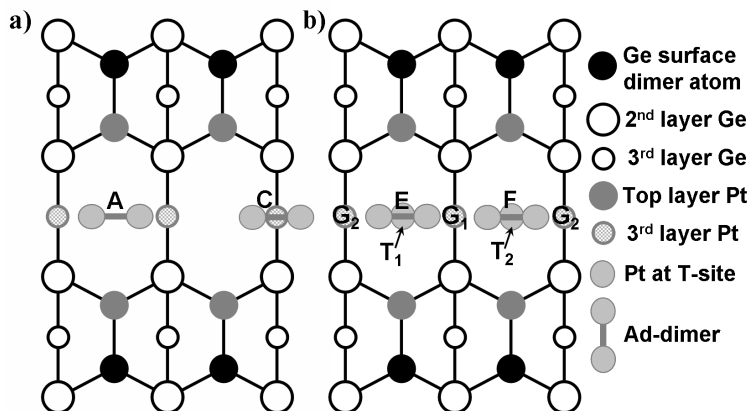


Figure 4.11: Schematic representation of the γ_{as}^* -structure with adsorption sites discussed in the text.

at the bottom positions of one trough of a system. Figure 4.11a shows a schematic representation of the geometry of the γ_{as}^* -structure. It contains 0.75 ML of Pt, with Pt atoms at positions 2, 3, 6, 7, and the two positions at the bottom of the Pt-lined trough. Keeping in mind the surface deformation from γ_{as} to γ_{as2} induced by a Pt NW, we also build a γ_{as2}^* -surface in similar fashion (*cf.* Fig. 4.9), by replacing the two Ge atoms at the bottom of the Pt lined trough of the γ_{as2} -surface. Pt and Ge dimers are adsorbed at sites A and C (*cf.* Fig. 4.11a) for the γ_{as}^* -surface and at site A for the γ_{as2}^* -surface. Table 4.3 shows that both the bare γ_{as}^* - and γ_{as2}^* -surfaces are stable reconstructions, with the γ_{as2}^* -surface roughly 1.0 eV more stable than the γ_{as}^* -surface. For both surfaces the adsorption of a Ge NW at site A is more favorable than the adsorption of a Pt NW. In case of the γ_{as}^* -surface, the Pt NW even has a small positive adsorption energy, making it unstable. Although the transition from γ_{as}^* to γ_{as2}^* shows an improvement in formation energy for the Ge NW system, the main contribution comes from the surface itself, decreasing the adsorption energy of the wire.

On the γ_{as}^* -surface, the Ge NW in the A configuration is stretched to a length of 2.72 Å (*cf.* Fig. 4.12a) and is located 0.52 Å above the average height of the surface atoms, while the Pt NW sinks in the trough 0.06 Å to stay almost level with the Pt atoms in the top layer of the surface. Contrary to the Ge NW on the γ_{as} -surface, the Ge NW on the γ_{as}^* is dimerised only through a σ -bond, located close to the Fermi level. The electrons used to fill the π -bond are now used in bonds with the Pt atoms at the bottom of the trough, as can be seen from the contour plots in Fig. 4.12b and c. The strong bonds with the two Pt atoms at positions 2 and 3 remain. The Pt NW on the other hand binds to the Pt atoms at the bottom of the trough, the surface Pt atoms at positions 2 and 3 and to the four second layer Ge atoms in the trough.

On the γ_{as2}^* -surface the Ge atoms of the second layer are pushed upward to above the average top layer level, and form bonds with the NW atoms in both cases.

Formation and adsorption energy.

	E_f (meV)	E_{ad} (meV)
γ_{as}^* bare	-1011	-
γ_{as2}^* bare	-1991	-
γ_{as}^* Ge NW A	-2055	-522
γ_{as}^* Pt NW A	-962	25
γ_{as}^* Ge NW C	-3364	-1176
γ_{as}^* Pt NW C	-2877	-933
γ_{as2}^* Ge NW A	-2488	-248
γ_{as2}^* Pt NW A	-2312	-160
γ_{as2}^* Ge NW + Ge NW	-2281	103
γ_{as2}^* Ge NW + Pt NW	-1597	445
γ_{as2}^* Pt NW + Ge NW	-2448	-68
γ_{as2}^* Pt NW + Pt NW	728	1520

Table 4.3: Formation and adsorption energies of Pt and Ge nanowires adsorbed on the γ_{as}^* and γ_{as2}^* surface geometry, shown in Fig. 4.11a. The adsorption energies for the X NW + Y NW geometries, are the adsorption energies only for the ‘Y NW’, and were calculated with regard to the same surface with the X NW adsorbed. The X and Y NWs were each time adsorbed at site A.

Figures 4.13(a–d) show calculated STM images of the Ge NW adsorbed at site A of the γ_{as}^* - and γ_{as2}^* -surface. Although the latter has a better formation energy, it are the pseudo STM images of the first that show good agreement with the experimentally observed images. The pseudo-STM images of the Ge NW on the γ_{as2}^* -surface on the other hand show great resemblance to the experimentally observed WT. In Sec. 4.4 we will look into the different structures which present a WT in their calculated STM images in more detail, and discard them or give them a place in the larger picture of the NW formation.

For the Ge NW on γ_{as}^* we can identify all the experimentally observed features: the symmetric bulges at the sides of the NW are present and the NW dimer images show a double peaked feature in the filled state image (Fig. 4.13a) and a single peaked one in the empty state image (Fig. 4.13b). In Sec. 4.4.1 we will show this surface reconstruction is a good model for the experimentally observed solitary NWs, so we refer the reader to that section for a more in depth discussion.

The Pt NWs on the other hand are invisible on both surface geometries, as is shown in Fig. 4.13g and h, making it possible to exclude them again from the realm of possibly observed NW atoms.

Because the γ_{as2}^* -surface has a better formation energy, and symmetric bulges are readily present, the γ_{as2}^* -surface might appear a suitable surface for NWs. However, although the Ge NW on the γ_{as2}^* -surface reconstruction has a better formation energy, the average height of the surface atoms (the bulges in particular) makes it hard

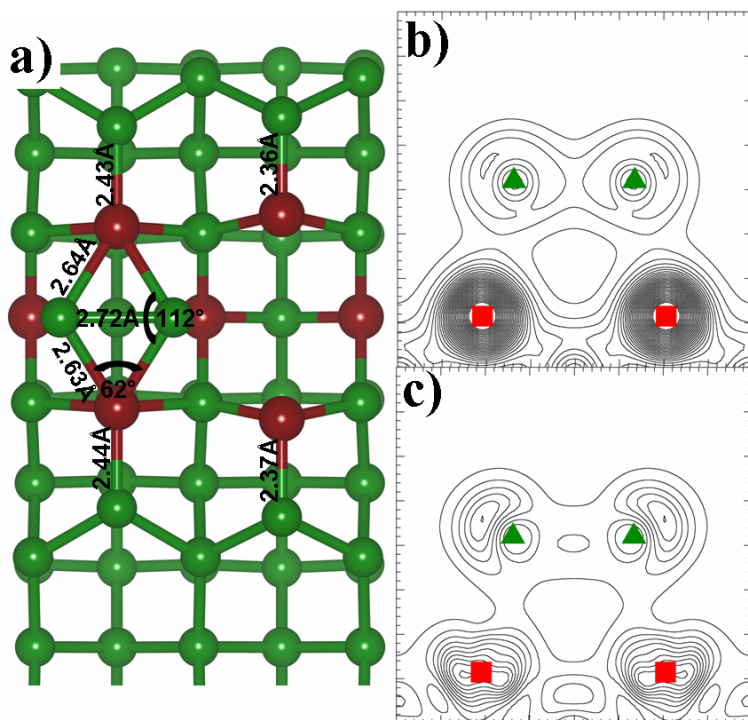


Figure 4.12: a) Geometric structure of the Ge NW on the γ_{as}^* -surface after relaxation. Pt atoms are shown in red, Ge atoms in green. b) Contour plot of the total charge density of the adsorbed Ge NW, in the vertical plane along the NW. c) Same as b) but now for the partial charge density, for all energy levels going from 0.7 eV below the Fermi level up to the Fermi level. Green triangles (red squares) indicate the position of Ge (Pt) atoms in the plane. The contours are separated 0.1 (0.01) $e/\text{\AA}^3$ for the total (partial) charge density plot.

to observe any NW in the trough. Therefore we again use a double layered NW, assuming the second layer of the NW will stick out of the (widened) trough far enough to be visible. For all these stacked NWs the formation energy, given in Table 4.3, is less than this of the Ge NW on the γ_{as2}^* -surface. Also the adsorption energy of the second NW dimer is shown in Table 4.3 to be unstable and only marginally stable in the best case. Furthermore, it again shows the preference for Pt atoms to be buried underneath Ge atoms (Compare γ_{as2}^* Ge NW + Pt NW to γ_{as2}^* Pt NW + Ge NW in Table 4.3). Exchanging the Pt and Ge NWs in the stack improves the formation energy by 0.85 eV. Furthermore, Table 4.3 shows that a Pt NW as top wire of the stack always has a large positive adsorption energy, meaning it would not stick to the surface.

The pseudo-STM images show bright NW images in each case. The NW peaks

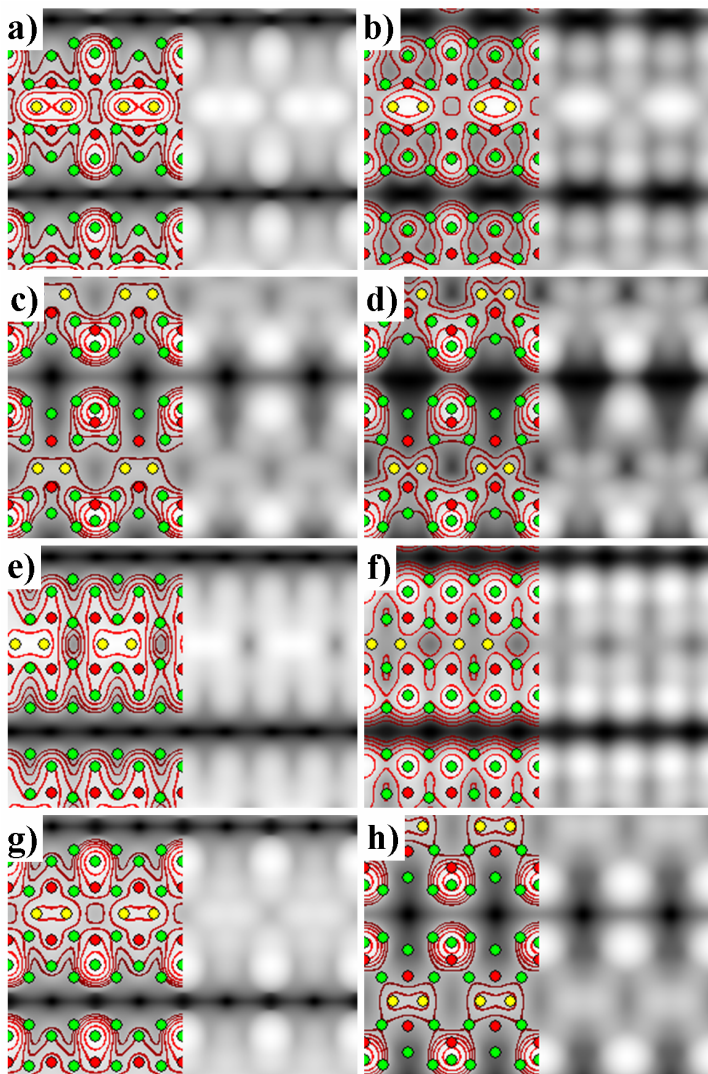


Figure 4.13: Calculated STM images of a Ge NW adsorbed at the A (a and b) and C (e and f) site on a γ_{as}^* -surface and on the A site of a γ_{as2}^* - (c and d) surface, and calculated filled state STM images of a Pt NW adsorbed at the A site of a γ_{as}^* - (g) and γ_{as2}^* -surface (h). The green/red discs show the positions of Ge/Pt atoms in the surface, and the yellow discs show the positions of the Ge/Pt NW atoms. Contours are added to guide the eye. (a, c, e, g, and h) Filled state calculated STM image, for $z = 3.0 \text{ \AA}$ and a simulated bias of -1.50 V . (b, d, and f) Empty state calculated STM image, for $z = 3.0 \text{ \AA}$ and a simulated bias of $+1.50 \text{ V}$.

are much higher in comparison to the surface than the ones discussed before. Unlike the structures with Pt NWs presented above, here the Pt NWs (*i.e.* the top wire in the stack) show up as bright images, this is because in this reconstruction the extra Pt NW sticks far out of the surface after relaxation. The stacked NWs however tend to topple over sideways in the trough, causing the pseudo STM pictures to show NW images shifted toward the QDR, in contradiction to the experimentally observed NWs. This allows us to discard these stacked NWs on the γ_{as2}^* -surface, based on their adsorption energies and calculated STM images.

Table 4.3 also shows the formation and adsorption energy of Pt and Ge NWs adsorbed at the C site on the γ_{as}^* -surface. It shows that adsorption at the C site is at least 1 eV more stable than at the A site, making the adsorbed NW at the A site metastable configurations.

After relaxation, the Ge NW stays centered in the trough at the C site. Contrary to the A site adsorption all Pt atoms in the top layer have a bond with the Ge NW. The difference in geometry also shows up in the pseudo-STM images, as can be seen in Fig. 4.13e and f. Although double peaked dimer images are present in the filled state image (Fig. 4.13e), the symmetric bulges are missing, and the dimer image is out of phase half a dimer length in comparison to the experimentally observed NWs. Since the NW dimers are now strongly bound to four Pt atoms in the top layer instead of two (in case of the A site), the previously empty states are now filled with extra charge from the two extra Pt atoms. Because of this, the empty state images (Fig. 4.13f) do not show a NW image, where in experiment it is clearly observed.

The adsorbed Pt NW sinks in the trough binding tetrahedrally to four neighboring Pt atoms, two in the top layer and two at the bottom of the trough. With an adsorption energy $E_{ad} = -933$ meV, these Pt atoms are bound very strongly in the trough. In the pseudo-STM images however the Pt NW remains invisible.

4.3.6 Nec plus ultra: Are further improvements possible?

In the previous section it was shown that Ge NWs at the A site of the γ_{as}^* -surface are in good agreement with the experimentally observed NWs, based on calculated STM images. It was however also shown that this structure is, although quite stable, not the most stable configuration with that specific stoichiometry. This raises the question if it is possible to stabilize the NW geometry without changing the electronic structure observed in STM experiments to much. Although experimentally 0.25 ML of Pt was deposited, it is reasonable to assume local gradients in the distribution. These variations in local Pt density over the entire surface however should not be to extreme, *i.e.* not become local densities of multiple ML.

In this section we will pursue two goals to improve our model. The first goal is to try and stabilize the geometry even further by adding extra Pt or Ge atoms to the trough of the NW, this we will do in the first part of this section. Since the local Pt density at this point is approaching a full monolayer, the second goal will be to try to minimize the amount of Pt in the surface without loss of stability or STM agreement. For this we will investigate \star -geometries based on surface structures with a local Pt density of no more than 0.5 ML. We will do this at the end of this section.

Formation and adsorption energy.

	E_f (meV)	E_{ad} (meV)
With a sunken Ge atom at each T-site of the trough.(2T)		
γ_{as}^* Ge NW	-2911	316
γ_{as}^* Pt NW	-2256	643
γ_{as}^* Pt NW †	-3689	-74
γ_{as2}^* Ge NW	-2784	634
γ_{as2}^* Pt NW	-4308	-127
With sunken Pt atoms at the T-sites of the trough.		
γ_{as}^* 2T Ge NW	-4763	-943
γ_{as}^* 1T Ge NW	-3696	-860
γ_{as2}^* 1T Ge NW	-3490	-757
γ_{as}^* 0.5T Ge NW	-2914	-710

† with ejected Ge atom

Table 4.4: Formation and adsorption energies of Pt and Ge nanowires adsorbed on the γ_{as}^* - and γ_{as2}^* -surface geometry with extra Pt or Ge atoms sunken into the trough at the T-sites shown in Fig. 4.11b. xT indicates the number of T sites per (4×2) surface cell that are occupied.

It was shown that Pt atoms sink into the trough while Ge atoms have a stable position above it. However, if the Ge atoms of the NW would sink in the trough more Pt-Ge bonds could be formed. In this case, each of the sunken Ge atoms binds to 4 Pt atoms in a tetrahedral configuration (at the T-sites shown in Fig. 4.11b) improving the formation energy by about 1.5 eV on both the γ_{as}^* - and γ_{as2}^* -surfaces. This again shows the Ge NW on γ_{as}^* -reconstruction to be only metastable. Table 4.4 shows that the adsorption on a γ_{as}^* -surface with sunken Ge atoms has a positive adsorption energy of 316 and 643 meV per NW adatom for the Ge and Pt NW respectively. This means that both wires will not even stick to the surface. For the equivalent situation on the γ_{as2}^* -surface only the Pt NW shows a small negative adsorption energy of -127 meV making it marginally stable. Furthermore, for all structures, the pseudo-STM images of the NWs do not show the expected signatures. The Ge NW dimer images are not double peaked, and only on the γ_{as2}^* -surface the side bulges are observed. In case of the Pt NW on γ_{as}^* with sunken Ge atoms, equidistant peaks are observed for each Pt NW dimer, but this structure tends to stabilize by ejecting a sunken Ge atoms on top of the Pt wire (*cf.* Table 4.4). On the γ_{as2}^* -surface with sunken Ge atoms this does not happen and the Pt NW remains invisible. Based on these results it can be concluded that the NWs are not stabilized by Ge atoms sunken into the trough.

Similar to the previous idea, extra Pt can be introduced in the trough. This assumption can be founded on the stability and geometry after relaxation of the Pt

NW adsorbed at site C of the γ_{as}^* -structure. With an adsorption energy $E_{ad} = -923$ meV per Pt NW atom, these Pt atoms are bound very strongly. During relaxation the Pt dimer has broken up (the distance between the two Pt NW atoms after relaxation is 3.98 Å) and the Pt atoms are adsorbed at both T sites (Fig. 4.11b), having a tetrahedral binding to the four surrounding Pt atoms.

If Pt atoms are adsorbed at all T-sites, the Ge NW dimers break up and the Ge NW atoms are spaced equidistantly along the trough. Figure 4.14a and b show the filled and empty state pseudo STM images for this structure. The NW has again toppled over, which is clearly seen in the asymmetric position of the NW image in the trough. Furthermore, in both pictures the NW image consists of atom images separated roughly 4 Å. No dimer images, as observed in experiment, are seen here. This shows that there must be less than two Pt atoms per (4×2) surface cell present. The reason is twofold, firstly to allow the dimerization of the Ge NW atoms and secondly to keep the NW centered in the trough.

We now place 1 Pt atom at the T_1 site (leaving T_2 empty) of the γ_{as}^* - and γ_{as2}^* -surface and then adsorb a single Ge NW at sites E and F. For the Ge NW on the modified γ_{as}^* we see after relaxation that both structures converge to the same structure with Ge atoms moving toward the center sites G_1 and G_2 . There is a small offset with regard to the G_1 and G_2 sites, away from the adsorbed Pt atom at site T_1 . Again the Ge atoms form a diamond shape reconstruction with 2 Pt atoms lining the trough. Contrary to the previous NW structures the 2 Ge NW atoms do not dimerise (the distance between these two Ge atoms is 3.27 Å), instead they form a strong bond with the sunken Pt atom at site T_1 . The configuration on the γ_{as}^* -surface, contrary to the systems studied up until now, has a better formation energy than the configuration on the γ_{as2}^* -surface, this is because in the latter case the Ge NW atoms bind to Ge atoms pushed up out of the surface instead of surface Pt atoms. The structure is also 0.7 eV more stable than the Ge NW on the same surface with sunken Ge atoms. With an adsorption energy $E_{ad} = -860$ meV per NW adatom, this wire is roughly ~ 0.3 eV more stable than the one on a clean γ_{as}^* -surface. Figures 4.14c and d show the calculated STM-images for this structure. In the filled state image (Fig. 4.14c), bright large double peaked dimer images and symmetric bulges at the sides of the wire are seen. The empty state image (Fig. 4.14d) however also shows a double peaked dimer image.

At this point it is important to remember the limitations of our applied method for generating STM images. The method used is implemented to simulate a ‘point’-like STM tip with infinite resolution. In reality however an STM tip has a finite width causing it to show two features, which are too close to one-another, as a single one. In our case the two peaks observed in the filled state image are bigger and spaced more widely than the ones seen in the empty state image, so it is reasonable to assume that in case of the empty state image a real STM might be able to resolve the peaks in the filled state image but not in the empty state image.

In case of the γ_{as2}^* -structure, the pseudo STM images show the already familiar signature of a WT. Here the Ge NW atoms bind to the Pt atoms at the bottom of the trough, the sunken Pt atom and the second layer Ge atoms which are pushed up by the structure.

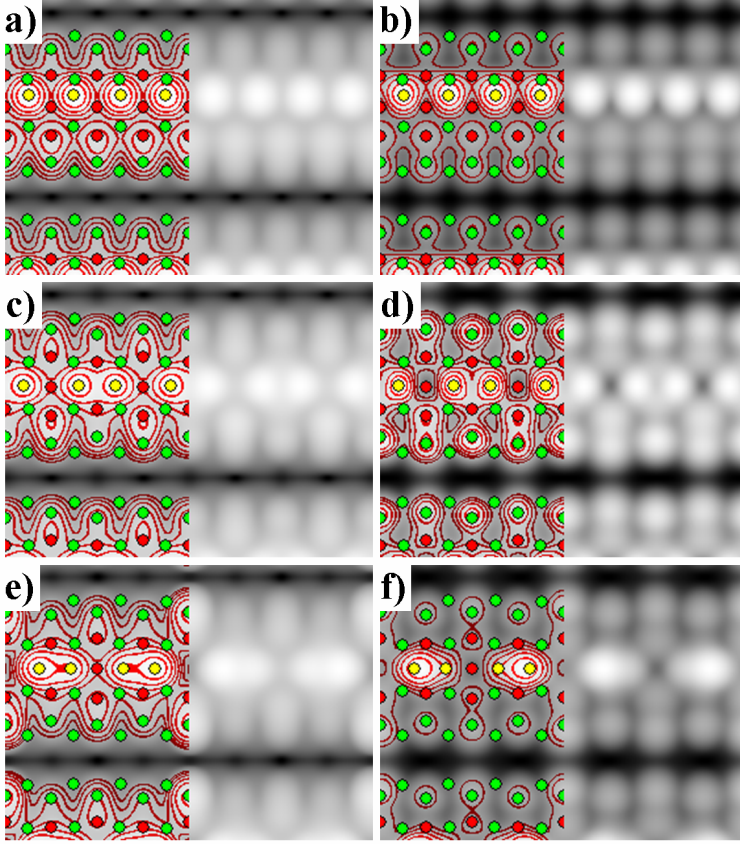


Figure 4.14: Calculated STM images of a Ge NW adsorbed on a γ_{as}^* -surface with extra Pt atoms adsorbed at the T-sites of the trough. a and b: Pt atoms are adsorbed at both T-sites of the (4×2) -surface cell ($2T$), c and d: only one T-site is occupied ($1T$), e and f: only one T-site per two surface-unit-cells is occupied ($0.5T$). The green discs show the positions of Ge atoms in the two top layers of the surface. The red discs show the positions of the Pt atoms in the top layer and the Pt atoms at the T-sites in the trough, and the yellow discs show the positions of the Ge NW atoms. Contours are added to guide the eye. a, c and e: Filled state calculated STM image, for $z = 3.0 \text{ \AA}$ and a simulated bias of -1.50 V . b, d and f: Empty state calculated STM image, for $z = 3.0 \text{ \AA}$ and a simulated bias of $+1.50 \text{ V}$.

Because both the Ge NW on the γ_{as}^* -surface and on the γ_{as}^* -surface with one sunken Pt atom in the trough per surface cell show good agreement with the experiment, and we want the Pt content to be as low as possible, a system with only one sunken Pt atom per two unit cells was examined (shown in Fig. 4.15). After relaxation of this 4×4 surface cell a formation energy $E_f = -2.914 \text{ eV}$ per sur-

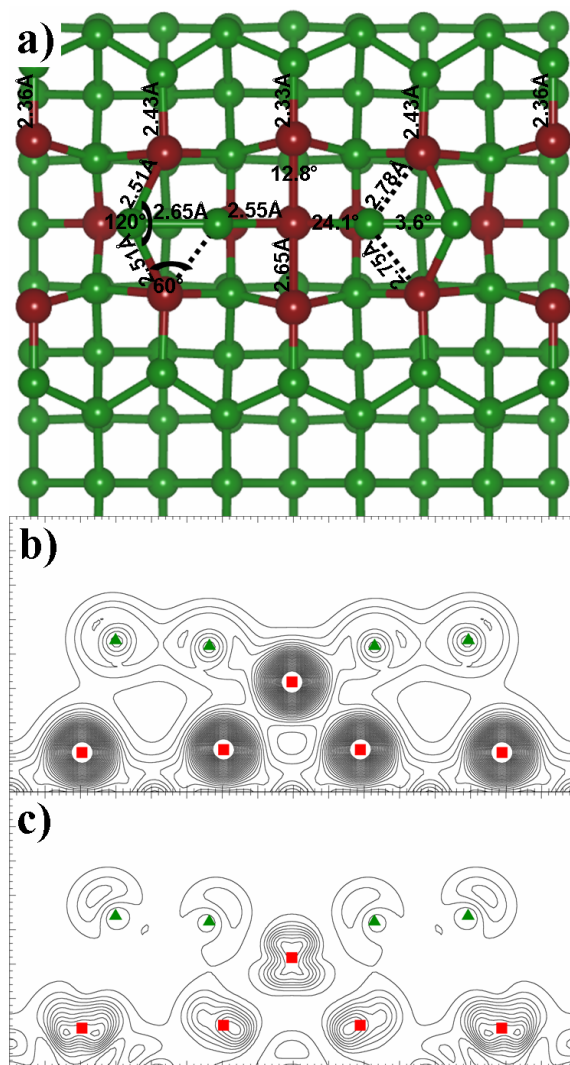


Figure 4.15: a) Geometric structure after relaxation of the Ge NW on the γ_{as}^* -surface containing one extra Pt atom in the trough per two (4×2) surface unit cells (NW2 structure). Pt atoms are shown in red, Ge atoms in green. Angles shown on the bonds are with regard to the xy -plane. b) Contour plot of the total charge density of the adsorbed Ge NW, in the vertical plane along the NW. c) Same as b) but now for the partial charge density, for all energy levels going from 0.7 eV below the Fermi level up to the Fermi level. Green triangles (red squares) indicate the position of Ge (Pt) atoms in the plane. The contours are separated $0.1(0.01)\text{ e}/\text{\AA}^3$ for the total (partial) charge density plot.

face unit was found and an adsorption energy per NW atom of -0.710 eV, in both cases roughly the average of Ge NW on the γ_{as}^* -surface and on the γ_{as}^* -surface with one sunken Pt atom in the trough per surface cell. There is however one important improvement over the smaller structures, the observed NW are double peaked and the two peaks are of a different height (Fig. 4.14e) at negative simulated bias. The calculated empty state images in Fig. 4.14f on the other hand shows the single peak image as observed in the experiment. In low temperature STM experiments the NWs in the NW-patches were observed to have a 4×1 periodicity along the NW. This periodicity however was absent for solitary NWs and the NWs at the edge of a NW-patch. The presence of this 4×1 periodicity was linked to the possible presence of a Peierls instability. [26] In Sec. 4.4 we will show that this geometry models the NWs in NW arrays, and we refer the reader to that section for further details. At this point structures with up to one full monolayer of Pt incorporated have been examined and the results indicate a steady shift toward the formation of a platinumgermanide around the trough region. Further increase of the Pt content will only move further into that direction, increasing the overall stability of the system, but also moving away from the NW arrays, *i.e.* the calculated STM images start to diverge from the experimental STM images.

In the natural flow of these iteratively built models, two concerns have not yet been addressed:

1. Would it be possible to remove some of the Pt atoms in the top layer while maintaining good agreement with the experiment in light of reducing the necessary gradient in the Pt density?
2. Could/should more Pt be located at the bottom of the empty trough lined with Ge atoms?

To answer these questions we investigate the stability of some modified geometries (modified by making them \star -geometries) and compare them to the γ_{as}^* -geometry. The Ge^* -geometry, is just a plain Ge(001) surface with Pt atoms at the bottom positions of every second trough. The same goes for the β_6^* -geometry. The β_3^* -geometry is a β_{3ud} -geometry (*cf.* Chapter 3) with Pt atoms at the bottom trough positions of the trough lined by the Pt atoms in the top layer. And finally, the γ_{as}^* -surface is a γ_{as} -surface with Pt atoms at the bottom trough positions of the Ge lined trough (contrary to the γ_{as}^* -surface where it is the Pt lined trough). Table 4.5 shows the formation and adsorption energy for these structures with and without adsorbed Ge NWs. The formation energies of the bare surfaces show a trend of stabilization with increasing Pt density. Contrary to the surface without Pt in the top layer (Ge^*), surfaces containing Pt in the top layer stabilize when a Ge NW is adsorbed. Comparison of the β_6^* - and β_3^* -structures with adsorbed Ge NW shows for the latter a more symmetric structure. The large increase in stability between these 2 systems is caused by different number of formed Pt-Ge bonds. For the β_6^* -surface both Ge NW atoms only bind to a single Pt atom. These Pt-Ge bonds have a bond length of 2.51 Å while the distance of the Ge NW atoms to the Ge surface dimer atom opposite to

Formation and adsorption energy.

	Bare structure	With adsorbed Ge NW		Formation energy of Pt- \star atoms.
	E_f (meV)	E_f (meV)	E_{ad} (meV)	E_f (meV)
Ge \star	194	503	154	97
β_6^*	-269	-459	-94	-98
β_3^*	-390	-1290	-450	-229
γ_{as}^*	-1011	-2055	-522	-383
γ_{as}^{*as}	-236	-	-	5

Table 4.5: Formation and adsorption energies of bare and Ge NW adsorbed structures containing Pt atoms at the bottom of one Pt-lined trough (the Pt- \star atoms). The γ_{as}^{*as} -structure refers to a γ_{as}^* -structure but with Pt atoms at the bottom of the Ge-lined trough instead of the Pt-lined trough. The right column gives the formation energy per Pt atom of the Pt atoms at the \star -positions.

this Pt atom is 4.20 Å, *i.e.* the Ge NW dimer is only bound to the side of the trough containing Pt atoms. This places the NW asymmetric at one side of the trough. In the β_3^* -geometry, the Ge NW dimer is bound to two opposing Pt surface atoms, with Pt-Ge bonds of 2.60 ± 0.01 Å. It shows that to have a NW centered in the trough, the Pt atoms need to be present at both sides of this trough in such a configuration that bonds can be formed with the Ge NW dimer. The influence of these Pt-Ge NW bonds becomes even clearer when comparing the adsorption energies. For the Ge \star -surface no such bonds appear while one set is present for the β_6^* -structure and two for the β_3^* and γ_{as}^* , resulting in a comparable adsorption energy for the last two. Neglecting for a while the difference in formation energy between the bare β_3^* - and γ_{as}^* -surfaces on grounds of different Pt stoichiometry, one might consider the β_3^* as a low Pt density replacement for the γ_{as}^* -surface. Calculated STM images for a Ge NW on the β_3^* -surface are shown in Fig. 4.16. Comparison to Fig. 4.13a and b however shows where the β_3^* -reconstruction fails. The typical symmetric bulges around the wire show up very asymmetric. The NW STM image in both the empty and filled state images is not even half the height of the side bulges. From our study of the β -terrace it is known that Ge dimers show up more brightly than Pt-Ge dimers, which seems to make the Ge dimers in this case too bright to be useful. From this we conclude that no Pt can be removed from the surface without loosing agreement with the experiment.

The second concern is a bit more complex. It not only entails the option for the Pt to be at the \star -positions in the second trough, but also why Pt in the \star -geometries should only be located in the Pt lined troughs. Tackling this concern however is rather simple. Combining the fact that the Ge \star structure is almost 0.5 eV per 4×2 surface unit cell less stable than the β_6^* structure, with the trend of increasing stability with increasing Pt density in the top layer shown in Table 4.5,

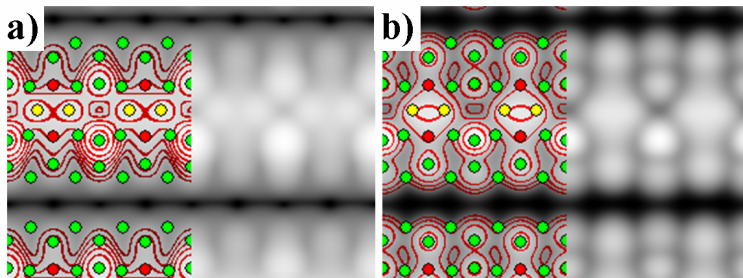


Figure 4.16: Calculated STM images of a Ge NW adsorbed on a β_3^* -surface. The green/red discs show the positions of Ge/Pt atoms in the top layers of the surface. The yellow discs show the positions of the Ge NW atoms. Contours are added to guide the eye. a: Filled state calculated STM image, for $z = 3.0$ Å and a simulated bias of -1.50 V. b: Empty state calculated STM image, for $z = 3.0$ Å and a simulated bias of $+1.50$ V.

indicates it to be preferable for Pt to build into the bottom of the trough lined with Pt atoms. Looking specifically at the Ge^* -structure we see that the Pt atoms substituting Ge atoms at the bottom of the trough actually destabilize the structure while the structures are stabilized in the other cases. Also the comparison of the γ_{as}^* - to the γ_{as}^{*as} -structure, with the Pt \star -atoms at the bottom of the Ge lined trough, show a preference for the first structure, and no stabilization of the γ_{as} -structure due to these Pt atoms. This allows us to put the second concern to rest and conclude no Pt needs to be added to the second trough and no Pt can be removed from the top layer of the surface.

4.4 Discussion

4.4.1 Modeling nanowires and examining possible formation paths

Based on a comparison of these results with experiments, a growth path as function of increasing Pt density can be suggested for the NWs. From experiments it is clear that the anneal temperature after deposition is crucial in the formation process. Firstly, the high temperature should cause the Pt not to move deeper into the substrate but rather move back to the surface. This requires the solubility of Pt in Ge to be very small, which is the case. [96] Secondly, this high temperature is needed to break the Ge surface dimers such that Pt atoms can replace Ge atoms and form surface Pt-Ge dimers. This bond breaking temperature is reported to be above 1000 K for the Ge(001) surface. [97] Thirdly, in combination with the anneal time, the high annealing temperature allows for larger kinetic barriers to be crossed, allowing the widened trough to transform into a NW.

Figure 4.17 shows a diagram indicating possible formation paths we will discuss

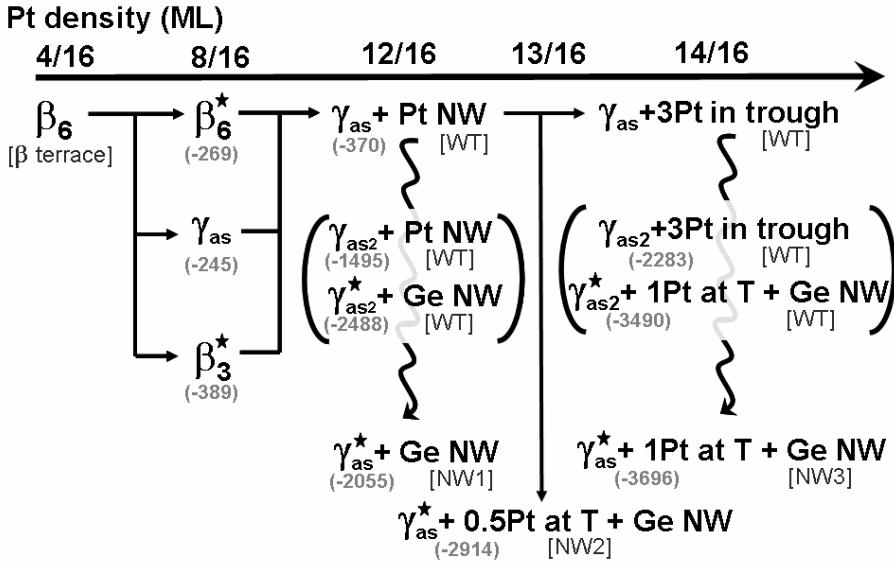


Figure 4.17: Schematic diagram of a possible formation path for NW arrays on Ge(001) with regard to increasing local Pt density, given from left to right in ML. Straight arrows indicate paths with increasing Pt density, curved arrows indicate possible relaxation paths during and after high temperature annealing. LDA formation energies are given in meV with regard to the Ge(001) $b(2 \times 1)$ surface reconstruction. WT and NW indicate if the pseudo-STM pictures show widened trough (WT) like images or nanowire (NW) like images. Formation paths are discussed in the text.

here. In our discussion we will assume that the high annealing temperature causes a large portion of the Pt that moved subsurface during deposition to be ejected onto the surface again. Starting with a quarter monolayer Pt atoms being ejected, and the high anneal temperature breaking the surface Ge dimers, the ejected Pt atoms can now form Pt-Ge dimers in the top layer of the surface, while the second Ge atom of the former Ge surface dimer moves away to a step edge. The formation of Pt-Ge dimers can be seen as a consequence of the fact that Pt-Ge bonds are preferred over Ge-Ge bonds, the larger bond strength allows for the Pt-Ge dimers to replace the broken Ge-Ge surface dimers. The most homogeneous way of spreading a quarter monolayer of Pt atoms in the top layer is the β_6 -geometry, which we showed in **Chapter 3** to be the geometry of the β -terrace.

If locally 0.5 ML of Pt is ejected onto the surface, either more Pt-Ge surface dimers can be formed, creating a surface only containing Pt-Ge dimers, or the extra Pt atoms can move to Ge positions at the bottom of the trough (\star -geometries). In case of a surface purely made up out of Pt-Ge dimers it was shown in **Chapter 3** that a γ_{as} -surface is most stable. The formation of surface Pt-Ge dimers could prohibit

these Pt atoms to move subsurface. However if this barrier is not large enough or the preference of forming Pt-Ge surface dimers is too small the β_6^* - and β_3^* -surfaces become available which are slightly more stable. Further STM studies of the surface near the edge between the β -terrace and a NW-patch could reveal which of these three structures is present. In the filled state images the β_6^* - and normal β_6 -surface are nearly indistinguishable, but at positive bias, close to the Fermi level the typical triangular structures of the β_6 -surface (*cf.* Fig. 3.5 in **Chapter 3**) are absent for the β_6^* -surface. This again shows that the β -terrace only contains 0.25 ML of Pt in its surface layers.

4.4.1.1 The NW1 geometry for solitary NWs.

If the ejected amount of Pt increases up to 0.75 ML, 0.5 ML can bind to Ge atoms of the top layer transforming all surface dimers into Pt-Ge dimers reconstructing the surface as a γ_{as} -surface. The remaining 0.25 ML end up in the Pt lined trough where they sink in, appearing as a WT. During this process the γ_{as} -reconstruction transforms into the γ_{as2} -reconstruction, also appearing as a WT. In the next step of the NW formation, the 0.25 ML of Pt atoms located in the Pt-lined trough exchange places with the Ge atoms at the bottom of this trough. The new structure $\gamma_{as2}^* + \text{Ge NW}$, still resembles the experimentally observed WT (*cf.* Fig. 4.13c and d). To elevate the Ge NW out of this trough and transform the γ_{as2}^* -geometry back to the γ_{as}^* -geometry a considerable amount of energy needs to be put into the system. At the end of this process a γ_{as}^* -surface + Ge NW is formed, we will refer to this structure as the NW1 structure. The fact that WTs are observed experimentally when only very short anneal times are used, suggests that the high anneal temperature has an important role in the formation process, however, it can not explain why no WT, due to the $\gamma_{as2}^* + \text{Ge NW}$, are present after a longer high temperature anneal step. Because the γ_{as2} -surface is much lower in energy than the γ_{as} -surface, the high temperature anneal step will only affect their relative fraction, and the amount of γ_{as} -surface will always be smaller than the amount of γ_{as2} -surface.⁵ The fact that no large amounts of WT (due to an γ_{as2} -geometry) are observed in experiment must have a different reason. If we look at the γ_{as2} -geometry in Fig. 4.9 we note quite a strong deformation of the surface with regard to the γ_{as} -geometry (*cf.* Fig. 4.7b). The Pt-Ge dimers tilting into the substrate is the most striking feature. In the above formation path we assume the γ_{as} -surface transforms into the γ_{as2} -surface, and then needs to transform back to a γ_{as} type surface (γ_{as}^*). However, if the barrier for this $\gamma_{as} \rightarrow \gamma_{as2}$ (and corresponding $\gamma_{as}^* \rightarrow \gamma_{as2}^*$) transformation is too high, then the first transformation in the suggested formation path would not occur, and there would be

⁵In case a GGA functional is used, the γ_{as} - and γ_{as}^* -surfaces are more stable than the γ_{as2} - and γ_{as2}^* -surfaces (*cf.* **Appendix C.3**). As a consequence, the $\gamma_{as2}^* \rightarrow \gamma_{as}^*$ transformation in the formation path described is energetically favorable. Since LDA is known to overbind, and GGA to underbind, the real energy values will be in between those of the LDA and GGA calculations. For this reason we have placed the γ_{as2} and γ_{as2}^* intermediate steps between brackets in Fig. 4.17. In the text we will follow the LDA values as a worst case scenario, and try to explain the existence of the experimentally observed NWs within the framework of these calculations.

no need for the second transformation back afterwards. The lack of WT structures in the experiments seems to support the idea that the barrier between the γ_{as} - and γ_{as2} -structures is too large to be overcome. As a result, the suggested formation path simplifies drastically. The 0.25 ML of Pt atoms in the Pt lined trough of the γ_{as} just sinks in, making the γ_{as} -surface appear in calculated STM images as a WT. Then these Pt atoms exchange positions with the Ge atoms at the bottom of the Pt lined trough, transforming the γ_{as} -surface directly into a γ_{as}^* -surface, while the exchanged Ge atoms dimerise and form the NW observed in experiment. Although the exchange might be energetically favorable, kinetic barriers could limit this exchange, making the high temperature anneal step crucial.

This NW structure shows a very good agreement with the experimentally observed NWs (*cf.* Fig. 4.13a and b). The double peaked NW dimer images are present in the filled state image, while a single peak dimer image is shown for the empty state image. The wire image is located nicely centered in the trough between the QDRs and symmetric bulges are visible as in experiment. In low temperature experiments however, a 4×1 periodicity along the NW appears for the NWs in the patches. For the NW at the edge of a NW-patch or for a solitary NW this 4×1 periodicity does not appear.

The unit cell used in the calculations above has a 4×2 surface unit cell, with a single NW dimer (2×1) on top, making it too small to observe this 4×1 periodicity. To be able to make a comparison with experiment two calculations with a large super cell (4×8 surface cell with four NW dimers on top) were carried out. In the first case the NW1 geometry was built without modifications, while in the second case the Ge NW dimers were tilted according to the observed 4×1 periodicity. After relaxation of both structures, the formation energies were calculated and pseudo-STM pictures were generated. The formation energies per 4×2 surface cell of both systems was the same (within the margin of error), $E_f = -2079$ meV per 4×2 surface cell, as for the NW1 structure. Furthermore, the pseudo-STM images showed the exact same results. The NW dimers, in the cell with the tilted NW dimers, had flattened out to a tilt angle of $< 0.2^\circ$. In correspondence to this very small tilt angle an equally small difference in the height of the two NW dimer peaks in the pseudo-STM images was observed. This indicates that the observed 4×1 periodicity, and the related tilting of the NW dimers, probably has a structural cause rather than being the signature for a Peierls instability. The above results also suggest the solitary NWs and the NWs at the edge of a NW patch to be different from those inside the patch. In experiment the difference between the array NWs and the NWs at the edge or solitary NWs presents itself in the appearance of the NW dimers. For the solitary and edge NWs symmetric NW dimers with a 2×1 geometry are found, while the array NWs show asymmetric NW dimers with a 4×1 geometry. Based on the good agreement with the experimental STM images we propose the NW1 geometry (*cf.* Fig. 4.12) as model for the solitary NWs and the NW at the edge of a NW-patch.

In this model the NW consists of flat stretched Ge dimers with a bond length of 2.72 Å. These dimers are bound to two opposing Pt atoms in the top layer, pinning the Ge NW dimers at the center of the trough. In addition, weak bonds with a length of 3.13 Å to the Pt atoms at the bottom of the trough are present as can be seen in

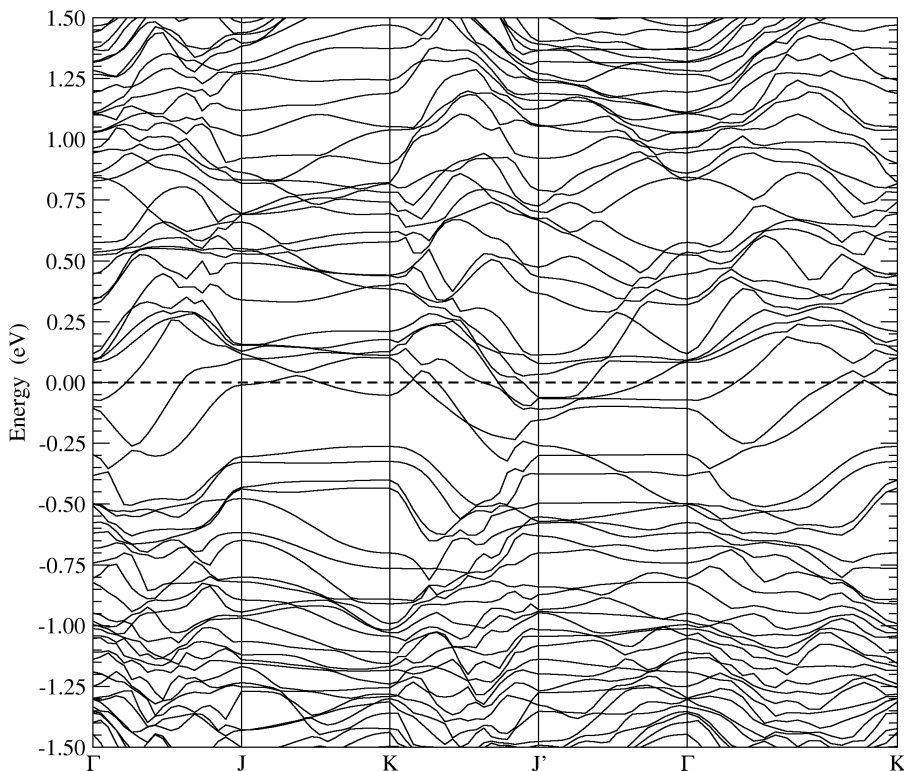


Figure 4.18: Band structure of the NW1 model shown in Fig. 4.12. The energy zero is given by the Fermi level.

the charge density plots (Fig. 4.12b and c). The Pt-Ge dimers bound to the NW are pulled slightly inward to the trough and stretched about 3% compared to the other Pt-Ge dimers.

Figure 4.18 shows the electronic band structure of the NW1 model along the (high) symmetry lines Γ -J-K-J'- Γ -K of the surface BZ (*cf.* Fig. 3.7 in **Chapter 3**). This shows a metallic behavior, as experimentally observed. [18] The bands near the Fermi level along the J-K and J'- Γ lines (perpendicular to the NW direction) show very little dispersion, while those along the Γ -J and K-J' lines (parallel to the NW direction) show a large dispersion. Close to the Fermi level the bands have a predominant Pt character. The band crossing the Fermi level near the middle of the Γ -J line (*cf.* Fig. 4.18) characterizes the π -bond of the Pt-Ge dimers which are not bound to the NW, while the band below is the one related to the bonds between the NW and the surface Pt atoms. This last band comes close to the Fermi level near the J point, where the character of the band has become mainly that of the Pt trough atoms, with a largely d_{xy} and some d_{xz} or d_{yz} orbital character. The remaining Ge NW orbital character of this band however is still sp_3 .

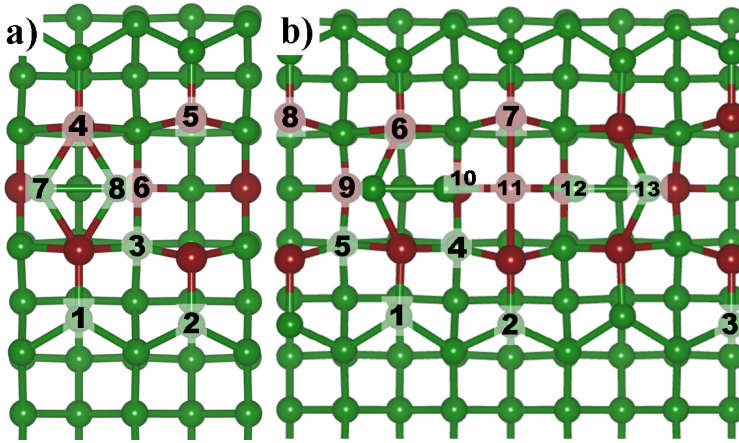


Figure 4.19: Ball-and-stick representations of the relaxed NW1 (a) and NW2 (b) models indicating the (inequivalent) atoms of which the LDOS is shown in Fig. 4.20 and 4.22.

The orbital character of the Ge NW contribution to these bands near the Fermi level is purely sp_3 , while the Pt atoms in the trough bottom have a mainly p_z and d_{z^2} character and the top layer Pt atoms a d_{xz} and d_{yz} character.

Around the middle of the J-K line there is a band crossing just above the Fermi level. The character of these crossing bands again has a large contribution from the Pt atoms at the trough bottom and the Ge NW. More interestingly there is, for both bands, also a large contribution from two top layer Pt atoms. The interesting part here is that it are the Pt atoms of the same QDR, and each time one Pt atom (the one bound to the NW) shows a mainly p_z and d_{z^2} orbital character, while the second Pt atom presents a mainly d_{xz} and d_{yz} orbital character, indicating the presence of empty bonds just above the Fermi level between all top layer Pt atoms and the NW along the NW direction.

Figure 4.20 shows the total DOS of the NW1 model and the LDOS of the different inequivalent surface atoms, as indicated in Fig. 4.19. The total DOS shows this model to be metallic, with a dip in the DOS just below the Fermi level. The general trend of the total DOS follows that of the DOS of bulk Ge quite well, with the exception of extra states in the BG region and some states near 5 and 9 eV below the Fermi level. From the LDOS we learn the peaks at -5 eV to be Pt states, and Pt induced states in second layer Ge atoms. The extra states at -9 eV come from surface Ge atoms and the Ge NW atoms.

The states in the bulk BG are most interesting, as they determine the properties of the system around the Fermi level. The LDOS of the surface atoms shows clearly that the major contribution comes from the Pt-Ge surface dimers. Only a minor contribution comes from the NW itself. Although presenting a metallic behavior, the NW (Ge atoms 7 and 8 in Fig. 4.20) only shows an increased contribution just above the Fermi level, and follows the Ge bulk DOS along the edge of the VB. The

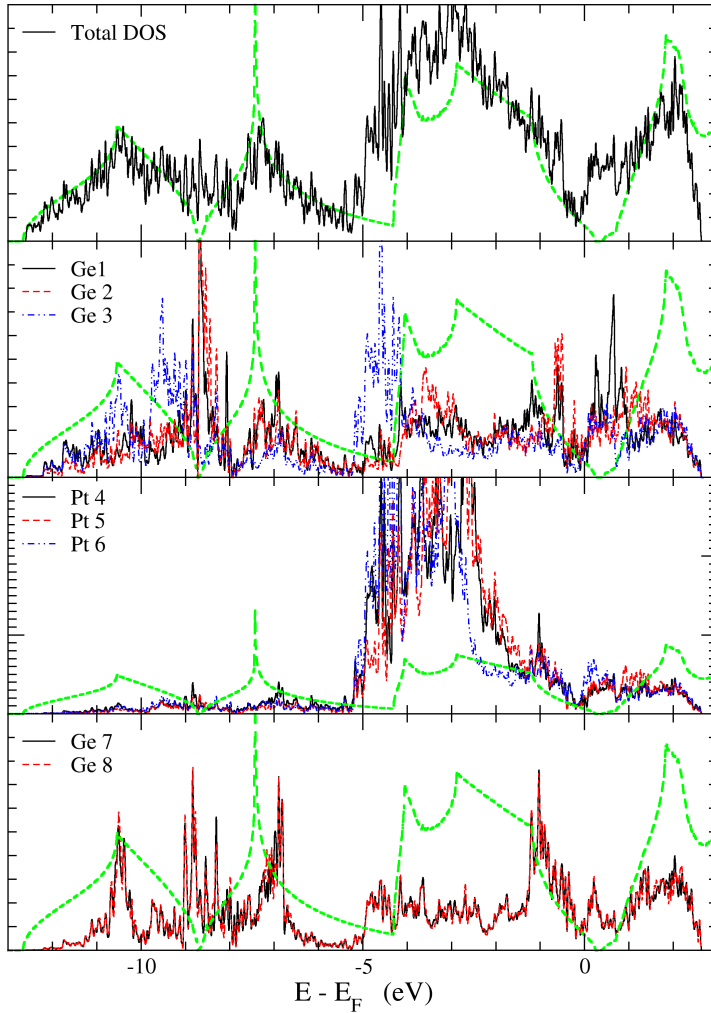


Figure 4.20: Total DOS of the NW1 structure and LDOS of the surface atoms as shown in Fig. 4.19a. The bold dashed green line shows the DOS of Bulk Ge, it was shifted to align the BG regions.

experimental observation of confined states between wires with a separation of 2.4 nm, can thus be interpreted as the observation of the states just above the Fermi level of the Ge atoms in the Pt-Ge surface dimers (Ge atoms 1 and 2). [27, 90]

4.4.1.2 The NW2 geometry for NW-patches

To find the geometry of the NWs inside the patches, an even higher local Pt density is assumed. If 0.875 ML of Pt is ejected, and we adopt the same argument as given in the previous paragraph, three Pt atoms will end up in the Pt lined trough.⁶ Again an exchange of two Pt atoms with the two Ge atoms in the bottom of the trough takes place, resulting in the γ_{as}^* -geometry containing one Pt atom and a Ge dimer in the trough. Based on our discussion for the NW1 formation path, we can also assume here that the energy barrier is too high to allow for the transformation from the γ_{as} - to γ_{as2} -substrate structure. In this case, however, even if such a transformation would take place the transformation back from the $\gamma_{as2}^* + 1$ Pt at T + Ge NW to $\gamma_{as}^* + 1$ Pt at T + Ge NW would be energetically favorable, removing the problem that existed for the NW1 formation path.

In this scenario all steps lead to energetically more favorable structures making it more likely to happen spontaneously.⁷ The pseudo-STM images of the final structure, shown in Fig. 4.14c and d, also show a NW structure, however the double peaked NW images at positive simulated bias are somewhat unsatisfying (*cf.* Sec. 4.3.6). Therefore we investigate a system with the average Pt density of the system just described and the NW1-system.

Such a system would again follow a similar formation path. The final structure would again be a γ_{as}^* -surface but now containing only one Pt atom in the trough per two surface unit cells and one Ge dimer per surface unit cell. We will refer to this $\gamma_{as}^* + 0.5\text{Pt} + \text{Ge}$ NW structure as NW2. In this NW2-geometry, shown in Fig. 4.15a, the two Ge NW dimers are bound to the extra Pt atom in the trough. This stabilizes the NW dimers at their position in the trough (it prevents them from slipping into a C-site adsorption geometry) and tilts the Ge NW dimers over an angle of 3.6° . This tilting causes a 4×1 periodicity along the wire. It is also clearly visible in the pseudo-STM images, where it causes a height difference of 0.36 Å between the peaks of the NW dimer in the filled state image at a simulated bias of -0.7 V. The empty state image shows a single peaked dimer image as is experimentally observed. Also the symmetric bulges are clearly visible, resulting in an excellent agreement between the pseudo-STM images of the NW2 structure and the low temperature STM images of NWs inside a NW-patch. Fig. 4.15a shows the relaxed NW2 structure we propose as model for the observed NWs inside a NW-patch.

In this model a periodicity doubling occurred with regard to the NW1-model. The Ge dimers forming the NW are, with a bond length of 2.65 Å, less stretched than is the case for the NW1-model. Every pair of Ge NW dimers is now bonded to a Pt atom located at a T-site in the trough. Through this bond the NW dimers are pulled toward the Pt atom, and tilted downward over an angle of 3.6° . The Pt-Ge dimers of the QDR bound to the NW are pulled slightly inward to the trough and stretched roughly 3%. Just like the NW1-model a weak bond between the NW and the Pt atoms in the trough bottom is present, as can be seen in the charge density contours of Fig. 4.15b and c. In this case the bond length with the up-Ge NW atom

⁶The number of atoms mentioned here is each time per 4×2 surface unit cell.

⁷The same is true in case GGA functionals are used (*cf.* Appendix C.3).

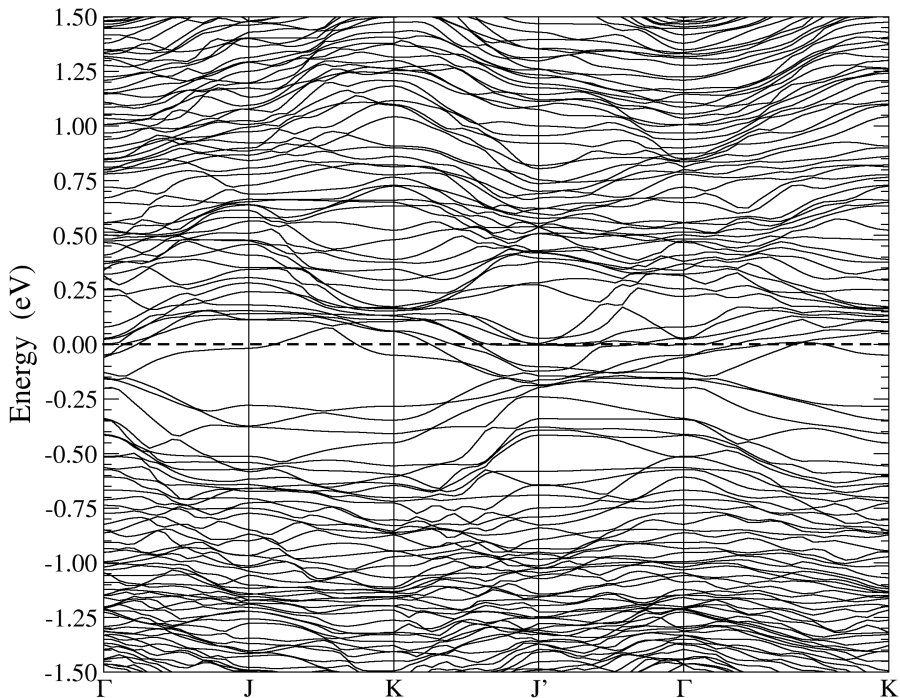


Figure 4.21: Band structure of the NW2 model shown in Fig. 4.15. The energy zero is given by the Fermi level.

is 3.40 Å, while only 3.04 Å with the down-Ge NW atom.

Figure 4.21 shows the band structure of the NW2-model. It shows quite similar trends as seen for the NW1-structure. Close to the Fermi level the bands have almost no dispersion. However, contrary to the NW1-model, even along the J-K and J'-Γ lines the bands close to the Fermi level show almost no dispersion. For the J'-Γ line there is even a band located roughly on top of the Fermi level along the entire line. This partially filled band has mainly a p_z orbital character and can be traced back to the Ge atoms of the surface Pt-Ge dimers bound to the NW dimers, making them responsible for the experimentally observed confined states between the NWs in the NW patches. [27, 90]

The two crossing bands just above the Fermi level along the J-K line, also seen for the NW1-model, have a slightly different character now. For the NW2-model the orbital character is dominated by the contribution of the extra Pt atom in the trough (Pt 11 in Fig. 4.19b), the two Pt atoms in the top layer bound to this Pt atom (both Pt 7 in Fig. 4.19b) and the Ge atoms forming a Pt-Ge dimer with the previous two Pt atoms (both Ge 2 in Fig. 4.19b). All these atoms give a strong z -oriented orbital contribution to these bands, showing the presence of a conduction band just above the Fermi level directed perpendicular to the NWs, but more importantly, connecting

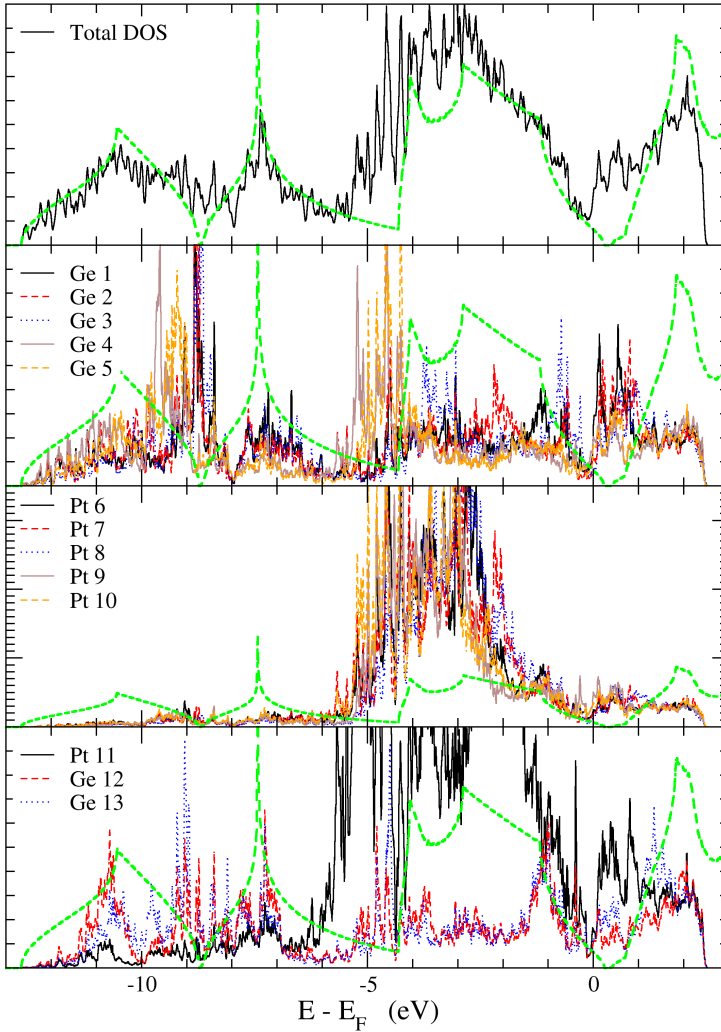


Figure 4.22: Total DOS of the NW2 structure and LDOS of the surface atoms as shown in Fig. 4.19b. The bold dashed green line shows the DOS of Bulk Ge, it was shifted to align the BG regions.

two sides of a NW, making the electronic structure of a NW patch 2D. The character of this band is even maintained along the Γ -J line, where it is located just below the Fermi level. This shows that NW patches are not purely 1D systems, but also contain a 2D (in plane) component, in contrast with the solitary NWs.

Figure 4.22 shows the total DOS of the NW2-model and the LDOS of the surface atoms as indicated in Fig. 4.19. The total DOS is nearly identical to the one found

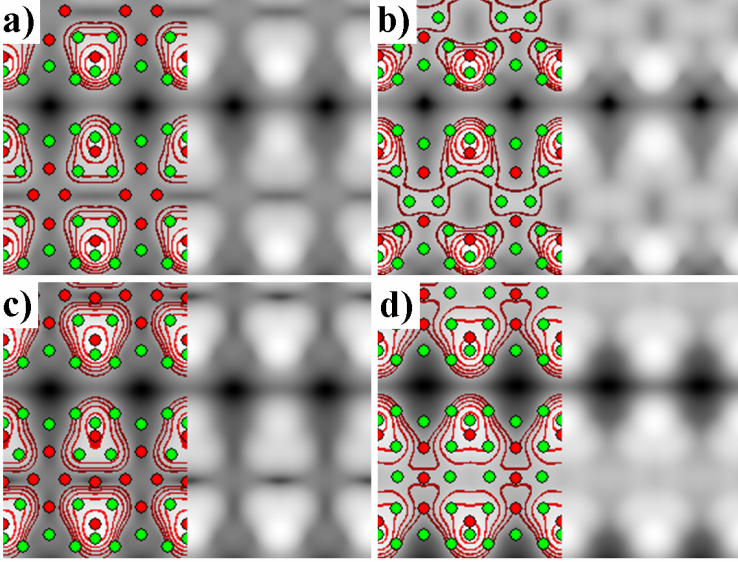


Figure 4.23: Calculated filled state STM images of some WT geometries indicated in Fig. 4.17, for $z = 3.0 \text{ \AA}$ and a simulated bias of -0.70 V . The green/red discs show the positions of Ge/Pt atoms in the two top layers of the surface and the adsorbed structure. Contours are added to guide the eye and are spaced 0.2 \AA in the z -direction.

a) $\gamma_{as2} + \text{Pt NW}$, b) $\gamma_{as2}^* + \text{Ge NW}$, c) $\gamma_{as2} + 3\text{Pt atoms in the trough}$, d) $\gamma_{as2}^* + 1\text{Pt at T} + \text{Ge NW}$.

for the NW1-model, with extra states around -5 and -9 eV . These states can be attributed to the Pt and the second layer Ge atom states for the first state at -5 eV , and surface Ge and Ge NW atom states for the second state at -9 eV . The main contribution to the states located in the bulk BG come from the Pt-Ge surface dimers, similar as was seen for the NW1-model. Also similar as to the NW1-model is the contribution of the Ge NW atoms, although in this case, the asymmetry in the geometry is also visible in the LDOS, resulting in small differences in the LDOS of the two inequivalent Ge NW atoms (*cf.* bottom part of Fig. 4.22). Although this LDOS does not show a BG, the LDOS of the NW atoms is significantly smaller than the LDOS of the Ge atoms in the Pt-Ge surface dimers, explaining the experimentally observed metallicity between the wires rather than on top of the wires. [18]

4.4.1.3 The WT geometry as precursor to NWs

In Sec. 5.3 it was already indicated that there are a few geometries of which the pseudo-STM images resemble the experimentally observed WTs (also indicated in Fig. 4.17) very well. Because the two proposed NW geometries require different WT structures and even multiple WT structures in a single formation path are present,

we will only look at the general properties shared by these WT geometries.

Comparison of the structures presenting a WT pseudo-STM image learns most have a γ_{as2} - (cf. Fig. 4.9) or the derived γ_{as2}^* -structure. The extremely tilted surface dimers cause the Ge atoms of those dimers to stick high out of the surface. This results in the $\times 2$ periodicity along the QDR. Also, because of this reconstruction the apparent trough in between becomes much deeper such that atoms and dimers located in this trough are not visible mainly due to the geometry. They sink in too deep. Fig. 4.23 shows filled state images of some WT geometries indicated in Fig. 4.17. The contours given show maxima directed away from the Pt lined trough giving the impression of a widening of the trough. However, small nuances are still clearly visible between the different structures. Troughs filled with Ge dimers or atoms seem to be more shallow than those filled only with Pt atoms and/or dimers. A bare γ_{as2} - and γ_{as2}^* -surfaces give pseudo-STM images comparable to Fig. 4.23a, but with even sharper peaks making the impression of the widening of the trough even stronger. The structures shown in Fig. 4.23 and the bare γ_{as2}^* -structure are all stable geometries with formation energies ranging from $E_f = -1.5$ eV to -3.5 eV. Since all of them have a place in the proposed NW formation paths, further high precision low temperature STM experiments might be needed to identify the nuances seen in the calculated STM images in Fig. 4.23.

4.4.2 Comparison to literature

At the moment of writing a few models for the NWs on Ge(001) are present. The first suggested with regard to this system was the one of Gürlü *et al.* in their experimental paper presenting this system. [18] In their model the entire reconstruction contained 0.5 ML of Pt atoms. 0.25 ML of Pt were imbedded in the top layer of the Ge(001) surface creating a checkerboard pattern of Ge-Ge and Pt-Ge dimers, called the β -terrace. The remaining 0.25 ML of Pt atoms formed Pt dimers which formed NWs in the troughs between the QDRs of Pt-Ge and Ge-Ge dimers. In **Sec. 4.3.2** the first models we calculated were based on this model. Despite the simplicity of this model and the successful prediction of the β -terrace model, we clearly showed in this work that this experimental model can not reproduce the experimentally observed STM images at all. This due to the unforeseen invisibility of the Pt atoms in the trough. In addition, the energetics for NWs on a β_6 geometry are shown to be very unfavorable.

More recently, Stekolnikov *et al.* published, almost simultaneously with the presenting authors, [98] a model where they propose a tetramer-dimer-chain (TDC) reconstruction for the studied system. [95, 99] Stekolnikov *et al.* present a careful DFT study of a set of Ge surfaces containing 0.25 ML of Pt. By comparing the formation energy of those structures and a comparison of calculated STM images with experimental STM images they conclude their TDC structure to represent the geometry of the observed NW arrays. Close examination of this structure, shown in figure 9 of Reference [99], shows it to be remarkably similar to the, in **Sec. 4.3.2** discussed, relaxed Ge $b(2 \times 1)$ T_{d1} structure. Figures 4.24a and b show the calcu-

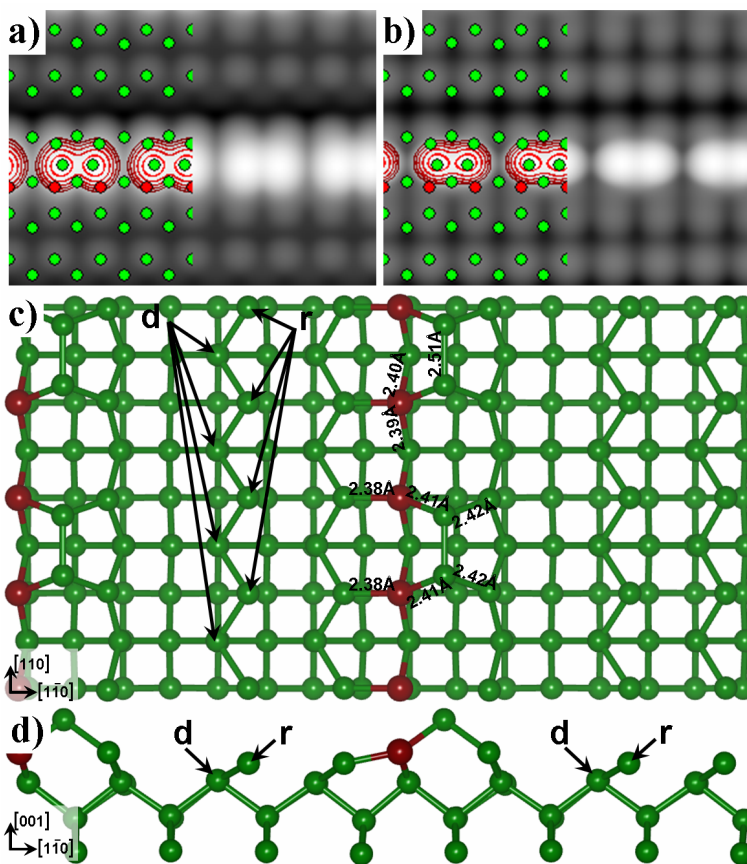


Figure 4.24: Calculated filled (a) and empty (b) state STM images of the Ge $b(2 \times 1)$ T_{1d} structure, for $z = 3.0 \text{ \AA}$ and a simulated bias of $\pm 1.50 \text{ V}$. The green/red discs show the positions of Ge/Pt atoms in the top layers of the surface and the adsorbed structure. The five highest contours are added to guide the eye. They are spaced 0.2 \AA in the z -direction.

c) and d) Top and side view of the Ge $b(2 \times 1)$ T_{1d} structure after relaxation, for comparison to figure 9 in Reference [99]. r and d indicate the Ge atoms that need to **d**imerize or be **r**emoved to have the TDC structure proposed by Stekolnikov *et al.* [99] Important bond lengths are shown.

lated filled and empty state images of our Ge $b(2 \times 1)$ T_{d1} structure. As noted by Stekolnikov *et al.* a dimerised NW image is visible. However, as already noted in **Sec. 4.3.2**, this image shows a double peak feature for both a positive and negative bias (also visible in both left columns of figure 10 of Reference [99]), in contradiction to the experimentally observed NWs. Furthermore, the stability of this system is unfavorable compared to a normal β_{6u} -surface reconstruction (which also contains

0.25 ML of Pt) by almost half an electronvolt per surface unit cell. We find the formation energy of the Ge $b(2 \times 1)$ T_{d1} structure to be roughly 2 eV more stable than for a structure with a Pt dimer on a Ge dimer row (*cf.* Table 4.1), in agreement with the observation of Stekolnikov *et al.* Figures 4.24c and d show ball and stick images of the Ge $b(2 \times 1)$ T_{d1} structure after reconstruction, indicating the necessary modifications needed to obtain the TDC structure of Stekolnikov *et al.* Bond lengths are given for comparison with figure 9 in Reference [99]. The differences between the bond lengths are of the order of 2 – 5%, what could be expected when comparing LDA and GGA calculations.

When the possible local Pt density of the NW system has to be limited to only 0.25 ML of Pt, then this model probably gives the best agreement to the experimental STM images one can get. However quite some problems remain. The unfavorable formation energy, *i.e.* the fact that this structure is less stable than a normal reconstructed Ge(001) surface, being the most unsettling one from the theoretical computational point of view. As can be seen in Fig. 4.2, the experimentally observed NW is located at the center of the trough between two QDRs, where in the TDC model proposed by Stekolnikov *et al.* only at one side a QDR is present. Furthermore, the fact that only partial agreement (*e.g.* symmetric bulges are missing and empty state pictures show double peaked NW dimer images in contrast to the experimental STM images) between experimental and calculated STM images is found also indicates this model not to be fully correct.

Expansion to local Pt densities beyond 0.25 ML is necessary to come to full agreement with the experiment, as we show in this paper. The experimental observation that after the deposition and annealing process a fraction of the surface is covered by β -terraces and a fraction of the β -terraces is covered with NWs combined with the model suggested for the β -terrace which already contains 0.25 ML of Pt further validates the expansion into larger local Pt densities.

4.5 Conclusions

We have studied a large number of Pt modified Ge(001) surfaces, with Pt densities varying from 0.25 ML up to 1.0 ML, using *ab initio* DFT calculations. Starting from simple structures with adsorbed Pt atoms and dimers on a clean Ge(001)- or β_{6u} -surface, based on the experimental observations and previous work, it was shown that these structures could not be responsible for the experimentally observed NW arrays. These calculations showed it to be unlikely for Pt dimers to form the observed wires due to the generally unfavorable energetics and the large discrepancy between calculated and experimental STM images. However, the calculated STM images indicated that Ge atoms might be responsible for the observed NW images.

In a second set of models, both Pt and Ge dimers were adsorbed on a surface reconstruction containing 0.5 ML of Pt in the top layer. For these structures the energetics were favorable and in case of the Ge dimers also a NW image was seen in the calculated STM images. It was found that Pt dimers sink into the trough, and the possibility of Pt atoms exchanging their position with the Ge atoms located at

the bottom of the trough led to a third set of models.

The reconstructed surface for these models contained 0.75 ML of Pt in the top layers. Again, both Pt and Ge dimers were adsorbed on these γ_{as}^* - and γ_{as2}^* -surfaces. The energetics of these structures are very favorable, and the calculated STM images for the Ge NW on γ_{as}^* (a.k.a. NW1) show very good agreement with the experimentally observed NWs.

However, one detail is still missing at this point: the experimentally observed 4×1 periodicity along the wires in NW-patches. To study this 4×1 periodicity, the obtained NW1 structure is modified to contain extra Pt or Ge atoms in trough with the wire. It is found that one extra Pt atom per two surface unit cells is sufficient to introduce the observed 4×1 periodicity. The extra Pt atom binds to two Ge NW dimers, fixing the position of both NW dimers and tilting them to create the observed 4×1 periodicity. This model for the NWs is named NW2.

Reviewing the calculated structures we propose a formation path for the formation of NW arrays on Ge(001) as a function of the local Pt density. In this formation path, the experimentally observed WTs are linked to the $\gamma_{as2}^{(*)}$ reconstruction. Furthermore, we conclude that the geometry of NWs inside a NW-patch is slightly different from that of the solitary NWs and the NWs at the edge of a NW-patch, as a result of a slightly different local Pt density. We propose the NW1-geometry as model for the solitary and patch-edge NWs, and the NW2-geometry as model for the NWs inside a NW patch. This most interestingly provides models, for the experimentally observed ‘platinum nanowires’, containing Pt induced *germanium nanowires*.

Finally, we make a comparison of the models present in literature and show their relation to the Pt-density dependent formation path and the NW models proposed in this paper.

Acknowledgements

We thank Harold Zandvliet and Arie van Houselt for making their experimental STM results available and for the many stimulating discussions on this topic. This work is part of the research program of the “Stichting voor Fundamenteel Onderzoek der Materie” (FOM) and the use of supercomputer facilities was sponsored by the “Stichting Nationale Computer Faciliteiten” (NCF), both financially supported by the “Nederlandse Organisatie voor Wetenschappelijk Onderzoek” (NWO).

Chapter 5

Adsorption of CO on Pt induced Ge nanowires.

It doesn't matter how beautiful your theory is, it doesn't matter how smart you are. If it doesn't agree with experiment, it's wrong.

– Richard P. Feynman

Using density functional theory, we investigate the possible adsorption sites of CO molecules on the recently discovered Pt induced Ge nanowires on Ge(001). Calculated STM images are compared to experimental STM images to identify the experimentally observed adsorption sites. The CO molecules are found to adsorb preferably onto the Pt atoms between the Ge NW dimer segments. This adsorption site places the CO in between two NW dimers, pushing them outward, blocking the nearest equivalent adsorption sites. This explains the observed long-rang repulsive interaction between CO molecules on these Pt induced nanowires.

5.1 Introduction

In the last several decades, CO adsorption on Pt surfaces has been studied extensively both experimentally and theoretically. This large interest is partly due to the deceiving simplicity of the system and its industrial importance in catalytic processes, such as CO oxidation and Fischer-Tropsch synthesis. [100, 101]

However, a simple system such as CO adsorbed on the Pt(111)-surface, has and still does cause quite some controversy. Three decades ago adsorption site preference and measured adsorption energies were the subject of discussion among experimental researchers. These problems have meanwhile been resolved and experimental results have converged to a coherent and detailed picture of this system. [102–106] On the theorists side however, a discussion has emerged during the last decade regarding the unexpected failure of prevalent DFT approximations to properly predict

the CO/Pt(111) site preference. From experiments it is found that the ontop site is most stable in the low density regime, while LDA and GGA calculations show a preference for the threefold coordinated hollow adsorption site. The cause of this CO/Pt(111) puzzle seems to originate from the tendency of LDA and GGA to favor higher coordination and the flatness of the potential surface describing adsorption of CO on the Pt(111) surface. [107] This has led to a search for better or alternative functionals in recent years. [108, 109]

Although the incorrect site prediction is a problem for DFT, this does not mean that the obtained geometries and derived physical properties are incorrect. [110] Even more, the calculated STM images derived from the geometries show excellent qualitative agreement with the experiment. [65, 66]

With the recent discovery of Pt induced NW arrays on Ge(001), a new Pt based adsorption surface becomes available. [18] Decoration of these NWs with CO-molecules opens the way to the formation of 1D molecular chains. Although the adsorption of single CO-molecules on these Pt induced NWs has been observed experimentally, true molecular chains remain to be observed. [31, 32]

Room temperature STM experiments, by Öncel *et al.* [31], showed the CO molecules to be very mobile along the NWs. Later, Kockmann *et al.* performed experiments at 70 K to suppress this mobility, and observed a long range repulsive interaction between pairs of CO molecules on a NW. [32] In those experiments the NWs were considered to be composed of Pt dimers in the troughs of a modified Ge(001) surface, called β -terrace, [18] allowing for a straight forward interpretation of the observed STM images. The CO molecules were suggested to be adsorbed on the bridge positions of the NW dimers, comparable to the adsorption of CO on the Pt(001) surface. [31, 32]

Calculations on the interaction of CO with a free standing Pt monatomic wire suggest a similar behavior. [111] However, in **Chapter 4** we showed the NWs to be modeled by Pt induced Ge NWs. In this model the NWs consist of Ge dimers placed in the Pt lined troughs of a Pt modified Ge(001) reconstructed surface. [98] Since the sticking probability and affinity for CO on Ge is known to be low, while being high for Pt, it would be surprising if CO molecules would adsorb on the Ge NW atoms. [112] This might lead to the suggestion that the theoretical models, proposed in **Chapter 4**, are in disagreement with the experiment. How can this theoretical model be reconciled with the experimental observations?

In this chapter we study the adsorption of CO on the Pt induced NWs starting from the theoretical models we proposed previously in **Chapter 4**. [98] Using *ab initio* DFT calculations, formation and adsorption energies are calculated. Theoretical STM images, generated using the Tersoff-Hamann method, are compared to experimental STM images to identify the adsorption sites and geometries observed in experiment.

This chapter is structured as follows: In **Sec. 5.2** the used theoretical methods are described. In **Sec. 5.3** we present our results, which will be discussed more in depth in **Sec. 5.4**. Finally, in **Sec. 5.5** the conclusions are given.

5.2 Theoretical method

The calculations are performed within the DFT framework using the PAW method and the CA LDA functional,¹ as implemented in the VASP program. [33, 34, 85, 86] A 400 eV kinetic energy cutoff is applied for the plane wave basis set. CO molecules are placed on the models of both types of Pt induced nanowires on Ge(001) we presented in **Chapter 4**. [98] The surface/NW system is modeled by periodically repeated slabs of 12 layers of Ge atoms with NW reconstructions on both surfaces. A vacuum region of ~ 15.5 Å is used to separate the periodic images of the slab along the z axis. Due to the computational cost and the small size of the CO molecule a (2×4) surface cell for the solitary wire geometry, and a (4×4) surface cell for the array wire geometry is used. The BZ of the (2×4) ((4×4)) surface unit cell is sampled using a 8×4 (4×4) Monkhorst-Pack special k -point mesh. [87] To optimize the geometry of the surface/adsorbate system the conjugate gradient method is used while the positions of the Ge atoms in the center two layers are kept fixed as to represent the bulk of the system.

STM images are calculated using the Tersoff-Hamann method in its most basic form, with the STM tip approximated as a point-source. [68] The integrated LDOS is calculated as $\bar{\rho}(\mathbf{r}, \varepsilon) \propto \int_{\varepsilon}^{\varepsilon_F} \rho(\mathbf{r}, \varepsilon') d\varepsilon'$, with ε_F the fermi energy. Because the tunneling current is proportional to the integrated LDOS in the Tersoff-Hamann model, an STM-tip following a surface of constant current can be simulated through plotting a surface of constant (theoretical) LDOS: $\bar{\rho}(x, y, z, \varepsilon) = C$, with C a constant. For each C this construction returns a height z as a function of the position (x, y) . This heightmap is then mapped linearly onto a gray scale. The constant C is chosen such that the isosurface has a height z between 2 and 3 Å above the highest atom of the surface.

5.3 Results

As is shown in literature, a small difference exists between solitary NWs (NW1) and NWs in arrays (NW2).² In experiment this difference presents itself as the appearance of a (4×1) periodicity at lower temperatures, which was traced back, in **Chapter 4**, to the presence of an extra Pt atom bound to every pair of NW dimers. [26] Since this extra Pt atom introduces new possible adsorption sites and geometries, CO adsorption on both NW geometries is studied.

Because some of the initial adsorption geometries relaxed into the same final structure, and because in some cases the geometry was modified extensively during relaxation, the adsorption sites presented in this manuscript are those found after

¹A comparison of LDA and GGA results is presented in **Appendix C.4**.

²The NW at the edge of a NW array next to bare β -terrace, just like a solitary NW, does not present the 4×1 periodicity typical for NWs in a NW-array. It was argued in **Chapter 4** that these edge NWs might have the same geometry as the solitary NWs. The latter could be understood to be an extreme case of a NW array, *i.e.* one only consisting of its edge. Because of this, we will refer to both solitary and edge NWs as solitary NWs, while array NWs refers to the none-edge NWs of a NW array.

relaxation.

The NW geometry is a metastable configuration and the adsorption of CO sometimes introduces large deformations of the surface. Therefore we define both a formation and adsorption energy in these systems. The formation energy E_f indicates the energy gain/loss of the entire system due to the CO adsorption and the subsequent changes in the surface structure. It is defined (per (4×2) -surface unit cell) as:

$$E_f = (E_{\text{NW+CO}} - E_{\text{pristNW}} - N_{\text{CO}}E_{\text{CO}})/2, \quad (5.1)$$

with $E_{\text{NW+CO}}$ the total energy of the adsorbate-surface system, E_{pristNW} the total energy of a pristine slab-NW system and E_{CO} the total energy of a free CO molecule. N_{CO} is the number of CO molecules per surface unit in the system and the division by two is because CO is adsorbed at both faces of the slab. A negative value of the formation energy E_f indicates an increase in stability of the system. The adsorption energy E_{ad} refers to the binding energy of the CO molecule to the surface. Here any contribution due to surface deformation is excluded. It is defined (per CO molecule) as:

$$E_{ad} = (E_{\text{NW+CO}} - E_{\text{NW+sd}} - N_{\text{CO}}E_{\text{CO}})/(2N_{\text{CO}}), \quad (5.2)$$

with $E_{\text{NW+sd}}$ the total energy of the surface with the adsorption induced deformations and without adsorbed CO molecule.

5.3.1 CO on solitary NWs

Solitary NWs consist of Ge dimers located in the Pt lined troughs of a Pt modified Ge(001) surface. Figure 5.1a shows the adsorption sites studied for this NW1 surface reconstruction. The adsorption and formation energies are given in Table 5.1, as are some geometrical parameters, defined in Fig. 5.1c, for the CO molecule on the surface. The dimer length r_{CO} of a free CO molecule was calculated to be 1.1330 Å, in good agreement with the experimental value. [113] Table 5.1 shows the CO bond lengths are only slightly stretched 1.59 – 1.85%, the one exception being CO adsorbed in the A3 configurations where the stretching is 13.95% and 7.15%. The difference between these last two configurations and the other configurations is the extra bond of the O atom with one of the surface atoms. In case of the A3a configuration the O atom has an extra bond with a Ge dimer atom (*cf.* Fig. 5.2a), while in the A3b configuration it is bound to a Pt atom of the top layer at the opposite side of the trough (*cf.* Fig. 5.2b). Another interesting geometrical feature is that in most cases the adsorbed CO molecule is tilted with regard to the surface, unlike the behavior of CO molecules on clean Pt surfaces. In case of CO adsorbed on top of Pt atoms, the C-Pt bond length is just slightly longer than what is found for CO on Pt(111) in an ontop configuration. [100, 114] The adsorption energies given in Table 5.1 show a very clear preference for CO adsorption on Pt (sites A1–A4). The values of E_{ad} might indicate that CO also binds weakly to the Ge NW atoms (sites A5 and A6), contrary to the experimental knowledge that CO does not bind to Ge. However, one needs to bare in mind that LDA tends to overbind, which in this case results in the small adsorption energies. Furthermore, the binding energies of CO on

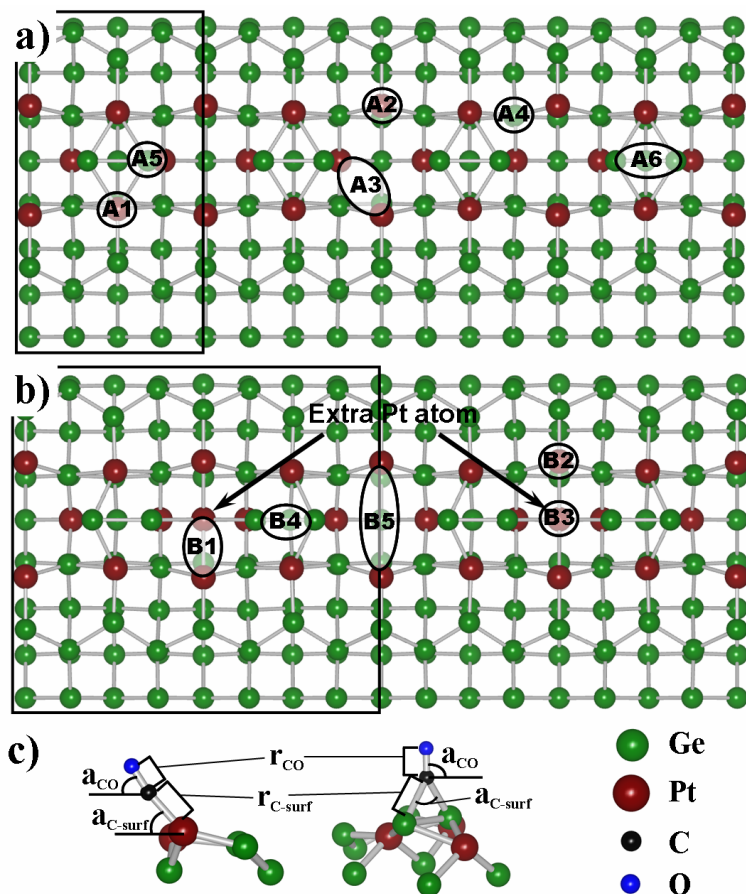


Figure 5.1: Adsorption sites of CO on a solitary NW geometry (a) and an array NW geometry (b). Green (red) balls indicate the positions of the germanium (platinum) atoms. Black rectangles indicate surface unit cells.

Ge are $E_{ad} \cong 0.5$ eV, while $E_{ad} \cong 2.0$ eV for CO adsorbed on Pt atoms, making the latter much more preferable.

The A3-structures are a bit peculiar, and, as we will show later, the A3a-structure results in calculated STM images that show extremely good agreement with the STM images obtained by Öncel *et al.* [31] Both A3-structures have a bridge like adsorption geometry (*cf.* Fig. 5.2) but their adsorption energies differ more than 1 eV, making them the best and worst cases for CO adsorbed on the Pt atoms in this system. The most important contribution to the adsorption energy in this system comes from the CO bond-stretching. To examine the effects of this bond stretching, one can use a modified version of Eq. (5.2), using the formation energy of a CO molecule with the same bond length as the adsorbed molecule, instead of the formation energy of a re-

Adsorption energies and geometrical parameters for CO on NW1.

	E_f (eV)	E_{ad} (eV)	coord.	r_{CO} (Å)	α_{CO} (°)	r_{C-surf} (Å)	α_{C-surf} (°)
NW1 A1	-1.300	-1.747	t	1.152	88	1.906	86
NW1 A2	-1.721	-1.990	t	1.154	57	1.920	48
NW1 A3 a	-1.156	-0.993	b	1.291	56	2.246 (2.150)	117
NW1 A3 b	-1.485	-2.069	b	1.214	47	2.012 (2.066)	101
NW1 A4	-2.859	-1.890	t	1.152	63	1.907	62
NW1 A5	-1.421	-0.439	t	1.151	70	2.015	70
NW1 A6	-0.349	-0.557	b	1.162	88	2.192	75

Table 5.1: Formation and adsorption energies for CO adsorbed on the NW1-surface. Adsorption sites are shown in Fig. 5.1a. *t* (*b*) refers to top (bridge) adsorption. r_{CO} and r_{C-surf} are the C-O and C-Pt(Ge) bond lengths. For the A3 adsorption site the value between brackets is the C-Pt bond length between C and the Pt atom in the bottom of the trough. α_{CO} and α_{C-surf} are the bond angles with regard to the surface plane. In case of bridge adsorption α_{C-surf} is the angle between the two C-surface bonds. For the adsorption sites A1 to A4, the C atom is bound to surface Pt atoms, for the sites A5 and A6 the C atom is bound to Ge NW atoms.

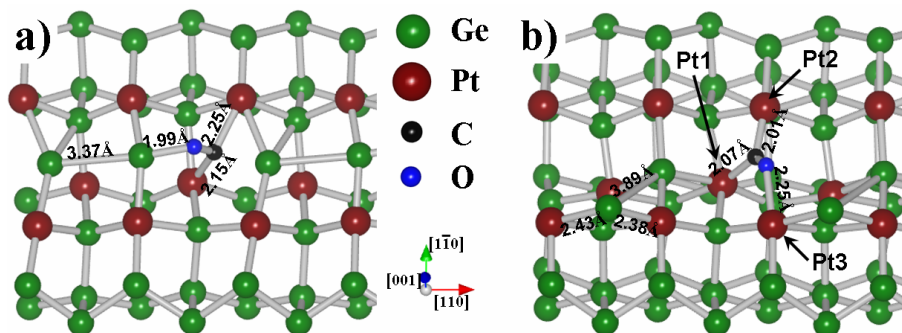


Figure 5.2: Ball-and-stick representations of the relaxed A3a (a) and A3b (b) adsorption structures.

laxed gas molecule. The resulting energy could then be considered the energy needed to desorb the molecule from the surface in a two step fashion. First the bond(s) to the surface atoms are broken while the CO bond length remains unchanged. Then the molecule moves away from the surface relaxing to its equilibrium bond length. Since most adsorption geometries show only slightly stretched CO molecules, this energy only differs a little (~ 50 meV) from E_{ad} . However, for the strongly stretched

CO on the $4 \times \text{NW1}$ surface cell.

	A1	A2	A3b	A4	A5	A6
E_f (eV)	-3.60	-3.58	-5.56	-2.72	-0.78	-1.35
E_{ad} (eV)	-1.94	-2.11	-2.00	-1.94	-0.67	-0.39

Table 5.2: Adsorption and formation energies for the adsorption of one CO molecule per four NW dimers.

A3-geometries a large difference with regard to E_{ad} is seen: -2.010 eV and -2.384 eV for the A3a- and A3b-structures respectively. This means that a CO molecule at an A3-site becomes the hardest to desorb from the surface using the path described above.

The somewhat peculiar adsorption geometry in case of the A3b-site can be understood when it is compared to the adsorption of CO on a monatomic Pt wire. In their theoretical study, Sclauzero *et al.* [111] found that for an intermediate inter-platinum-distance of $3.7\text{--}5.3$ Å a configuration with the CO molecule bridging the gap between two Pt atoms is the most stable configuration, while for an inter-platinum-distance around 2.50 Å the bridge configuration, with the C atom bound to two Pt atoms, was found to be most favorable. In the A3b-situation three Pt atoms are involved. Two (Pt1 and Pt2) are bound to the C atom and one (Pt3) is bound to the O atom. The distance between Pt1 and Pt2 is 3.145 Å, while the distance between Pt1 and Pt3, and Pt2 and Pt3 is 3.958 and 5.008 Å respectively. Both the latter values are nicely in the intermediate range for the bridging configuration, while the former lies in the range where a simple bridge configuration was found most stable by Sclauzero *et al.*

From Eqs. 5.1 and 5.2 follows that the energy due to the surface deformation induced by the adsorption of a CO molecule is given by: $E_{sd} = E_f - E_{ad}$. Positive values of E_{sd} indicate a destabilization due to the adsorbed CO molecule (A1, A2, A3b, and A6), while negative values indicate a stabilization (A3a, A4, and A5). In **Chapter 4** we showed the NW1-geometry to be a metastable configuration, and we also showed the adsorption configuration with the Ge NW dimer bound to four surface dimers (site C in Fig. 4.11a) to have a more favorable formation energy than the NW1 structure (*cf.* Table 4.3, compare γ_{as}^* Ge NW A (NW1) to γ_{as}^* Ge NW C). This explains the increased surface stability seen for CO adsorption sites A3a, A4 and A5. From the large differences between the adsorption and formation energies, and, as can be seen for example in Fig. 5.2, follows that adsorption of CO on the NW1-system has a large influence on the geometry of the wire. Because the range of the (destructive) influence of a CO molecule on the wire is larger than the size of the used surface cell, some calculations are carried out using a surface cell $4 \times$ the unit cell length. Only a single CO molecule is absorbed on it, effectively reducing the CO density by a factor of four. Since the relaxation of such a huge cell is computational very demanding, lower accuracy relaxation parameters are used. E_f and E_{ad} are given in Table 5.2 showing even more clearly the effect of the CO molecule on the NW1 geometry

Adsorption energies and geometrical parameters for CO on NW2.

	E_f (eV)	E_{ad} (eV)	coord.	r_{CO} (Å)	a_{CO} (°)	r_{C-surf} (Å)	a_{C-surf} (°)
NW2 B1	-1.424	-2.336	b	1.171	76	2.086 (2.004)	82
NW2 B2	-0.761	-1.911	t	1.154	77	1.911	74
NW2 B3	-1.033	-2.090	t	1.155	90	1.868	90
NW2 B5	-0.784	-2.197	t	1.170	20	1.883	28
NW2 B4	-0.319	-0.916	b	1.163	62	2.003 (2.411)	72

Table 5.3: Formation and adsorption energies for CO adsorbed on the NW2 surface. Adsorption sites are shown in Fig. 5.1b. t (b) refers to top (bridge) adsorption. In case of the B5 adsorption site, the C atom is bound to only one Pt atom, however, the O is bound to the Pt atom at the opposite side of the trough resulting in the entire CO molecule forming a bridge. r_{CO} and r_{C-surf} are the C-O and C-Pt(Ge) bond lengths. a_{CO} and a_{C-surf} are the bond angles with regard to the surface plane. For the B1 adsorption site the value between brackets is the C-Pt bond length between C and the Pt atom at the bottom of the trough. For the B4 adsorption site the value between brackets is the C-Ge bond length to the Ge atom bound to the extra Pt atom in the trough. In case of bridge adsorption a_{C-surf} is the angle between the two C-surface bonds. Only for the B4 site C is bound to Ge NW atoms, in all other cases C is bound to a Pt atom in the surface.

The large differences between E_f and E_{ad} again indicate large modifications of the NW1-structure. Comparing the relaxed geometries, we find that for larger differences between E_f and E_{ad} , more NW dimers are displaced or destroyed. In case of the A3b-structure even all four NW dimers are somehow modified. This behavior might be the basis of the experimentally observed long-ranged repulsive interaction between CO molecules. [32] We will look into this in more detail in **Sec. 5.4**.

5.3.2 CO on NW-arrays

In **Chapter 4** it was shown that the NWs in NW-arrays only differ very little from solitary NWs: a single extra Pt atom in the NW trough for every two NW1 unit cells. This extra Pt atom (indicated in Fig. 5.1b) binds to two NW dimers, inducing the observed 4×1 periodicity. This extra bond also stabilizes the NW, as was shown in **Chapter 4**. [115] Through its construction, the unit cell of a NW2 surface is twice the size of that of the NW1 surface and since we only adsorb 1 CO molecule per surface, this effectively halves the CO-coverage compared to that on the NW1 system. Figure 5.2b shows the adsorption sites of CO on the NW2 4×4

surface cell after relaxation of the system.³ Only the adsorption sites different from those already present in the NW1-geometry, *i.e.* those where the extra Pt atom is involved directly or indirectly, are investigated. Our observations for the adsorption sites on the NW1-surface are assumed to be also valid for the equivalent sites on the NW2-surface.

The adsorption energies per CO molecule and the formation energies per 4×2 surface cell are shown in Table 5.3. Just as for the the CO molecules adsorbed on Ge in the NW1 case, CO molecules adsorbed on Ge in the NW2 case have a much lower binding energy than CO molecules bound to Pt atoms, indicating the strong preference of CO toward Pt. The adsorption energies for CO molecules on the Pt atoms are in the same range as for the NW1-system, albeit slightly higher on average. This might be due to the lower CO coverage in the NW2-systems, reducing the direct and indirect interaction between the CO molecules. The A2 and B2 adsorption sites, on the NW1- and NW2-geometries respectively, differ only by the presence of the extra Pt atom, resulting in comparable adsorption energies. However, the presence of the extra Pt atom in case of the NW2-system prevents the CO molecule of bending far toward the surface, increasing the angle $\mathbf{a}_{\text{C-surf}}$ from 48° to 74° . In case of the B5-site, where no extra Pt atom is present in the trough, the CO molecule bends very much toward the surface and actually bridges the through connecting two Pt atoms at opposing sides of the trough.

The distance between these Pt atoms is 4.826 \AA , placing them in the regime where Sclauzero *et al.* [111] found a “*tilted bridge*” configuration to be the energetically preferred configuration. In their study of CO adsorption on a freestanding monatomic Pt wire, Sclauzero *et al.* identified 3 regimes for the CO adsorption geometry. i) For an unstretched (with Pt-Pt bond length $d_{\text{Pt-Pt}} = 2.34 \text{ \AA}$) freestanding Pt wire, the bridge configuration was found to be favored with respect to the ontop configuration by about 1 eV. The energy of the bridge configuration was shown to have a minimum for a value for $d_{\text{Pt-Pt}} = 2.50 \text{ \AA}$ just slightly above the equilibrium Pt bond length of the chain. We will refer to this as the unstretched regime. ii) In case of a hyperstretched configuration an energy minimum was found at $d_{\text{Pt-Pt}} = 5.05 \text{ \AA}$. In this case the substitutional geometry was found to be more favorable than the bridge configuration. In the substitutional configuration the CO molecule is aligned parallel with the Pt wire, and the C and O atom are bound each to a half of the Pt wire. iii) However, Sclauzero and his collaborators found the energy minimum of the substitutional geometry to be still slightly higher than the tilted bridge configuration. In this tilted bridge configuration the CO bond lies in a plane trough the wire, but it is not aligned parallel or orthogonal to the wire. Although no energy minimum for this configuration was found, Sclauzero *et al.* found it to be preferred over the bridge and substitutional configuration for intermediate stretching lengths of the Pt-Pt distance (about $3.8 \text{ \AA} \leq d_{\text{Pt-Pt}} \leq 5.1 \text{ \AA}$).

Although the monatomic wire studied by Sclauzero *et al.* are quite different from our current system, the inter-platinum-distances are comparable. Even more, in case of the NW2-geometry there are three Pt atoms (two on opposing sides of the trough,

³Two surface unit cells are shown in Fig. 5.2b.

and the extra Pt atom in the trough) forming a mini monatomic wire spanning the trough, with three inequivalent adsorption sites located on it.

The adsorption site with the highest binding energy of all adsorption sites studied is the B1-site. In this case the CO molecule binds to two Pt atoms through a bridge configuration. The distance between the two Pt atoms is 2.682 Å, slightly longer than the optimum inter-platinum-distance for a CO molecule adsorbed in a bridge configuration on a monatomic freestanding Pt wire. The B2- and B3-sites have an atop configuration, and are 0.43 eV and 0.25 eV lower in adsorption energy. This shows a nice qualitative agreement between the 3-atom monatomic Pt wire present in the NW2-system and a freestanding monatomic Pt wire. For all adsorption sites studied on the NW2-surface, the CO bond lengths are only stretched slightly, 1.85 – 3.35%. Even more, comparing the values of r_{CO} and $r_{\text{C-surf}}$ with those found by Sclauzero *et al.* shows perfect agreement for the CO bond length, and just fractionally larger lengths for the C-Pt distances in our embedded 3-atom Pt wire. This slightly larger length is a simple consequence of the Pt atoms being embedded in the NW2-surface. The B3-site is the only site where the CO molecule is perfectly perpendicular to the surface, this is due to the symmetry of the chemical environment. In contrast, the B2 adsorption site has a lower symmetry and the molecule bends along the asymmetry direction toward the 3-atom monatomic Pt wire.

Contrary to CO adsorbed on the NW1-surface, CO adsorbed on the NW2-surface seems much less destructive. This is because the NW dimers are anchored at their position by the presence of the extra Pt atom. Only CO adsorbed at the B1- or B3-site modifies the NW significantly. In both cases, the CO molecule has a bond to the extra Pt atom, weakening the bonds with the NW dimers. Furthermore, just like for the NW1-surface, the CO molecules are positioned between the NW dimers, pushing them outward, away from the molecule. The combination of these two effects is large enough to break the bonds between the NW dimers and the extra Pt atom. Due to the periodic boundary conditions and the size of our unit cell, the two NW dimers recombine to form a tetramer-chain between the two copies of the CO molecule. Contrary to the NW1-surface, the free NW dimers will not be able to block the next equivalent adsorption site due to the presence of a NW dimer anchored in place by its accompanying extra Pt atom.

5.4 Discussion

The results from the previous section show no clear-cut image for the CO adsorption system based solely on calculated energies, which might already be suspected from the history of CO adsorption on pure Pt surfaces. However, direct comparison with experiment is possible by means of calculated STM images. This method has already been shown very successful at identifying correct adsorption sites for CO, even when the calculated energies fail to do so. [65, 66] At the moment of writing only very little experimental work is available, and the actual underlying NW type is not always entirely clear. The earliest experimental work on this system was done by Öncel *et al.* [31] This work presents the adsorption of CO molecules on NWs sep-

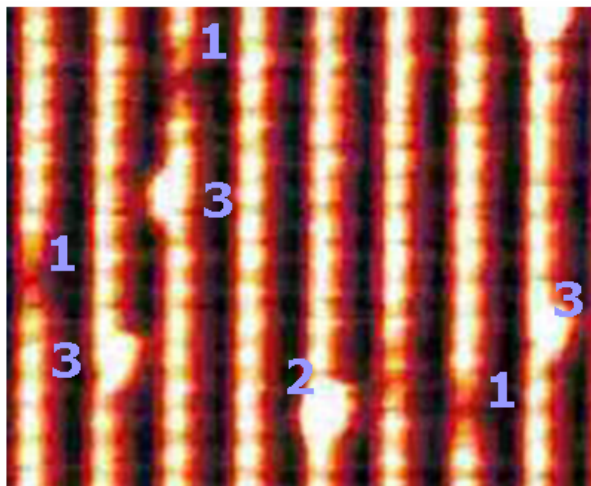


Figure 5.3: Zoom out of a section of figure 1 in Reference [32], an empty state STM image (+1.8 V; 0.5 nA) of CO-decorated NWs, recorded at 77 K. We have indicated three CO adsorption sites. Site 1 shows a large depression in the wire. Sites 2 and 3 show large protrusions. In case of site 2 nicely centered on the NW, while for site 3 the protrusion is centered either left or right of the NW.

arated 2.4 Å, which based on our previous calculations (*cf.* **Chapter 4**) leads to the assumption that these wires can be considered solitary NWs. In these experiments only one adsorption site was observed. It appears as a protrusion at negative bias, and as a depression at positive bias. Later work by Kockmann *et al.* [32], studied the adsorption of CO molecules on arrays of NWs spaced only 1.6 Å. Based upon the results presented in **Chapter 4**, we assume these wires to have a NW2-geometry. Unlike Öncel *et al.*, Kockmann and collaborators observed two adsorption sites, both different from the one observed by Öncel *et al.*

Based on this we will compare our results for solitary wires with the experiments of Öncel *et al.*, and those for array-NWs with the experiments of Kockmann *et al.*

5.4.1 CO adsorption on Pt induced nanowires

As reference images for the experiment we will use figure 2a and b in Reference [31] for the solitary NWs and figure 1 in Reference [32] for the NW arrays. Close examination of figure 1 in reference [32] shows three distinctly different adsorption sites, indicated in Fig. 5.3. Kockmann and collaborators on the contrary only identify two, considering sites 2 and 3 the same adsorption site. It is well known from literature that the electric field of the STM tip can influence the position and orientation of molecules adsorbed on a surface. [116] This can result in an extra broadening of the

CO image along the scan lines.⁴ This, however, can not cause the CO molecules at the adsorption site 2 in Fig. 5.3, to appear as site 3, since the latter is observed at both sides of the NW (*cf.* Fig. 5.3).

In addition to the formation and adsorption energies, STM images are calculated for all adsorption NW1-geometries. All NW1 CO-adsorption geometries show protrusions for both positive and negative simulated bias, with the exception of the A3a adsorption site. For the latter, a protrusion is visible in the filled state image (*cf.* Fig. 5.4c), while a depression is clearly present in the empty state image (*cf.* Fig. 5.4c). The comparable A3b-structure on the other hand shows a clear protrusion on the adjacent QDR for all biases (*cf.* Fig. 5.4e). However, this protrusion is not caused by the CO-molecule present, but by the Ge NW atom ejected from the trough instead (*cf.* Fig. 5.2b). Removal of this Ge atom removes the protrusion and only a brightened Pt-Ge dimer, bound to the O atom, remains (*cf.* Fig. 5.4f). The CO molecule itself remains invisible.

From all adsorbed CO molecules only those on the A3 sites and on the Ge NW, are located “on” the NW. However, these are not the only CO molecules resulting in a CO-image “on” the wire. Due to the large tilt angle of the CO molecule at the A2-site the resulting image gives the impression of a CO molecule sitting, just slightly asymmetric, on top of the NW, as can be seen in Fig. 5.4a and b. For large negative bias the image is round, while becoming more and more bean-shaped for smaller negative biases and all positive biases. CO molecules bound to Ge NW atoms show images which look bean-shaped for the A5 adsorption site, and two-lobbed donut-shaped for the A6 adsorption site.

Based on the adsorption energies found in **Sec. 5.3**, the adsorption of CO on the Ge NW dimers can be excluded. Only the Pt adsorption sites near the NWs remain. For the solitary NWs the A3b-site can be excluded because for both positive and negative bias a depression is found, which is not observed in the reporting experiments.

The sites A1, A2, and A4 show a comparable behavior. Both in the filled and empty state pictures a large protrusion is clearly visible, slightly asymmetric to the NW position. Figures 5.4a and b show an A2 adsorbed CO molecule as example. The A3a-site despite its low adsorption energy shows something interesting. The filled state picture shows a pear shaped image for the NW dimer (*cf.* Fig. 5.4c), just as was observed by Öncel *et al.*, and the empty state picture shows no NW dimer image (*cf.* Fig. 5.4d). Comparison to figures 2a and b in Reference [31] shows good agreement. Figure 5.5 shows linescans along the NW for the A3a adsorption site, in comparison to a pristine NW. Due to periodic boundary conditions and the fact that our unitcell only contains 1 NW dimer, this image can only be used to compare to the region $\sim 0.5 - \sim 1.5$ nm in figure 3 of Reference [31]. Note that the linescans in figure 3 of Reference [31] and Fig. 5.5 of this work are mirror images of each other (mirrored around the center of a NW dimer), indicating that the CO molecule was bound (the O-Ge bond) to the ‘left’ side of the NW dimer in experiment, while it is bound to the right side in our calculations (*cf.* Fig. 5.4c). For the linescan of the filled state pic-

⁴This means orthogonal to the NWs in the cited experimental pictures.

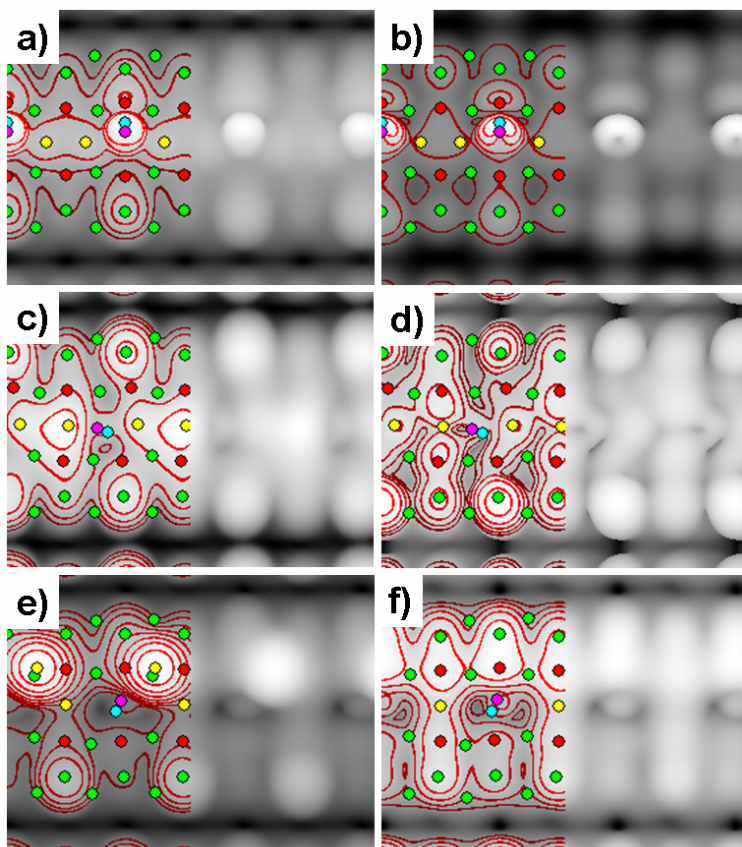


Figure 5.4: Calculated filled and empty state STM images for the A2 (filled (a) and empty (b)), A3a (filled (c) and empty (d)), A3b (filled (e)), and A3b1 (filled (f)) adsorption geometries. The simulated biases are for (a), (e), and (f) -1.50 V, (b) $+1.50$ V, (c) -0.70 V, (d) $+0.30$ V. Contours are added to guide the eye, they are separated 0.3 Å. Colored discs indicate atomic positions: green and red represent Ge and Pt atoms in the top two layers of the surface, yellow represent the Ge atoms forming the NW, and cyan and fuchsia represent the C and O atoms respectively.

ture, the asymmetric shape and the width of the protrusion match very well. There is also a good agreement between the linescans of the empty state pictures. Note that in both cases the two small peaks have a different height, with the highest peak at the lower side of protrusion in the filled state picture. Furthermore, comparison to the linescan of a pristine NW shows the maximum of the filled state protrusion to be located near the center of the dimer, giving the impression that the CO molecule is located on top of the NW dimer in a bridge configuration (compare to figure 6.1b in Reference [117]). Also the location of the larger of the two small protrusions,

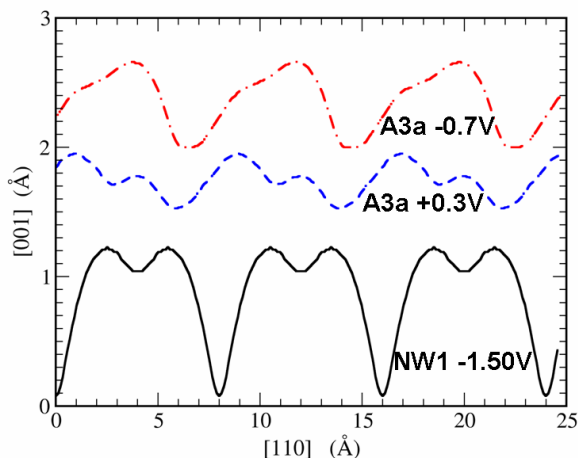


Figure 5.5: Linescan images along the NW for the clean NW at a simulated bias of -1.50 V (solid black curve), the CO molecule adsorbed at the A3a-site at a simulated bias of -0.70 V (dash-dotted red curve) and $+0.30$ V (dashed blue curve). For each system $z = 2.5$ Å is used to generate the calculated STM images from which the line scans are taken. The lines are shifted along the [001]-axis.

in the empty state picture linescan, at the minimum between two NW dimers is in excellent agreement with the experimental observations (see figure 6.2b in Reference [117]). This shows that a CO molecule in between two NW dimers, bound to one trough the O atom, can look like a molecule bound on top of a NW dimer. The low binding energy found here remains problematic. However, the fact that taking into account the stretching of the molecule returns an energy comparable and better than most of the other adsorption structures might indicate the energy barrier for desorption to play an important role. This also indicates that for RT experiments where a much lower CO density is present, reducing the contributions of direct and indirect interaction between CO molecules, this might not be as problematic. The good agreement of this structure with the experiment seems to support this idea.

Although Öncel *et al.* do not report observing any other adsorption sites, they do report the CO molecules to perform a 1D random walk along the NW. Since the A3a adsorption site does not easily allow for a CO molecule to just jump from one site to the next, some intermediate stable adsorption sites should be present to accommodate this mobility. Looking at the geometry of the relaxed structures a path can be imagined going from A3a to A2, by breaking the bond between the C atom and the Pt atom at the bottom of the trough and breaking the O-Ge bond. Rotation from the A2 to the A4 configuration and onto the A1 adsorption site, followed by the same path in reverse to the next A3a site. The binding energies of these three adsorption

sites (A1, A2 and A4) differs only little making it an energetically possible path at RT.⁵ These sites are also present on the NW2-surface, where the adsorption site B2 can be considered an alternative for the A2-site. The calculated STM pictures of the B2-site also show the same asymmetric protrusion in the filled and empty state pictures, while the adsorption energy (shown in Table 5.3) lies in the range of the three A-sites. Site 3 in Fig. 5.3 clearly shows such an asymmetric adsorption site. Although the resolution in Fig. 5.3 is not sufficient to distinguish between the four adsorption sites mentioned above, it is sufficient to indicate their existence.

The calculated STM images for the adsorption sites on the NW2-surface show quite a complex picture. For the B4-site, the most simple behavior is observed, both for the filled and empty state pictures, a round, slightly asymmetric CO image is seen, sticking out far above the surface and the NW. Conversely, a CO molecule at the B1-site shows a sharp round image which becomes smaller (even invisible) for biases close to the Fermi level (*cf.* Fig. 5.6a and b). CO at the B3 adsorption site, on the other hand, shows a nice round image for negative bias (*cf.* filled state picture in Fig. 5.6e), which becomes a two lobbed image for small positive bias but becomes invisible for large positive bias (*cf.* empty state picture in Fig. 5.6f). In each of the above cases the CO image appears nicely centered on the NW, which can be understood from the underlying geometry. In case of CO adsorbed at the B2-site the tilting of the molecule over the trough causes the CO image to appear only slightly shifted away from the center of the NW, giving the impression the CO molecule might be located on the wire itself (*cf.* Fig. 5.6c and d). Both the filled and empty state pictures show nice elliptical CO images for large biases, while close to the Fermi level the elliptical image becomes two-lobbed. As with all the previous cases where a donut or two-lobbed CO image was observed, this are the π -orbitals of the molecule that are being observed. [65]

The only remaining adsorption site is the B5-site. Here the CO molecule bridges the entire trough, so a serious modification of the calculated STM pictures might be expected. Amazingly, the calculated STM images show *nothing*. Both for filled and empty state pictures a normal NW image is observed, and not even the slightest indication of the CO molecules presence can be observed, making the CO molecule effectively *invisible*.

Figure 5.6 shows the calculated STM images for B1, B2, and B3 adsorbed CO molecules. When comparing these images with experimental STM images, there are a few things we need to keep in mind. i) The way the STM images were calculated. By using a point source as tip, almost infinitely sharp images are obtained, while in reality tip-size and geometry will influence the obtained STM image. This will mainly manifest itself in a broadening of the observed features (*cf.* **Appendix A.1**). ii) No dynamic tip-substrate interactions are included in the calculated STM images. Although for a clean surface the effect of the tip on the surface geometry is almost negligible, this is not the case for a molecule bound to the surface. [116] At low coverage, molecules retain a large freedom to move, even if their anchor point re-

⁵The computational cost to calculate diffusion barriers between these intermediate steps is, due to the system size, too large.

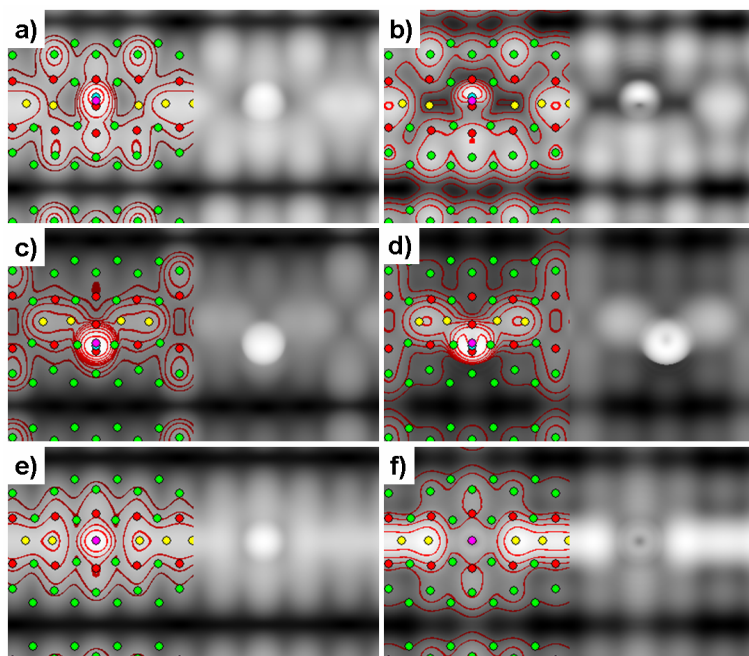


Figure 5.6: Calculated STM images of CO molecules adsorbed at the B1- (a and b), B2- (c and d) and B3-sites (e and f). The distance above the highest atom was chosen $z = 2.0 \text{ \AA}$. Filled state images (a), (c) and (e) are at a simulated bias of -1.80 V , while for the empty state images (d) and (f) a simulated bias of $+1.80 \text{ V}$ was used. For the empty state image (b) a simulated bias of $+1.50 \text{ V}$ was used. Contours are added to guide the eye. All contours are separated 0.2 \AA in the z direction. Colored discs indicate the atom positions in the top layers. Ge and Pt atoms in the two top layers are shown in green and red respectively. Yellow discs are used to indicate the Ge NW atoms, while cyan and fuchsia is used for the C and O atoms respectively.

mains fixed, resulting in a blurring of their observed STM image. iii) The position of the molecular orbitals, especially the states above the Fermi level are not that well described in DFT (this is the well known band gap problem). This means that it is not always possible to use the same simulated bias as the experimental one. Points i and ii explain why the CO images in Fig. 5.3 show up to be sometimes two dimers long with a width larger than that of the NW.

With this in mind, the three adsorption sites shown in Fig. 5.3 can be identified by comparing the calculated empty and filled state pictures to experimental STM pictures. Site 1 shows a depression in the empty state picture, centered between two NW dimers. The filled state pictures on the other hand show a small protrusion. [32] Figures 5.6e and f show the same behavior for the B3 adsorbed CO molecule. Its geometry, shown in Fig. 5.7c, shows the CO molecule bound in an on-top con-

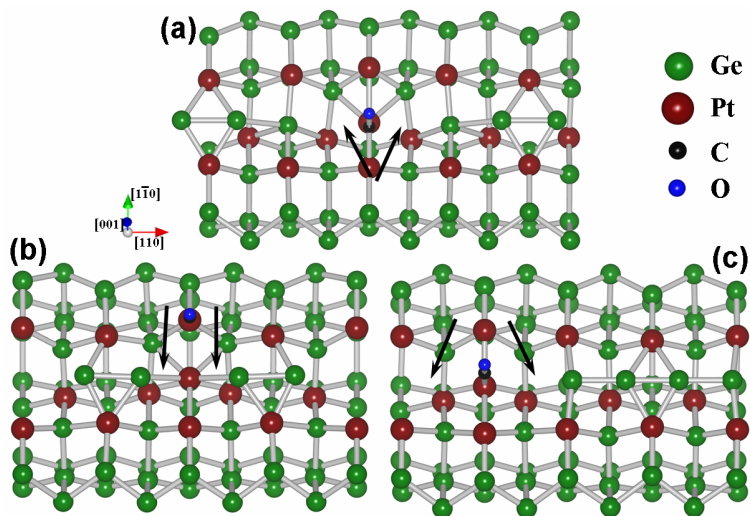


Figure 5.7: Ball-and-stick representation of the relaxed geometries of CO molecules adsorbed at sites B1 (a), B2 (b) and B3 (c). Arrows indicate broken bonds between the Ge NW atoms and the extra Pt atom for the B1 (a) and B3 (c) adsorption sites. For the B2 adsorption site (b) these bonds, indicated with the arrows, are not broken.

figuration to the extra Pt atom. This bond weakens the bonds between the extra Pt atom and the NW dimers, allowing for the presence of the CO molecule to break them entirely, pushing the two NW dimers away from the CO molecule. The limited size of the surface cell and the periodic boundary conditions results in the formation of a Ge tetramer, and a limitation of the length of the depression to roughly 5–6 Å. In experiment however the NW dimers could be pushed even further apart resulting in a large gap around the CO molecule, which explains the experimentally observed length of the depression to be roughly two dimer lengths. The lack of small depressions on either side of the CO molecule in the experimental filled state pictures can be understood as a consequence of the molecule-tip interactions mentioned earlier.

The second site seen in Fig. 5.3, shows a protrusion in both filled and empty state pictures. Figures 3a and b in Reference [32] also show that the relative height with regard to the NW is smaller in the empty state picture than in the filled state picture. This turns out to be in agreement with the images found for the B1 adsorbed CO molecule, see Fig. 5.6a and b. At this adsorption site the CO molecule is bound in a bridge configuration to the extra Pt atom and a Pt atom of the surface dimer row, see Fig. 5.7a. Again the bond with the extra Pt atom allows for the bonds between the NW dimers and the extra Pt atom to be broken, and the NW dimers to move away from the CO molecule resulting in a large gap around the CO molecule. Table 5.3 shows this bridge configuration to have the highest adsorption energy, in agreement with the *ab initio* calculations of Schlauzero *et al.* [111]

The third and last adsorption site indicated in Fig. 5.3 shows a clearly asymmetric protrusion in the empty states picture. Unfortunately no experimental filled state pictures have been published for this adsorption site, but based on all the other adsorption sites observed in experiment we will assume that also in this case a protrusion is observed in the filled state image. Figures 5.6c and d, show the filled and empty state pictures of a CO molecule adsorbed at site B2. This CO molecule is bound to a Pt atom in the surface dimer row, see Fig. 5.7b. Because it is tilted toward the NW, the resulting image appears just slightly asymmetric of the NW, making it a very good candidate for the adsorption site 3 indicated in Fig. 5.3. In combination with the adsorption sites A1, A2, and A4, this adsorption site gives a possible migration path for the mobility observed by Öncel *et al.* [31]

In their investigation of CO adsorption on the Pt induced NWs Kockmann *et al.* also observe a, what they call, *remarkably long-ranged repulsive interaction* between the CO molecules. This repulsion, they found, has a range up to 3–4nm (or 4–5 NW dimers) along the NW direction. Due to its long range they concluded that this repulsive interaction can not just be a mere electrostatic repulsion. Furthermore, Kockmann *et al.* note that the characteristic long-ranged repulsive interaction is independent of the adsorption sites involved. This long range interaction along the NW is sharp contrast with the fact that no significant interaction is observed between CO molecules on adjacent wires. This means the origin of the repulsive interaction needs to be linked to the NW itself. We have shown for the adsorption sites on the NW1- and the NW2-surface that the presence of CO molecules modifies the nearby NW dimers in varying degrees. When the CO molecule is located between NW dimers (*eg.* A3, B1, and B3) it seems to repel the nearby NW dimers. For example, for the A3-site we find the resulting modifications to extend up to two NW dimers in each direction. Two other examples are shown in Fig. 5.7a and c. They show the interaction between two periodic copies of a CO molecule on the NW2-surface. These copies are separated 2 NW dimer apart and can press their neighboring NW dimers toward one-another far enough such that they form a tetramer. This effectively results in an indirect interaction between the two CO molecules. The surface strain mediating the indirect CO interaction is directed purely along the NW itself. The NW dimers which are pressed away from their original position will in their turn press further neighboring NW dimers from their equilibrium position and so on. These dislocated NW dimers block the possible adsorption sites resulting in an effective long range repulsive interaction.

As a final remark in this paragraph, we would like to point out the B5 adsorption configuration. Its high adsorption energy (only 140 meV below that of the B1 configuration) makes it also a reasonable adsorption configuration. Figures 5.8a and b show the calculated filled and empty state pictures. These show the CO molecule to be invisible, while the rest of the NW image remains unchanged. This is also the case for other simulated biases (± 0.30 and ± 0.70 eV), leading to the conclusion that this adsorption configuration could well be present in experiment, but invisible for STM. Only high resolution linescans orthogonal to the NWs at the position indicated in Fig. 5.8a could show the induced asymmetry of the QDRs, possibly combined with the observation that these asymmetric linescans are on average lower than those

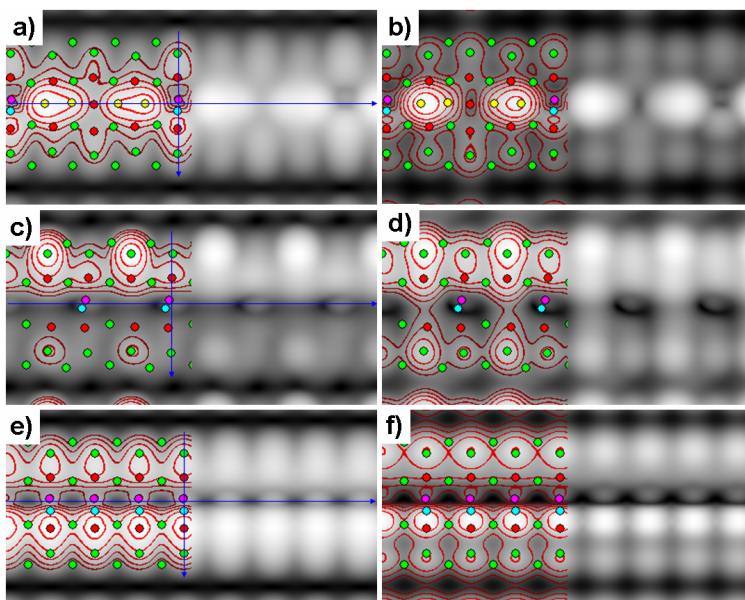


Figure 5.8: Calculated STM images of CO molecules adsorbed in bridging configurations B5 (a and b), A3b2 (c and d) and A7_{2CO} (e and f). The distance above the highest atom was chosen $z = 2.0$ Å. Filled state pictures (a), (c) and (e) are at a simulated bias of -1.50 V, while for the empty state pictures (b), (d) and (f) a simulated bias of $+1.50$ V is used. Contours are added to guide the eye, and are separated 0.2 Å. Colored discs indicate the atom positions in the top layers. Ge and Pt atoms in the two top layers are shown in green and red respectively. Yellow discs are used to indicate the Ge NW atoms, while cyan and fuchsia is used for the C and O atoms respectively. Blue arrows show the position and direction of the linescans shown in Fig. 5.10

symmetric ones on locations where no CO molecule is present. Another option one could imagine to make the CO molecule appear is by breaking its O-Pt bond with a small current surge through the STM tip. The CO molecule might then revert to the B2 adsorption configuration, which would be clearly visible in both filled and empty state pictures (*cf.* Fig. 5.6c and d).

This was for the case where the substrate is a NW array. For solitary NWs, which we have already shown to be less stable under CO adsorption, observation might be a little bit easier. Table 5.4 shows the A7 configuration (*cf.* Fig. 5.9b, it is the analog of the B5 configuration) to have a very high adsorption energy. Here the steric repulsion between the CO molecule and the NW dimers will create a hole in the NW centered around the CO molecule. This defect should show up as a depression over a wide range of biases. This wide depression would have a small protrusion in its

Adsorption energies and geometrical parameters for bridging CO molecules on a Pt modified Ge(001) surface.

	E_f (eV)	E_{ad} (eV)	coord.	r_{CO} (Å)	a_{CO} (°)	r_{C-surf} (Å)	a_{C-surf} (°)	r_{O-Pt} (Å)
NW1 A3b	-1.485	-2.069	b	1.214	47	2.012 (2.066)	101	2.249
NW1 A3b1	-1.163	-2.276	b	1.207	43	1.960 (2.106)	90	2.167
NW1 A3b2	0.390	-2.094	b	1.204	44	1.964 (2.084)	87	2.190
NW2 B5	-0.784	-2.197	t	1.170	20	1.883	28	2.433
NW1 A7	-1.589	-2.361	t	1.169	17	1.884	28	2.401
NW1 A7 _{2CO}	-3.741	-2.214	t	1.167	19	1.882	27	2.394

Table 5.4: Formation and adsorption energies for CO adsorbed in configurations bridging the trough between two neighboring QDRs. Adsorption sites are shown in Fig. 5.9a. The B5 and A3b values are duplicated from Table 5.1 for ease of comparison. r_{CO} , r_{C-surf} , and r_{O-Pt} are the C-O, C-Pt and O-Pt bond lengths, the value between brackets for r_{C-surf} is the bond length of the C atom to the Pt atom at the bottom of the trough. a_{CO} and a_{C-surf} are the bond angles with regard to the surface plane. In case of bridge adsorption a_{C-surf} is the angle between the two C-surface bonds.

center and a width of at least 8 Å.⁶

5.4.2 Molecular electronics on Pt modified Ge(001)?

From these calculations and the experiments presented in literature, the possible application of this system for 1D molecular electronics becomes very unlikely. The long-ranged interaction observed by Kockmann *et al.* and its explanation in light of the calculations performed in this work, seems to be the main problem.

Up to this point we mainly focussed on identifying the experimentally observed structures. The B5 adsorption configuration, and the comparable A3b configuration have not yet been discussed in light of experiments, while showing almost the best adsorption energies. The calculated STM images for these structures show something very peculiar, more specifically, the total lack of an image for the CO molecule. In case of the A3b adsorption site a large protrusion is still visible, however this is an ejected Ge atom of the NW dimer (*cf.* Fig. 5.2b). This ejection was due to the limited unitcell size. The steric repulsion between two periodic copies of the CO molecule and the single Ge NW dimer prohibited the Ge dimer to be displaced sufficiently along the NW direction. To remove this ‘computational artefact’ the ejected Ge atom is removed (A3b1), and in a second calculation both Ge atoms forming the NW dimer are removed (A3b2). Also an adsorption structure with B5 configuration on a NW1 surface is build (A7), using a double NW1 surface cell. Table 5.4 shows

⁶In our limited surface cell the NW dimers could not spread further before colliding with periodic copies, limiting the width of the depression to ~ 8 Å.

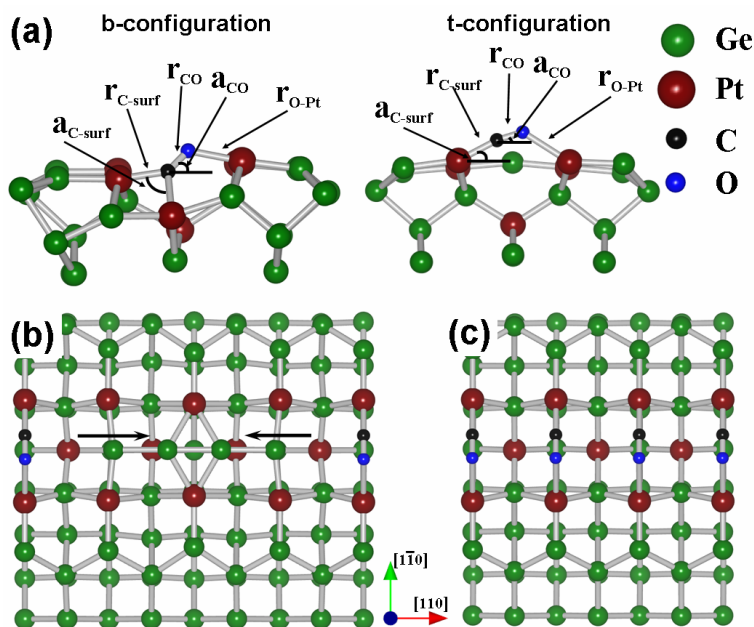


Figure 5.9: (a) Ball-and-stick representation of the two bridging CO configurations. Geometrical parameters given in Table 5.4 are indicated. Ball-and-stick representation of the A7 (b) and A7₂CO (c) structures. Arrows in (b) show the drift direction of the NW dimers.

the formation and adsorption energies for these new structures in comparison to the B5- and A3b-structures. Removal of the Ge NW atoms clearly decreases the formation energy of the surface, which is due to the uncovering of the imbedded Pt atoms. The adsorption energy of the CO molecule however remains roughly the same. Also the geometrical parameters barely change. The bond lengths decrease slightly, due to the reduced steric repulsion between the CO molecules and the Ge dimer atoms, moving the CO molecule closer to the surface.

In case of the A7 adsorption configuration, the lack of anchor point for the NW dimers causes them to drift away from the CO molecule due to the steric repulsion. Which, because of the limited unit cell size, results in the formation of a Ge tetramer as is shown in Fig. 5.9b. The geometric parameters for the CO molecules in the B5 and A7 adsorption configurations are almost identical. However the distance between a CO molecule and the nearest Ge atom of a NW dimer is approximately 4.3 Å in case of the A7 configuration, while it is only 3.3 Å in case of the B5 configuration. This indicates the improvement in adsorption energy, going from the B5 to the A7 configuration, can be attributed to the reduction of the steric repulsion between the CO molecule and the Ge NW dimers.

Because uncovering the imbedded Pt atoms has a negative influence on the forma-

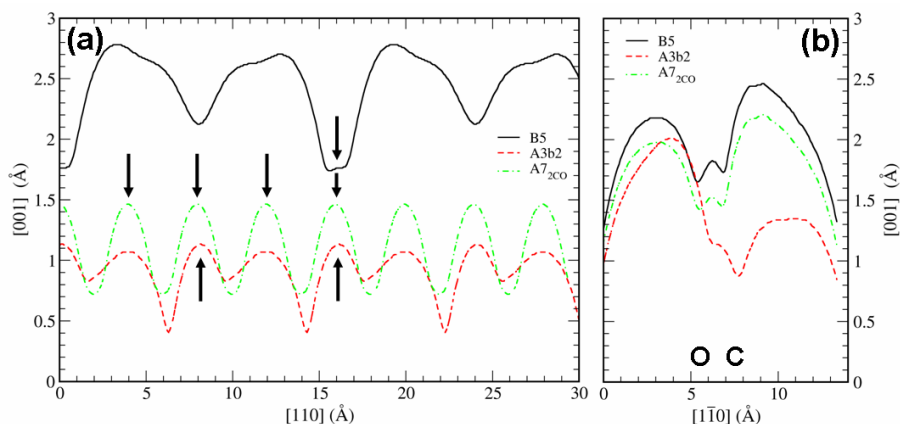


Figure 5.10: Calculated linescan images along (a) and orthogonal (b) to the trough/NW for the B5 (solid black curve), the A3b2 (red dashed curve) and the A7_{2CO} (green dash-dot curve) configuration. The linescans are taken along the arrows shown in Fig. 5.8 (a), (c), and (e). The arrows in (a) indicate the positions of the CO molecules, while C and O show the positions of the C and O atom in (b).

tion energy, a model is build with the entire NW removed and replaced by a maximum coverage of CO molecules in an A7 configuration (A7_{2CO}). The A7_{2CO} contains two CO molecules per 4×2 surface cell (*cf.* Fig. 5.9c), making this a four times higher coverage than the A7 case. A large increase in the formation energy is found, while the steric repulsion only has a minute influence on the adsorption energy of the CO molecules. Furthermore, the geometrical parameters remain almost unchanged making this, from the geometrical point of view, a very good candidate for 1D molecular electronics. However, there is one small problem. These CO molecules in either b or t bridging configuration are invisible in STM. Figure 5.8 shows both filled and empty state pictures of the B5, A2b2, and A7_{2CO} adsorption geometries. For the B5 adsorption configuration the linescan, shown in Fig. 5.10, is almost unmodified compared to the linescan of the pristine NW. The only modification is found in the line scan orthogonal to the trough/NW. In case of a t bridging configuration, the dimer of the QDR which is bound to the C atom is higher than the dimer bound to the O atom, while the opposite is true for the b bridging configuration. So if one would succeed in stripping away the Ge NW without damaging the underlying substrate, a high coverage of CO molecules in bridging configuration could be recognized by this asymmetry in the QDR images. The formation and adsorption energies are highly favorable, making this also energetically an interesting template for 1D molecular electronics.

5.5 Conclusions

In this paper we have studied the adsorption of CO molecules on Pt induced NWs on Ge(001) using *ab initio* DFT calculations. We show CO has a strong preference for adsorption on the Pt atoms imbedded in the Ge(001) surface. As a consequence CO molecules do not bind directly on top of the Ge dimers forming the NWs, contrary to the experimental assumptions. By direct comparison of calculated STM images to experimental STM images we have successfully identified the observed adsorption sites. We have shown that the Pt atoms lining the troughs in which the Ge NWs are imbedded provide the necessary adsorption sites to explain all experimentally observed CO adsorption sites. CO molecules in ontop configurations next to the NW tilt toward it, presenting STM images located on the NW. CO molecules bound in between NW dimers, with the O atom also bound to a Ge NW dimer modify the electronic structure of this Ge atom sufficiently to give the appearance of a protrusion on this Ge dimer. This gives rise to the short-bridge CO adsorption site observed by Öncel *et al.* A CO molecule bound in an ontop configuration on the extra Pt atom of the NW₂-surface, showing a protrusion at negative bias and a depression at positive bias, is found to show good agreement with the experimentally observed long-bridge site, seen by Kockmann *et al.* The short-bridge site observed by this group is identified as a CO molecule in a bridge configuration in between NW dimers.

A path for mobility along the wire is presented, showing the CO molecule to move along the Pt atoms of the underlying QDRs. The long-ranged interaction observed by Kockmann *et al.* is explained through the dislocation of NW dimers, in the vicinity of the CO molecule. These dislocated NW dimers in turn block the nearby CO-adsorption sites.

We also predict the presence of invisible bridging CO molecules, and present methods for observing them experimentally. Also the possibility of 1D molecular electronics is touched. After removal of the Ge NW dimers, stable, invisible wires of parallel CO molecules, along the Pt lined troughs, can be obtained. This configuration has a large formation energy $E_f = -3.74$ eV and an adsorption energy per CO molecule $E_{ad} = -2.21$ eV at maximum CO coverage.

Acknowledgements

This work is part of the research program of the “Stichting voor Fundamenteel Onderzoek der Materie” (FOM) and the use of supercomputer facilities was sponsored by the “Stichting Nationale Computer Faciliteiten” (NCF), both financially supported by the “Nederlandse Organisatie voor Wetenschappelijk Onderzoek” (NWO).

Chapter 6

onclusions and outlook

The only way to discover the limits of the possible is to go beyond them into the impossible.

– Arthur C. Clarke
 (“Technology and the Future” – Clarke’s second law)

6.1 Conclusions: Questions and answers

At the beginning of this work we posed a set of questions with regard to the system under study. Now, with our model at hand answers can be formulated.

- Although a quarter ML of Pt is deposited, only a fraction of the surface is covered with β -terraces, and only a fraction of the β -terraces contains NWs. So what is the local Pt density in the NW arrays?

It is already clear from the experimental picture that the local Pt density ρ_{Pt} is not uniform over the entire surface. Three different types of terraces appear with increasing Pt deposition. At very low deposition amounts (a few % of a ML) the Ge(001) surface gets riddled with vacancy defects. [91] This is called the α -terrace. If the deposited amount is increased, β -terraces appear, and expand with further increasing Pt deposition. For deposition amounts of ~ 0.25 ML and higher, NWs start appearing on the β -terraces, growing with increasing deposition amount. [18] This shows a kind of surface hierarchy as function of Pt deposition, which allows us to assume $\rho_{\text{Pt}}(\alpha\text{-terrace}) \leq \rho_{\text{Pt}}(\beta\text{-terrace}) \leq \rho_{\text{Pt}}(\text{NWs})$. For our model of the β -terrace in **Chapter 3** and the two types of NWs in **Chapter 4** we have:

$$\begin{cases} \rho_{\text{Pt}}(\beta\text{-terrace}) & = & 0.25 \text{ ML} \\ \rho_{\text{Pt}}(\text{NW1}) & = & 0.75 \text{ ML} \\ \rho_{\text{Pt}}(\text{NW2}) & = & 0.8125 \text{ ML} \end{cases} \quad (6.1)$$

These values satisfy the Pt density relation assumed above, moreover, the two types of NWs also indicate the correct gradient in the Pt density. The low Pt deposition

(~ 0.25 ML) in comparison to the high Pt density calculated for the NW regions (0.8125 ML), might make one wonder if these values are reasonable. In the following we will investigate whether these values do not contradict experiment.

Given the deposited amount of Pt, M_{dep} , the relation with the surface phases is given by:

$$M_{\text{dep}} = \rho_{\text{Pt}}(\alpha)X_{\alpha} + \rho_{\text{Pt}}(\beta)X_{\beta} + \rho_{\text{Pt}}(\text{NW1})X_{\text{NW1}} + \rho_{\text{Pt}}(\text{NW2})X_{\text{NW2}} + M_{\text{sub}}, \quad (6.2)$$

with X_I the surface fraction covered by a terrace of type I and M_{sub} the amount of Pt which is located deep in the subsurface, *i.e.* below the third layer of *all* the terraces. Since this equation has five unknowns, five different sets (M_{dep} , X_{α} , X_{β} , X_{NW1} , X_{NW2}) suffice to find an exact solution for the local densities. At the moment of writing no experimental data has been published presenting Pt densities of the different terraces. However, Prof. Zandvliet was so kind to provide us with two such data sets: ($M_{\text{dep}} = 0.25\text{-}0.3$ ML, $X_{\alpha} = 30\%$, $X_{\beta} = 52.5\text{-}56\%$, $X_{\text{NW1}+\text{NW2}} = 14\text{-}17.5\%$) and ($M_{\text{dep}} = 0.5\text{-}0.6$ ML, $X_{\alpha} = 10\%$, $X_{\beta} = 58.5\%$, $X_{\text{NW1}+\text{NW2}} = 31.5\%$).

Because the solubility of Pt in Ge is very small, the term M_{sub} can be assumed to be zero, for low deposition amounts (dataset 1). [96] Furthermore, if the surface is filled with large NW arrays, we can assume the fraction of solitary nanowires to be small compared to the total amount of NWs, which allows us to replace the two separate terms for the NWs with a single term for all nanowires with Pt density $\rho_{\text{Pt}}(\text{NW1} + \text{NW2}) = \rho_{\text{Pt}}(\text{NW2})$. This reduces Eq. (6.2) to:

$$M_{\text{dep}} = \rho_{\text{Pt}}(\alpha)X_{\alpha} + \rho_{\text{Pt}}(\beta)X_{\beta} + \rho_{\text{Pt}}(\text{NW1} + \text{NW2})X_{\text{NW1}+\text{NW2}}, \quad (6.3)$$

which still requires three sets of data for an exact solution. This simplified equation can be used in the low deposition case. Using the data sets provided by Prof. Zandvliet we can calculate the required Pt density for the α -terrace.

Starting from the first data set we find a Pt density in the range of -0.07 to $+0.15$ ML, well below the 0.25 ML of the β -terrace, as expected.¹

Due to relatively high deposition amount for the second dataset we can not make use of the simplified equation. Based on the results of the first dataset we will assume the Pt density in the α -terrace to be ~ 0.15 ML. This means that another 0.085 to 0.185 ML of Pt should have dissolved into the Ge bulk. This is comparable to the Pt density for the α -terrace and could be considered reasonable.

This means that the Pt densities of the proposed models show no contradiction with the experimental observations.

- Connected to this issue, and the chemical insensitivity of an STM: Where are the Pt atoms located? To put it bluntly: what is the geometry of the NWs? And more specifically, why do NWs grow only every *second* trough of the β -terrace?

The geometry of the NWs is a rather complex structure, where a **germanium monatomic nanowire**, which is observed in experiments, covers a **platinum lined**

¹The negative lower boundary is not a problem, since there is a significant error present in the values provided, and in case of a low NW fraction, the the Pt density for the NW region is somewhat overestimated due to our second assumption.

trough. The double peaked dimer images, seen in filled state STM pictures, are a direct consequence of the bonds the Ge NW forms with the underlying Pt atoms.

- And more specifically, why do NWs grow only every *second* trough of the β -terrace?

The answer to this question is directly related to the NW geometry. First of all, the underlying terrace is not a β -terrace, but instead a surface reconstruction with $3\times$ the Pt density. The Pt-Ge dimers on this surface are aligned such that every second trough is lined only with Pt atoms, while the other troughs are lined only with Ge atoms. This configuration is necessary to pin the Ge NW at the center of the trough between the QDRs. Because Pt surface dimers are very unstable (see **Chapter 3**), it is impossible for neighboring Pt lined troughs to exist, within the constraints of the studied experiments.

- What causes this long-range repulsive interaction between adsorbed CO molecules?

The long-range repulsive interaction observed for CO molecules on the NW arrays was traced back to the interaction between the CO molecules and the Ge NW dimers. The repulsive interaction between them, displaces NW dimers, which in their turn block nearby CO adsorption sites. The interaction between the CO molecules is not a direct interaction but rather an indirect interaction mediated through the Ge NW.

- Why are there conducting states between the wires, while the wires themselves are not clearly metallic, although they are supposed to consist of metal (Pt) atoms?

The reason why the wires themselves are not conducting follows directly from the fact that the wires consist of Ge. The hybridization of Ge p and Pt d states introduces surface states which render the surface between the wires metallic.

6.2 Outlook: Metal induced nanowires on semiconductor surfaces and phase-space searching

Modern technology is driven by the constant further miniaturization of devices. With the scale of these devices reaching deeper and deeper in the microscopic regime, standard fabrication methods are quickly becoming too crude to build these near-atomic scale devices. An alternative for the current lithographic techniques that is pursued actively is self-assembly, *i.e.* we let nature do the hard work. [4] However, before it really becomes possible to actively design devices at an atomic scale, a large database of possible different components, containing an accurate description of their properties and structure and all the necessary prerequisites, will be required. To design such components, a symbiotic collaboration between experimental and theoretical researchers will not just be a plus, it will become a necessary prerequisite to

succeed. This necessity follows from the nature of this subject. The limitations on experiment and theory prohibit each to have a full understanding individually.

On the one hand, the experimentalist can build new structures, but he can never be absolutely certain of the exact atomic structure forcing him to make assumptions which greatly influence the interpretation of the observations.² Close collaboration with theoretical researchers can illuminate the situation. Through *ab-initio* calculations and direct comparison, the experimentally observed structures can be identified, making the interpretation of the observations less of a guessing game.

On the other hand, since such structures are mostly metastable configurations, the theoretician will be at a loss without an experimental counterpart. The phase-space of possible structures he is working with is horrendous, and the number of local minima is large. Identifying which of these minima correspond with ‘real’ (metastable) experimental configurations can only be done through direct comparison with real experiments. Furthermore, since the most commonly used methods are ground-state methods, they are ideally suited to find the ground-state, *i.e.* global minimum, of a system, however when dealing with metastable configurations the ground-state is the configuration we are not looking for. Because metastable configurations show a strong dependence on the experimental conditions (*e.g.* deposition rate and amount, temperature, . . .), accurate and full experimental information is necessary to reduce the phase-space of possible structures to a size that can be handled by the theoretician. Conversely, theoretical work can also help to fine tune the setup parameters of the experiment, or even predict other closely related metastable configurations.

Let us now focus on a more specific device: ‘nanowires on Ge’. The formation of nanowires, chains, and rods³ has been observed on Ge surfaces after deposition of Pt, [18, 27, 28, 93, 98, 99] Au, [19, 20, 25], In, [23, 24, 118, 119] Er, [22] and Ho. [21] Each of these systems shows a large variety of surface reconstructions at different submonolayer depositions and temperatures (*cf.* the surface phase-diagram for In on Ge(001) given in Reference [120]). The fact that ‘nanowires’ have been observed for each of these combinations shows that this type of reconstruction is not a rare exception, highly dependent on the constituent atomic species.

Based on these examples and the system studied in this thesis we can formulate some beneficial properties to design nanowires.

The dimer row reconstruction of the Ge(001) surface provides a 1D template facilitating the formation of NWs that can be hundreds of angstroms long. [18, 25] (But also on the threefold symmetric Ge(111) surface, wires/rods have been observed. [21])

To preserve the semiconducting nature of our substrate it is beneficial if the ‘metal’ atoms have a (nearly) zero solubility in the semiconductor. Furthermore, this also has the advantage that the amount deposited will be exactly the amount needed for

²The NWs studied in **Chapter 4** of this thesis, and consequently the adsorption of CO on the NWs, studied in **Chapter 5** is a good example.

³For simplicity we will refer to all these structures as nanowires. So we refer to all atomic scale linear structures which stand out clearly from the surface in STM experiments as nanowires.

the surface reconstruction, giving a better control over the process.

Because the reconstruction aimed at, can be considered an extreme case interface system, and the bulk diffusion should be negligible, submonolayer deposition should suffice in most cases.

The Er/Ge(001) system shows that surface mobility plays an important role, resulting in distinctly different structures when a sample is only annealed for a short period of time, compared to deposition at an elevated temperature. [22] Here the short period annealing has the advantage that bulk diffusion is limited.

Also, the anneal temperature can play a crucial role, as is shown for the Pt/Ge(001) system. [18] Studying the Pt-Ge phase-diagram, we note that the anneal temperature of 1050 K lies roughly on top of the phase-boundary between solid and (solid +) liquid phases. More specifically we find the reaction $L \leftrightarrow \text{Ge}_{\text{bulk}} + \text{Ge}_2\text{Pt}$ at a temperature of 770°C (= 1043 K). [96] Similarly, we find for the Au NWs presented by Schäfer *et al.* [25] and the In NWs presented by Falkenberg *et al.* [24, 118] a sample temperature just above the solid/solid+liquid phase-boundary. In each case a substantial rearrangement of the surface atoms takes place, which means bonds of the surface atoms need to be broken. To achieve this bondbreaking, temperatures close to the melting temperature will be needed.

The examples given above are a good indication that even more metal/Ge(001) NW systems should exist, each with their own unique properties. One could imagine magnetic NW systems using Co, where the $L \leftrightarrow \text{Ge}_{\text{bulk}} + \text{CoGe}$ reaction at 817°C could give an estimate for the needed anneal temperature. But also metals like Cu and Ni have a negligible solubility in Ge while showing interesting reactions in their phase-diagrams, resulting in anneal temperatures of 644°C for Cu/Ge(001) and 762°C for Ni/Ge(001). [96]

Although this all sounds very optimistic, it does not allow for simple one-sided theoretical prediction. Because each metal species has its specific electronic structure and consequent binding behavior,⁴ we can not simply copy the geometry found for the Pt/Ge(001) nanowires to the Au/Ge(001) or Ni/Ge(001) systems. Furthermore, ground-state calculations are unable to give single structure predictions for metastable configurations, instead multiple structures will appear as possible solutions. Even more, it might even be possible that the actual experimental metastable configuration is missing. Due to the size of the phase-space one cannot do an exhaustive search covering all possible configurations,⁵ instead a clever search algorithm, such as a genetic algorithm (GA), can be used. [121–124] These GA can cover the

⁴*e.g.* Investigation of the Pt-Pt, Ge-Ge and Pt-Ge free dimers, shows the Pt-Ge dimer to be most stable of all, while for the Au-Au, Ge-Ge and Au-Ge free dimers, the Ge-Ge dimer is found to be most stable, followed by the Au-Ge dimer.

⁵In Reference [121] the number of possible starting configurations for a binary alloy containing 30 atoms in the unit cell is estimated to be 10^{47} . The number of inequivalent atoms in our unit cell is 50.

entire phase-space searching for specific properties, and have already been successfully applied for simple problems with relatively small supercells. [121–123] Such GA can be combined with *ab initio* calculations, and thus can be used to approach the current problem of nanowire-design. The average system size and the fact that a few hundred structures are often needed for the GA to converge to its solution makes this technique quite expensive, but not impossible to use unlike a simple brute force exhaustive search. Next to the computational cost, which at the moment of writing might be just too steep for common use in systems of the current size, there is also the inherent complexity of the “fitness”-algorithm. Where magnetism and total energy are given in absolute numbers, the property ‘*resembles a nanowire in STM*’ is too vague for simple binary logic. For a human being however, this problem does not exist. In fact, if we look back at **Chapter 4**, the method applied there for finding the NW geometry can be considered a type of GA. Only in this case it was the author who performed all GA operations manually.

The library of possible geometrical structures obtained from the study presented in this thesis can be used as a starting point for future metal induced NW-formation studies. Calculated STM images will allow for simple assessment of the structures fitness, and close collaboration, with a free flow of information, between experimental and theoretical researchers will allow for relatively quick identification of observed structures.

Appendix A

canning Tunneling Microscopy

A.1 The STM program

The identification of an experimentally observed geometry via comparison of calculated and real STM images is a rather complex task. The real STM image is the result of electronic transport between surface states and tip states, which are results of the underlying geometry of sample and tip respectively. Because both are unknown, one would need to try different combinations of possible tip and surface structures, leading quickly to a very large set of systems to study. However, because we are not really interested in the tip geometry and it can be assumed that STM images for different tips give qualitatively similar images, we have excluded the tip from the problem by assuming it to be a point-source at first instance. This has the added advantage that the set of systems that need to be studied reduces dramatically since we do not have to check possible tip-surface combinations anymore. However, this does not mean that the tip geometry has no effect at all. Distortions of the STM image due to different tip geometries are widely recognized, most of them resulting in a deterioration of the STM image. [125] Also an improvement of the resolution can be obtained through chemical modification of the tip, as was shown by Qing-Min Xu *et al.* [126] This shows an extra advantage of the point-source approach, because it is tip independent: the resulting images can qualitatively be compared to any high resolution STM image of reasonable quality.

The procedure used to generate the STM images is quite straightforward. If the tip is assumed to be a point-source, and transmission matrix element effects are neglected, then a constant-current mode STM experiment corresponds to a surface of constant LDOS, as shown in **Chapter 2.2.2**. We only need a representation of the LDOS for energies close to the Fermi level on a real-space grid. This can be obtained from a short calculation performed by VASP, using the bias voltage and the Fermi

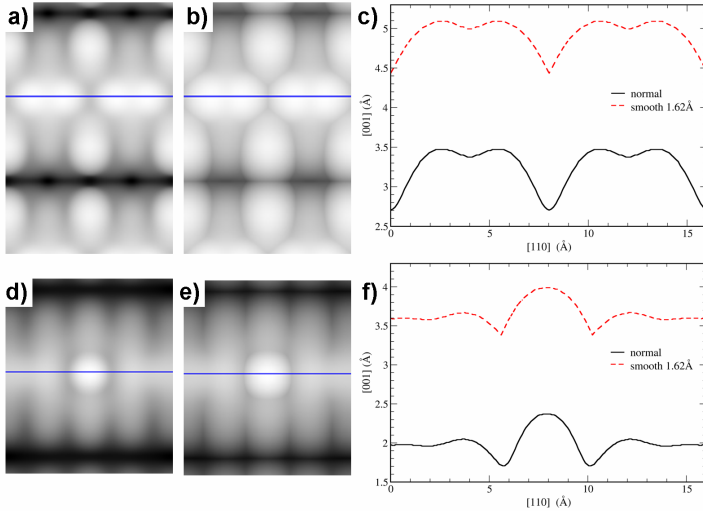


Figure A.1: Smoothing of the of the NW1-structure (a, b, c) and CO on NW2 B3 adsorption site (d, e, f). a and d show the original images (same as Fig. 4.13a and 5.6e), b and e show the same images after a smoothing procedure. The tip size was set to the covalent radius of a W atom (1.62 Å). [127] c and f show a comparison of the line scans along the NW.

level as boundaries for the energy of the states of interest. The resulting file containing this partial charge density is then used to plot calculated STM images. The later is done using the STM program developed as a part of this Ph.D. project.

In the STM program, a surface with constant charge density C is plotted. There are two ways of obtaining C . The first one is by giving it as direct input. The second is by finding the charge density at a certain height z_C above the atom that sticks out highest from the surface. Using this C a heightmap is generated as function of (x, y) , which is plotted in grayscale. By manually defining the spatial range of the grayscale interval, and fixing the value of C , different structures can be compared in the same grayscale, allowing better contrast comparison. The use of a graphical user interface (GUI) combined with the almost instant generation of calculated STM images allows for interactive modification of the input parameters, making qualitative comparison easy and fast. Some graphical tools are also implemented, such as the possibility to add contour-lines and atom positions, or to generate line-scans of the STM image of the studied structure. A graphical smoothing algorithm was implemented to simulate the tip width. Starting from the point-source image $S1$, a sphere with radius R is traced over this heightmap, resulting in a new heightmap/image, $S2$. This results in a smearing of sharp features. Depressions become less pronounced and protrusions widen. Figure A.1 shows two examples where we applied the smoothing algorithm. For the NW1-structure, a broadening of the features is observed. This broadening does not conceal the double peak of the NW dimer images, as can be

seen in Fig. A.1c, showing that the point-source STM approach gives the qualitative correct picture of this system. For the second system, a CO molecule adsorbed at the B3 site, the broadening of the CO protrusion is more pronounced. It becomes ~ 0.75 Å larger, showing the finite tip size in experiment will give a major contribution to the observed size of the CO molecule image.

Appendix B

eometric data for β and γ surface reconstructions

In **Chapter 3** Table 3.2, geometrical parameters are given for the two types of surface dimers present on the β_{6u} -geometry. In Table B.1 this table is expanded to include all Ge(001) surface reconstructions, containing 0.25 and 0.5 ML of Pt in the top layer, which were studied in **Chapter 3**. The geometrical parameters are shown in Fig. 3.10. The tilt angle ω is given in degrees and the values for all other parameters are given in Å. We refer to the Ge-Ge surface dimers as Ge and to the Pt-Ge (or in case of the β_{1ud} -structure Pt-Pt) surface dimers as Pt. In case of the β_{1ud} -structure the Ge-Ge dimer mentioned in Table B.1 is the Ge dimer of the QDR.

The subscripts *up* and *dn* refer to the dimer in the QDR with the Pt atom at the up or down side of the QDR, as defined in Fig. 3.12. In case of the β_{4u} -, the β_{4d} - and the β_{5ud} -structure, the *up* and *dn* subscripts indicate the same but then with regard to the line of dimers orthogonal to the QDRs. For the γ -reconstructions the subscripts *up* and *dn* just indicate the Pt atom at the up or down side of the QDR.

Different geometries are separated by horizontal lines to avoid confusion.

Table B.1: Bond lengths and dimer tilt angle.

	ω	A	B ₁	B ₂	C ₁	C ₂	C ₃	C ₄	d ₁	d ₂	d ₃	t ₁	t ₂	t ₃	t ₄
$\beta_{1ud} \text{ Ge}$	19.18	2.446	2.507	2.423	2.461	2.440	2.536	2.463	0.804	0.754	0.069	3.810	0.003	-0.003	-0.0004
$\beta_{1ud} \text{ Pt}$	20.57	2.578	2.361	2.369	2.456	2.456	2.540	2.453	0.906	0.265	0.014	3.942	0.155	-0.452	-0.406
$\beta_{2u} \text{ Ge}_{up}$	21.03	2.463	2.554	2.433	2.482	2.435	2.490	2.470	0.884	0.729	0.032	3.760	0.151	0.042	-0.009
$\beta_{2u} \text{ Pt}_{up}$	-4.42	2.357	2.378	2.524	2.482	2.435	2.490	2.470	0.182	1.371	0.032	3.760	0.151	-0.042	0.009
$\beta_{2d} \text{ Ge}_{dn}$	18.23	2.462	2.508	2.475	2.455	2.455	2.481	2.474	0.770	0.786	0.032	3.803	0.138	-0.400	-0.411
$\beta_{2d} \text{ Pt}_{dn}$	-0.15	2.349	2.494	2.360	2.455	2.455	2.481	2.474	0.006	1.249	0.032	3.803	0.138	0.400	0.411
$\beta_{3ud} \text{ Ge}_{dn}$	18.12	2.473	2.507	2.466	2.461	2.460	2.481	2.479	0.769	0.794	0.004	3.822	0.147	-0.419	-0.416
$\beta_{3ud} \text{ Ge}_{up}$	21.85	2.465	2.557	2.432	2.479	2.435	2.489	2.466	0.917	0.740	0.059	3.737	0.166	0.066	0.003
$\beta_{3ud} \text{ Pt}_{dn}$	-1.82	2.348	2.490	2.362	2.461	2.460	2.481	2.479	0.075	1.221	0.004	3.822	0.147	-0.419	-0.416
$\beta_{3ud} \text{ Pt}_{up}$	-4.43	2.358	2.378	2.529	2.479	2.435	2.489	2.466	0.182	1.387	0.059	3.737	0.166	0.066	0.003
$\beta_{4u} \text{ Ge}_{up}$	18.85	2.444	2.511	2.425	2.462	2.447	2.536	2.475	0.789	0.760	0.059	3.822	0	0	0
$\beta_{4u} \text{ Pt}_{up}$	1.92	2.353	2.364	2.480	2.502	2.434	2.470	2.461	0.079	1.197	0.103	3.719	0	0	0
$\beta_{4d} \text{ Ge}_{dn}$	18.85	2.444	2.512	2.428	2.463	2.445	2.536	2.475	0.790	0.767	0.063	3.815	0	0	0
$\beta_{4d} \text{ Pt}_{dn}$	0.50	2.354	2.485	2.375	2.466	2.466	2.432	2.496	0.021	1.197	0.016	3.723	0	0	0
$\beta_{5ud} \text{ Ge}_{dn}$	18.43	2.444	2.506	2.425	2.464	2.447	2.540	2.475	0.773	0.754	0.047	3.831	0.011	-0.028	-0.016
$\beta_{5ud} \text{ Ge}_{up}$	19.06	2.441	2.507	2.423	2.464	2.447	2.540	2.475	0.797	0.735	0.047	3.831	0.011	-0.028	-0.016
$\beta_{5ud} \text{ Pt}_{dn}$	7.38	2.354	2.585	2.373	2.476	2.441	2.445	2.474	0.303	1.149	0.055	3.719	0.100	0.584	0.576
$\beta_{5ud} \text{ Pt}_{up}$	-5.04	2.352	2.368	2.578	2.476	2.441	2.445	2.474	-0.207	1.388	0.055	3.719	0.100	0.584	0.576
$\beta_{6u} \text{ Ge}_{up}$	20.82	2.462	2.552	2.433	2.479	2.435	2.492	2.469	0.875	0.731	0.027	3.764	0.153	0.049	0.003
$\beta_{6u} \text{ Pt}_{up}$	-4.25	2.354	2.378	2.521	2.479	2.435	2.492	2.469	-0.174	1.358	0.027	3.764	0.153	-0.049	-0.003
$\beta_{6d} \text{ Ge}_{dn}$	18.13	2.464	2.506	2.473	2.452	2.457	2.481	2.473	0.766	0.787	0.020	3.808	0.146	-0.399	-0.405
$\beta_{6d} \text{ Pt}_{dn}$	-0.88	2.348	2.491	2.360	2.452	2.457	2.481	2.473	-0.036	1.243	0.020	3.808	0.146	0.399	0.405
$\beta_{7ud} \text{ Ge}_{dn}$	18.06	2.468	2.505	2.469	2.459	2.439	2.480	2.478	0.765	0.786	0.013	3.820	0.150	-0.396	-0.397
$\beta_{7ud} \text{ Ge}_{up}$	21.43	2.462	2.555	2.435	2.473	2.434	2.487	2.467	0.899	0.728	0.038	3.739	0.167	0.061	0.003
$\beta_{7ud} \text{ Pt}_{dn}$	-1.30	2.349	2.490	2.361	2.459	2.459	2.480	2.478	-0.053	1.236	0.013	3.820	0.150	0.396	0.397
$\beta_{7ud} \text{ Pt}_{up}$	-4.83	2.358	2.379	2.528	2.473	2.434	2.487	2.467	-0.198	1.393	0.038	3.739	0.167	-0.061	-0.003
$\gamma_1(1 \times 2) \text{ Pt}_{up}$	1.95	2.351	2.362	2.475	2.498	2.431	2.465	2.465	0.080	1.181	0.089	3.717	0	na	na
$\gamma_2(2 \times 2) \text{ Pt}_{dn}$	6.46	2.353	2.588	2.372	2.474	2.438	2.440	2.476	0.265	1.149	0.008	3.719	0.090	0.560	0.558
$\gamma_2(2 \times 2) \text{ Pt}_{up}$	-6.13	2.353	2.372	2.588	2.474	2.438	2.440	2.476	-0.251	1.404	0.008	3.719	0.090	-0.560	-0.558
$\gamma_3(4 \times 2) \text{ Pt}_{dn}$	6.11	2.350	2.579	2.368	2.476	2.440	2.442	2.477	-0.250	1.139	0.009	3.723	0.104	0.612	0.611
$\gamma_3(4 \times 2) \text{ Pt}_{up}$	-5.75	2.350	2.369	2.580	2.476	2.440	2.442	2.477	0.235	1.376	0.009	3.723	0.104	-0.612	-0.611

Appendix C

omparison of LDA to GGA

All calculations in **Chapters 3, 4** and **5** of this thesis are performed using LDA-based PAW potentials. This choice is based on the fact both LDA and GGA show a zero BG band structure for bulk Ge and the fact that LDA functionals give a more accurate geometry. Also the slightly better convergence behavior made the LDA functionals more favorable (*cf.* **Sec. 2.3**).

It is well known that LDA overestimates the binding energy of a system while GGA underestimates it. This allows us to place upper and lower boundaries on the binding energy of a certain configuration once both LDA and GGA values of the binding energy are known. For this reason, we performed static self-consistent GGA calculations for all systems presented in this work.

Furthermore, **Table C.1** shows the change in bulk formation energy for Pt to be twice as large as for Ge, going from LDA to GGA. So a second reason to perform these static self-consistent GGA calculations is to check if the relative stability of the structures remains unchanged. In the following sections we will repeat the relevant tables given in **Chapters 3** through **5** and briefly discuss qualitative differences and similarities.

C.1 GGA setup

We used the Perdew-Wang 91 (PW91) GGA functional as implemented in the VASP. Only the $4s$ and $4p$ electrons were included in the valence shell. The kinetic energy cutoff for the plane-wave basis set was set to 345 eV, and an $8 \times 4 \times 1$ Monkhorst-Pack special k -point mesh was used. We used the relaxed geometries obtained during the LDA calculations, only modifying the bulk-lattice constant to GGA bulk-lattice constant of Ge. No geometry optimizations were performed, only static self-consistent calculations.

GGA bulk and formation energies.

	Bulk Ge (eV/atom)	Bulk Pt (eV/atom)	CO molecule (eV/molecule)
LDA	-5.175	-7.451	-15.587
GGA	-4.521	-6.044	-14.833

Table C.1: Comparison between LDA and GGA values for the formation energies of bulk Ge, bulk Pt and CO molecules. For the bulk Ge and Pt calculations the plane wave kinetic energy cutoff was set to 345 eV and a $21 \times 21 \times 21$ k -point mesh was used. For the CO molecule the kinetic energy cutoff was set to 400 eV and only the Γ -point was used. The CO molecule was placed in a $15 \times 15 \times 15 \text{ \AA}^3$ unit cell.

C.2 The β -terrace

Table C.2 presents the GGA versions of Tables 3.1 (left) and 3.3 (right). In this case, contrary to Tables 3.1 and 3.3, the formation energies are given per 4×2 surface unit cell, resulting in a factor two difference for the β -geometries (except β_{1ud})

Table C.2: GGA formation energies per 4×2 surface unit cell for Chapter 3.

β -and γ -reconstructions	E_f (meV)	Pt in second and third layer		E_f (meV)
		Layer	Pt position(s)	
β_{1ud}	142	2	A (down)	-158
β_{2u}	-655	2	B (up)	-239
β_{2d}	-372	2	A & D (down)	-380
β_{3ud}	-512	2	B & C (up)	-578
β_{4u}	-707	3	a (row)	-1033
β_{4d}	-628	$3^*(k_1)$	a (row)	-43
β_{5ud}	-465	3	b (trough)	-96
β_{6u}	-668	3	a & b	-1329
β_{6d}	-383	$3^*(k_1 \& k_2)$	a & b	677
β_{7ud}	-521	3	a & c	-1040
$\gamma_1 (1 \times 2)$	-1341	$3^*(k_1)$	a & c	-235
$\gamma_2 (2 \times 2)$	-920	3	a & d	-1356
$\gamma_3 (2 \times 4)$	-945	$3^*(k_1 \& k_3)$	a & d	-102
		3	a & e	-2136
		$3^*(k_1 \& k_4)$	a & e	-537

and a factor four for the γ -geometries. Similar factors should be implemented when comparing the GGA and LDA values of the geometries with Pt in the second and third layer.

First of all we note that the β - and γ -geometries are much more stable according to the GGA calculations. Only the β_{1ud} -structure remains unstable with a formation energy of 0.14 eV per Pt-Pt dimer, while the formation energy of the Pt-Ge dimers in all other β -structures ranges from -0.19 eV to -0.35 eV per Pt-Ge dimer, the same range as to what is found in LDA calculations. Just as was found in the LDA calculations, the β_{6u} -geometry is also in GGA calculations the second most stable structure after the β_{4u} -geometry. Also the preference for Pt_u-Ge rows is retained, so we can conclude that the relative stability remains unchanged under GGA, although a general increase of stability is observed. This increased stability is the result of the decreased stability of Pt bulk in GGA (compared to LDA). Because we are using the Pt bulk energy as reference energy in Eq. (3.1) an increase in stability of the systems is observed in GGA.

Looking at the γ -structures, we see again that the formation energy per Pt-Ge dimer of the γ_1 -structure is the average of that of the β_{4u} - and β_{4d} -structures. Also the formation energy of the Pt-Ge dimers in the β_{5ud} -, γ_2 - and γ_3 -structures is the same (within the error), showing that also under GGA there is limited interaction between neighboring dimer rows.

For Pt atoms imbedded in the second layer, an increased stability is found as well. Also the relative stability between *up* and *down* positions is maintained.

For Pt atoms imbedded in the third layer the stability only increase only marginally, in some cases it even does not anymore. However, the same relative stability trends are found as for the LDA calculations, *e.g.* the cost for removal of the second layer pushed up Ge atoms is the same for LDA and GGA.

This leaves us to conclude that the use of either LDA or GGA functionals does not lead to qualitative different conclusions for the Pt modified Ge(001) surface reconstructions. The only qualitative difference present is the increased preference for Pt in the top layer of the system, making the top layer imbedding more competitive than was the case in the LDA calculations.

C.3 Nanowires

For the nanowire systems, Table C.3 shows the GGA versions of Tables 4.1, 4.2, 4.3 and 4.4 joined together. Formation energies are given per 4×2 surface unit cell, and adsorption energies per adatom. In general the formation energies improve going from LDA to GGA calculations while maintaining their relative stability. This behavior has the same origin as was explained above in Sec. C.2.

With all four tables placed together, the increasing stability for every further model substrate becomes very clear. This behavior is independent of the LDA/GGA functionals. The adsorption energies become slightly worse than the LDA case, with GGA favoring the Pt NWs in case of the γ_c -surface of the second model set (*cf.* Sec. 4.3.4). Also in case of the γ_{as} -surface reconstructions the Pt nanowires have a

Table C.3: GGA formation and adsorption energies for Chapter 4.

First model			Second model		
	E_f (meV)	E_{ad} (meV)		E_f (meV)	E_{ad} (meV)
β_{6u} B _{a1}	-1186	-260	γ_c Ge NW	-1083	-75
β_{6u} B _{a2}	1513	1090	γ_c Pt NW	-1323	-195
β_{6u} T _{a1}	-104	281	γ_c Ge NW \times 2	-649	71
β_{6u} T _{a2}	-675	-4	γ_c Pt NW \times 2	-993	-15
β_{6u} B _{d1}	525	596	γ_{as} Ge NW	-1597	-130
β_{6u} B _{d2}	-1033	-183	γ_{as} Pt NW	-1576	-119
β_{6u} T _{d1}	-1379	-357	γ_{as2} bare	617	-
β_{6u} T _{d2}	230	448	γ_{as2} Pt NW	-1420	-41
Ge(001) B _{d1}	1217	609	γ_{as} Pt+Ge NW	-1863	-143
Ge(001) B _{d2}	1608	804	γ_{as} Pt+Pt NW	116	846
Ge(001) T _{d1}	109	54	γ_{as2} Pt+Ge NW	-943	238
Ge(001) T _{d2}	151	76	γ_{as2} Pt+Pt NW	-1006	207

Third model			Nec plus ultra		
	E_f (meV)	E_{ad} (meV)		E_f (meV)	E_{ad} (meV)
γ_{as}^* bare	-2393	-	With a sunken Ge atom at each T-site of the trough.		
γ_{as2}^* bare	-1677	-	γ_{as}^* Ge NW	-3180	420
γ_{as}^* Ge NW A	-2958	-282	γ_{as}^* Pt NW	-2902	559
γ_{as}^* Pt NW A	-2290	52	γ_{as}^* Pt NW [†]	-4286	-132
γ_{as}^* Ge NW C	-3997	-802	γ_{as2}^* Ge NW	-2288	654
γ_{as}^* Pt NW C	-3856	-732	γ_{as2}^* Pt NW	-4022	-213
γ_{as2}^* Ge NW A	-2015	-169	With sunken Pt atoms at the T-sites of the trough.		
γ_{as2}^* Pt NW A	-2440	-381	γ_{as}^* 2T Ge NW	-5225	-684
γ_{as2}^* Ge+Ge NW	-2054	-19	γ_{as}^* 1T Ge NW	-4216	-527
γ_{as2}^* Ge+Pt NW	-1924	46	γ_{as2}^* 1T Ge NW	-3218	-28
γ_{as2}^* Pt+Ge NW	-2503	-31	γ_{as}^* 0.5T Ge NW	-3665	-707
γ_{as2}^* Pt+Pt NW	-248	1096	[†] with ejected Ge atom		

stability comparable to the Ge NW.

For the surfaces and wires of the third model (*cf.* **Sec. 4.3.5**) the relative behavior remains the same, with C adsorption sites for Ge being ~ 0.6 eV more stable than the A site on γ_{as}^* . Only in case of the γ_{as2}^* -surface, the Pt NW is slightly more stable than the Ge NW.

Similar as for the LDA calculations we find the structures with sunken Pt and Ge atoms to have very high formation energies. More importantly we see the NW2-structure (aka γ_{as}^* 0.5T Ge NW) to have the highest adsorption energy of all. The NW2-structure also has 0.5 eV higher adsorption energy than the NW1-structure in GGA, making it much more stable in comparison, while in LDA calculations this difference was only 0.2 eV.

Table C.4: GGA formation and adsorption energies for Chapter 5.

CO on NW1			
	E_f (eV)	E_{ad}^g (eV)	E_{ad}^s (eV)
NW1 A1	-0.618	-1.184	-1.272
NW1 A2	-0.990	-1.331	-1.427
NW1 A3 a	0.125	0.49	-1.218
NW1 A3 b	-0.338	-1.036	-1.528
NW1 A3 b1	-0.009	-1.215	-1.647
NW1 A3 b2	1.300	-1.100	-1.507
NW1 A4	-1.972	-1.288	-1.374
NW1 A7	-0.969	-1.475	-1.647
NW1 A7 _{2CO}	-1.962	-1.340	-1.487
NW1 A5	-0.791	-0.048	-0.131
NW1 A6	0.164	-0.063	-0.197
CO on NW2			
	E_f (eV)	E_{ad}^g (eV)	E_{ad}^s (eV)
NW2 B1	-0.878	-1.547	-1.727
NW2 B2	-0.429	-1.306	-1.400
NW2 B3	-0.577	-1.409	-1.510
NW2 B5	-0.332	-1.279	-1.456
NW2 B4	-0.041	-0.391	-0.528

One important difference between the LDA and GGA values in case of the NWs is the fact that for the GGA functional the stability of the γ_{as} and γ_{as2} (and similar γ_{as}^* and γ_{as2}^*) structures is reversed, making the formations paths shown in Fig. 4.17 of Chapter 4 successions of ever more stable structures.

C.4 CO on Pt induced NWs

In this section we present the GGA values of the formation and binding energies of CO molecules on the NW1 and NW2 substrates, in comparison to the values presented in Chapter 5. Table C.4 combines the GGA versions of Tables 5.1, 5.3 and 5.4. All formation energies are given per 4×2 surface unit cell, and the adsorption energies E_{ad}^g and E_{ad}^s are given per CO molecule. E_{ad}^g and E_{ad}^s are calculated using Eq. (5.2), the former using the formation energy of the relaxed CO molecule, while for the later the formation energy of the stretched CO molecule is used.¹

¹This was done by removing the surface slab from the cell, fixing the carbon and oxygen atoms and performing a self-consistent calculation.

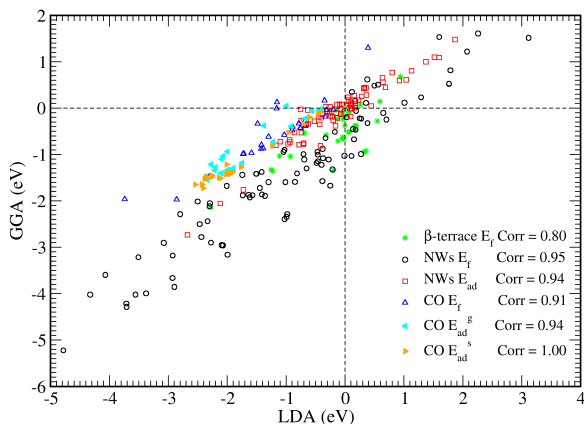


Figure C.1: Correlation between LDA and GGA formation and adsorption energies.

Table C.4 shows a large decrease in formation energies for all structures, in some cases this decrease goes up to almost 2 eV. For the adsorption energies a decrease is observed as well, albeit rather of the order of 0.5 eV.

As was the case for the LDA calculations, the GGA calculations also show the CO molecule adsorbed on Ge to have a binding energy roughly 1 eV lower than when adsorbed on Pt. If the stretching of the CO molecule is taken into account, the relative stability does not change. However, for the E_{ad}^g values the relative stability has changed pushing back the A3b from the highest stability to the one but lowest for adsorption on Pt, for the structures shown in Table 5.1. Here I would like to point at the fact that we did not relax the structures to obtain their GGA energies, which means the error bar on these values is larger than was the case for the LDA calculations. Since the stretching of the CO molecule has a large non-linear influence on the binding energy values obtained, taking these into account will give a better relative behavior.

The bridging CO geometries A7 and A7_{2CO}, which we propose as possible 1D molecular system remain, just as for the LDA case, the most stable adsorption geometries.

Although the transition from LDA to GGA shows some changes in the relative adsorption energies, the qualitative conclusions remain the same: CO does not bind on top of the NWs, instead it binds to the Pt atoms lining the trough, and, there exist highly stable bridging CO configurations which might be interesting with regard to 1D molecular electronics.

C.5 Correlating LDA and GGA values

In this last section we approach the transition from LDA to GGA functionals from a different angle. We do this through looking at the correlation of the formation energies and adsorption energies. Figure C.1 shows a scatter plot of the data sets containing all structures studied in **Chapter 3** (β -terrace), **Chapter 4** (NWs), and **Chapter 5** (CO). The correlations (Corr) are given in the legend of Fig. C.1. It is clear that all data sets have a very high correlation, which means LDA and GGA give the same qualitative results. This independence of our qualitative conclusions only makes them stronger.

Appendix D

List of abbreviations and symbols

In the following the symbols for natural constants and abbreviations used in this thesis are listed. Abbreviations for chemical elements and molecules are omitted.

Abbreviations

1D	one dimensional
2D	two dimensional
3D	three dimensional
AE	all-electron
APM	atomic pinball machine
BG	band gap
BZ	Brillouin zone
CA	Ceperley-Alder
CB	conduction band
CDW	charge density wave
CPU	central processing unit
DB	domain boundary
DFT	density functional theory
DOS	density of states
FFT	fast Fourier transform
GA	genetic algorithm
GGA	generalized gradient approximation
GUI	graphical user interface
GWA	GW approximation
HF	Hartree-Fock
HKS	Hohenberg-Kohn-Sham

IBM	International Business Machines Corporation
LC	linear combination
LDA	local density approximation
LDOS	local density of states
ML	monolayer
NCPP	norm-conserving pseudo-potentials
NW	nanowire
PAW	projector augmented waves
PP	pseudo-potentials
PW91	Perdew-Wang 91
QM	quantum mechanics
RT	room temperature
SARA	Stichting Academisch Rekencentrum Amsterdam
STM	scanning tunneling microscope/microscopy
TDC	tetramer-dimer-chain
UHV	ultra-high vacuum
USPP	Ultra-Soft pseudo-potentials
VASP	Vienna Ab-initio Simulation Package
VB	valence band
WT	widened trough
QDR	quasi-dimer row

Constants

e	elementary charge	$1.602176487(40) \times 10^{-19} \text{ C}$
\hbar	Planck constant/ (2π)	$1.054571596(82) \times 10^{-34} \text{ J s}$
m_e	electron mass	$9.10938188(72) \times 10^{-31} \text{ kg}$
N_A	Avogadro's number	$6.02214179(30) \times 10^{23} \text{ mol}^{-1}$
ε_0	electric constant	$8.8541878 \dots \times 10^{-12} \text{ C}^2 \text{ J}^{-1} \text{ m}^{-1}$
π	ratio of the circumference to the diameter of a circle in Euclidean space	$3.14159265 \dots$

ibliography

- [1] G. E. Moore, “Cramming more components onto integrated circuits,” *Electronics*, vol. 38, p. 8, 1965. [1](#)
- [2] M. Kanellos, “New life for Moore’s law,” *news.cnet.com*, 2005. [1](#)
- [3] R. Kurzweil, “The law of accelerating returns,” *KurzweilAI.net*, 2001-03-07. [1](#), [68](#)
- [4] J. V. Barth, G. Constantini, and K. Kern, “Engineering atomic and molecular nanostructures at surfaces,” *Nature*, vol. 437, pp. 671–679, 2005. and references therein. [1](#), [2](#), [36](#), [68](#), [139](#)
- [5] J. Shen, R. Skomski, M. Klaua, H. Jenniches, S. S. Manoharan, and J. Kirschner, “Magnetism in one dimension: Fe on Cu(111),” *Phys. Rev. B*, vol. 56, pp. 2340–2343, Aug 1997. [1](#), [68](#)
- [6] J. Dorantes-Dávila and G. M. Pastor, “Magnetic anisotropy of one-dimensional nanostructures of transition metals,” *Phys. Rev. Lett.*, vol. 81, pp. 208–211, Jul 1998. [1](#), [68](#)
- [7] P. Gambardella, A. Dallmeyer, K. Maiti, M. C. Malagoli, W. Eberhardt, K. Kern, and C. Carbone, “Ferromagnetism in one-dimensional monatomic metal chains,” *Nature*, vol. 416, pp. 301–303, 2002. [1](#), [2](#), [68](#)
- [8] N. Nilius, T. M. Wallis, and W. Ho, “Development of one-dimensional band structure in artificial gold chains,” *Science*, vol. 297, pp. 1853–1856, 2002. [1](#), [68](#)
- [9] J. N. Crain and D. T. Pierce, “End states in one-dimensional atom chains,” *Science*, vol. 307, pp. 703–706, 2005. [1](#), [68](#)
- [10] J. Lagoute, X. Liu, and S. Folsch, “Electronic properties of straight, kinked, and branched Cu/Cu(111) quantum wires: A low-temperature scanning tunneling microscopy and spectroscopy study,” *Phys. Rev. B*, vol. 74, p. 125410, 2006. [1](#), [68](#)

- [11] D. K. Lim, D. Lee, H. Lee, S. Bae, J. Choi, S. Kim, C. Ji, R. Ragan, D. A. A. Ohlberg, Y. A. Chang, and R. S. Williams, "Structure and electronic properties of self-assembled Pt silicide nanowires on Si(100)," *Nanotechnology*, vol. 18, no. 9, p. 095706, 2007. [1](#), [68](#)
- [12] J. Hong, "Ferromagnetic one-dimensional tungsten atomic chain: Magnetic anisotropy and x-ray magnetic circular dichroism study," *Phys. Rev. B*, vol. 76, p. 092403, 2007. [1](#), [68](#)
- [13] J. M. Luttinger, "An exactly soluble model of a many-fermion system," *J. Math. Phys.*, vol. 4, pp. 1154–1162, 1963. [2](#), [68](#)
- [14] H. W. Yeom, S. Takeda, E. Rotenberg, I. Matsuda, K. Horikoshi, J. Schaefer, C. M. Lee, S. D. Kevan, T. Ohta, T. Nagao, and S. Hasegawa, "Instability and charge density wave of metallic quantum chains on a silicon surface," *Phys. Rev. Lett.*, vol. 82, pp. 4898–4901, Jun 1999. [2](#), [68](#)
- [15] Z. Yao, H. W. C. Postma, L. Balents, and C. Dekker, "Carbon nanotube intramolecular junctions," *Nature*, vol. 402, pp. 273–276, 1999. [2](#), [68](#)
- [16] D. M. Eigler and E. K. Schweizer, "Positioning single atoms with a scanning tunneling microscope," *Nature*, vol. 344, pp. 524–526, 1990. [2](#), [68](#)
- [17] A. I. Yanson, G. R. Bollinger, H. E. van den Brom, N. Agrait, and J. M. van Ruitenbeek, "Formation and manipulation of a metallic wire of single gold atoms," *Nature*, vol. 395, pp. 783–785, 1998. [2](#), [68](#)
- [18] O. Gürlü, O. A. O. Adam, H. J. W. Zandvliet, and B. Poelsema, "Self-organized, one-dimensional Pt nanowires on Ge(001)," *Appl. Phys. Lett.*, vol. 83, pp. 4610–4612, 2003. [2](#), [36](#), [37](#), [41](#), [60](#), [68](#), [69](#), [71](#), [76](#), [101](#), [107](#), [108](#), [114](#), [137](#), [140](#), [141](#)
- [19] J. Wang, M. Li, and E. J. Altman, "Scanning tunneling microscopy study of self-organized Au atomic chain growth on Ge(001)," *Phys. Rev. B*, vol. 70, p. 233312, 2004. [2](#), [36](#), [68](#), [140](#)
- [20] J. Wang, M. Li, and E. J. Altman, "Scanning tunneling microscopy study of Au growth on Ge(001): Bulk migration, self-organisation, and clustering," *Surf. Sci.*, vol. 596, pp. 126–143, 2005. [2](#), [36](#), [68](#), [140](#)
- [21] C. Eames, C. Bonet, M. I. J. Probert, S. P. Tear, and E. W. Perkins, "STM and ab initio study of holmium nanowires on a Ge(111) surface," *Phys. Rev. B*, vol. 74, no. 19, p. 193318, 2006. [2](#), [68](#), [140](#)
- [22] S. Pelletier, E. Ehret, B. Gautier, F. Palmino, and J. C. Labrune, "Scanning tunneling microscopy study of the Er/Ge(111) $c(2 \times 8)$ interface," *J. Vac. Sci. Technol. A*, 2000. [2](#), [140](#), [141](#)

- [23] D. H. Rich, T. Miller, and T.-C. Chiang, “Electronic and chemical properties of In and Sb adsorbed on Ge(100) studied by synchrotron photoemission,” *Phys. Rev. B*, vol. 41, pp. 3004–3016, Feb 1990. [2](#), [140](#)
- [24] G. Falkenberg, O. Bunk, R. L. Johnson, J. A. Rodriguez, and N. Takeuchi, “Atomic structure of the indium-induced Ge(001)($n \times 4$) surface reconstruction determined by scanning tunneling microscopy and ab initio calculations,” *Phys. Rev. B*, vol. 66, p. 035305, Jul 2002. [2](#), [140](#), [141](#)
- [25] J. Schäfer, C. Blumenstein, S. Meyer, M. Wisniewski, and R. Claessen, “New model system for a one-dimensional electron liquid: Self-organized atomic gold chains on Ge(001),” *Phys. Rev. Lett.*, vol. 101, no. 23, p. 236802, 2008. [2](#), [68](#), [82](#), [140](#), [141](#)
- [26] A. van Houselt, T. Gnielka, J. M. J. Aan de Brugh, N. Öncel, D. Kockmann, R. Heid, K. P. Bohnen, B. Poelsema, and H. Zandvliet, “Peierls instability in platinum chains on Ge(001),” *Surf. Sci.*, vol. 602, no. 10, pp. 1731–1735, 2008. [3](#), [70](#), [95](#), [115](#)
- [27] N. Öncel, A. van Houselt, J. Huijben, A. S. Hallback, O. Gürlü, H. J. W. Zandvliet, and B. Poelsema, “Quantum confinement between self-organized Pt nanowires on Ge(001),” *Phys. Rev. Lett.*, vol. 95, p. 116801, 2005. [3](#), [36](#), [37](#), [49](#), [70](#), [103](#), [105](#), [140](#)
- [28] J. Schäfer, D. Schrupp, M. Preisinger, and R. Claessen, “Conduction states with vanishing dimerization in Pt nanowires on Ge(001) observed with scanning tunneling microscopy,” *Phys. Rev. B*, vol. 74, no. 4, p. 041404, 2006. [3](#), [36](#), [68](#), [69](#), [140](#)
- [29] R. J. de Vries, A. Saedi, D. Kockmann, A. van Houselt, B. Poelsema, and H. J. W. Zandvliet, “Spatial mapping of the inverse decay length using scanning tunneling microscopy,” *Appl. Phys. Lett.*, vol. 92, p. 174101, 2008. [3](#), [70](#)
- [30] A. Saedi, A. van Houselt, R. van Gastel, B. Poelsema, and H. J. W. Zandvliet, “Playing pinball with atoms,” *Nano Letters*, vol. 9, no. 5, pp. 1733–1736, 2009. [3](#)
- [31] N. Öncel, W. J. van Beek, J. Huijben, B. Poelsema, and H. J. W. Zandvliet, “Diffusion and binding of CO on Pt nanowires,” *Surf. Sci.*, vol. 600, pp. 4690–4693, 2006. [4](#), [114](#), [117](#), [122](#), [123](#), [124](#), [130](#)
- [32] D. Kockmann, B. Poelsema, and H. J. W. Zandvliet, “Remarkably long-ranged repulsive interaction between adsorbed CO molecules on Pt modified Ge(001),” *Phys. Rev. B*, vol. 78, p. 245421, 2008. [4](#), [114](#), [120](#), [123](#), [128](#), [129](#)
- [33] P. E. Blöchl, “Projector augmented-wave method,” *Phys. Rev. B*, vol. 50, pp. 17953–17979, Dec 1994. [7](#), [17](#), [37](#), [69](#), [115](#)

- [34] G. Kresse and D. Joubert, “From ultrasoft pseudopotentials to the projector augmented-wave method,” *Phys. Rev. B*, vol. 59, pp. 1758–1775, Jan 1999. [7](#), [17](#), [37](#), [69](#), [115](#)
- [35] E. Schrödinger, “An undulatory theory of the mechanics of atoms and molecules,” *Phys. Rev.*, vol. 28, pp. 1049–1070, Dec 1926. [7](#)
- [36] M. Born and J. R. Oppenheimer, “Zur Quantentheorie der Molekeln,” *Ann. Physik*, vol. 84, p. 457, 1927. [8](#)
- [37] W. Pauli, “Über den Zusammenhang des Abschlusses der Elektronengruppen im Atom mit der Komplex Struktur der Spektren,” *Z. Phys.*, vol. 31, p. 765, 1925. [9](#)
- [38] B. H. Bransden and C. J. Joachain, *Physics of atoms and molecules*. Pearson Education, 2 ed., 2003. [9](#), [10](#), [11](#)
- [39] J. C. Slater, “The theory of complex spectra,” *Phys. Rev.*, vol. 34, pp. 1293–1322, Nov 1929. [9](#)
- [40] G. B. Arfken and H. J. Weber, *Mathematical Methods for Physicists*. Burlington: Harcourt Academic Press, 5 ed., 2001. International Edition. [10](#)
- [41] L. Euler, *Mechanica, sive motus scientia analytice exposita*. St. Petersburg: , 1736. [10](#)
- [42] V. Fock, “Näherungsmethode zur Lösung des quantenmechanischen Mehrkörperproblems,” *Z. Phys.*, vol. 61, pp. 126–148, 1930. [11](#)
- [43] R. M. Martin, *Electronic Structure, Basic Theory and Practical Methods*. Cambridge University Press, 1 ed., 2004. [11](#)
- [44] P. J. Mohr, B. N. Taylor, and D. B. Newell, “CODATA recommended values of the fundamental physical constants: 2006,” *Rev. Mod. Phys.*, vol. 80, no. 2, p. 633, 2008. [11](#)
- [45] A. Avogadro, “Essai d’une manière de déterminer les masses relatives des molécules élémentaires des corps, et les proportions selon lesquelles elles entrent dans ces combinaisons,” *Journal de Physique*, vol. 73, pp. 58–76, 1811. [11](#)
- [46] P. Hohenberg and W. Kohn, “Inhomogeneous electron gas,” *Phys. Rev.*, vol. 136, pp. B864–B871, Nov 1964. [11](#)
- [47] W. Kohn and L. J. Sham, “Self-consistent equations including exchange and correlation effects,” *Phys. Rev.*, vol. 140, pp. A1133–A1138, Nov 1965. [11](#), [13](#)
- [48] I. Turek, V. Drchal, J. Kudrnovsky, M. Sob, and P. Weinberger, *Electronic Structure of Disordered Alloys, Surfaces and Interfaces*. Norwell, Massachusetts: Kluwer Academic Publishers, 1997. [13](#)

- [49] G. Floquet, “Sur les équations différentielles linéaires à coefficients périodiques,” *Ann. École Norm. Sup.*, vol. 12, pp. 47–88, 1883. [14](#)
- [50] F. Bloch, “Über die Quantenmechanik der Elektronen in Kristallgittern,” *Z. Phys.*, vol. 52, pp. 555–600, 1928. [14](#)
- [51] H. Hellmann, *Einführung in die Quantumchemie*. Leipzig: Franz Deutsche, 1937. [14](#)
- [52] R. P. Feynman, “Forces in molecules,” *Phys. Rev.*, vol. 56, pp. 340–343, Aug 1939. [14](#)
- [53] P. Pulay, “Ab initio calculation of force constants and equilibrium geometries in polyatomic molecules I. Theory,” *Mol. Phys.*, vol. 17, no. 2, pp. 197–204, 1969. [14](#)
- [54] E. Fermi, “Sopra lo spostamento per pressione delle righe elevate delle serie spettrali,” *Nuovo Cimento*, vol. 11, no. 3, pp. 157–166, 1934. [14](#)
- [55] D. R. Hamann, M. Schlüter, and C. Chiang, “Norm-conserving pseudopotentials,” *Phys. Rev. Lett.*, vol. 43, pp. 1494–1497, Nov 1979. [15](#), [16](#)
- [56] G. P. Kerker, “Non-singular atomic pseudopotentials for solid state applications,” *J. Phys. C: Sol. State Phys.*, vol. 13, no. 9, pp. L189–L194, 1980. [16](#)
- [57] D. Vanderbilt, “Optimally smooth norm-conserving pseudopotentials,” *Phys. Rev. B*, vol. 32, pp. 8412–8415, Dec 1985. [16](#)
- [58] N. Troullier and J. L. Martins, “Efficient pseudopotentials for plane-wave calculations,” *Phys. Rev. B*, vol. 43, pp. 1993–2006, Jan 1991. [16](#)
- [59] P. E. Blöchl, “Generalized separable potentials for electronic-structure calculations,” *Phys. Rev. B*, vol. 41, pp. 5414–5416, Mar 1990. [17](#)
- [60] D. Vanderbilt, “Soft self-consistent pseudopotentials in a generalized eigenvalue formalism,” *Phys. Rev. B*, vol. 41, pp. 7892–7895, Apr 1990. [17](#)
- [61] G. Binnig, H. Rohrer, C. Gerber, and E. Weibel, “Tunneling through a controllable vacuum gap,” *Appl. Phys. Lett.*, vol. 40, no. 2, pp. 178–180, 1982. [18](#)
- [62] G. Binnig, H. Rohrer, C. Gerber, and E. Weibel, “Surface studies by scanning tunneling microscopy,” *Phys. Rev. Lett.*, vol. 49, pp. 57–61, Jul 1982. [18](#)
- [63] G. Binnig, H. Rohrer, C. Gerber, and E. Weibel, “ 7×7 reconstruction on Si(111) resolved in real space,” *Phys. Rev. Lett.*, vol. 50, pp. 120–123, Jan 1983. [18](#)
- [64] The Royal Swedish Academy of Sciences, “The nobel prize in physics 1986,” *nobelprize.org*, 1986. [18](#)

- [65] M. L. Bocquet and P. Sautet, "STM and chemistry: a qualitative molecular orbital understanding of the image of CO on a Pt surface," *Surf. Sci.*, vol. 360, no. 1-3, pp. 128–136, 1996. [20](#), [114](#), [122](#), [127](#)
- [66] M. Ø. Pedersen, M.-L. Bocquet, P. Sautet, E. Lægsgaard, I. Stensgaard, and F. Besenbacher, "CO on Pt(111): binding site assignment from the interplay between measured and calculated STM images," *Chem. Phys. Lett.*, vol. 299, pp. 403–409, 1999. [20](#), [114](#), [122](#)
- [67] J. Tersoff and D. R. Hamann, "Theory and application for the scanning tunneling microscope," *Phys. Rev. Lett.*, vol. 50, pp. 1998–2001, Jun 1983. [20](#)
- [68] J. Tersoff and D. R. Hamann, "Theory of the scanning tunneling microscope," *Phys. Rev. B*, vol. 31, pp. 805–813, Jan 1985. [20](#), [43](#), [69](#), [115](#)
- [69] J. Bardeen, "Tunnelling from a many-particle point of view," *Phys. Rev. Lett.*, vol. 6, pp. 57–59, Jan 1961. [20](#)
- [70] M. J. Winter, "Webelements," <http://www.webelements.com/>, 1993. [22](#), [23](#)
- [71] D. M. Ceperley and B. J. Alder, "Ground state of the electron gas by a stochastic method," *Phys. Rev. Lett.*, vol. 45, pp. 566–569, Aug 1980. [22](#), [37](#)
- [72] J. P. Perdew and A. Zunger, "Self-interaction correction to density-functional approximations for many-electron systems," *Phys. Rev. B*, vol. 23, pp. 5048–5079, May 1981. [22](#)
- [73] J. P. Perdew and Y. Wang, *Electronic Structure of Solids '91*. Berlin: Academic Verlag, 1991. p. 11. [22](#)
- [74] M. Rohlfing, P. Krüger, and J. Pollmann, "Quasiparticle band-structure calculations for C, Si, Ge, GaAs, and SiC using gaussian-orbital basis sets," *Phys. Rev. B*, vol. 48, pp. 17791–17805, Dec 1993. [23](#), [24](#), [25](#)
- [75] C. Kittel, *Introduction to Solid State Physics*. New York: John Wiley and Sons, Inc., 7 ed., 1996. p. 57. [23](#)
- [76] M. Needels, M. C. Payne, and J. D. Joannopoulos, "High-order reconstructions of the Ge(100) surface," *Phys. Rev. B*, vol. 38, pp. 5543–5546, Sep 1988. [32](#), [37](#)
- [77] M. Needels, M. C. Payne, and J. D. Joannopoulos, "Ab initio molecular dynamics on the Ge(100) surface," *Phys. Rev. Lett.*, vol. 58, pp. 1765–1768, Apr 1987. [33](#), [37](#), [42](#)
- [78] S. J. Jenkins and G. P. Srivastava, "Theoretical evidence concerning mixed dimer growth on Si(001)(2×1)-Ge surface," *J. Phys.: Condens. Matter.*, vol. 8, pp. 6641–6651, 1996. [33](#), [37](#)

- [79] S. C. A. Gay and G. P. Srivastava, "Dimer length variation for different reconstructions of Si, Ge, and mixed Si-Ge dimers on Si(001) and Ge(001) substrates," *Phys. Rev. B*, vol. 60, pp. 1488–1491, Jul 1999. [33](#), [37](#), [42](#), [54](#), [56](#), [57](#)
- [80] P. Krüger and J. Pollmann, "Dimer reconstruction of diamond, Si, and Ge (001) surfaces," *Phys. Rev. Lett.*, vol. 74, pp. 1155–1158, Feb 1995. [34](#)
- [81] X. F. Lin, K. J. Wan, J. C. Glueckstein, and J. Nogami, "Gold-induced reconstruction of the Si(001) surface: The 5×3 and $\sqrt{26} \times 3$ phases," *Phys. Rev. B*, vol. 47, pp. 3671–3676, 1993. [36](#)
- [82] M. Kageshima, Y. Torii, Y. Tano, O. Takeuchi, and A. Kawazu, "Study of Au-induced reconstruction on Si(001) surface by scanning tunneling microscopy and low energy electron diffraction," *Surf. Sci.*, vol. 472, pp. 51–58, 2001. [36](#)
- [83] T. Shimakura, H. Minoda, Y. Tanishiro, and K. Yagi, "In-situ study of gold-induced surface structures and step rearrangements on the Si(001) surface by high-temperature STM," *Surf. Sci.*, vol. 407, pp. L657–L664, 1998. [36](#)
- [84] R. H. M. Smit, C. Untiedt, A. I. Yanson, and J. M. van Ruitenbeek, "Common origin for surface reconstruction and the formation of chains of metal atoms," *Phys. Rev. Lett.*, vol. 87, p. 266102, 2001. [36](#)
- [85] G. Kresse and J. Hafner, "Ab initio molecular dynamics for liquid metals," *Phys. Rev. B*, vol. 47, pp. 558–561, Jan 1993. [37](#), [69](#), [115](#)
- [86] G. Kresse and J. Furthmüller, "Efficient iterative schemes for ab initio total-energy calculations using a plane-wave basis set," *Phys. Rev. B*, vol. 54, pp. 11169–11186, Oct 1996. [37](#), [69](#), [115](#)
- [87] H. J. Monkhorst and J. D. Pack, "Special points for brillouin-zone integrations," *Phys. Rev. B*, vol. 13, pp. 5188–5192, Jun 1976. [37](#), [69](#), [115](#)
- [88] M. K. Niranjana, L. Kleinman, and A. A. Demkov, "Electronic structure, elastic properties, surface energies, and work function of NiGe and PtGe within the framework of density-functional theory for various surface terminations," *Phys. Rev. B*, vol. 75, p. 085326, 2007. [42](#), [75](#)
- [89] O. Gürlü, *On the Atomic and Electronic Structure of Clean and Pt Covered Si(001) and Ge(001) Surfaces*. PhD thesis, University of Twente, 2004. [48](#), [52](#)
- [90] A. van Houselt, N. Öncel, B. Poelsema, and H. Zandvliet, "Spatial mapping of the electronic states of a one-dimensional system," *Nano Letters*, vol. 6, no. 7, pp. 1439–1442, 2006. [49](#), [103](#), [105](#)
- [91] O. Gürlü, H. J. W. Zandvliet, B. Poelsema, S. Dag, and S. Ciraci, "Initial stages of Pt growth on Ge(001) studied by scanning tunneling microscopy and density functional theory," *Phys. Rev. B*, vol. 70, p. 085312, Aug 2004. [57](#), [137](#)

- [92] H. J. W. Zandvliet. private communication, 2008. 72
- [93] M. Fischer, A. van Houselt, D. Kockmann, B. Poelsema, and H. J. W. Zandvliet, "Formation of atomic Pt chains on Ge(001) studied by scanning tunneling microscopy," *Phys. Rev. B*, vol. 76, no. 24, p. 245429, 2007. 72, 76, 82, 140
- [94] A. van Houselt, *Structural and electronic properties of Pt/Ge(001) and Au/Ge(001)*. PhD thesis, University of Twente, 2008. 76
- [95] A. A. Stekolnikov, F. Bechstedt, M. Wisniewski, J. Schafer, and R. Claessen, "Atomic nanowires on the Pt/Ge(001) surface: Buried Pt-Ge versus top Pt-Pt chains," *Phys. Rev. Lett.*, vol. 100, no. 19, p. 196101, 2008. 77, 108
- [96] T. B. Massalski and H. Okamoto, *Binary Alloy Phase Diagrams*, vol. 1–3. Cleveland: ASM, 1990. 97, 138, 141
- [97] X. Zeng and H. E. Elsayed-Ali, "Time-resolved electron diffraction study of the Ge(100)-(2 × 1)-(1 × 1) phase transition," *Surf. Sci.*, vol. 497, p. 373, 2002. 97
- [98] D. E. P. Vanpoucke and G. Brocks, "Formation of Pt-induced Ge atomic nanowires on Pt/Ge(001): A density functional theory study," *Phys. Rev. B*, vol. 77, no. 24, p. 241308(R), 2008. 108, 114, 115, 140
- [99] A. A. Stekolnikov, J. Furthmüller, and F. Bechstedt, "Pt-induced nanowires on Ge(001): *Ab initio* study," *Phys. Rev. B*, vol. 74, p. 155434, 2008. 108, 109, 110, 140
- [100] A. Eichler, "CO oxidation on transition metal surfaces: reaction rates from first principles," *Surf. Sci.*, vol. 498, pp. 314–320, 2002. 113, 116
- [101] R. Imbihl and G. Ertl, "Oscillatory kinetics in heterogeneous catalysis," *Chem. Rev.*, vol. 95, pp. 697–733, 1995. 113
- [102] G. Ertl, M. Neumann, and K. M. Streit, "Chemisorption of CO on the Pt(111) surface," *Surf. Sci.*, vol. 64, pp. 393–410, 1977. 113
- [103] H. Froitzheim, H. Hopster, H. Ibach, and S. Lehwald, "Adsorption sites of CO on Pt(111)," *Appl. Phys.*, vol. 13, pp. 147–151, 1977. 113
- [104] H. Steininger, S. Lehwald, and H. Ibach, "On the adsorption of CO on Pt(111)," *Surf. Sci.*, vol. 123, pp. 264–282, 1982. 113
- [105] D. F. Ogletree, M. A. V. Hove, and G. A. Somorjai, "LEED intensity analysis of the structures of clean Pt(111) and of CO adsorbed on Pt(111) in the c(4 × 2) arrangement," *Surf. Sci.*, vol. 173, pp. 351–365, 1986. 113
- [106] Y. Y. Yeo, L. Vattuone, and D. A. King, "Calorimetric heats for CO and oxygen adsorption and for the catalytic CO oxidation reaction on Pt{001}," *J. Phys. Chem.*, vol. 106, no. 1, pp. 392–401, 1997. 113

- [107] P. J. Feibelman, B. Hammer, J. K. Norskov, F. Wagner, M. Scheffler, R. Stumpf, R. Watwe, and J. Dumesic, "The CO/Pt(111) puzzle," *J. Phys. Chem. B*, vol. 105, pp. 4018–4025, 2001. and references herein. [114](#)
- [108] P. van Beurden, H. G. J. Verhoeven, G. J. Kramer, and B. J. Thijsse, "Atomistic potential for adsorbate/surface systems: CO on Pt," *Phys. Rev. B*, vol. 66, p. 235409, Dec 2002. [114](#)
- [109] M. Alaei, H. Akbarzadeh, H. Gholizadeh, and S. de Gironcoli, "CO/Pt(111): GGA density functional study of site preference for adsorption," *Phys. Rev. B*, vol. 77, no. 8, p. 085414, 2008. [114](#)
- [110] I. Dabo, A. Wieckowski, and N. Marzari, "Vibrational recognition of adsorption sites for CO on platinum and platinum-ruthenium surfaces," *J. Am. Chem. Soc.*, vol. 129, pp. 11045–11052, 2007. [114](#)
- [111] G. Scлаuzero, A. D. Corso, A. Smogunov, and E. Tosatti, "Interaction of a CO molecule with a Pt monatomic wire: Electronic structure and ballistic conductance," *Phys. Rev. B*, vol. 78, no. 8, p. 085421, 2008. [114](#), [119](#), [121](#), [129](#)
- [112] K. Fukutani, T. T. Magkoev, Y. Murata, M. Matsumoto, T. Kawauchi, T. Magome, Y. Tezuka, and S. Shin, "Electronic structure of a Pt(111)-Ge surface alloy and adsorbed CO," *J. Electron Spectrosc. Relat. Phenom.*, vol. 88, pp. 597–601, 1998. [114](#)
- [113] O. R. Gilliam, C. M. Johnson, and W. Gordy, "Microwave spectroscopy in the region from two to three millimeters," *Phys. Rev.*, vol. 78, no. 2, pp. 140–144, 1950. [116](#)
- [114] R. Hirschl, F. m. c. Delbecq, P. Sautet, and J. Hafner, "Pt₈₀Fe₂₀ surface from first principles: Electronic structure and adsorption of CO and atomic H," *Phys. Rev. B*, vol. 66, p. 155438, Oct 2002. [116](#)
- [115] D. E. P. Vanpoucke and G. Brocks, "The formation of self-assembled nanowire arrays on Ge(001): a DFT study of Pt induced nanowire arrays," *MRS eproceedings 2009 spring meeting*, vol. Z, 2009. submitted. [120](#)
- [116] M. M. D. Ramos, A. P. Sutton, and A. M. Stoneham, "Effects of the STM tip on adsorbate image," *J. Phys.: Condens. Matter.*, vol. 3, no. S, pp. S127–S131, 1991. [123](#), [127](#)
- [117] N. Öncel, *Scanning Tunneling Microscopy and Spectroscopy Studies on Pt-Modified Ge(001) and Metallic (Pd,Au)-Quantum Dots on Self-Assembled Monolayers*. PhD thesis, University of Twente, 2007. [125](#), [126](#)
- [118] G. Falkenberg, L. Seehofer, and R. L. Johnson, "Structure and morphology of In on Ge(001) studied by scanning tunneling microscopy," *Surf. Sci.*, vol. 371, no. 1, pp. 86–94, 1997. [140](#), [141](#)

- [119] Q. Zhi-Hui, S. Dong-Xia, P. Shi-Jin, and G. Hong-jun, "STM study of In nanostructures formation on Ge(001) surface at different coverages and temperatures," *Chinese Physics B*, vol. 17, no. 3, p. 1055, 2008. 140
- [120] L. Seehofer, G. Falkenberg, and R. L. Johnson, "Structure and phases of In on Ge(001)," *Surf. Sci.*, vol. 352-354, pp. 425-429, 1996. Proceedings of the 15th European Conference on Surface Science. 140
- [121] A. R. Oganov and C. W. Glass, "Crystal structure prediction using ab initio evolutionary techniques: Principles and applications," *J. Chem. Phys.*, vol. 124, no. 24, p. 244704, 2006. 141, 142
- [122] C. J. Pickard and R. J. Needs, "High-pressure phases of silane," *Phys. Rev. Lett.*, vol. 97, no. 4, p. 045504, 2006. 141, 142
- [123] C. J. Pickard and R. J. Needs, "Metallization of aluminum hydride at high pressures: A first-principles study," *Phys. Rev. B*, vol. 76, no. 14, p. 144114, 2007. 141, 142
- [124] M. d'Avezac and A. Zunger, "Identifying the minimum-energy atomic configuration on a lattice: Lamarckian twist on Darwinian evolution," *Phys. Rev. B*, vol. 78, no. 6, p. 064102, 2008. 141
- [125] T. David and J. Goudonnet, "Simulation of the scanning of surface structures by STM tips of different shapes application to the Si(111)- 7×7 reconstruction," *Thin Solid Films*, vol. 223, no. 1, pp. 7-10, 1993. 143
- [126] Q.-M. Xu, L.-J. Wan, S.-X. Yin, C. Wang, and C.-L. Bai, "Effect of chemically modified tips on STM imaging of 1-octadecanethiol molecule," *J. Phys. Chem. B*, vol. 105, no. 43, pp. 10465-10467, 2001. 143
- [127] B. Cordero, V. Gomez, A. E. Platero-Prats, M. Reves, J. Echeverria, E. Cremades, F. Barragan, and S. Alvarez, "Covalent radii revisited," *Dalton Transactions*, no. 21, pp. 2832-2838, 2008. 144

Summary

The microelectronics industry is driven by the ever further miniaturization of electronic components and devices. Monatomic nanowires present the physical limits of miniaturization for wires, and much research interest is directed toward the construction of wires closer to this physical limit and understanding the associated physical phenomena. In 2003, Gürlü *et al.* observed self-assembled nanowire arrays after deposition of 0.25 ML of Pt on a clean Ge(001) surface and subsequent high temperature annealing. The NWs are equally spaced at 1.6 nm, virtually defect and kink free, and only a single atom wide while being hundreds of nanometers long. The NWs, dubbed Pt-nanowires, turn out not to be conductive. Instead, the regions between the NWs show conductive behavior. In experiment about 0.25 ML of Pt was deposited on a clean Ge(001) surface, and after high temperature annealing three types of terraces were observed: i) The α -terrace, showing a Ge(001) surface reconstruction riddled with dimer vacancies, ii) the β -terrace, showing dimer rows with two types of dimers, and iii) the NW arrays, which are always observed on a β -terrace. The presence of the three types of terraces suggests that the Pt is not distributed homogeneously over the surface.

In this thesis, we study this NW-system using *ab-initio* DFT calculations in combination with calculated STM images. Direct comparison of the latter with experimental STM images allowed us to identify the major observed reconstructions.

In **Chapter 1** we present an overview of the existing experimental research on ‘Pt nanowires’ on Ge(001). A short review of the theoretical background is given in **Chapter 2**, formulating some of the basic ideas behind the *ab-initio* calculations performed. In **Sec. 2.2** the idea behind STM is described and the Tersoff-Hamann approach for simulation of STM images was given. We also look at the (convergence) behavior of bulk Ge and the reconstructed Ge(001) surface in DFT, and the well known band gap problem was pointed out in **Sec. 2.3**.

In **Chapter 3** we start our study of the NW system by investigating the β -terrace. Since the on Ge(001) observed NWs are inherently connected to the β -terrace, a study of this β -terrace is a necessary first step toward understanding the formation of self-assembled NWs on Ge(001). Experimental STM images of the β -terrace show the presence of dimer rows with a $c(4 \times 2)$ symmetry, consisting of two different types of dimers. Starting from the assumption that the β -terrace contains 0.25 ML of Pt, or two Pt atoms per 4×2 surface unit cell, two Ge atoms in the first layer are substi-

tuted by Pt atoms, giving rise to seven different geometries. Taking into account the buckling of the surface dimers and the symmetry, the number of different geometries increases to ten. For all these structures, the formation energy per surface unit cell is calculated. The structure with the embedded Pt dimer turned out to be very unstable with a formation energy that is 0.4–0.7 eV per surface unit cell higher than of the other structures. For all other structures the formation energies per Pt-Ge surface dimer are found within a range of 150 meV, making them all accessible at the annealing temperature of > 1000 K.

STM images are calculated for all the structures, and it turns out that the filled state images can be composed of three different dimer images, each connected to a specific dimer geometry. i) A bright big round image for the Ge-Ge dimer. ii) A bright rectangular image for the Pt-Ge dimer with the Pt atom at the down side of the dimer. iii) A smaller dim round dimer for the Pt-Ge dimer with Pt at the up side of the dimer. Comparison to the experimental images allows us to identify the geometry of the β -terrace, on the basis of simple elimination. The only remaining structure is the β_{6u} -geometry, which has the second most favorable formation energy. In addition, this also allows us to identify the bright dimers in the experiment as Ge-Ge dimers, while the darker dimers are found to be Pt-Ge dimers, with the Pt atom at the dark side of the dimer. Furthermore, the experimentally observed triangular dark areas in the empty state images are only present in calculated empty state STM images of the β_{6u} geometry. This permits us to propose the β_{6u} -geometry as the structural model for the β -terrace.

In **Chapter 4**, starting from the structure found for the β -terrace, two simple scenarios for NW formation are proposed. In the first scenario the Pt atoms of the β -terrace are ejected onto the surface during annealing and form dimers in the troughs, thus creating the NW arrays. The vacancies in the top layer are then filled with Ge atoms from the bulk, in the course of which a normal Ge(001) surface is recovered. In this scenario a homogeneous Pt distribution of 0.25 ML is maintained. In the second scenario, the Pt atoms in the top layer of the β -terrace remain at their positions, but extra Pt atoms located deeper into the bulk are ejected onto the surface during annealing, and form dimers in the troughs of the β -terrace creating NW arrays.

For both scenarios several adsorption structures are examined, and the binding energy is calculated. The nanowire binding energies show the adsorption of Pt dimers on the Ge(001) and β_{6u} -surface to be very unstable. Calculated STM images of these structures reveal only one structure vaguely resembling a NW. This is the Pt dimer adsorbed in the trough, parallel to the dimer row of a Ge(001) surface. The Pt atoms bound to the Ge atoms of the surface dimers, which show up as bright dimers in the calculated STM images. Despite the resemblance to the experimental NWs some crucial differences are present. Besides having an unfavorable binding energy of ~ 0.4 eV per Pt dimer, the NW image is also located on top of the dimer row, in contradiction with experiment. Furthermore, specific image details, like the symmetric bulges are missing. However, this structure gives an important insight, namely, that experimentally observed NWs could consist of Ge atoms, since these are the atoms showing bright images in calculated STM pictures.

Based on these results, a second surface model was presented, containing 0.5 ML of Pt in the top layer. Pt and Ge dimers are placed in the Pt-lined trough of this new surface model and the formation and binding energies are calculated. The binding energy for the adsorbed Ge (Pt) dimer is -0.76 (-1.25) eV per dimer. Although the Pt dimer is more stable, this structure presents a problem. The calculated STM images of this structure show no NWs. At the position of the NW only a widened trough is visible in the image. Furthermore, the dimer row images have changed. Only one feature for every two dimers is visible in the calculated STM image. However, this image of a Pt NW adsorbed on this substrate model, shows very good agreement with the experimentally observed widened troughs, which are considered to be a precursor to the formation of the NWs.

In contrast, the calculated STM images of an adsorbed Ge NW show a very clear NW image, displaying most of the features observed in experimental NWs. However, some inconsistencies with the experiment remain, making this a good, but not the final model.

Geometrically, the Pt NW sinks into the trough while the Ge NW stays slightly above it. This directs us to a third surface model. In this final model the Ge atoms at the bottom of the Pt lined trough are replaced by Pt atoms. The adsorption of Pt dimers is marginally unstable on this surface model, while the binding energy of the Ge dimer is -1.04 eV. Furthermore, going from the structure with the Pt NW on the second surface model, *i.e.* the structure which showed good agreement with the experimentally observed widened trough, to this Ge dimer structure can be done by the exchange of the Pt NW dimer atoms with the Ge atoms at the bottom of the trough underneath. The gain in formation energy by this exchange is found to be 0.33 eV per dimer, indicating the spontaneous transformation from the widened trough to a Ge NW is energetically very favorable. The calculated STM images for this Ge NW show perfect agreement with the experimentally observed NWs. This means that the experimentally observed ‘Pt nanowires’ are composed of “*germanium atoms*”, explaining the unexpected lack of conductivity on the wires.

This however, is not yet the end of the story: one minor difference with experiment needs tackling. Experimentally a 4×1 periodicity is observed along a NW, but only for those NWs that are situated on the inside of a patch of NWs. Our calculations do not show this because of the size of the unit cell used, which is only half the length needed for this periodicity. Calculations for a doubled cell however show no spontaneous appearance of a 4×1 periodicity along the NW. The NW dimers remain flat. Even geometries starting with tilted dimers relax back to horizontal NW dimers. However, when extra Pt and/or Ge atoms are added to the trough, we find that by adding a single Pt atom per two Ge NW dimers a 4×1 periodicity can be obtained. This extra Pt atom resides at the bottom of the trough, and binds to two Ge NW dimers. This pins both dimers at their location and stabilizes the structure. It also pulls the dimers slightly inward tilting them over an angle of 3.6° , resulting in the observed 4×1 periodicity along the NW. This leads to the conclusion that the 4×1 periodicity is not caused by a Peierls instability.

In **Chapter 5**, we study the adsorption of CO molecules on the NWs. CO shows great promise with regard to engineering 1D molecular chains on ‘Pt nanowires’ be-

cause the sticking probability of CO is high for Pt, while it is low for Ge. This sticking probability combined with the experimental observation of CO on the NWs suggested a discrepancy with the model we proposed in **Chapter 4**.

In our study we show that CO molecules do not bind to the Ge NW itself, as is expected from their sticking probability and affinity. Contrary to the interpretation of the experimental observations we find the CO molecules to bind to the Pt atoms lining the trough in which the NW is located. We also show that the CO molecules tilt toward the NW giving rise to STM images of the molecule *on* the wire. An adsorption configuration where the O atom forms an additional bond with the Ge NW is shown to explain the RT observed adsorption site. And we show that CO molecules adsorbed on Pt atoms in between NW dimers act repulsively on these NW dimers. These displaced NW dimers in turn block nearby adsorption sites resulting in the experimentally observed “*long-ranged repulsive interaction*”. We also propose the existence of invisible bridging configurations. After removal of the NW dimers, a high density coverage of CO molecules could be obtained with these bridging configurations, transforming the former Ge NW location into a chain of parallel CO molecules, possibly opening the way to 1D molecular electronics, albeit in a slightly different way than was first imagined.

In **Chapter 6**, the answers are given to the questions we posed at the beginning of this thesis. We also look toward the future: the possibility of engineering metal induced NWs on semiconductor surfaces using *ab initio* calculations. The enormous phase spaces obtained when trying to model new systems from limited experimental data could be searched using calculated STM images as a possible fitness parameter.

amenvatting

De ontwikkeling van de micro-elektronica wordt voortgedreven door de steeds verder doorgedreven miniaturisatie van elektronische componenten. Bij de miniaturisatie van draden vormen monoatomaire nanodraden de fysische limiet. Heel wat onderzoeksinspanning gaat uit naar het creëren van draden die dichter tegen deze ultieme limiet aanliggen en naar het begrijpen van de bijhorende fysische fenomenen. In 2003 observeerden Gürlü *et al.* arrays van zelfgeassembleerde nanodraden na de depositie van een kwart monolaag Pt op een schoon Ge(001)-oppervlak, gevolgd door annealing op hoge temperatuur. De nanodraden, die slechts één atoom breed zijn en honderden nanometer lang, bevinden zich op een regelmatige afstand van 1.6 nm van elkaar. Ze vertonen geen knikken en zijn vrijwel zonder defecten. De platina-nanodraden, zoals ernaar wordt verwezen, blijken niet geleidend te zijn, terwijl de gebieden tussen de draden wel elektrisch geleidend gedrag vertonen. Bij de experimenten, zoals van Gürlü *et al.*, konden er drie types terrassen worden geobserveerd: i) het α -terras, bestaande uit een Ge(001)-oppervlak met vele ontbrekende dimeren, ii) het β -terras, bestaande uit dimeerrijen opgebouwd uit twee soorten dimeren, en iii) de arrays van nanodraden, die enkel op β -terrassen voorkomen. Het bestaan van de drie types terrassen suggereert een inhomogene verdeling van het Pt over het oppervlak.

In deze thesis bestuderen we dit nanodradensysteem met behulp van *ab initio* dichtheidsfunctionaaltheorie (DFT) berekeningen, gecombineerd met berekende raster-tunnel microscopie (STM) afbeeldingen. Op basis van de directe vergelijking van deze berekende afbeeldingen met experimentele STM afbeeldingen kon de geometrie van de belangrijkste reconstructies geïdentificeerd worden.

In **Hoofdstuk 1** geven we een overzicht van het bestaande experimentele onderzoek aan ‘Pt nanodraden op het Ge(001)-oppervlak’. Een korte bespreking van de theoretische achtergrond wordt gegeven in **Hoofdstuk 2**. Daar worden enkele van de basisideeën achter de uitgevoerde *ab initio* berekeningen beschreven. In **Sectie 2.2** beschrijven we kort de werking van STM evenals de Tersoff-Hamann benadering voor het simuleren van STM-afbeeldingen. Verder werd het convergentiegedrag in DFT van bulk Ge en het gereconstrueerde Ge(001)-oppervlak bekeken en wezen we op het bekende band gap probleem van Ge in **Sectie 2.3**.

In **Hoofdstuk 3** starten we onze studie van het nanodradensysteem met het onderzoeken van het β -terras. Gezien de op Ge(001) geobserveerde nanodraden inhe-

rent verbonden zijn aan het β -terras, is een studie van dit β -terras een noodzakelijke eerste stap wil men de vorming van zelfgeassembleerde nanodraden op Ge(001) begrijpen. De dimeerrijen, te zien in de experimentele STM-afbeeldingen van het β -terras, bestaan uit twee verschillende types dimeren en vertonen een $c(4 \times 2)$ symmetrie. Uitgaande van de aanname dat het β -terras een kwart monolaag Pt bevat, oftewel twee Pt-atomen per 4×2 oppervlakte-eenheidscel, werden twee Ge-atomen in de eerste laag van het systeem vervangen door Pt-atomen. Dit resulteert in zeven verschillende geometrieën. Wordt de symmetrie en de helling van de oppervlakte dimeren in rekening gebracht, dan verhoogt het aantal mogelijk geometrieën tot tien. Voor elk van deze structuren werd de vormingsenergie per oppervlakte-eenheidscel berekend. De structuur met het ingebouwde Pt-dimeer bleek zeer instabiel, met een vormingsenergie die 0.4–0.7 eV per oppervlakte-eenheidscel groter is dan de vormingsenergie voor de andere structuren. Bij alle andere systemen lagen de vormingsenergieën per Pt-Ge oppervlakedimeer binnen een interval van 150 meV, zodat al deze structuren energetisch bereikbaar bij een annealtemperatuur van > 1000 K.

Voor elke structuur zijn STM-afbeeldingen berekend. Hieruit blijkt dat alle ‘filled state’ afbeeldingen kunnen worden opgebouwd uit combinaties van drie verschillende dimeerbeelden, elk verbonden aan een specifieke dimeergeometrie. i) Een groot helder rond dimeerbeeld voor het Ge-Ge dimeer. ii) Een helder rechthoekig dimeerbeeld voor het Pt-Ge dimeer met het Pt-atoom langs de lage kant van de dimeerrij. iii) Een klein rond zwak dimeerbeeld voor het Pt-Ge dimeer met het Pt-atoom aan de hoge kant van de dimeerrij. Door vergelijking met de experimentele STM-afbeeldingen was het op basis van simpele eliminatie mogelijk de structuur van het β -terras te identificeren. Na eliminatie resteert enkel de β_{6u} -geometrie, welke de op één na beste vormingsenergie bezit. Dit laat daarenboven toe de experimenteel geobserveerde heldere dimeren te identificeren als Ge-Ge dimeren, en de donkere dimeren als Pt-Ge dimeren met het Pt-atoom aan de donkere zijde van het dimeer. Meer nog, de experimenteel geobserveerde driehoekige, donkere gebieden in de ‘empty state’ afbeeldingen komen enkel voor in de berekende STM-afbeeldingen van de β_{6u} -geometrie. Dit laat ons toe de β_{6u} -geometrie voor te stellen als model voor het β -terras.

In **Hoofdstuk 4**, startend vanuit de geometrie die we vonden voor het β -terras, worden twee eenvoudige scenarios voor de vorming van nanodraden voorgesteld. In het eerste scenario worden de Pt atomen van het β -terras tijdens het annealen uitgeworpen op het oppervlak en vormen deze dimeren in de geul tussen de dimeerrijen om zo arrays van nanodraden te vormen. De ontstane gaten in de dimeerrijen worden dan opgevuld met Ge-atomen uit de bulk waardoor opnieuw een normaal Ge(001)-oppervlak ontstaat. In dit scenario wordt een homogene Pt-verdeling van een kwart monolaag behouden. In het tweede scenario blijft het β -terras zelf intact maar worden extra Pt atomen van dieper in de bulk uitgeworpen tijdens het annealen. Deze extra Pt-atomen vormen dan net zoals in het eerste scenario de arrays van nanodraden.

Voor beide scenarios werden verschillende adsorptiestructuren bestudeerd en voor elke structuur werd de bindingsenergie berekend. De bindingsenergie van deze geadsorbeerde Pt-dimeren toonde dat zowel op het Ge(001)- (eerste scenario) als op het β_{6u} -oppervlak (tweede scenario) deze nanodraden zeer instabiel zijn. Berekende

STM-afbeeldingen van deze structuren toonden maar voor één systeem een beeld dat vage gelijkenissen vertoont met de experimenteel geobserveerde nanodraden. Dit was voor het Pt-dimeer dat parallel aan de dimeerrij in de geul van het Ge(001) oppervlak is geadsorbeerd. Deze Pt atomen vormen een binding met Ge atomen van de oppervlaktedimeren, welke op hun beurt als heldere dimeren in de berekende STM afbeeldingen verschenen. Ondanks de grote gelijkenis met de experimentele nanodraden waren enkele cruciale verschillen aanwezig. Buiten de ongunstige bindingsenergie van ~ 0.4 eV per Pt dimeer, lag de nanodraad afbeelding ook nog eens boven op de dimeerrij, in tegenspraak met wat in experimenten wordt gezien. Meer nog, specifieke details in het beeld, zoals de symmetrische bulten, ontbreken volledig. Desondanks levert deze structuur een belangrijk inzicht, namelijk dat de experimenteel geobserveerde nanodraden ook uit Ge atomen kunnen bestaan, gezien dit de atomen zijn welke de oorzaak van het heldere beeld in de berekende STM afbeeldingen zijn.

Op basis van deze resultaten wordt een tweede model, met een halve monolaag Pt in de bovenste laag, als substraatoppervlak voorgesteld. Zowel Pt- als Ge-dimeren worden in de met Pt afgezette goot van het nieuwe substraatmodel geplaatst en de vormings- en bindingsenergieën worden berekend. De bindingsenergie voor het geadsorbeerde Ge- (Pt-) dimeer is -0.76 (-1.25) eV per dimeer. Hoewel het Pt-dimeer een grotere stabiliteit vertoont, is er een ernstig probleem met deze structuur. In de berekende STM-afbeeldingen zijn er geen nanodraden zichtbaar. In plaats daarvan is op de positie van de Pt-nanodraad een verbrede goot zichtbaar in de berekende STM-afbeeldingen. Verder zijn ook de beelden van de dimeren van de dimeerrij veranderd. Voor elke twee opeenvolgende dimeren is er maar één beeld meer zichtbaar in de berekende STM-afbeeldingen. In tegenstelling tot de experimentele afbeeldingen van de nanodraden vertoont deze structuur wel een goede overeenkomst met de eveneens geobserveerde “verbrede goten”, welke gezien worden als een precursor bij de vorming van de nanodraden.

In tegenstelling tot de Pt-nanodraad geeft de Ge-nanodraad wel een heel duidelijk beeld van de nanodraad in de berekende STM-afbeeldingen. Dit beeld vertoont ook de meeste kenmerken van de experimenteel geobserveerde nanodraden. Niettemin zijn er nog steeds enkele inconsistenties met de experimentele afbeeldingen wat dit model ondanks de goede benadering toch geen definitief model maakt.

Geometrisch gezien zinkt de Pt-nanodraad in de goot terwijl de Ge-nanodraad een kleine afstand boven de goot hangt. Dit brengt ons bij een derde substraatmodel. In dit laatste model worden ook de Ge-atomen in de bodem van de met Pt-atomen afgelijnde goot vervangen door Pt-atomen. Op dit substraat blijken de Pt-dimeren net niet stabiel te zijn, terwijl de bindingsenergie van het Ge-addimeer -1.04 eV is. Meer nog, de overgang van de Pt-nanodraad op het tweede substraatmodel, *i.e.* de structuur welke een goede overeenkomst vertoont met de experimenteel geobserveerde verbrede goot, naar deze structuur met Ge-addimeer kan gebeuren door de uitwisseling van de Pt-nanodraad atomen in het eerste systeem met de Ge-atomen in de bodem van de onderliggende trog. De winst in vormingsenergie bij deze uitwisseling is 0.33 eV per dimeer van de nanodraad, wat erop wijst dat de spontane overgang van verbrede goot naar nanodraad energetisch zeer voordelig is. De berekende STM-afbeeldingen voor deze Ge-nanodraad tonen perfecte overeenkomst met

de experimenteel geobserveerde nanodraden. Dit betekent dat de experimenteel geobserveerde ‘Pt-nanodraden’ bestaan uit “*germanium atomen*”, wat het onverwachte gebrek aan elektrische geleidbaarheid van deze draden verklaart.

Dit is echter niet het einde van het nanodradenverhaal, er bestaat immers nog een klein verschil met de experimenten dat aangepakt dient te worden. Experimenteel wordt er een 4×1 periodiciteit langs de nanodraden waargenomen. Dit weliswaar enkel voor nanodraden die zich binnenin een array van nanodraden bevinden. Een dergelijke periodiciteit wordt niet in onze berekeningen teruggevonden gezien de gebruikte eenheidscel maar half de hiervoor benodigde lengte is. Berekeningen voor grotere eenheidcellen vertonen geen spontaan verschijnen van deze 4×1 periodiciteit langs de nanodraad. De dimeren waaruit de nanodraad is opgebouwd bleven vlak liggen. Zelfs structuren waarbij we met hellende nanodraaddimeren starten relaxeren terug naar vlakke dimeren. Daarentegen vinden we, na het toevoegen van extra Pt-en/of Ge-atomen in de goot met de nanodraad, dat het toevoegen van één Pt-atoom per twee Ge-nanodraaddimeren voldoende is om de 4×1 periodiciteit terug te vinden. Dit extra Pt-atoom bevindt zich op de bodem van de goot en vormt een binding met de twee aanliggende Ge nanodraaddimeren. Hierdoor worden beide nanodraaddimeren vastgepind op hun plaats en wordt de structuur gestabiliseerd. Deze bond trekt de Ge-dimeren ook lichtjes naar het extra Pt-atoom toe, wat een kleine helling met een hoek van 3.6° tot gevolg heeft. Dit resulteert in het verschijnen van de geobserveerde 4×1 periodiciteit langs de nanodraad. Hieruit kan geconcludeerd worden dat de 4×1 periodiciteit niet het gevolg is van een Peierls instabiliteit, maar wel een puur geometrisch effect.

In **Hoofdstuk 5** bestuderen we de adsorptie van CO-moleculen aan de nanodraden. Gezien de plakkans groot is voor CO op Pt en klein voor CO op Ge, wordt CO zeer beloftevol beschouwd met betrekking tot het ontwikkelen van 1D moleculaire draden op ‘Pt-nanodraden’. Deze plakkans in combinatie met de experimentele waarneming van CO-moleculen op de nanodraden suggereert een discrepantie met het model dat we in **Hoofdstuk 4** voorstelden.

In onze studie wordt aangetoond dat de CO-moleculen niet met de nanodraad zelf een verbinding vormen, zoals verwacht vanwege hun plakkans en -affiniteit. In tegenstelling tot de interpretatie van de experimentele waarnemingen vonden we dat de CO-moleculen wel een binding aangingen met de Pt-atomen welke de rand van de goot, waarin de nanodraad rust, bekleeden. We toonden eveneens aan dat de CO-moleculen naar de nanodraad toe buigen wat (berekende) STM-beelden van de CO-moleculen *op* de nanodraad tot gevolg heeft. Een adsorptieconfiguratie waarbij het O-atoom een extra verbinding vormt met de Ge-nanodraad blijkt de adsorptie site bij kamertemperatuur, waargenomen door Gürlü *et al.*, te verklaren. Verder wordt getoond dat CO-moleculen, geadsorbeerd tussen de nanodraaddimeren, zich afstotend gedragen ten opzichte van deze dimeren. Deze weggedrukte nanodraaddimeren op hun beurt bemoeilijken de adsorptie van CO-moleculen aan naburige adsorptiesites wat resulteert in de experimenteel geobserveerde “*long-ranged repulsive interaction*”. Verder stellen we ook het bestaan van, voor STM onzichtbare, brugconfiguraties voor. Na het verwijderen van de nanodraaddimeren kan een hoge dichtheid aan CO-moleculen met deze brugconfiguratie verkregen worden, wat de

nanodraadlocatie verandert in een 1D keten van parallelle CO-moleculen. Zulk een configuratie zou een aanzet kunnen zijn tot 1D moleculaire elektronica, weliswaar in een enigszins aangepaste vorm van wat men origineel voor ogen had met dit systeem.

In **Hoofdstuk 6** worden de conclusies gegeven in de vorm van antwoorden op de vragen welke we aan het begin van deze thesis hadden voorop gesteld. We kijken ook naar de toekomst: de mogelijkheid om metaalgeïnduceerde nanodraden op halfgeleideroppervlakken te ontwikkelen met behulp van *ab initio* berekeningen en hoe hiervoor de gigantische faseruimte met mogelijke structuren doorzocht kan worden, met berekende STM-afbeeldingen in de rol van mogelijke fitheidsparameter bij deze zoektocht.

Acknowledgements

Although a Ph.D. project is a one-man project, many contribute to its success, be it through support, advice or just making life enjoyable. At the end of this thesis I would like to thank all the people who had a large influence on my life during these last four years.

First of all, I would like to express my gratitude to my promoter professor Paul Kelly for his guidance and for giving me the opportunity to work in this multicultural group. Also my supervisor Dr. Geert Brocks, thank you for all the sound advice you gave me. Geert, your questions have been of great help in understanding the system which is the subject of this work. Also our discussions on science and politics I always enjoyed very much.

Dr. Claudia Filippi, although during my time in Enschede you were employed in the CMS group only for one day a week, your presence went never unnoticed. Your sparkling personality adds color to our group. I am also deeply grateful for the work you did as a member of my Ph.D. committee.

Next, I would like to thank our secretary Els. Without your help, like most of us, I would have been lost in the Dutch and university bureaucracy. Especially during the first days I arrived in the Netherlands it was always a comforting thought to know that you would be there to help us out. I also would like to thank Gerrit and Enno for maintaining our cluster, without which this work would have been impossible.

Coming to the CMS group has been an interesting experience. With almost as many cultures and nationalities as members, life becomes colorful, and it is easy to forget how much we actually learn from one another's culture by seeing it through each other's eyes.

Mohand and Victor, you were the first people I shared an office with. Victor your supersonic sneezing still sends shivers down my spine. And Mohand our many discussions on almost any topic imaginable remain fresh in mind. I also wish to thank you for your patience with me, when I was again crashing my linux system in new and interesting ways, and for teaching me the basics of bash scripting. Zhicheng, your limitless enthusiasm has always been a source of joy and inspiration to me. I enjoyed our talks about China and Chinese culture, and your excitement about my

trip to China only increased my own excitement.

Anton, when thanking you it is impossible to neglect all the time you spend, day and night, keeping our cluster running smoothly. Also, the BBQs at your place and the cycling trip to Germany, which was a personal cycling record, should not be forgotten. I always enjoyed our discussions over drinks, and the interesting stories you always had to tell.

Suleyman, we started on the same day at CMS, which tied us together for the last four years. We shared confusion about the Dutch tax system, and struggled together to get to know the behavior of VASP. I look back fondly at the laughter we shared and I am really glad to have met you and learned to know you, over drinks and at the conferences we went to.

Many more remain to be thanked, many of which have already left the group but of which it has been a great pleasure knowing. Illya, Qinfang, Petr, Volodymyr, Tulika, Paul, Gianluca, Dharendra, Pengxiang, Sanjeev, Theo, and Menno, I want to thank you guys for everything. Also the new members of our group, which I have learned to know better and better over the last year. Thijs, Diana, Omar, Deniz and Rien, thanks for the good times we had together.

The work in this thesis has been done in close collaboration with the experimental group of professor Harold Zandvliet. Arie and Harold, theoreticians and experimentalists have somewhat different approaches to problems and as a theoretician one sometimes forgets there are limitations to what can be done experimentally. This became apparent during many of our discussions. Luckily, we always managed to understand one-another in the end. Thank you for all the efforts you made to answer my sometimes impossible questions and for sharing your experimentally data. Without, it would have been impossible to successfully complete this Ph.D. project.

Op deze plek wil ik ook de tijd nemen om mijn ouders en zus te danken. Zonder jullie steun en liefde zou ik hier nooit gestaan hebben. Ik kan jullie niet genoeg voor dit alles danken.

Als laatste wil ik nog iemand danken die ik heel graag zie, mijn vriendin Sylvia. Je bent de zon in mijn leven. Jouw liefde en steun betekenen alles voor mij. Als jij er bent verdwijnen de wolken en gaat alles beter. Dank je voor alles!

Enschede, September 2009
Danny Vanpoucke



ist of Publications

[1] *Formation of Pt-induced Ge atomic nanowires on Pt/Ge(001): A density functional theory study*

D. E. P. Vanpoucke and G. Brocks

Phys. Rev. **B** **77**, 241308(R) (2008); ([arXiv:0804.1903](#)).

(**Chapters 3 and 4**)

[2] *The formation of self-assembled nanowire arrays on Ge(001): a DFT study of platinum induced nanowire arrays*

D. E. P. Vanpoucke and G. Brocks

Submitted to 2009 MRS spring meeting eproceedings.

(**Summary**)

[3] *DFT study of Pt-induced nanowires on Ge(001) I: β - terrace substrate*

D. E. P. Vanpoucke and G. Brocks

Phys. Rev. **B** (to be submitted); ([arXiv:0901.2969](#)).

(**Chapter 3**)

[4] *DFT study of Pt-induced nanowires on Ge(001) II: Nanowire Formation*

D. E. P. Vanpoucke and G. Brocks

Phys. Rev. **B** (to be submitted); ([arXiv:0901.2973](#)).

(**Chapter 4**)

[5] *CO adsorption on Pt induced Ge nanowires*

D. E. P. Vanpoucke and G. Brocks

Phys. Rev. **B** (to be submitted).

(**Chapter 5**)



Curriculum Vitae

Name: Danny Eric Paul Vanpoucke

Date of birth: April 10th, 1980

Place of birth: Ghent, Belgium

EDUCATION

2005–2009 Ph.D. in Computational Solid State Physics

Computational Materials Science, Faculty of Science and Technology at the university of Twente (The Netherlands)

Thesis: *Ab Initio Study of Pt Induced Nanowires on Ge(001)*

Supervisors: Prof. Dr. P. J. Kelly and Dr. G. H. L. A. Brocks.

1998–2004 Licentiaat Natuurkunde (M.Sc. Physics)

University of Ghent (Belgium)

Master thesis: *Bose-Einstein Condensation in Exactly Solvable Systems*

Supervisors: Dr. S. Rombouts and Ir. L. Pollet.

1992–1998 Algemeen Secundair Onderwijs (High school)

Sint-Jan Berghmanscollege, St-Amandsberg (Belgium)

Study: *Latin-Mathematics*

EMPLOYMENT

2005–2009 Research assistant (oio)

Computational Materials Science group of Prof. Dr. P. J. Kelly under supervision of Dr. G. Brocks, at the university of Twente (The Netherlands)

2004–2005 Interim Teacher Physics/Chemistry

KTA de Merodelei, Turnhout (Belgium)

2003 Tutor

Memento-Mementec-Memodi, Ghent (Belgium)



ISBN: 978-90-365-2873-3